Inverting otic tissue curvature during early development of the zebrafish inner ear semicircular canals

By

Ana Jones

School of Biosciences

The University of Sheffield

A Thesis submitted in partial fulfilment of the requirements for the degree of Doctor of Philosophy

October 2023

ACKNOWLEDGEMENTS

I would first like to express my gratitude to my supervisors Professor Tanya Whitfield and Professor Alejandro Frangi for creating this project and granting it to me, their support and guidance throughout my PhD. A special thank you to Professor Tanya Whitfield and all members who were part of the lab during my PhD for their constant encouragement, advice, support and discussions, and for providing a great environment to work in. I would also like to acknowledge Professor Alejandro Frangi, Dr Tania Mendonca and Dr Jose M. Pozo, who I collaborated with for the manuscript presented in chapter 3. Equally, I acknowledge and thank Professor Tanya Whitfield and Dr Sarah Baxendale for their collaboration in the manuscript presented in chapter 3 and the manuscript presented in chapter 5, together with Dr Elvira Diamantopoulou.

I am very grateful to my advisors Dr Emily Noël and Dr Natalia (and temporary advisor Dr Martin Zeidler) for their essential feedback, support and advice throughout the course of my PhD. I would also like to acknowledge Dr Emily Noël and Dr Henry Roehl for sharing resources of their labs with me, and the members of their labs for being a great company to work alongside with. Thank you to all the staff of the aquarium facilities as well, for looking after the fish I used during my PhD.

A very special thank you to my close friends Juliana Sánchez-Posada and Steph Popa who supported me, both academically and in my personal life, and provided endless advice and encouragement. I am also very grateful for all my friends who prayed with and for me over the last five years.

Thank you to my amazing family: parents, brother, grandparents, uncles and aunts, cousins, parents-in-law and brother-in-law. Thank you all for the love, support and encouragement you have always given me, and for all your visits to the UK (those that live in Portugal). A big thank you to my mum, for coming to live with us for the past month and keeping us alive while I was writing up. A special thank you to my wonderful husband, Phil, for his love and support, and to my beautiful daughter, Sofia, for putting a smile on my face in the midst of tiredness.

Thank you to God, for sustaining me each day.

ABSTRACT

Epithelial sheet folding is a common morphogenetic process in early development of organisms across different species, allowing the formation of organs and structures with a diversity of shapes. During zebrafish inner ear development, different events of tissue folding occur in which the epithelium folds through invagination to form the endolymphatic sac, and through evagination to form the epithelial projections of the semicircular canals. Evagination events, specifically those that invert tissue curvature, have not been studied in much detail.

This project aimed to characterise the evagination event that initiates epithelial projection formation in the zebrafish inner ear. Light-sheet microscopy data was used to develop and test an automated cell shape analysis tool, *Origami*; whereas confocal microscopy data was used to perform, with the help of *Origami*, a 4D quantitative analysis of cell shape changes. I have demonstrated that cells in the regions of projection outgrowth, undergo several shape changes during the folding event, including basal constriction, elongation of the apico-basal axis and apical relaxation. I observed a redistribution of F-actin, myosin-II and E-cadherin from the apical to the basolateral domain, in epithelial projection cells, that was coincident with the inversion of tissue curvature. In addition, I have shown that deposition of chondroitin sulphate precedes otic epithelium folding and is localised to the sites of projection outgrowth. Study of a mutant with low levels of heparan sulphate, showed that biosynthesis of this polysaccharide is essential for normal epithelial projection outgrowth. Finally, preliminary work revealed that production of hyaluronan might be dispensable for the folding event that precedes projection outgrowth. Further work is needed to better understand the mechanisms at work during evagination of the otic epithelium; however, the observations in this thesis brought to light a new model to study folding events through evagination, and more specifically events of epithelial curvature inversion.

STATEMENT OF CONTRIBUTION

I, Ana Jones, declare that the work presented in this Thesis is my own, except where explicitly stated, and that the observations reported within it, have not been submitted for consideration for the award of a degree or other qualification, either in part or in full, at the University of Sheffield or any other University or similar institution.

LIST OF ABBREVIATIONS

Actb2 – Actin beta 2

Adgrg6 – Adhesion G protein-coupled receptor G6

AP – Anterior projection

ArhGEF11 - Rho guanine exchange factor 11

Bmp – Bone morphogenetic factor

Bp – Base pairs

BSA – Bovine Serum Albumin

Cdh2 – Cadherin 2

Celsr1 - Cadherin EGF LAG seven-pass G-type receptor 1

Chsy1 – Chondroitin Sulphate Synthase 1

CSPG – Chondroitin Sulphate proteoglycan

CytoD - Cytochalasin D

2/3/4D – Two/Three/Four dimension(al)

Dfna5 – Deafness autosomal dominant 5

DIC – Differential interference contrast

DLS – Dorsolateral septum

Dlx – distal-less transcription factors

DMSO - dimethyl-sulfoxide

DNA – Deoxyribonucleic acid

Dpf – Days post fertilisation

Dzip1 – DAZ Interacting Zinc Finger Protein 1

EB3 – End-binding protein 3

E-cad – E-cadherin

ECM – Extracellular matrix

EGFP – Enhanced green fluorescent protein

ES – Endolymphatic Sac

EVL – Enveloping layer

Ext2 - Exostosin glycosyltransferase-2

EYA – Eyes absent gene family

F-actin – Filamentous actin

FAK - focal adhesion kinase

FGF – Fibroblast growth factor

Fig – Figure

Foxi1 – Forkhead box 1

Foxn4 – Forkhead box n4

GAG – Glycosaminoglycan

GFP - green fluorescent protein

Gpr126 – G-protein coupled receptor 126

HA – Hyaluronan

Habp – Hyaluronic acid binding protein

Hapln1 - Hyaluronan And Proteoglycan Link Protein 1

Has3 – Hyaluronan synthase 3

Hdac1 – Histone deacetylase 1

Hip1 - Huntingtin Interacting Protein 1

H2B – Histone 2b

Hpf – Hours post fertilisation

Hr – hour(s)

HSPG – Heparan Sulphate proteoglycan

KSPG – Keratan Sulphate proteoglycan

Lau – Lauscher

Log – Logarithm

Mitfa - Melanocyte inducing transcription factor a

Mpv17 - Mitochondrial Inner Membrane Protein MPV17

mRNA – Messenger ribonucleic acid

4-MU - 4-Methylumbelliferone

Myl12.1 – Myosin light chain 12 genome duplicate 1

NE – Neural ectodermal

OC – otic cup

OEPD – otic-epibranchial domain

OP – otic placode

Otx – Orthodenticle homeobox gene family

OV – Otic vesicle

Par(d)1/3 - Protease-activated receptor-1/3

Pdlim7 - PDZ and LIM domain 7

PBS – Phosphate-buffered saline

PBS-Tr - PBS Triton

PCR - polymerase chain reaction

PFA - paraformaldehyde

PP – Posterior projection

PPR – Pre-placodal region

Ptc2 – Patched-1

PTU - 1-phenyl 2-thiourea

RA – Retinoic acid

RFP – Red fluorescent protein

Sgl – Sugarless

Smad6b – SMAD Family Member 6

Sna – snail

Sox10 - SRY-box transcription factor 10

SSC(s) – semicircular canal(s)

Supp – supplementary

Tbx1/2 – T-box transcription factor

Tg – Transgenic

Twi - twist

UDP - uridine 5’-diphosphate

UDP-GlcA - UDP-glucuronic acid

UDP-GlcNAc - UDP-N-acetylglucosamine

UGDH – UDP-glucose 6-dehydrogenase

UGT – UDP-glucuronosyltransferase

VB – Ventral bulge

Vcana/b – versican a and b

VP – Ventral Projection

Wnt – wingless/integrated

xEF1a – Xenopus elongation factor 1a

ZO-1 – Zonula occludens 1

TABLE OF CONTENTS

LIST OF FIGURES

LIST OF VIDEOS

LIST OF TABLES

CHAPTER 1

Introduction

1.1 Epithelial folding in morphogenesis

1.1.1 Morphogenesis

Morphogenesis means creation of shape, and this process can happen at different levels within the organism: from cells, to tissues, organs, and also at the organismal level (Gilmour et al., 2017). The reshaping of these systems is a complex process that depends on the harmonious integration of and the reaction to chemical and physical signals, and the information of space and time provided by developmental patterning. Chemical communication can occur between neighbouring cells - through gap junctions (Guthrie et al., 1988), membrane bound ligands and receptors (Adam et al., 1998), and planar transcytosis (Dierick and Bejsovec, 1998) - or at a range of distances – through nanotubes and cytonemes (Sanders et al., 2013), exosomes (Gross et al., 2012), and passive diffusion (Driever and Nüsslein-Volhard, 1988). Physical communication between cells also occurs through a variety of mechanisms, including cytoskeletal reorganisation, changes in cell adhesion, extracellular matrix (ECM) remodelling, activation of mechanically regulated channels or mechanosensitive adhesions, and changes in cell shape and/or volume (Espina et al., 2023). These mechanisms of cell communication do not happen in isolation but instead, some of these happen simultaneously and/or sequentially in different combinations, hence morphogenesis is a very dynamic process and is capable of generating such a variety of shapes (tissues, organs and organisms).

Study of morphogenesis has been focused, for many years, within the context of embryogenesis; however, embryonic development is not the only time when morphogenesis occurs. It is also observed, for instance, during wound healing (Wood et al., 2002) and cancer establishment and progression (Suhail et al., 2019). Successful morphogenesis is therefore essential for creating, restoring and maintaining functional organs, and sometimes for organism survival (Kumai et al., 2000).

1.1.2 Generating shape from epithelial sheets during embryonic development

Embryonic tissues are organized as two main tissue types: epithelium and mesenchyme. Mesenchymal tissue is characterised by loosely packed cells within the ECM. Cartilage, bone and muscle are examples of tissues that derivate from the mesenchyme (Buxboim and Discher, 2012). In contrast, epithelial tissue generally consists of tightly packed cells that delineate organs or are positioned at the interface between two different systems/environments. Some major roles of epithelial tissues include sensory reception, filtration, secretion, providing a physical barrier, absorption, filtration and diffusion (Edelblum and Turner, 2015). Epithelial tissues exhibit an intercellular cohesion and a clear apicobasal polarity that dictates the distribution of different features of the cells along their apicobasal axis (Gilmour et al., 2017). The apical, basal and lateral domains of these cells are determined by the distribution of cell-cell adhesion molecules and the organization of their actomyosin and microtubule cytoskeletons, which in turn are regulated by a network of epithelial polarity factors (St Johnston and Sanson, 2011).

Epithelial sheets are very often the substrate for generating shape during the formation of organs. Animals present more shapes than we could ever count; however, the number of fundamental processes that can re-shape epithelial layers during embryonic development is more limited (John and Rauzi, 2021). These can include, for example, growing, shrinking, twisting, thinning, thickening, folding and converging/extending (John and Rauzi, 2021) (Figure 1.1A). Another process of reshaping an epithelium is sculpting it through programmed cell death (Hurle and Colvee, 1982). A more extreme transformation of tissues can occur when epithelial layers undergo epithelial-to-mesenchymal transition (EMT) or mesenchymal-to-epithelial transition (MET). In the first case, polarised epithelial cells undergo a progressive loss of epithelial markers and acquire mesenchymal markers which allow these cells to gain different levels of migratory activity (Barrallo-Gimeno and Nieto, 2005; Wang et al., 2005; Zoltan-Jones et al., 2003). In the second case, mesenchymal cells undergo a reverse process to adopt epithelial features (Bedzhov and Zernicka-Goetz, 2014; Campbell et al., 2010; Pei et al., 2019). It is important to mention that these transitions are not necessarily a binary process and that the ability of cells to adopt intermediate features in between the two opposing states has been shown to be crucial during embryogenesis (Campbell and Casanova, 2016).

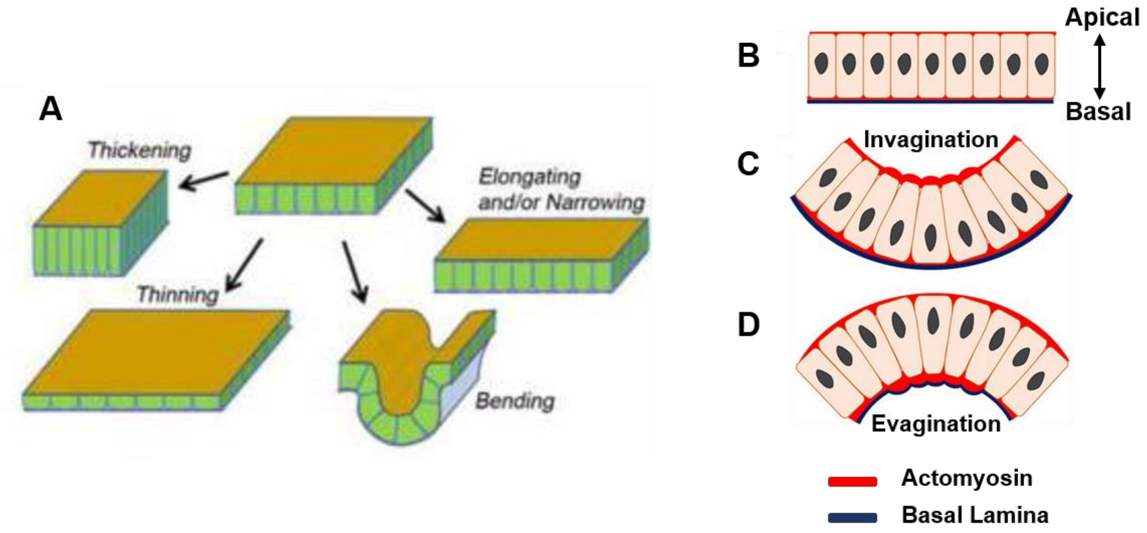

Figure 1.1 - Mechanisms of epithelium re-shaping during morphogenesis.

(**A**) Diagram illustrating examples of mechanisms through which epithelial layers can be transformed into different shapes during embryonic development (adapted from (Davidson, 2012)). (**B**) Illustration of an epithelial sheet which can undergo invagination (**C**), resulting in a concave aspect due to apical constriction and/or basal relaxation; or evagination (**D**) which results in a convex aspect due to basal constriction and/or apical expansion (adapted from (Wang et al., 2022)).

1.1.3 Epithelial folding

Folding is one of the essential mechanisms able to transform a 2D sheet of epithelial cells into a 3D structure and it is present across organisms of different levels of complexity, such as corals (Hayward et al., 2004), invertebrates like the fly (Spencer et al., 2015), and vertebrates like the chick (Kinoshita et al., 2008) or the mouse (Sulistomo et al., 2019). Epithelial layers can either fold through invagination or evagination. Invagination of an epithelial sheet (sometimes described as folding apically) results in a concave shaped epithelium in which the inner surface is made from the apical surface of cells (Lewis, 1947) (Figure 1.1C). This tissue shape change often requires changes at the cellular level like apical constriction and/or basal relaxation. Contrarily, an evagination is characterised by a folding event in which the basal cell surface makes up the inner ring resulting in a convex shaped epithelium (Sinn and Wittbrodt, 2013) (Figure 1.1D). This type of tissue folding commonly involves basal constriction and/or apical relaxation. Traditionally, epithelial folding mechanisms described in the literature are based on events of invagination, possibly because this type of tissue folding has been more observed and therefore studied in more detail.

These two types of folding can happen separately; however, they can also occur together to achieve more complex structures during organ development. Folded epithelia flanked by epithelium with an opposite curvature has recently been named as ‘reverse curves’ (Wang et al., 2022). In this review, authors describe three examples of ‘reverse curves’ formation during morphogenesis of the circumvallate papillae of the tongue, the crypt-villus structure of the intestine, and the tooth germ (Wang et al., 2022). Not only are the mechanisms involved in simple evagination not just an inversion of invagination mechanisms, but to generate ‘reverse curves’ a more sophisticated coordination of these sets of mechanisms might be required.

1.2 A classic model of epithelial folding

One of the longest standing and most well established models of epithelial folding is the formation of the ventral furrow and mesoderm invagination in the *Drosophila* embryo. This folding event is the first stage during morphogenesis of the mesoderm layer, a comprehensively studied process of *Drosophila* gastrulation (Gheisari et al., 2020).

Ventral furrow formation is initiated by a group of presumptive mesoderm cells along the anterio-posterior axis in the ventral region of the Drosophila embryo (VF in Figure 1.2). The cells closer to the midline undergo flattening of their apical surfaces - surfaces facing the outside of the embryo (Figure 1.2B) (Kam et al., 1991; Sweeton et al., 1991), and soon after, constriction of the apical domain. These two cell shape changes result in a protrusion visible on the ventral surface of the embryo (Figure 1.2C) (Leptin and Grunewald, 1990; Sweeton et al., 1991). During apical constriction, the nuclei of the ventral cells move in an apical-to-basal direction and the apico-basal axes elongate (Figure 1.2C) (Costa et al., 1993). Following this elongation, cells shorten back and their basal domain expands making these cells lose their columnar morphology and acquire a skewed/wedge shape (Figure 1.2D) (Costa et al., 1993). A narrow furrow forms, and as the apical constriction propagates to neighbouring cells, the invaginating process occurs and the furrow deepens (Figure 1.2E). There is a population of mesoderm cells flanking the ventral cells, called lateral cells, that do not undergo apical constriction. Instead, these cells undergo apical expansion, and stretch towards the ventral furrow (Figure 1.2E) (Fuse et al., 2013; Leptin and Grunewald, 1990; Rauzi et al., 2015). Finally, the furrow closes to form an epithelial tube inside the embryo (Figure 1.2F) (Sweeton et al., 1991; Turner and Mahowald, 1977).

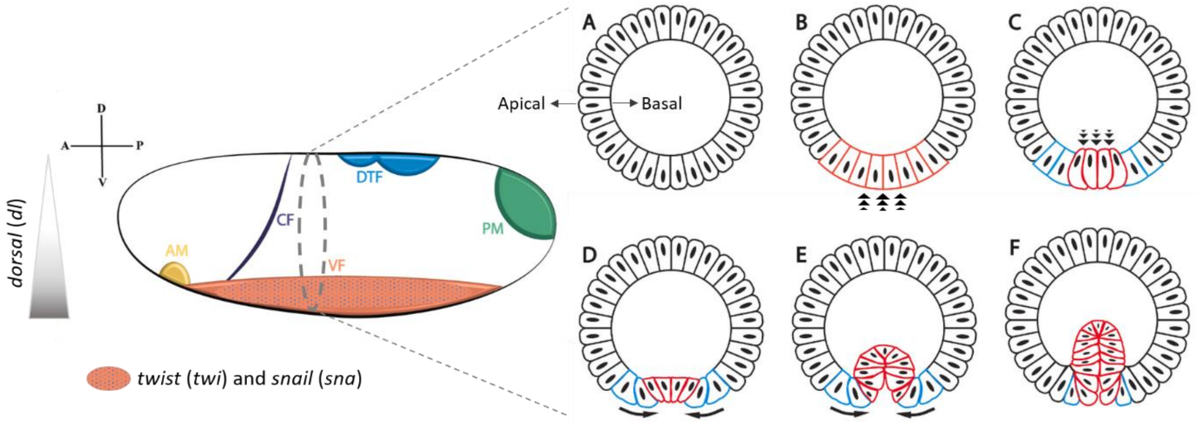

Figure 1.2 – Cell movements and shape changes during ventral furrow formation and mesoderm invagination in the *Drosophila* embryo.

The diagram on the left summarises the morphogenetic events during *Drosophila* embryo gastrulation from a lateral view: invagination of the anterior and posterior midguts (AM and PM respectively), formation of the cephalic and ventral furrows (CF and VF respectively), and dorsal transversal fold (DTF) formation. Ventral furrow formation is induced and regulated by the expression of three genes: *twist* (*twi*) and *snail* (*sna*), which are expressed along the anteroposterior axis in the ventral region of the embryo; and *dorsal* (*dl*), which is expressed as a ventral-to-dorsal gradient. (**A-F**) Transverse cross-section diagrams of the central region of the embryo. A group of cells in the ventral region (red cells) undergoes flattening of the apical surface (**B**), followed by apical constriction and increase in length along the apico-basal axis, also accompanied by a basal shift of their nuclei (**C**). Next, cells shorten making a furrow (D) which is deepened when apical constriction propagates (**E**). During this invagination process, the basal domain of the ventral furrow cells expands (**E**, and **F**), whilst in the cells adjacent to the ventral furrow (blue cells) the apical domain is the one expanding (**E**). When invagination is completed, the mesoderm is shaped as an epithelial tube inside the embryo. Abbreviations: A – Anterior; P – Posterior; D – Dorsal; V – Ventral. (Adapted from (Gheisari et al., 2020)).

Extensive research has been done on the genetic and biomechanic regulation of the ventral furrow formation. Three genes expressed in the presumptive mesoderm tissue before ventral furrow formation – *twist* (*twi*), *dorsal* (*dl*) and *snail* (*sna*) - are known to be essential for this process (Figures 1.2 and 1.3) (Grau et al., 1984; Leptin and Grunewald, 1990; Simpson, 1983; Thisse et al., 1988). *Twi* and *dl* cooperate to activate mesoderm-specific genes in the blastoderm, including *sna* (Roth et al., 1989; Rushlow et al., 1969; Sandmann et al., 2007); whereas *sna* promotes mesoderm development both by repressing lateral and dorsal genes (Nibu et al., 1998; Qi et al., 2008) and by activating mesodermal enhancers in the ventral region (Figure 1.3) (Rembold et al., 2014).

One of the target genes of twi is *folded gastrulation* (*fog*) (Costa et al., 1994). This gene encodes a secreted signalling protein important for coordinating changes in the morphology of the apical domain, including apical flattening in the ventral furrow cells (Costa et al., 1994; Dawes-Hoang et al., 2005; Morize et al., 1998). Fog was shown to act through G-protein-coupled receptors to recruit the Rho guanine nucleotide exchange factor RhoGEF2 and to activate the small GTPase Rho1 (Figure 1.3) (Kerridge et al., 2016; Manning et al., 2013). There is also evidence for a Fog-independent pathway that depends on Sna (Costa et al., 1994; Dawes-Hoang et al., 2005;

Kolsch et al., 2007; Morize et al., 1998). This pathway requires the transmembrane protein T48 which promotes accumulation of RhoGEF2 and therefore activation of apical Rho1 (Figure 1.3) (Kolsch et al., 2007). Rho1, in turn, regulates the contractility of the actomyosin cytoskeleton and therefore apical constriction through its effectors, Rho Kinase and Diaphanous (Figure 1.3) (Barrett et al., 1997; Dawes-Hoang et al., 2005; Häcker and Perrimon, 1998; Manning and Rogers, 2014). In a sna- and twi- dependent manner, pulsed contractions of the apical myosin-II network are translated into apical constriction by the adherens junction-associated F-actin filaments which also bind to myosin-II (Coravos and Martin, 2016; Martin et al., 2009; Mason et al., 2013). Higher epithelial tension along the anteroposterior axis of the embryo has been shown to explain why the presumptive mesoderm cells undergoing apical constriction do not constrict their apical apices isotropically - their ventrolateral axes are shorter than their anteroposterior axes (Martin et al., 2010; Sweeton et al., 1991). This causes the ventral furrow to look narrow and elongated along the anteroposterior axis, instead of having a circular geometry.

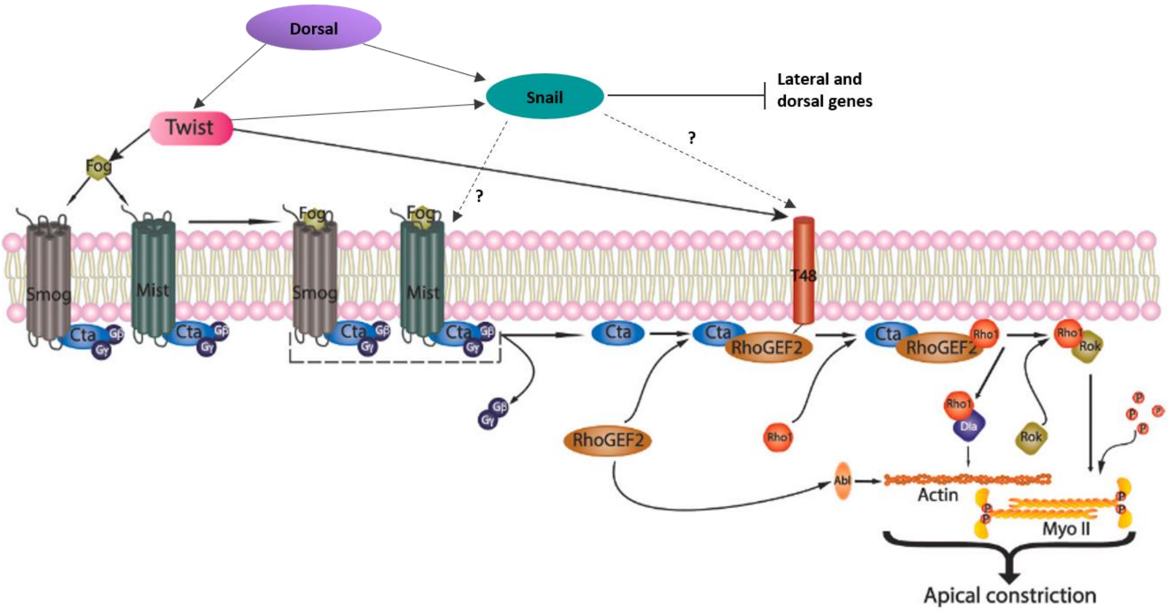

Figure 1.3 – Signalling pathways promoting apical constriction required for mesoderm invagination.

In the presence of *dorsal*, *twist* and *snail* activate G-protein coupled receptors like Smog and Mist (normally through the ligand Fog) resulting in the activation of a trimeric G-protein (made of Concertina (Cta), Gβ13F and Gγ1). This initiates a signalling cascade to activate RhoGEF2 (Rho guanine nucleotide exchange factor 2). However, RhoGEF2 can also be activated by the transmembrane protein T48, which is also downstream of *twist* and *snail*. Either way, once activated, RhoGEF2 is able to activate GTPase Rho1, which in turn, works with its effector proteins Rho kinase (Rok) and Diaphanous (Dia) to regulate the assembly and activity of the actomyosin network required for apical constriction. (Adapted from (Gheisari et al., 2020)).

The observation that ectopic expression of Fog was able to induce apical flattening and constriction but not furrow invagination (Morize et al., 1998), made it clear that the first process is differently regulated from the later. A few mechanisms have been reported to contribute to mesoderm invagination. One is based on the ability of E-cadherin-mediated adhesions to integrate overall tissue tensile forces, helping to shape the furrow (Oda et al., 1998). This is supported by the fact that disrupting adherens junctions during ventral furrow formation leads to a breakdown of the ventral furrow and prevents its invagination (Martin et al., 2010). A second mechanism is linked to the shortening of mesoderm cells during ventral furrow formation. A study has shown that myosin-II cables form along the apico-basal axes of ventral furrow cells. When these cables are ablated, invagination of the ventral furrow is disrupted, suggesting a role for the apico-basal myosin-II cables in facilitating this process (Gracia et al., 2019).

Mesoderm invagination during *Drosophila* gastrulation has been used as a model of epithelial folding for decades. Despite not being completely understood yet, it is extremely well studied and, for this reason, it has provided a starting point for other tissue folding studies in different organisms. Other cell mechanisms and cell behaviours have, in the meantime, been observed and discussed, especially in systems when the epithelium folds through evagination.

1.3 Cellular mechanisms and behaviours driving epithelial folding

1.3.1 Cell shape changes

Cells are the units of epithelial sheets, and therefore it is not surprising that they undergo all sorts of shape changes during morphogenesis. The model system of the *Drosophila* mesoderm invagination showed that during epithelial folding, cells can undergo a variety of shape changes. Examples of such cell shape changes and others have also been described in a number of organisms and structures.

The formation of neuromasts in the zebrafish lateral line is an example of a drastic change in cell shape involving apical constriction. The cells that form these organs have to migrate from the cranial placode to different locations along the lateral line, transition from mesenchymal to epithelial, and then constrict their apical domain to form radially organised rosettes (Ernst et al., 2012). Another case where we see an epithelium adopting a concave curvature is the neural tube closure in developing *Xenopus* embryos. The neural epithelial cells undergo an extensive apicobasal elongation and an apical constriction, which seem to be two independent processes (Lee et al., 2007). Apical constriction mediated by myosin-II accumulation also occurs in early intestinal crypt formation in mice, which is an interesting invagination example because this process happens postnatally (Sumigray et al., 2018).

Contrary to many systems where epithelium folding is associated with apical constriction, it was reported that basal constriction followed by apical expansion, dependent on Wnt5b and Fak, occurs in the zebrafish midbrain-hindbrain boundary constriction (Gutzman et al., 2018). Though less common, basal constriction is not a newly described mechanism, and it has been described in other systems like the *Ciona* notochord tubulogenesis, in which basal cell constriction allows cell elongation (Dong et al., 2011); during development of the hydrozoan *Dynamena pumila*, at the margins of the folds in the anchoring disc (Kupaeva et al., 2018); or the retinal neuroepithelium during folding of the zebrafish optic cup (Sidhaye and Norden, 2017). During optic cup folding in the zebrafish, the retinal neuroblasts undergo a reduction of their basal surface area, whilst the area on the apical domain remains the same (Nicolás-Pérez et al., 2016). Through time-lapse imaging of live zebrafish larvae, the authors showed that at the time of acute bending of the retinal epithelium, the neuroblasts reach their highest level of basal constriction. A folding event through evagination can also be found in the developing endocardial cushions of the atrioventricular canal (Beis et al., 2005). Initially the heart tube of the zebrafish embryo consists of a layer of endocardial cells surrounded by myocardial cells.

Eventually the endocardial layer (and later the myocardial one) starts bending as the cells change their shape from squamous to cuboidal to form the endocardial cushions of the heart (Beis et al., 2005).

In addition, through the analysis of the epithelial folds in the *Drosophila* embryo and the zebrafish epithelium at 50% epiboly stage, a new cell shape has been proposed – scutoid (Gómez-Gálvez et al., 2018a). In this study, scutoids are suggested to help stabilisation of the three-dimensional packing in curved epithelia by compensating the difference in area between the two surfaces of the epithelium. In the past, epithelial cells have been consistently represented as prisms with apical and basal faces that are polygonal, regardless of the system being studied and despite not always matching with data observations. As this study shows, examples of those anisotropic shapes can be seen especially when tissues exhibit high levels of curvature where cells contact different neighbours at different points along the apico-basal axis (Gómez-Gálvez et al., 2018a).

Although individual cell shape changes are crucial for the reshaping of an epithelial layer, in order to have an effect at the tissue level, cells need to be responsive to their own internal instructions from genetic pathways, and to mechanical forces from their surrounding environment; to communicate with each other, and often with the ECM, usually through integrin and cadherin receptors (Nicolás-Pérez et al., 2016).

1.3.2 Rearrangement of the cytoskeleton

The activity of the cellular cortex is the main generator of internal force, helping the cell to resist to external mechanical stresses, but also to maintain or rearrange its shape. It consists of actin filaments, myosin II motors and actin-binding proteins that are able to interact and generate local contractions (Bray and White, 1988).

The most well established model of epithelial folding through apical constriction assumes that the change in cell conformation is driven by a spatially restricted activation of the non-muscle myosin activity that generates contractions of the actin filaments (Sawyer et al., 2010). One example of cell apical constriction due to locally restricted myosin-II activity in the zebrafish is the formation of the rosettes in the lateral line mentioned in the previous section (Ernst et al., 2012). Here the non-muscle myosin in the apical domain of the rosette cells is phosphorylated and therefore activated by Rho kinases, which in turn seem to be activated by locally restricted Shroom3, a transcriptional target of FGF signalling (Ernst et al., 2012). In phase two of otic morphogenesis during chick embryonic development, these active Rho kinases are restricted to the apical junction region of the cell due to the activity of ArhGEF11 (Rho guanine exchange factor) and upstream of that Celsr1 (a transmembrane protein that regulates planar cell polarity) which also co-localises to this apical domain of the cell (Sai et al., 2014). Another example of epithelial invagination is seen during *Drosophila* gastrulation when the cephalic furrow forms (Spencer et al., 2015). Myosin-II is known to help generate the force necessary for the movement of actin filaments, therefore helping to change cell shape as well. What is interesting about the cephalic furrow formation in *Drosophila*, is that cell apical constriction in the invaginating tissue is not driven by myosin-II activity but rather the myosin-II rearrangement is a response to apical constriction (Spencer et al., 2015). Cell shape changes – apico-basal shortening and basal expansion – associated with an increase in cortical F-actin in the apices of those cells are the ones driving the formation of the cephalic furrow instead (Spencer et al., 2015). Epithelial folding was recently found and described even in a colonial marine hydrozoan called *Dynamena pumila* (Kupaeva et al., 2018). In this case, invagination of the epithelium is associated with the accumulation of actin in the apical domain of bottle-shaped cells, whilst their nuclei move to the basal domain (Kupaeva et al., 2018).

As described in section 1.3.1, the folding of the optic cup in the zebrafish involves a change of cell shape involving basal constriction (Nicolás-Pérez et al., 2016). In this system, both the accumulation of myosin at the basal surface in scattered neuroblasts and laminin-mediated adhesion to the extracellular matrix play a role in maintaining the pulsatile dynamics and contractility of the basal feet of the retinal cells (Nicolás-Pérez et al., 2016). F-actin has also been found to be strongly localised to the basal surface of basally constricted neuroepithelial cells during zebrafish midbrain-hindbrain barrier formation (Gutzman et al., 2008). Upon knockdown of myosin-II, distribution of F-actin alongside cell shape changes (in length and width) and ultimately the evagination process were disrupted (Gutzman et al., 2015).

1.3.3 Redistribution of adhesion proteins

In mature polarised epithelia, cell-cell contacts are fairly stable in order to maintain the integrity and shape of the tissue and organ (Figure 1.4A). In contrast, during morphogenesis, cell-cell contacts are much more dynamic which facilitates their redistribution and enables tissues to change their shape. Adherens junctions, a main intercellular adhesion mechanism, are often involved in re-shaping tissues.

Not all apical constriction driving epithelial folding is dependent on differential cortical contractility along the apico-basal axis of the cell, as described in the previous section. During the formation of the dorsal transverse folds during *Drosophila* gastrulation, the beginning of epithelial folding is associated to an apical to basal shift of adherens junctions (movement of the cadherin complex) in the initiating cells but not in the surrounding cells, forcing the tissue to bend towards the initiating cells (Wang et al., 2012). This cellular behaviour is regulated by polarity proteins like Bazooka/Par-3 and Par-1 (Wang et al., 2012). In the case of the developing endocardial cushions of the zebrafish atrioventricular canal, the transition of cellular morphology is accompanied by the expression of Dm-grasp, a cell surface adhesion molecule that seems to appear when these endothelial cells become cuboidal (Beis et al., 2005). Knockdown of genes like *foxn4*, *tbx2* (Chi et al., 2008) and *pdlim7* (Camarata et al., 2010) result in cells remaining squamous, and in the case of *pdlim7* knockdown, Dm-grasp fails to be expressed.

Recent work has suggested that zebrafish neural plate cells undergo internalisation through a mechanism dependent on myosin-II, which is coordinated by Cdh2 (Araya et al., 2018). Even though this is a different morphogenetic process from epithelial folding, this study shows that these neural plate cells change their shape – constriction of dorsal surface membrane – by adopting strategies typical of epithelial sheets like cell-cell adhesion rearrangement.

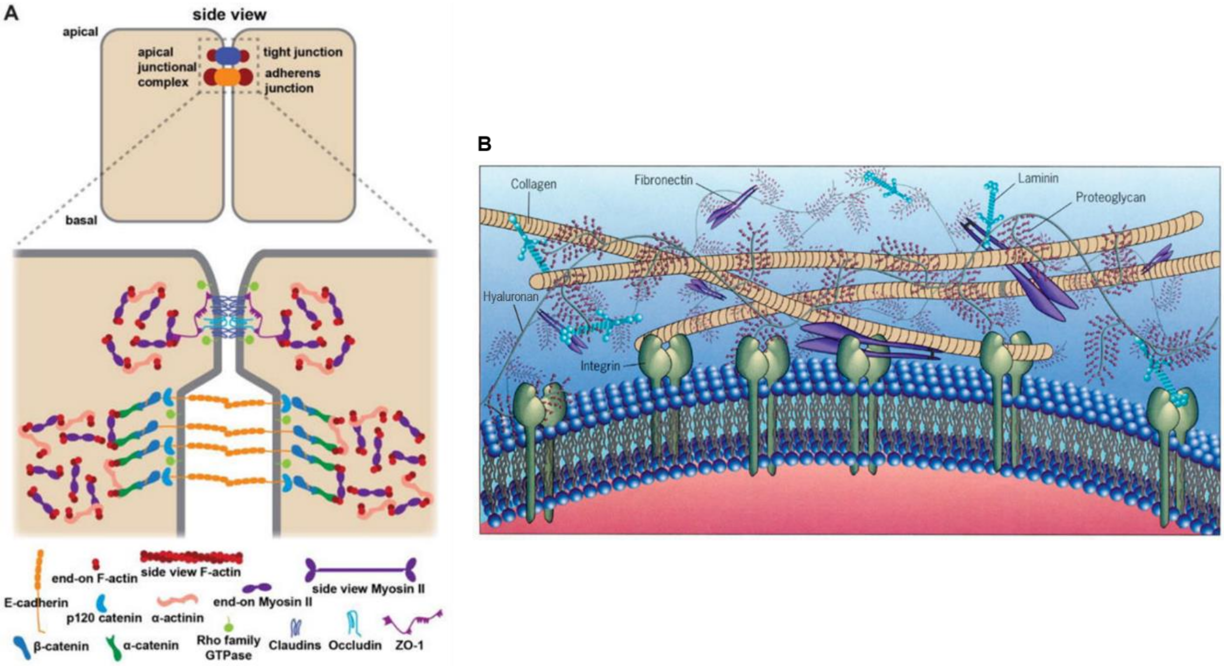

Figure 1.4 - Structure of the apical junctional complex and the extracellular matrix.

(**A**) Diagram of an apical junctional complex between two epithelial cells, including the typical structure of a tight junction and an adherens junction. Transmembrane proteins like occludins, claudins and E-cadherins, establish intercellular interactions; whilst scaffolding proteins such as ZO-1 and catenins, link the previous proteins to the contractile actomyosin cytoskeleton (adapted from (Arnold et al., 2017)). (**B**) Illustration of the composition and structure of the extracellular matrix. Extracellular matrix tissue specificity is determined by the combination of its different components, in particular the types of proteins and glycans. The transmembrane proteins integrins establish the connection between the cytoskeleton and the extracellular matrix (Landry et al., 2018).

1.3.4 ECM production and signalling

The ECM is a non-cellular network of macromolecules including collagens, proteoglycans, fibronectins, and elastin, that also contains a reservoir of water, growth factors and bioactive molecules (Aumailley and Gayraud, 1998; Streuli, 1999) (Figure 1.4B). The composition of the ECM is specific to each type of tissue and depending on the ratios of the different components, it can present a variety of biochemical and biophysical properties. The ECM can adhere to the cells through ECM receptors linking this extracellular environment to the cytoskeleton and intracellular activity. The ECM is extremely dynamic, capable of undergoing remodelling a) in response to external stimuli like force (Yu et al., 2011), damage (Jakeman et al., 2014), stresses (Dzamba et al., 2009) or disease (Mott and Werb, 2004); or b) to induce/support morphogenetic and biological processes such as cell migration (Trinh and Stainier, 2004), growth (Williams et al., 2008), differentiation (Czyz and Wobus, 2001) and epithelial folding (Sui et al., 2018).

Neural tube formation in vertebrates often requires some form of epithelial folding. A new study has recently explored the role of extracellular matrix in tissue folding within the human fetal cortical plate (Long et al., 2018). Inhibition of hyaluronic acid or of its receptor leads to reduced cortical folds. The same study also shows that along with hyaluronic acid, other components of the extracellular matrix, including HAPLN1, lumican and collagen I, induce the formation of cortical folds in the human neocortex, therefore playing a role in its expansion (Long et al., 2018). A component of the basal lamina called laminin has been shown to be required for basal constriction, apical expansion and, as a result, epithelial evagination in zebrafish midbrain-hindbrain boundary formation (Gutzman et al., 2008). In contrast, local reduction of ECM components has been shown to induce basal relaxation and be sufficient for epithelial folding of the wing imaginal discs in *Drosophila* (Sui et al., 2018).

1.4 The zebrafish inner ear as a model to study epithelial folding

Historically, the *Drosophila* embryo has been by far the preferred model when it comes to studying mechanisms involved in epithelial folding. Despite this, in recent years, there has been a gradual emergence of studies starting to explore epithelial folding events during zebrafish embryogenesis (Bryan et al., 2016; Gutzman et al., 2015; Nicolás-Pérez et al., 2016; Peal et al., 2009, 2011; Visetsouk et al., 2018). The zebrafish has been extremely useful for biological and biomedical research. Its advantages include optically clear embryonic stages, ease of maintenance and breeding, tool availability for generating mutant and transgenic lines, and conserved genes, pathways and body structures.

The inner ear is the most internal part of the ear and the organ that mediates the senses of hearing and balance. Its structure is described as a 3D fluid-filled labyrinth that includes sensitive sensory structures responsible for detecting sound, motion and gravity (Alsina and Whitfield, 2016). During embryonic development of the zebrafish inner ear, one can observe a few events of tissue folding (Mendonca et al., 2021), including a scenario in which the otic epithelium folds in the opposite direction of its initial curvature through evagination. This can potentially offer a new model of an evagination process and case of study for ‘reverse curves’. In addition, these events of tissue folding are essential for semicircular canal morphogenesis in the zebrafish inner ear, a system that is responsible for detecting motion and gravity. Malformation and aplasia of the semicircular canals can lead to severe impairment of vestibular function. For these reasons, there is a clear need to start exploring epithelial folding events during zebrafish inner ear morphogenesis.

1.4.1 Early development of the inner ear: formation of the otic vesicle

The inner ear has its origin in the otic placode (OP), which together with other cranial placodes emerges from the common pre-placodal region (PPR) – an area of ectoderm around the anterior boundaries of the neural plate (Figure 1.5A, A’) (Bailey and Streit, 2005). The PPR is progressively segregated into individual placodal fates through expressing specific combinations of transcription factors and specific placode inducing signals. In the case of most vertebrates, the OP emerges from the *Pax2/8*-expressing otic-epibranchial precursor domain (OEPD) located near the hindbrain (McCarroll et al., 2012). Movement and convergence of

PPR cells to form the zebrafish OEPD seem to depend partially on the functioning ECM receptor Integrin-α5, which relies on Fgf signalling (Bhat and Riley, 2011b). In turn, induction of the OP from the OEPD relies on the expression of transcription factors of the Gata, Dlx, Foxi and Tfap families, and on signalling molecules of the Fgf and Wnt families from the surrounding mesoderm and neural ectoderm (Bhat et al., 2013; Freter et al., 2008; Khatri et al., 2014; Ohyama et al., 2006; Padanad et al., 2012; Yao et al., 2014). In the zebrafish embryo, like in mice and chick, a gradient of Pax transcription factors was also shown to play a role in segregating otic and epibranchial fates, in which high Pax2a levels, driven by the activation of the Wnt pathway, contribute to an otic identity (McCarroll et al., 2012). The signalling involved in the clustering of the OP cells and their physical segregation from other placodes is not yet fully understood. It was suggested that cellular displacements that follow mitotic events could be involved in this process due to the observation of long cytokinetic bridges during placode formation in the chick embryo (Alvarez and Navascués, 1990). Movements of cells from surrounding tissues have also been shown to impact on the coalescence of other placodes (olfactory and epibranchial) in the zebrafish and chick embryos but this has not been shown for the otic placode (Harden et al., 2012; Theveneau et al., 2013; Torres-Paz and Whitlock, 2014).

The OP becomes morphologically recognisable by the 10 somites stage as a thickened region in the chick and mouse or a mass of cells in the zebrafish embryos, separate from the surrounding ectoderm (Figure 1.5C, C’) (Graham and Begbie, 2000; Kimmel et al., 1995a). In both cases, the OP is visible due its cells undergoing elongation and acquiring apicobasal polarity (Hoijman et al., 2015; Ladher, 2017). In the zebrafish embryo, both a tight junction protein (ZO-1) and a polarity establishing protein (Pard3) locate apically at this stage in the OP cells (Hoijman et al., 2015). When it comes to the chick embryo, a basal lamina is deposited on the basal side of the otic placode (Hilfer and Randolph, 1993). Epithelial elongation is accompanied by interkinetic nuclear migration, a process in which cell nuclei are located at different levels along the apicobasal axis depending on the phase of the cell cycle (Spear and Erickson, 2012). This pseudostratified tissue architecture is thought to help the dense packing of these cells, which in turn promotes faster tissue growth. Signals thought to contribute for this particular placodal tissue arrangement and cell shape include *Pax2*, *Spalt4* and Sox3 (Abelló et al., 2010; Barembaum and Bronner-Fraser, 2007; Christophorou et al., 2010).

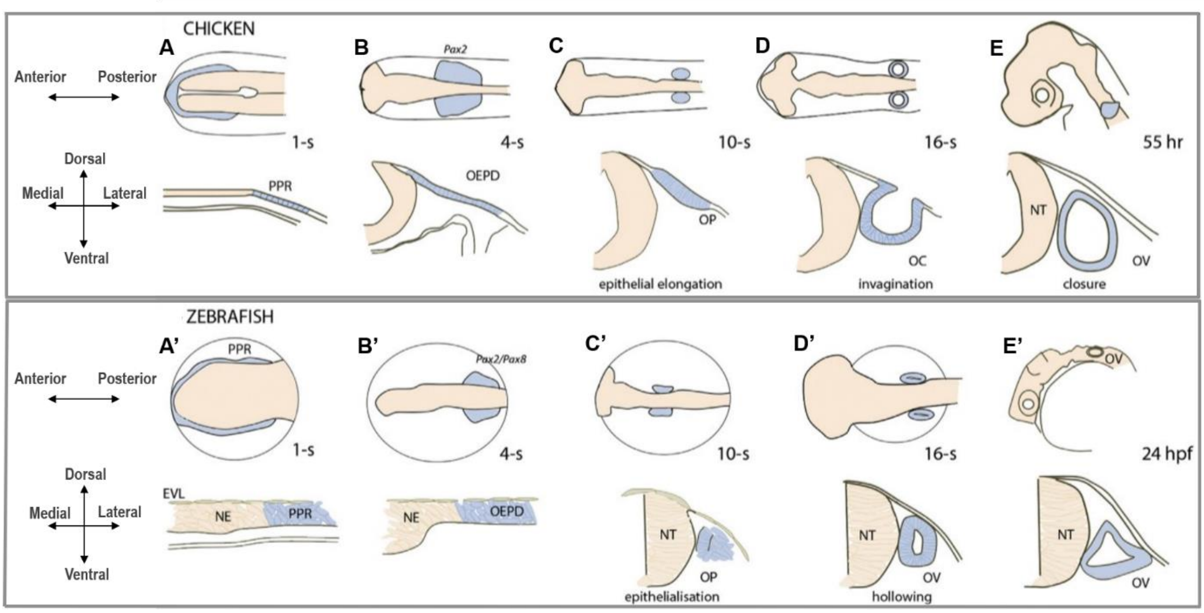

Figure 1.5 - Early morphogenesis of the inner ear in chick and zebrafish.

(**A** – **E**) In the chick embryo, the pre-placodal region (PPR) is visible at one somite stage (1-s) as a band surrounding the anterior end of the neural plate. From this region, the otic-epibranchial domain (OEPD) forms at four somite stage (4-s). At ten somite stage (10-s), part of this domain thickens and becomes the otic placode (OP), which will then start to invaginate around the sixteen somite stage (16-s) and originate the otic cup (OC). At last, this cup closes and separates from the ectoderm forming the otic vesicle (OV). (**A' – E'**) In the zebrafish embryo, the pre-placodal region also appears by one somite stage, under the enveloping layer (EVL) and surrounding the neural ectoderm (NE). By four somite stage the otic-epibranchial domain is visible and from this structure the otic placode arises at ten somite stage. After undergoing epithelialisation and hollowing the otic placode becomes an otic vesicle by sixteen somite stage. Abbreviations: hpf – hours post-fertilisation. (Adapted from (Alsina and Whitfield, 2016))

After the otic placode is established, it undergoes several shape changes that will lead to the formation of a hollowed vesicle called the otic vesicle or otocyst (Figure 1.5E, E'). In amniotes, the otic placode folds through invagination to form the otic cup (OC), and eventually the otic vesicle; whereas in anamniotes, the otic vesicle is generated from hollowing within the dense mass of OP cells (Figure 1.5D-E'). Moreover, it was shown that F-actin concentrates in the apical domain of OP cells just before this tissue invaginates in the chick embryo or undergoes hollowing in the zebrafish embryo (C. Haddon & Lewis, 1996; X. R. Sai & Ladher, 2008). These observations suggested a link between the establishment of apicobasal polarity in the OP and the onset of otic vesicle formation. Invagination of the OP in the chick embryo is a biphasic process that starts with basal expansion followed by apical constriction (Sai and Ladher, 2008;

Sai et al., 2014). Myosin-II activity was shown to be involved at both of these stages: depolymerising basal F-actin and enriching it apically to promote basal expansion; and driving F-actin contraction on the apical domain to promote apical constriction. After invagination, the otic cup closes, separating the otic vesicle form the overlying non-neural ectoderm. In contrast, the process of otic vesicle formation through hollowing, involves a first stage of opening the initial lumen and then a second stage of lumen expansion (C. Haddon & Lewis, 1996; Hoijman et al., 2015) (Figure 1.5D', E'). In the zebrafish embryo, once the medial OP epithelium is polarized, marked by a stripe of F-actin in the tissue midline, two small unconnected cavities arise at the anterior and posterior poles. These two lumens then unzip, forming a single elongated lumen, and only later, the lateral side of the otic vesicle is epithelialised (Hoijman et al., 2015). Lumen expansion results from the asymmetric ingression of fluid from the otic vesicle cells, which contributes to the elongation of the dorsoventral and mediolateral axes, and also leads to the thinning of the otic epithelium. In addition, mitotic cells, due to their rounded shape, exert a pulling force on the luminal side of the otic epithelium and expand the lumen along the anteroposterior axis (Hoijman et al., 2015).

During the next stage of development of the inner ear, two processes happen in parallel: otic neurogenesis, and the differentiation of hair cells and sensory chambers (Alsina and Whitfield, 2016; Haddon et al., 1998; Maier et al., 2014). The second process involves several cell shape changes which will determine their identity in terms of sensory versus non-sensory epithelia (Alsina and Whitfield, 2016; Maier and Whitfield, 2014). In more ventral regions of the otic vesicle, the epithelium undergoes a thickening process and gives rise to pseudostratified otic sensory patches – maculae and cristae - which are composed of sensory hair cells and their supporting cells. On the contrary, cells in dorsolateral regions of the otic vesicle adopt a thin squamous morphology and will eventually give rise to non-sensory structures - the semicircular canals and the endolymphatic sac.

1.4.2 Events of tissue folding during inner ear development

There have been many studies revealing the different genes involved in the several stages of embryonic development of the inner ear, however there is a need to better understand the direct link between cellular pathways, behaviours, and tissue shape changes, particularly when it comes to mechanisms driving curvature in the inner ear. Throughout the embryonic development of the inner ear, we see several events of tissue folding that seem to be crucial to give the right shape and function to different structures of this organ, including those that reveal high levels of curvature. Between 1 and 2 days post fertilization in the zebrafish embryo, we see the genesis of both the endolymphatic sac and the epithelial projections that initiate formation of the semicircular canals (Figure 1.6A). These are particularly interesting examples of structures generated by epithelial folding in the inner ear, since they bend the otic tissue in opposite directions, but not necessarily with opposite mechanisms. The endolymphatic sac forms through invagination, with the apical cell surface making up the inner surface of the resulting curved epithelium (Figure 1.6B and Supp. Video 1); whereas the epithelial projections are generated through evagination, displaying the basal cell surface along the inner surface (Figure 1.6C and Supp. Video 2).

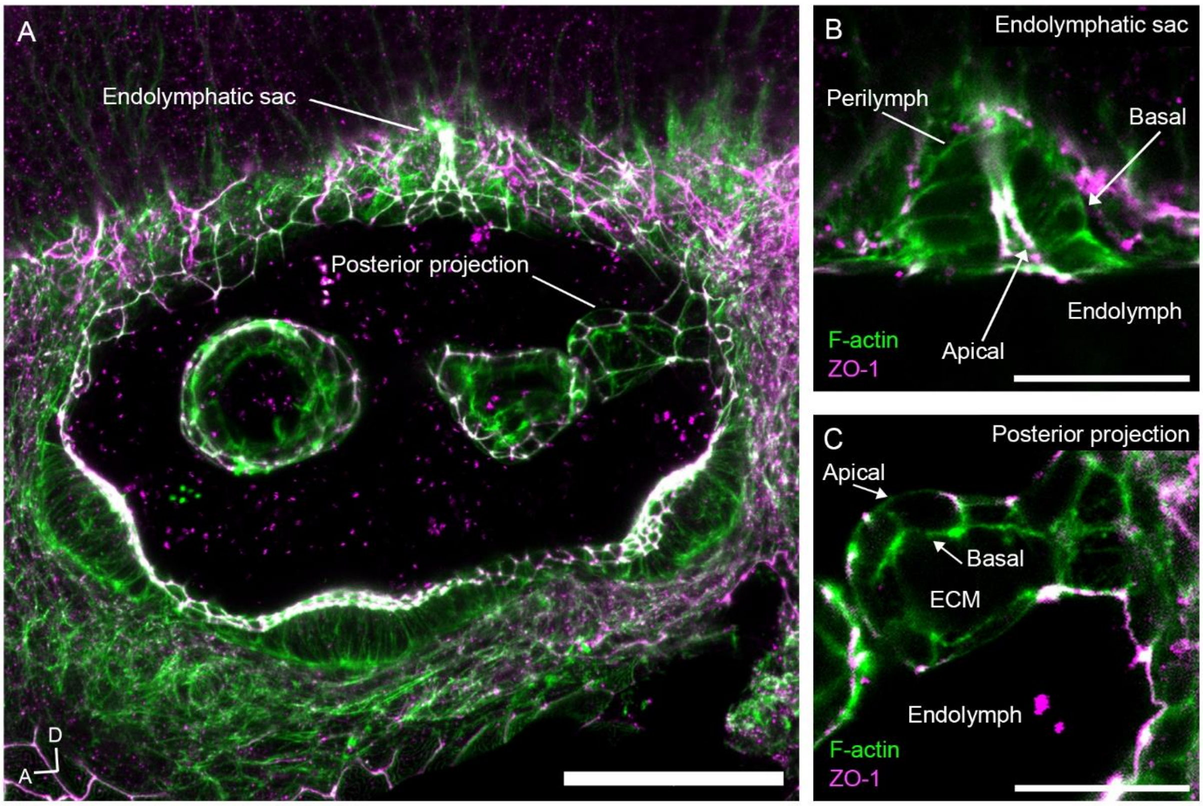

Figure 1.6 – Endolymphatic sac and posterior projection – inner ear structures formed by folding events.

Phalloidin staining and ZO-1 antibody staining were performed in 50 hours post-fertilisation zebrafish fixed embryos. F-actin is shown in green and ZO-1 (marking tight junctions) is shown in magenta. Pictures were taken on the Nikon inverted confocal microscope with a 40X oil immersion objective. (**A**) Maximum intensity projection of fourteen optical slices of the inner ear is shown here. Anterior – A - is to the left and dorsal is up - D. Scale bar measures 50 µm. (**B, C**) A single slice of a *z*-stack is shown here. Scale bars measure 20 µm. (**B**) The endolymphatic sac forms through invagination of the otic epithelium and, as a result, the apical surface of its cells face the inside of the vesicle (endolymph), whilst the basal surface of the cells faces the outside environment (perilymph). (**C**) The epithelial projection forms through evagination, bringing the otic epithelium into the lumen of the vesicle (therefore surrounding it with the endolymph). The space delineated by the basal surface of the projection cells is filled with extracellular matrix (ECM).

1.4.2.1 Formation of the endolymphatic sac

This structure has the appearance of a dead end tube and is present in the ear of basal vertebrates (Swinburne et al., 2018). It seems to be responsible for regulating the pressure of the inner ear by acting as pressure relief valve, but also for regulating endolymph homeostasis (Swinburne et al., 2018). In situations where the ear pressure is not properly regulated, it can lead to deafness and balance disorders such as Pendred syndrome and Meniere's disease (Belal and Antunez, 1980; Schuknecht and Gulya, 1983).

Recently, it has been shown in the zebrafish that the initial stages of development of the endolymphatic sac happen around 36 hpf (Swinburne et al., 2018) (Figure 1.7). In this study, the authors show that at this time point, a portion of the otic epithelium in the dorsal region of the otic vesicle starts folding in the opposite direction of the cavity. This structure will then grow and elongate until 60 hpf, a time point by which the diffusion barrier will start to open and becomes functional. The endolymphatic sac is observed to exhibit cycles of slow inflation and rapid deflation (Swinburne et al., 2018).

Figure 1.7 - Early morphogenesis of the endolymphatic sac in zebrafish.

Schematic representation of the formation of the endolymphatic sac (blue arrows). Its development starts around 36 hours post-fertilisation (hpf) and between 2 and 3 days post fertilisation (dpf) it becomes functional.

There have been very few genes associated to the development of this structure. For example, it is known that in the zebrafish, *foxi1* (at 52 hpf) and *bmp4* (at 76hpf) are expressed specifically in the endolymphatic sac (Geng et al., 2013), and for this reason these are often used as markers for this structure. In the chick, from stages 26 to 32, Dlx3 gradually becomes specifically expressed in the endolymphatic sac (Brown et al., 2005). Dlx5 and Dlx6 expression is also found in this structure by stage 30, but is not restricted to it, since it is also expressed in most of the developing semicircular canal system (Brown et al., 2005). A lot less is known about the morphogenesis of the endolymphatic sac in the zebrafish compared with the morphogenesis of the semicircular canals. However, the way the otic epithelium folds to form the endolymphatic sac, with the apical side of the cells making up the inner ring of this tube like structure (Figure 1.6A), resembles an invagination, which is a very common process described in the organogenesis of different species.

1.4.2.2 Formation of the epithelial projections that generate the semicircular canals

The zebrafish inner ear exhibits three orthogonally arranged semicircular canals, as do all jawed vertebrates, and their main function is to detect rotational movements of the head. As the head moves, there is a relative movement of the fluid inside the sac of each semicircular canal which is registered by the crista (sensory epithelium) housed in the ampulla at the base of each semicircular canal.

In the zebrafish and Xenopus embryos, semicircular canal formation starts in four different regions of the otic vesicle with the folding of the otic epithelium towards its lumen, in the form of finger-like projections (Waterman & Bell, 1984). This is, at least, partially driven by ECM production (Geng et al., 2013; C. M. Haddon & Lewis, 1991; Munjal et al., 2021; Waterman & Bell, 1984). In contrast, in amniotes like the chick and mouse embryos, semicircular canal formation has not been described as a folding event but instead, it is known to initiate through pouches or diverticula that appear on the dorsal and lateral regions of the otic vesicle. The genesis and growth of these pouches is driven by quick thinning of the dorsolateral otic epithelium, which, depending on the species, can involve different cellular behaviours, such as cell shape and adhesion changes, disruption of the basement membrane, and cell proliferation of the surrounding mesenchyme (Lang et al., 2000; P. Martin & Swanson, 1993; Ohta et al., 2010; Pirvola et al., 2004; Salminen et al., 2000).

One of the first characterisations of early semicircular canal formation in zebrafish revealed that by 44 hpf the lateral wall of the otic vesicle is protruding into the cavity, being the first projection to form (Waterman & Bell, 1984). By 45 hpf, an epithelial projection develops from the region of the anterior otic epithelium (Figure 1.8B), the posterior projection begins to form around 48 hpf (Figure 1.8C), and from 52 hpf the ventral projection starts forming (Figure 1.8D), which my observations show is slightly earlier than previously reported (Geng et al., 2013; Waterman & Bell, 1984). Later on, between 57 and 68 hpf, the lateral projection exhibits three bulges and the anterior and posterior projections meet with the respective bulges of the lateral projection, adhere to its apical contacting surface and fuse to form the pillars (Figure 1.8E; see Supp. Video 3 for an example of an anterior pillar) (Geng et al., 2013; Waterman & Bell, 1984). By 72 hpf, all three pillars are formed, becoming the hubs of the semicircular canals (Figure 1.8F). The pillars then undergo widening and extending to give the right shape to the canals (Alsina and Whitfield, 2016).

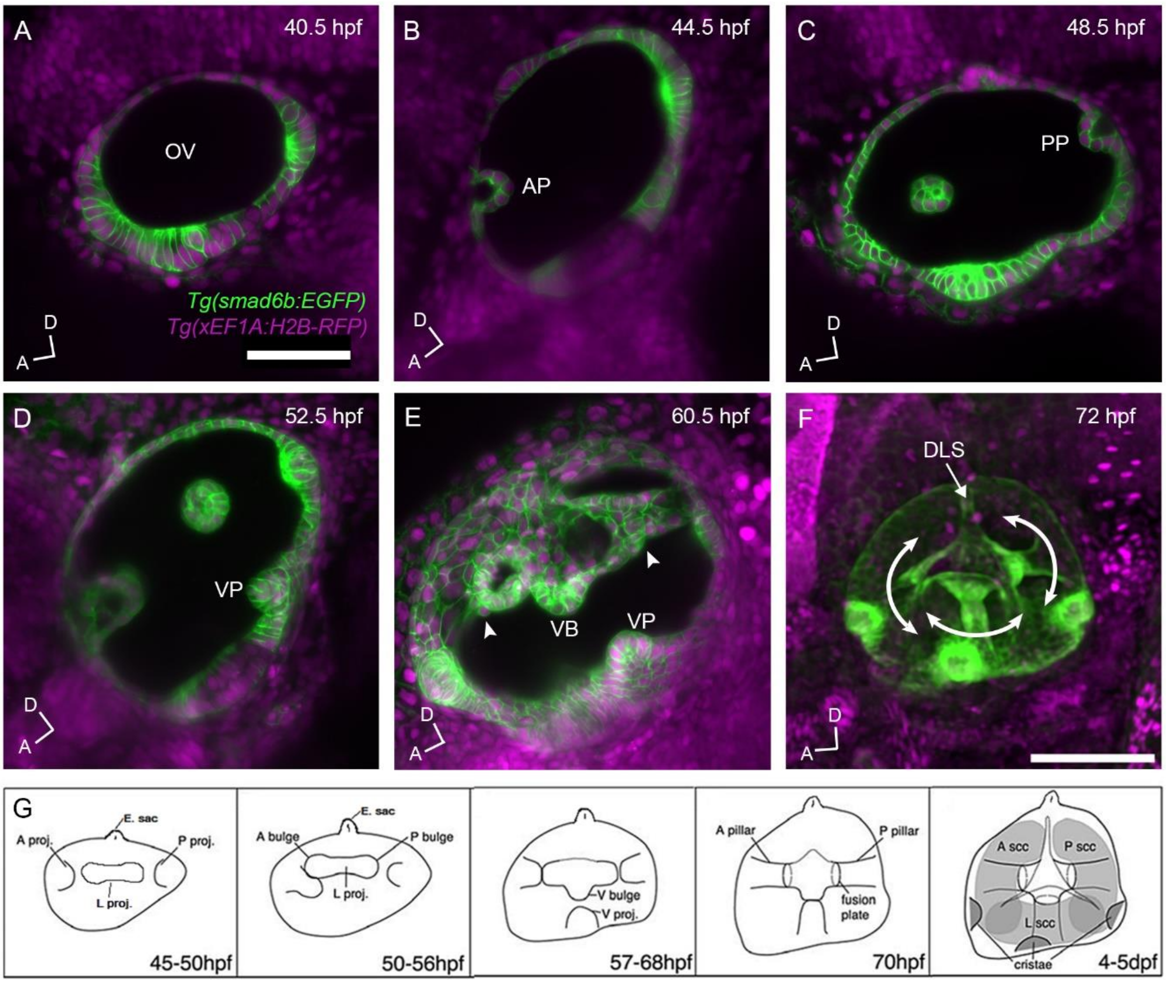

Figure 1.8 – Early morphogenesis of the zebrafish semicircular canals.

(**A-E**) Inner ear of *Tg(smad6b:EGFP); Tg(xEF1A:H2B-RFP)* double transgenic embryos. Images were acquired in the Zeiss Z1 Light-sheet microscope between 40 and 60 hours post fertilisation (hpf). Lateral views of the ear are shown with roughly the anterior to the left and dorsal to the top (A – anterior; D -

dorsal). Scale bar measures 50 μm. A single *z*-slice is shown in pictures **A-C** and a maximum intensity projection from a *z*-stack is shown in **D-E**. (**B**) The anterior projection (AP) is formed by 45 hpf, and the posterior projection (PP) appears around 48 hpf (**C**). (**D**) The ventral projection (VP) appears from 52 hpf. (**E**) At 60 hpf, we can see the ventral bulge (VB), and the anterior and posterior pillars (white arrowheads). (**F**) Adapted from (Baldera et al., 2023). Maximum intensity projection of a zebrafish inner ear at 72 hpf. Same transgenic line was used as in (**A-E**); imaged with a Nikon CSU-W1 spinning disk confocal microscope. Scale bar measures 100 μm. All three pillars have been formed at this stage and the dorsolateral septum (DLS) can also be seen. Curved white arrows mark the anterior, posterior and lateral canals. (**G**) Diagram illustrating main morphological changes in the otic vesicle during formation of the semicircular canals. Adapted from (Geng et al., 2013). Abbreviations: A proj. – Anterior projection; E – Endolymphatic; proj. – projection; A – anterior; P – posterior; L – lateral; V – ventral; scc – semicircular canal; dpf – days post fertilisation.

In order for the inner ear to detect motion and gravity properly, the semicircular canals are required to form in the correct position, with the right shape and at the right time during embryonic development. Several genes have been described in the literature to be essential for epithelial projection and semicircular canal formation. For instance, a complete loss of the lateral canal and crista is seen when the function of *otx1b* is lost, both in zebrafish (Hammond and Whitfield, 2006) and in mouse (Morsli et al., 1999). Regulation of the *otx1b* expression domain in the otic vesicle involves a balance between the Fgf-promoting and the Retinoic acid (RA)-repressing signalling activity (Maier and Whitfield, 2014). In addition, disruption of the mouse RA-synthesising enzyme gene *Raldh3* leads to smaller and thinner semicircular canals (Romand et al., 2013).

Epithelial projections, and therefore semicircular canals, are unable to form in *hdac1* mutants (Cunliffe, 2004); and in *sox10* mutants, some epithelial projections form but look very abnormal (Dutton et al., 2009). Mutations of different Hedgehog pathway inhibitor genes (*dzip1*, *hip1* and *ptc2*) lead to an overgrown ventral projection (Hammond et al., 2010). A more severe phenotype is observed in *lauscher* zebrafish mutants, which have a disruption in *adgrg6* (*gpr126)*, an adhesion class G protein-coupled receptor gene (Geng et al., 2013). This leads to continuous high expression of several extracellular matrix genes, including *vcan* and *chsy1*, and all projections overgrow and never fuse (Geng et al., 2013). Loss of *bmp2b* in the zebrafish leads to absent semicircular canals but the cristae form normally (Hammond et al., 2009). The *tbx1* zebrafish mutant, in most cases, exhibits an even more drastic phenotype with a complete absence of all semicircular canals as well as cristae (Dutton et al., 2009). Knockout or knockdown of zebrafish genes coding for proteins involved in synthesising different ECM components, such as *dfna5*, *ugdh*, *has3*, *chsy1* and *ext2* (Busch-Nentwich et al., 2004; Jones et al., 2022; Li et al., 2010a; Munjal et al., 2021; Neuhauss et al., 1996), also leads to absent canals as the epithelial projections fail to grow and look truncated.

1.5 Aims and hypotheses

Tissue folding can be driven by a cocktail of mechanisms specific to the organism/structure such as mechanical forces, tissue elasticity, cytoskeletal and cell adhesion rearrangements, cell death, extracellular matrix dynamics, cell shape changes, etc. As reported here, the gross morphogenetic events happening during embryonic development of the zebrafish semicircular canals have been described. However, the very first cell shape changes and cell movements happening before and as the projections start forming, and the mechanisms driving folding of the otic epithelium are still poorly understood.

My project was carried out to address these main objectives and hypotheses:

1. Describe tissue and cell shape changes during early development of the zebrafish semicircular canals (formation of the epithelial projections). Hypothesis: As the epithelial projections form through evagination, basal constriction of otic epithelium cells would be very likely to be happening in this system.
2. Select and apply computational image analysis tools to gain a quantitative appreciation of the morphogenetic changes being studied. This was done in collaboration with Professor Alex Frangi’s lab. Hypothesis: Membrane-based segmentation tools will more likely be suitable for my data as the transgenic zebrafish line used in this project expresses membrane-linked EGFP, and other zebrafish datasets have been successfully segmented with these tools.
3. Identify and describe specific cell behaviours (like cytoskeleton and extracellular matrix rearrangements, cellular adhesion changes, etc) involved in otic epithelium folding. Hypothesis: As seen in other events of tissue folding through evagination, basal accumulation of some cytoskeletal proteins was expected to be observed; and since the otic epithelium has to invert its curvature, a change in or loss of cell polarity could happen.
4. Take advantage of chemical manipulation tools and mutant zebrafish lines available in the lab to start testing the role of different genes and proteins in generating the correct 3D cell and tissue morphology during epithelial projection formation. Hypothesis: Knowing the crucial role of hyaluronan in semicircular canal formation, ECM components will be strong candidates for driving the folding event that initiates epithelial projection formation.

CHAPTER 2

Materials And Methods

Here I describe the materials and methods used for the data presented in all chapters except chapters three and five, as these chapters are published manuscripts that include their own methods and materials' sections.

2.1 Zebrafish husbandry

All wild-type, transgenic and mutant zebrafish lines, used in the work presented here, were raised and maintained in the Bateson Centre aquaria facilities of the University of Sheffield, under standard husbandry protocols (Alestrom et al., 2020; Westerfield, 2007) and all animal research was performed under licence from the UK Home Office. Embryos were kept in E3 medium (5 mM NaCl, 0.17 mM KCl, 0.33 mM CaCl2, 0.33 mM MgSO4, pH 7.2) (Westerfield, 2007) at different temperatures ranging from 23ºC to 33ºC and staged according to hours post fertilization, using the appropriate formula (Kimmel et al., 1995).

2.1.1 Wild-type lines

The wild-type (WT) lines used in this study were AB (ZDB-GENO-960809-7), London Wild Type (LWT) and *nacre* (*mitfa*$^{w2/w2}$) (ZDB-GENO-990423-18). Nacre embryos were used because they lack melanophores, enabling better imaging of the inner ear (Lister et al., 1999).

2.1.2 Transgenic lines

The transgenic line used for imaging the development of the epithelial projections, was made by crossing the (recently renamed) enhancer trap line *Et(smad6:EGFP-CAAX)* (Baldera et al., 2023), with the transgenic line *Tg(xEF1A:H2B-RFP)* (Rodríguez-Aznar et al., 2013). In the work presented in this thesis, this line is referred to as *Tg(smad6b:EGFP); Tg(xEF1A:H2B-RFP)*. The transgenic line *Tg(actβ2:myl12.1-EGFP)* (Maître et al., 2012), donated to us by Emily Noël, was used to visualise myosin-II.

2.2 Drug treatments

Table 2.1– List of compounds.

Short name	**Product name**	**Stock concentration**	**Working concentration**	**Supplier**
Blebbistatin	Blebbistatin	50 mM (in DMSO)	25 µM and 50 µM	B0560, Sigma-Aldrich
4-MU	4-Methylumbelliferone	25 mM, 50 mM and 100mM	250 µM, 500 µM and 1000 µM	M1381, Sigma-Aldrich

2.2.1 Blebbistatin treatment

Embryos were either treated at 42 hpf for six hours, to investigate the role myosin-II in anterior and posterior projection formation; or at 48 hpf for four hours to test the role of myosin-II in the elongation and maintenance of these epithelial projections.

At the desired stage, embryos were dechorionated with forceps and moved into a 24-well plate: 4 wells with 10 embryos in 1000 µL of E3 each. For each of the groups another 500 µL was added to the respective well with the following:

- E3 group: 500 µL of E3
- DMSO group: 498.5 µL of E3 + 1.5 µL DMSO
- 25 µM Blebbistatin group: 499.25 µL of E3 + 0.75 µL Blebbistatin (from 50 mM stock)
- 50 µM Blebbistatin group: 498.5 µL of E3 + 1.5 µL Blebbistatin (from 50 mM stock)

At the end of the treatment, embryos were removed from the 24-well plate and moved into a petri dish with E3 (without washing off the drug) to take pictures.

2.2.2 4-MU treatment

Stocks of 25, 50 and 100 mM 4-MU were prepared by adding 8.8385, 17.677 and 35.354 mg of 4-MU powder respectively to 2 mL of DMSO. For details of the starting times and duration of treatments please see chapter six. At the stage of interest, embryos were removed from their chorion with forceps (if necessary) and moved into a 24-well plate: 10 embryos in 1000 µL of E3 each. For each of the groups another 500 µL was added to the respective well with the following:

- DMSO group: 485 µL of E3 + 15 µL DMSO
- 250 µM 4-MU group: 485 µL of E3 + 15 µL 4-MU (from 25 mM stock)
- 500 µM 4-MU group: 485 µL of E3 + 15 µL 4-MU (from 50 mM stock)
- 1000 µM 4-MU group: 485 µL of E3 + 15 µL 4-MU (from 100 mM stock)

During the 12-hour-treatments, the 24-well-plate was placed in a box with a wet tissue under the plate to prevent evaporation of E3 from the wells. At the end of the treatment, embryos were removed from the 24-well plate and either moved into a petri dish with E3 (and washed in E3 3 x 5 min, unless otherwise specified) to take pictures or transferred to 4% PFA to perform staining/immunofluorescence.

2.3 Staining and Immunohistochemistry

Table 2.2– List of antibodies and staining agents used.

Type of antibody / staining agent	Short name	Product name	Isotype / Host	Dilution	Supplier
Primary Antibody	αE-cad	Purified Mouse Anti-E-Cadherin	Mouse IgG2a, κ	1:200	610182, BD Biosciences
Primary Antibody	αPar3	Anti-Partitioning-defective 3	Rabbit IgG	1:100	07-330, Merck
Primary Antibody	αZO-1	ZO-1 Monoclonal Antibody (ZO1-1A12)	Mouse IgG1	1:100	33-9100, Thermo Fisher Scientific
Secondary Antibody	αMouse Alexa 647	Goat anti-Mouse IgG (H+L) Cross-Adsorbed Secondary Antibody, Alexa Fluor™ 647	Mouse IgG / Goat	1:200	A21235, Invitrogen
Secondary Antibody	αRabbit Alexa 568	Donkey anti-Rabbit IgG (H+L) Highly Cross-Adsorbed Secondary Antibody, Alexa Fluor™ 568	Rabbit IgG / Donkey	1:200	A10042, Invitrogen
Toxin	Phalloidin	Alexa Fluor® 488 Phalloidin #8878		1:100	8878, Cell Signalling Technology
Nanobody	GFP-booster	ChromoTek GFP-Booster Alexa Fluor® 488	- / Alpaca	1:400	gb2AF488, Chromotek

In order to prevent skin pigmentation from developing in the embryos, at 24 hpf, the E3 medium they were kept in was replaced by E3 with 0.003% 1-phenyl 2-thiourea (PTU; 0.003%). However, embryos from drug treatments were not treated with PTU. At the stages of interest, embryos were dechorionated with forceps and fixed in 4% paraformaldehyde (PFA) for 2-4 hours at room temperature (except for 40 hpf embryos, which were kept in PFA overnight at 4ºC).

Day 1

- Rinse embryos once in PBS-Tr (phosphate-buffered saline (PBS), 1% Triton X-100).
- Wash in PBS-Tr 3 x 5 minutes (min).
- Block in Blocking Solution (PBS-Tr, 10% sheep/donkey serum according to the secondary antibody used) for 60 min.
- Incubate overnight at 4ºC (with gentle rocking) in Blocking Solution with 1% DMSO and the primary antibody chosen (concentrations for each antibody are shown in Table 2.2).

Day 2

- Wash in PBS-Tr 3 x 5 min
- Wash again in PBS-Tr 4 x 30 min
- Incubate overnight at 4ºC (with gentle rocking) in Blocking Solution with 1% DMSO, the appropriate secondary antibody, and either Phalloidin or GFP-booster (concentrations are shown in Table 2.2).

Day 3

- Wash in PBS-Tr 4 x 5 min
- Transfer to PBS with 0.1% Triton X-100 and keep at 4ºC until mounting.

Note: For each combination of primary-secondary antibodies used, a control was performed in which only the secondary antibody was added (no primary antibody added).

2.4 Microscopy

2.4.1 Light-sheet microscopy

The microscope used was a Zeiss Z1 light-sheet microscope with the software Zen (black edition).

2.4.1.1 Embryo mounting

Embryos were anaesthetised with 0.5 mM tricaine and dechorionated. Using a ZEISS Axio Zoom.V16 microscope, embryos were screened for fluorescence. Dechorionated embryos were transferred to 0.8% low melting point agarose (in E3) and mounted in a glass capillary, which was then placed into the microscope chamber filled with E3 and 0.5 mM tricaine.

2.4.1.2 Data acquisition

Table 2.3 – Acquisition settings for Light-sheet microscope.

Detection Optics	W Plan-Apochromat 20x/1.0 UV-VIS_4909000084
Emission Selection	CAM BS: SBS LP 580 EF1: BP 525-565 EF2: LP 585
Laser Block Filter	LBF 405/488/561
Laser Power	561 nm: 6.0% 488 nm: 20.0%
Exposure time	99.9 ms
Light-sheet thickness	2.96 µm
Z-stack	Continuous Drive

Zoom	2.3
Track	Single Track
Light Sheet Pivot	On
Scaling	X 0.225 µm Y 0.225 µm Z 1.000 µm

2.4.2 Confocal microscopy - Nikon A1 Confocal Microscope

A Nikon A1 Confocal Microscope was used to image fixed samples in which staining or immunohistochemistry had been performed.

2.4.2.1 Embryo mounting

Fixed embryos were transferred to a petri-dish with PBS and dissected to remove yolk and eyes. A small volume (200-300 mL) of pre-warmed 1-1.5% Low Melting Point Agarose in PBS was placed in the centre of a 35mm Wilco glass-bottomed Petri dish, the dissected embryos were transferred with a glass pipette into the agarose and mounted laterally with their heads as close to the bottom of the dish as possible.

2.4.2.2 Data acquisition

Image stacks were acquired by a Nikon A1 Confocal Microscope with a 40X oil objective.

Table 2.4 – Acquisition settings for Nikon A1 Confocal Microscope.

Pixel Dwell	6.2
Pinhole	1.2
Size (pixels)	1024

488 nm Laser	HV (detector sensitivity)	70 – 95
	Offset	-11
	Laser power	1.5 – 3
647 nm Laser	HV (detector sensitivity)	100 – 110
	Offset	-11
	Laser power	2.5 – 3.5
568 nm Laser	HV (detector sensitivity)	90 – 95
	Offset	-11
	Laser power	2 – 3
Z-step	1 μm	
Zoom	1.68 – 2.18	
Scan Direction	One Direction	
Scan Speed	0.125	

2.4.3 Confocal microscopy - ZEISS LSM 880 Airyscan Confocal Microscope

A ZEISS LSM 880 Airyscan Confocal Microscope was used for performing time-lapses of transgenic embryos.

2.4.3.1 Embryo mounting

Embryos were anaesthetised with 0.5 mM tricaine, dechorionated and screened for fluorescence using a ZEISS Axio Zoom.V16 microscope. A small volume (around 300 ml) of 0.8% Low Melting Point Agarose (in E3) was added in the centre of a 35mm Wilco glass-bottomed Petri dish. With a glass pipette fish were transferred into the agarose and mounted laterally with their heads touching the bottom of the dish. After agarose had settled, E3 with Tricaine (0.5 mM) was added on top of it. The temperature within the imaging chamber was maintained at 28.0°C.

2.4.3.2 Data acquisition

Table 2.5 – Acquisition settings for ZEISS LSM 880 Airyscan Confocal Microscope.

Objective	LD LCI Plan-Apochromat 40x/1.2 Imm Korr DIC M27	
Beam Splitters	MBS: MBS 488/561 MBS_InVis: Plate DBS1: Plate	
Laser Power	Embryos 2 and 3 561 nm: 7.0% 488 nm: 6.5%	Embryo 4 561 nm: 6.5% 488 nm: 6.5%
Scaling	X 0.050 µm Y 0.050 µm Z 1.000 µm	X 0.099 µm Y 0.099 µm Z 1.000 µm
Zoom	1.3	1.0
Acquisition Interval	30 minutes	

2.4.4 Stereomicroscopy

A ZEISS Axio Zoom.V16 microscope together with a ZEN (blue edition) was used to image embryos following drug treatments and to screen embryos for fluorescence.

2.5 Image Analysis

2.5.1 Manual segmentation

Data set: image *z*-stacks of inner ears from *Tg(smad6b:EGFP); Tg(xEF1A:H2B-RFP)* double transgenic embryos at different time-points acquired in the Zeiss Z1 light-sheet microscope.

Manual segmentation was performed in Fiji using the plugin called 'Segmentation Editor'. 3D rendering of stacks and rotation videos were also generated in Fiji using the '3D Project' function.

2.5.2 3D Cell shape analysis

Data set: image *z*-stacks from time-lapses of inner ears from *Tg(smad6b:EGFP); Tg(xEF1A:H2B-RFP)* double transgenic embryos acquired in the ZEISS LSM 880 Airyscan confocal microscope (example in Figure 2.1A).

I selected image *z*-stacks for every hour of the time-lapses which were then cropped to regions of interest (ROI) in Zen Black. Fiji was used to convert these images into tiff files, to separate the two channels, and to convert the green channel (cell membrane) into mha files. Cell segmentation was performed on the mha files using the segmentation software ACME (Mosaliganti et al., 2012) with the following parameters:

1. Radius of median filter for denoising: 0.3 pixels
2. Resampling ratio (to isotropic voxel resolution)*: 4.0, 4.0, 0.2 - embryos 2 and 3
   2.0, 2.0, 0.198 - embryo 4
3. Neighbourhood size for membrane signal enhancement filter: 0.7
4. Neighbourhood size for tensor voting: 1.0
5. Watershed segmentation threshold: 2.0

* Choose *x* resize factor first, then calculate *z* resize factor: *z* resize factor = (*x* pixel dimension/z pixel dimension) X *x* resize factor

After cell segmentation, I used the open-source MATLAB-based software *Origami* (Mendonca et al., 2021) in order to assign epithelial polarity direction vectors and extract cell shape features (Figure 2.1B and D). The polarity vector was chosen to match the apico-basal axis of the inner ear cells as this was a known feature (Figure 2.1B) - apical cell surface lines the inside of the otic vesicle (Haddon & Lewis, 1996). In the step where the software allows assigning groups, I defined Group 1 as the cells belonging to the projection (those that come out of the plane of the otic wall); and Group 2 as the surrounding cells (Figure 2.1C). At early stages, before projection formation, I initially assigned all cells to Group 2 and later, after tracking some of the cells belonging to the projections, I was able to relabel those as belonging to Group 1. At the end of the pipeline, cell shape features were exported to an Excel file.

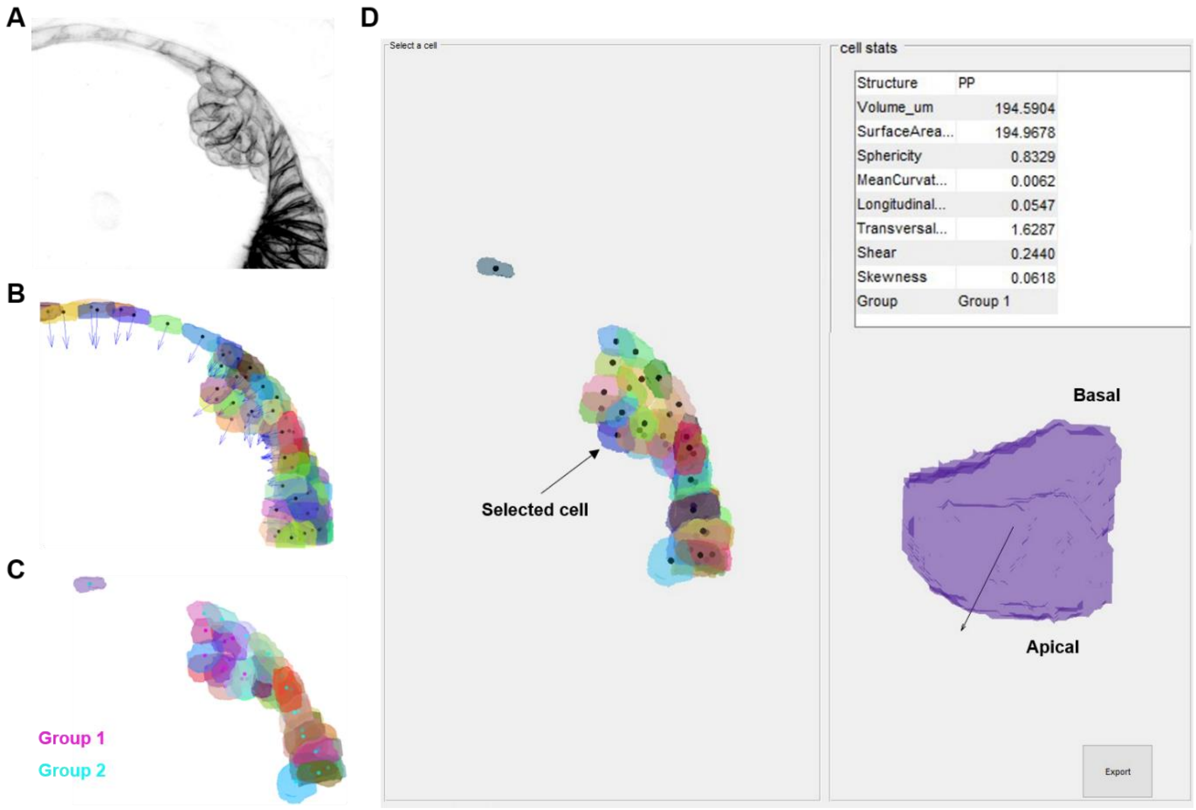

Structure	PP
Volume_um	194.5904
SurfaceArea...	194.9678
Sphericity	0.8329
MeanCurvat...	0.0062
Longitudinal...	0.0547
Transversal...	1.6287
Shear	0.2440
Skewness	0.0618
Group	Group 1

Figure 2.1 – *Origami* pipeline applied to epithelial projection cells.

(**A**) Maximum intensity projection of a posterior projection as an example data set from Airyscan confocal microscopy used for cell segmentation and cell shape feature extraction. (**B-D**) Representative pictures of different steps of the *Origami* pipeline. Assignment of polarity vectors and groups is shown in **B** and **C** respectively. Group 1 (magenta) was used for projection cells and group 2 (cyan) was used for surrounding cells. (**D**) Visualisation of cell shape features by selecting an individual cell.

2.5.3 Cell tracking

Data set: time-lapse images of inner ears from *Tg(smad6b:EGFP); Tg(xEF1A:H2B-RFP)* double transgenic embryos acquired in the ZEISS LSM 880 Airyscan confocal microscope.

Each inner ear time-lapse was cropped to regions of interest (ROI) in Zen (in order to reduce file sizes and reduce processing times). Arivis was then used to perform a drift correction and to manually track individual cells. The drift correction was performed for *x* and *y* axes in order to keep the developing projection (more specifically its base) in the same position, but not for the *z* axis as I didn't have a reference point for it. The manual cell tracking was performed using the 'Place objects' and the 'Track Editor' tools. Track features were also calculated by Arivis and exported as Excel files.

2.5.3.1 Changing the position of the axes' origin

Data acquired in the Airyscan confocal microscope is automatically given a orientation in space with the origin of the axes allocated to the bottom left corner of the image. This means that some track features, like initial and final cell positions and displacement in x or y, were presented in relation to that automatically placed axes' origin. This didn't present any biological meaning, so the *y* axis was manually redefined to start in the otic epithelium where the initiating cells appear (future base of the projection), and its direction was redefined to pass through the tip of the projection (Figure 2.2). The *x* axis was redefined, perpendicularly to the y axis, to be on the plane of imaging (Figure 2.2), leaving the *z* axis to run perpendicularly to both the *x* and *y* axis, running along the mediolateral body axis. All cell coordinates and displacement measurements were adjusted accordingly following the Euler-Rodrigues formula (Figure 2.2) (Dai, 2015; Gray & Kline, 1980).

1 **Define new Y axis using the two points defined as projection base and projection tip.**

2 **Calculate θ - rotation angle between the original (x_{OY}, y_{OY}, z_{OY}) and new (x_{FY}, y_{FY}, z_{FY}) *y* vectors/axes.**

OY – original *y* vector **FY – final *y* vector**

$$\theta = \arccos \frac{(x_{OY} \cdot x_{FY} + y_{OY} \cdot y_{FY} + z_{OY} \cdot z_{FY})}{(|OY|_2 \cdot |FY|_2)}$$

3 **Calculate the values for a, b, c and d (parameters of the rotation matrix.**

$$a = \cos\frac{\theta}{2}; \qquad c = k_y \sin\frac{\theta}{2};$$
$$b = k_x \sin\frac{\theta}{2}; \qquad d = k_z \sin\frac{\theta}{2}.$$

4 **Calculate the rotation matrix.**

$$\vec{x}' = \begin{pmatrix} a^2+b^2-c^2-d^2 & 2(bc-ad) & 2(bd+ac) \\ 2(bc+ad) & a^2+c^2-b^2-d^2 & 2(cd-ab) \\ 2(bd-ac) & 2(cd+ab) & a^2+d^2-b^2-c^2 \end{pmatrix} \vec{x}.$$

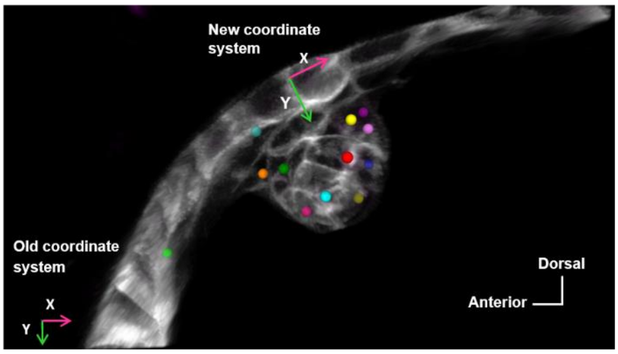

5 **For each tracked cell, multiply the old coordinates of their initial and final positions by the rotation matrix. (Note: Here, the coordinate system has been rotated but not placed in the new axes' origin).**

6 **Again, for each tracked cell, calculate the new initial and final positions by subtracting the coordinates of the axes' origin from each cell's coordinates from step 5.**

Figure 2.2 – Step-by-step process to change the coordinate system to a biologically relevant position.

Diagram of the steps taken to change the position of the coordinate system based on the Euler-Rodrigues formula (Dai, 2015; Gray & Kline, 1980), and to adjust cell coordinates and displacement measurements according to the new axes.

After obtaining the cell shape features and performing the cell tracking, for each cell that was successfully tracked, I manually matched it with the respective shape measurements for each time-point.

2.5.4 Quantification of staining and immunofluorescence signal

Dataset: image *z*-stacks of inner ears acquired in the Nikon A1 confocal microscope.

To measure the antibody/staining signal intensity, I used Fiji. A *z*-slice where three cells of the otic epithelium or the projection (once formed) could be seen in focus was chosen (Figure 2.3A) and duplicated twice (Figure 2.3B). The second duplicate was converted to 8-bit, inverted and submitted through a threshold (making it binary) (Figure 2.3C), keeping the same threshold for all pictures of the same experiment and same channel. The first duplicate (Figure 2.3B) was multiplied by this last thresholded picture (Figure 2.3C) to remove any background signal of the original picture, obtaining a third image which was converted to 16-bit (Figure 2.3D). In this picture, and for each projection, a box was drawn over the apical half of three cells next to each other (Figure 2.3E in red) and over the basal half of the same cells (Figure 2.3E in yellow). The mean intensity and area of the box were measured. The mean intensity of the staining in the apical and basal domains was multiplied by the correspondent box area to obtain a measure of total signal (indirect measure of protein levels in that cell domain) and then the apical/basal ratio was calculated.

I presented the apical/basal ratio data as a Log(10) of that ratio, which means that any data points above zero show that the protein is mostly localised on the apical half of the cell, whereas if the data points are below zero, then the protein is mostly localised on the basal half (Figure 2.3F).

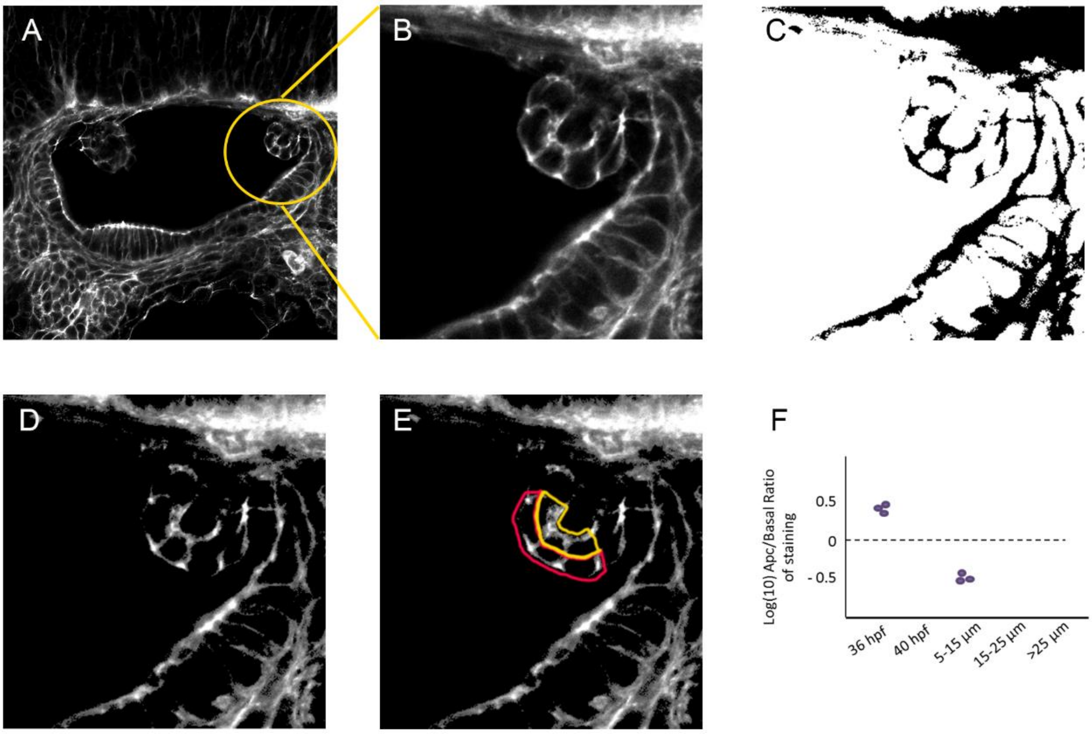

Figure 2.3 – Step-by-step methodology for staining/antibody signal quantification in the projections of the semicircular canals.

(**A, B**) Representative *z*-slice of a stack taken of the inner ear stained with Phalloidin in which the posterior projection is in focus (inside yellow circle in A). Picture taken on the Nikon inverted confocal microscope with a 40X oil immersion objective. (**C**) Duplicated picture of B to which a threshold was applied. (**D**) Result picture of the multiplication of B by C (in order to remove background). (**E**) Picture of D with the apical half of three cells in the projection highlighted in red and the basal half of the same cells highlighted in yellow. (**F**) Schematic of a graph illustrating the type of results obtained - apical/basal ratio of the staining per time point.

2.5.5 Measuring projection and embryo length

Projection length was measure in Zen for data acquired in the Airyscan confocal microscope, and in Fiji for data acquired in the ZEISS Axio Zoom.V16 microscope and the Nikon A1 confocal microscope. The 'Straight line' tool was used to measure the distance from the otic wall to the tip of the projection, on an optical section roughly mid-way through the structure (white line in Figure 4.3A from chapter four; and Figure 2.4A).

Embryo length was measured in embryos used in drug treatment experiments using the 'Segmented line' tool in Fiji. A line was drawn starting on the top of the head, passing through the inner ear and continuing down along the antero-posterior axis, finishing at the tail (Figure 2.4B).

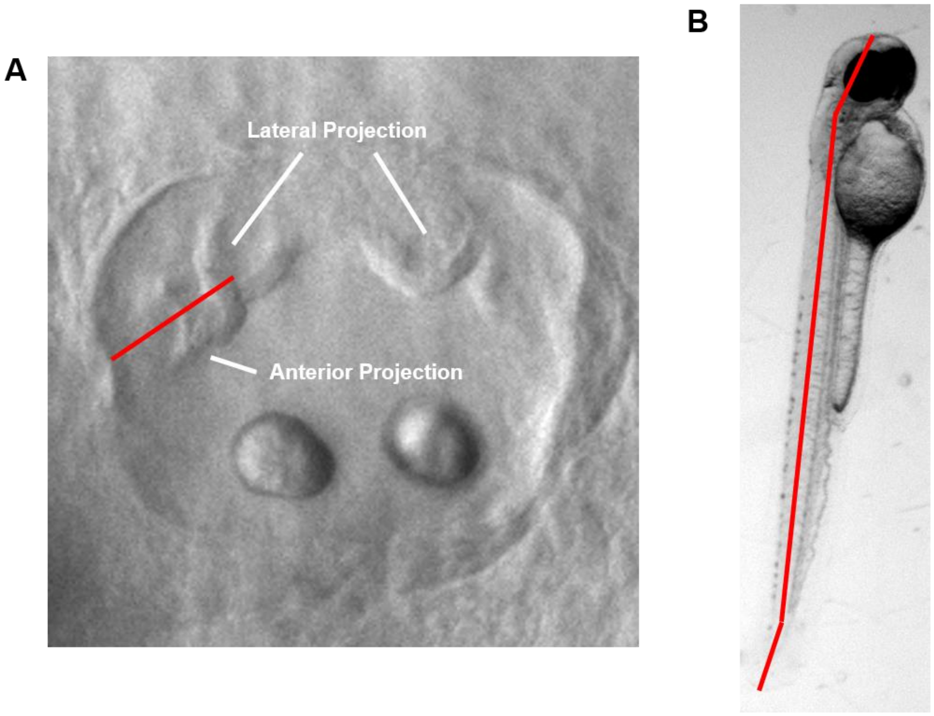

Figure 2.4 – Measuring projection and embryo length in Fiji.

(**A**) Picture of a zebrafish inner ear with anterior to the left and dorsal side to the top. Red line shows how projection length was measured using 'Straight line' tool in Fiji. (**B**) Picture of a *nacre* zebrafish embryo from a lateral view. Red line shows how embryo length was measured using the 'Segmented line' tool in Fiji. Both pictures were acquired in the ZEISS Axio Zoom.V16 stereoscope with a 60X zoom (**A**) and a 7X zoom (**B**).

All other post-acquisition processing of raw files was carried out in Fiji or in Zen (black edition): brightness adjustments, cropping, 3D rendering and videos.

2.6 Statistical Analysis

All statistical analysis and data presentation were performed in GraphPad Prism 9. The D’Agostino and Pearson normality test was performed for each data set prior to data analysis (except when sample size was not large enough, in which case a Shapiro-Wilko test was used). Statistical tests performed are specified in the respective figure legends.

CHAPTER 3

Origami: Single-Cell 3D Shape Dynamics Oriented Along The Apico-Basal Axis Of Folding Epithelia From Fluorescence Microscopy Data

3.1 Introduction

Advances in biological imaging tools, and particularly in fluorescence microscopy, are making a great impact on the imaging quality of developing complex multicellular organisms at single-cell resolution (Keller et al., 2008). As a result, scientists have been able to visualise morphogenetic processes in detail which has been an essential tool to help develop mechanistic models of morphogenesis. This has been accompanied by an increasing need of computational image analysis tools in order to make sense of all the data collected (Mikut et al., 2013).

3.1.1 Imaging the zebrafish inner ear

The zebrafish embryo, as mentioned before, is optically clear which is extremely useful for imaging. With the aid of tools that generate fluorescent embryos, and the improvement of fluorescence microscopy techniques, it has been possible to watch organogenesis live better than ever (Bryan et al., 2020; Hartmann et al., 2020; Mosaliganti et al., 2019; Taylor et al., 2019). In this section I will focus on the microscopy techniques most relevant to my project.

Light-sheet fluorescence microscopy has been successfully used to obtain images and perform time-lapses of the zebrafish inner ear (Dyballa et al., 2017; Swinburne et al., 2018). Light-sheet fluorescence microscopy allows high-speed live imaging of a variety of specimens with medium to high resolution, and for extended periods of time (Adams et al., 2015; Kaufmann et al., 2012; Taylor et al., 2019). As it illuminates the sample orthogonally to the detection objective only with a thin planar sheet of light, it minimizes the exposure of the sample to the light. As a result, the damage (photobleaching and phototoxicity) inflicted to the sample is quite low (Adams et al., 2015) compared with other types of microscopy, such as confocal microscopy for instance. This allows imaging of live samples for long periods of time.

However, in order to be fast, it slightly compromises the resolution, in particular in thicker and deeper tissues. For this reason, this type of microscopy is most often used to image whole developing organisms or entire organs/structures (Keller et al., 2008; Tomer et al., 2012), but not so much for studies at the cellular or subcellular level.

Confocal laser scanning microscopy, in turn, is much more useful for cellular and subcellular imaging studies, and is commonly used for imaging fixed samples (and, in a few cases for live imaging) (Baldera et al., 2023; Gunawan et al., 2019; Swinburne et al., 2018). This is due to its ability to produce a point source of light and eliminate out-of-focus light, which creates high-resolution images; and to generate very thin optical sections of biological samples, which allows 3D reconstruction of the sample (reviewed in (Elliott, 2020)). The main disadvantage of this microscopy technique is the phototoxicity and the low speed. Improvements on the technology of the confocal microscope keep being developed and the Airyscan microscope is an example of that. It offers greater sensitivity, and as a result, it generates images with very high resolution and better speed than a standard laser scanning confocal microscope (Huff, 2015; Wu and Hammer, 2021). As in all techniques, there are some disadvantages to the Airyscan confocal microscope, which include phototoxicity and longer processing time (due to higher quantity of data collected).

For the work presented in this chapter, I chose to image the zebrafish inner ear using the Light-sheet fluorescence microscope. The aim of this work was to develop a pipeline to extract a variety of cell shape metrics in tissues with high levels of curvature so that, later, I would have the ability to analyse cell shape changes in the inner ear during formation of the projections of the semi-circular canals. The advantages of using the Light-sheet microscope were that three to five embryos could be imaged at a time, for each stage of interest, and therefore I could obtain a good overview of the epithelial projection development and build up a robust dataset in order to validate the cell shape analysis pipeline.

3.1.2 Cell segmentation

During events of epithelium folding, as described in chapter one, cell shape changes are almost inevitable. An accurate and robust delineation of individual cells through cell segmentation tools is necessary to quantify those cell shape changes and to further understand tissue folding mechanisms, including those present in the inner ear (Swinburne et al., 2018). Several studies on *Drosophila* and zebrafish morphogenesis have shown how analysing cell shape changes as well as tracking them can help to understand the genetic and behavioural mechanisms driving the different tissue shape changes. Most of these studies and techniques that unravel the mechanics under shape acquisition by epithelial layers are limited to two dimensions (Merks et al., 2018; Sanchez-Corrales et al., 2018), but recently there has been a few studies venturing on the three-dimensional world (Hartmann et al., 2020; Khan et al., 2014; Swinburne et al., 2018). Both manual and automated segmentation methods have been used in this field, and types of automated methods will be briefly covered in the manuscript presented in this chapter.

3.1.3 Challenges of imaging and segmenting the developing zebrafish inner ear

Finding the right imaging technique that offers sufficient resolution to allow detecting shape changes at the cellular level during tissue folding events has been a challenge, and the formation of the epithelial projections of the semicircular canals are no exception. This is partially due to the convoluted structure of the inner ear that results from the epithelial projections growing into its lumen, ending up deeper into the tissue as the ear grows. As a result, the fluorescent signal in these structures becomes harder to detect. In addition, there is the challenge of finding the microscopy technique that offers the right balance between high resolution, a high speed of acquisition and low levels of phototoxicity and photobleaching.

When it comes to segmenting cells in the zebrafish inner ear there is the challenge of cells in the dorsal half being very squamous. This means that they appear very thin in the acquired images and as a result, membrane-based cell segmentation tools perform poorly. In addition, there is a lack of image analysis tools for curved and curving epithelia (covered in more detail in the manuscript presented in this chapter). As a result, cell segmentation in this field is often limited to two dimensions, as mentioned before, and in some cases still performed manually (Bryan et al., 2016; Gutzman et al., 2018). Manual cell segmentation can be quite accurate and very useful for gaining familiarity with the system being studied (I benefited from this myself – see Figure 1.7), or to train certain cell shape analysis tools based on deep learning (Cao et al., 2020; Stringer et al., 2021). However, manual segmentation alone is highly time-consuming, drastically bringing down the number of samples one can realistically analyse.

The ultimate dream for the developmental biology and medical communities is that standardised, publicly available, adaptable and automated image analysis tools, such as segmentation and tracking tools, would be developed to allow us to quantitatively and comparatively analyse data and extract the most information possible in a fast, precise, efficient and meaningful manner.

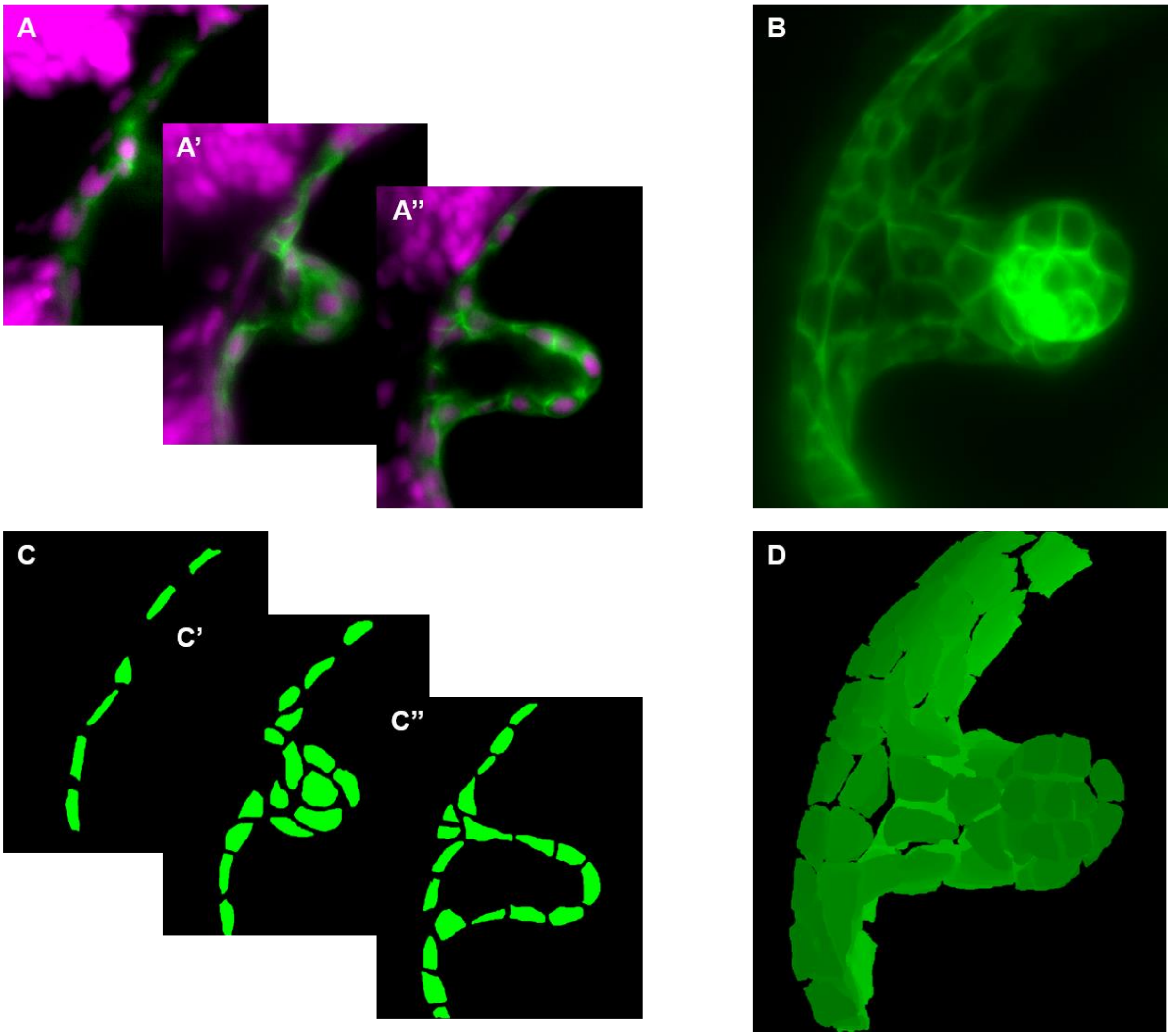

Figure 3.1 - Example of manual segmentation of an epithelial projection of the zebrafish inner ear.

(**A-B**) Anterior projection of *Tg(smad6b:EGFP); Tg(xEF1A:H2B-RFP)* double transgenic embryos. Images acquired in the Zeiss Z1 Light-sheet microscope at 50.5 hours post fertilisation (hpf). Lateral views of the structure are shown. A single *z*-slice is shown in **A-A’** and a maximum intensity projection from a *z*-stack is shown in **B**. (**C-D**) Manually segmented cells from data in **A-B** are shown in these images. This was performed in Fiji (see methods 2.5.1 for details). A single *z*-slice is shown in **C-C’** and a three-dimensional projection of the segmented *z*-stack is shown in **D**.

3.1.4 Choosing shape metrics that are relevant to study epithelial folding in the inner ear

With the advance of image analysis techniques comes the possibility of extracting a vast amount of information from the data acquired, as well as the opportunity to ask more and more questions from a single data set. In response to this, we ought to consider which information we want to extract in order to address the questions we are investigating in an efficient manner to avoid creating a bank of unused information that can present storage challenges.

As explained in sections 1.1.3 and 1.3.1, events of tissue folding are associated with cell shape changes, the most common being apical or basal constriction, apical or basal expansion, and elongation of the apico-basal axis. For this reason, I wanted to make sure the right tools to capture these particular changes in cell morphology were included in the cell shape analysis pipeline we developed and present in the manuscript included in this chapter – *Origami*. The columnar and squamous aspect of cells was captured by a combination of measuring the longitudinal and transversal spread. The first being the spread of the three dimensional cell mass along the apico-basal axis, and the latter being the spread of that mass along the other two perpendicular axes (Figure 3.2). The asymmetry between the apical and basal domains (cell skewness) was captured by measuring the asymmetry of the three dimensional cell mass between the apical and basal halves of the cell (Figure 3.2). More information on these cell shape metrics and others used in the pipeline can be found in the manuscript presented in this chapter.

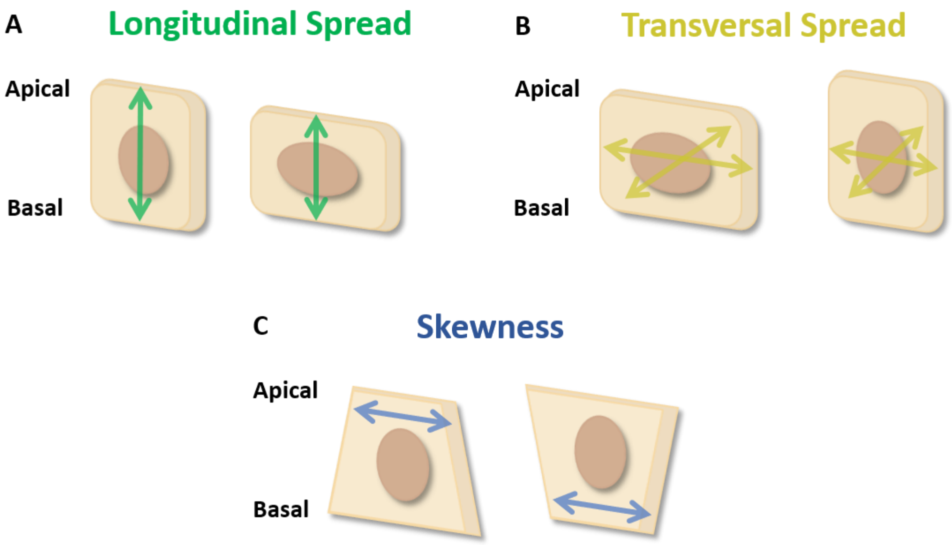

Figure 3.2 – Some of the cell shape measurements used to investigate changes in cell morphology during otic tissue folding.

(**A**) Longitudinal spread is the cell mass along the apico-basal axis marked by the green arrows. Higher values of longitudinal spread suggest a columnar cell (on the left), whereas lower ones suggest a squamous cell (on the right). (**B**) Transversal spread is the cell mass along the two axes perpendicular to the apico-basal axis, marked by the yellow arrows. Higher values of transversal spread suggest a squamous cell (on the left), whereas lower ones suggest a columnar cell (on the right). (**C**) Skewness is the asymmetry of cell mass between the apical and basal halves of the cell. Positive values of skewness suggest a smaller apical half of the cell (blue arrow on the left), whereas negative ones suggest a smaller basal half (blue arrow on the right).

3.2 Manuscript

Declaration of content and author contribution:

This chapter is a published manuscript that contains collaborative work of two teams supervised by Prof. Tanya T. Whitfield and Prof. Alejandro F. Frangi. I have decided to include this manuscript in this thesis for two reasons. First, this study addresses the need for cell shape analysis tools that are able to extract direction-variant 3D cell shape metrics of epithelia with high levels of curvature. Second, I am a co-author in this manuscript and have contributed with significant work. This includes acquiring all the light-sheet microscopy data (inner ear image *z*-stacks) used to validate the pipeline, acquiring the airyscan confocal microscopy data displayed in Figure 1, writing the methods for this experimental work, testing the finalised pipeline in different datasets to screen for errors (bugs), reviewing and editing. Contributions from all authors are as follows:

Conceptualization: Sarah Baxendale, Tanya T. Whitfield, Alejandro F. Frangi.

Data curation: Tania Mendonca, Ana A. Jones, Sarah Baxendale, Alejandro F. Frangi.

Formal analysis: Tania Mendonca.

Funding acquisition: Sarah Baxendale, Tanya T. Whitfield, Alejandro F. Frangi.

Investigation: Sarah Baxendale, Tanya T. Whitfield, Alejandro F. Frangi.

Methodology: Tania Mendonca, Ana A. Jones, Jose M. Pozo, Sarah Baxendale, Tanya T. Whitfield, Alejandro F. Frangi.

Project administration: Tania Mendonca, Sarah Baxendale, Tanya T. Whitfield, Alejandro F. Frangi.

Resources: Sarah Baxendale, Tanya T. Whitfield, Alejandro F. Frangi.

Software: Tania Mendonca, Jose M. Pozo.

Supervision: Tanya T. Whitfield, Alejandro F. Frangi.

Validation: Tania Mendonca, Jose M. Pozo.

Visualization: Tania Mendonca.

Writing – original draft: Tania Mendonca.

Writing – review & editing: Tania Mendonca, Ana A. Jones, Jose M. Pozo, Sarah Baxendale, Tanya T. Whitfield, Alejandro F. Frangi.

This is a *PLOS Computational Biology* Software paper.

Citation: Mendonca T, Jones AA, Pozo JM, Baxendale S, Whitfield TT, Frangi AF (2021) Origami: Single-cell 3D shape dynamics oriented along the apico-basal axis of folding epithelia from fluorescence microscopy data. PLoS Comput Biol 17(11): e1009063. https://doi.org/10.1371/journal.pcbi.1009063

Editor: Dina Schneidman-Duhovny, Hebrew University of Jerusalem, ISRAEL

Received: May 5, 2021; **Accepted:** October 13, 2021; **Published:** November 1, 2021

Data Availability: Code can be found on GitHub: https://github.com/cistib/origami Data can be found on FigShare: https://doi.org/10.6084/m9.figshare.14531421.v1.

Funding: Work was supported by a Biotechnology and Biological Sciences Research Council (BBSRC; https://bbsrc.ukri.org/) project grant to TTW, SB and AFF (BB/M01021X/1). Imaging was carried out in the Wolfson Light Microscopy Facility at the University of Sheffield, supported by a Biotechnology and Biological Sciences Research Council BBSRC ALERT14 award to TTW and SB for light-sheet microscopy (BB/M012522/1). AAJ was funded by a Doctoral Training Award from the Biotechnology and Biological Sciences Research Council BBSRC White Rose Doctoral Training Partnership in Mechanistic Biology (BB/M011151/1). AFF is supported by the Royal Academy of Engineering Chair in Emerging Technologies Scheme (CiET1819\19) and the MedIAN Network (EP/N026993/1) funded by the Engineering and Physical Sciences Research Council (EPSRC; https://epsrc.ukri.org/). The funders had no role in study design, data collection and analysis, decision to publish, or preparation of the manuscript.

Competing interests: The authors have declared that no competing interests exist.

Origami: Single-cell 3D shape dynamics oriented along the apico-basal axis of folding epithelia from fluorescence microscopy data

Tania Mendonca[1,2,#]*, Ana A. Jones[2], Jose M. Pozo[1,3], Sarah Baxendale[2], Tanya T. Whitfield[2] and Alejandro F. Frangi[1,3,4]*

[1] Centre for Computational Imaging and Simulation Technologies in Biomedicine (CISTIB), Department of Electronic and Electrical Engineering, University of Sheffield, Sheffield, UK

[2] Department of Biomedical Science, Bateson Centre and Neuroscience Institute, University of Sheffield, Sheffield, UK

[3] Centre for Computational Imaging and Simulation Technologies in Biomedicine (CISTIB), School of Computing and School of Medicine, University of Leeds, Leeds, UK.

[4] Medical Imaging Research Center (MIRC), University Hospital Gasthuisberg, Cardiovascular Sciences and Electrical Engineering Departments, KU Leuven, Belgium

[#] Current Address: Optics and Photonics Research Group, Department of Electrical and Electronic Engineering, University of Nottingham, Nottingham, UK

*Corresponding Authors

Email: A.Frangi@leeds.ac.uk; Tania.Mendonca@nottingham.ac.uk

Abstract:

A common feature of morphogenesis is the formation of three-dimensional structures from the folding of two-dimensional epithelial sheets, aided by cell shape changes at the cellular-level. Changes in cell shape must be studied in the context of cell-polarised biomechanical processes within the epithelial sheet. In epithelia with highly curved surfaces, finding single-cell alignment along a biological axis can be difficult to automate *in silico*. We present ‘Origami’, a MATLAB-based image analysis pipeline to compute direction-variant cell shape features along the epithelial apico-basal axis. Our automated method accurately computed direction vectors denoting the apico-basal axis in regions with opposing curvature in synthetic epithelia and fluorescence images of zebrafish embryos. As proof of concept, we identified different cell shape signatures in the developing zebrafish inner ear, where the epithelium deforms in opposite orientations to form different structures. Origami is designed to be user-friendly and is generally applicable to fluorescence images of curved epithelia.

Author Summary:

During embryonic development, two-dimensional epithelial sheets bend and fold into complex three-dimensional structures – like paper in the origami art form. The genetic and biomechanical processes driving epithelial folding can be polarised in the epithelium, leading to asymmetric shape changes at the single cell level. Defects in such epithelial shaping have been linked to many developmental anomalies and diseases. It is, therefore, important not only to quantify shape change at the single cell level, but also to orientate these asymmetrical changes along an epithelial axis of polarity when studying morphogenetic processes. Origami is a MATLAB-based software that has been developed to automatically extract such single-cell asymmetrical shape features along the epithelial apico-basal axis from fluorescence microscopy images of folding epithelia. Origami provides a solution to computing directional vectors along the epithelial apico-basal axis followed by extracting direction-variant shape features of each segmented cell. It is generally applicable to epithelial structures regardless of complexity or direction of folding and is robust to imaging conditions. As proof of concept, Origami successfully differentiated between different cell shape signatures in highly curved structures at different developmental timepoints in the zebrafish inner ear.

Introduction

Complex morphologies across taxa and tissue types are generated through the deformation of epithelial sheets [1–3]. In the embryo, many developing epithelia form highly curved surfaces. Epithelial folding processes are driven by polarised mechanical forces and involve three-dimensional changes in shape at the cellular level [4,5]. Fluorescence imaging techniques have made it possible to follow such shape changes at cellular resolution, *in vivo* and in real-time [6–8]. These imaging advances have consequently driven the development of tools to quantify epithelial dynamics, especially cell shape changes.

Many image analysis tools measuring cell shape change have been limited to two-dimensional [9–12] or quasi-3D fluorescence microscopy data [13]. Extending these measurements to 3D has been aided by the development of membrane-based 3D segmentation methods such as ACME [14], RACE [15], 3DMMS [16], CellProfiler 3.0 [17], and more recently, deep-learning-based methods [18–21]. Some image analysis tools, such as CellProfiler 3.0 [17], MorphoGraphX [22] and ShapeMetrics [23], provide pipelines to compute direction invariant cell shape features. However, finding the position of 3D-segmented cells along biologically relevant axes to quantify directionally variant shape features is still a challenging problem that has so far not seen a generalised solution.

Solving the orientation of individual cells relative to the known overall polarity of the epithelial sheet is critical, as cell-polarised biomechanical processes drive cell shape changes; constriction or expansion can occur along either the apical [24,25] or baso-lateral [26] cell surfaces and can be detected by any skew in mass distribution within a cell along an apico-basal axis of symmetry. Epithelial folding may be initiated or influenced by cell proliferation, cell death, cytoskeletal remodelling, or changes in cell surface properties [27,28]. These mechanisms can lead to changes in cell shape features, including cell height and width, volume, surface area and sphericity.

Cell orientation or polarity can be defined along the plane of the epithelium (planar cell polarity) or perpendicular to the epithelial plane, along the apico-basal axis of the cell. Existing automated methods for assigning polarity to segmented cells often rely on additional biochemical markers for polarity [29–31]. Including such additional markers in fluorescence imaging experiments increases the time taken to generate each image, potentially leading to phototoxicity, and the resulting larger volume of image data makes analysis computationally expensive. Moreover, producing the required animals carrying multiple transgenes for live imaging can be challenging and costly. Some image analysis methods compute direction vectors for individual cells by drawing normal vectors to polynomial functions, often ellipsoids, used to estimate the surface of the specimen — for example, entire embryos [15] or blastoderms [32] undergoing morphogenesis. These methods are specific to the geometry of the specimen and are unsuitable for analysing complex folded topologies at advanced morphologic developmental stages. A third method uses known features of cell shape to assign cell orientation, for example by applying principal component analysis (PCA) to compute the apico-basal axis in columnar cells in EDGE4D [33] and the anterior-posterior axis in zebrafish lateral line primordia using landmark-based geometric morphometrics [31], or orienting cells along their long axis in the zebrafish optic cup as in LongAxis [34]. These strategies will be applicable only if a dominant cell shape feature, for example cell height/width ratio, is known and remains unchanged over space and time.

We introduce a new automated and easy-to-use tool, Origami, for extracting direction-variant shape features along the apico-basal axis by reconstructing the epithelial surface using a triangular mesh (Fig 1). Origami applies to a wide range of geometries of specimens undergoing morphogenesis and automatically extracts direction vectors for individual cells aligned to the apico-basal axis of the epithelial sheet without requiring additional labels for polarity. Direction-variant shape features are calculated by computing the geometric moments for the volume enclosed by the polygon representation of each segmented cell [35]. We showcase the versatility of our method using data from an assortment of structures at a range of developmental stages within the otic vesicle (developing inner ear) of zebrafish embryos.

Design and Implementation

The Origami pipeline is preceded by a membrane-based segmentation step. For this, we employed the open-source ACME segmentation software [14]. The segmented data are subjected to two main operations within Origami; epithelial polarity direction vector assignment (Fig 1b) and extraction of shape features (Fig 1c).

Assigning polarity direction to individual cells

To compute directionally-variant cell shape features, such as skewness (asymmetry in cell mass), and longitudinal and transversal spread, the positioning of segmented cells must be found in 3D space along a biologically relevant axis – we chose the known apico-basal axis of the cell. The folding epithelium was reconstructed *in silico* as a thin ‘crust’ – an open surface mesh that triangulates the centroids of the segmented cells in 3D space using the Crust algorithm [36,37] (Fig 1b). The Crust method computes a surface mesh from unorganised points – cell centroids in our case, using the Voronoi diagram of the cell centroids.

Following this, our automated method corrects imperfections in the estimated surface mesh that can cause errors in the resulting direction vectors. The mesh is refined by removing duplications (in vertices or triangular faces computed) and any self-intersecting triangular faces. Non-manifold edges, that is, those edges shared by more than two triangular faces, are re-meshed as a manifold mesh using the ball-pivoting algorithm [38,39].

The triangular faces of the refined mesh are ordered, and so by applying the right-hand rule when generating normal vectors to the surface mesh, these vectors all point to the same side of the mesh representation of the epithelial surface (Fig 1b). At this point, there are still two possible opposing orientations for each computed vector – facing the apical or the basal face of the epithelium, with a difference only in sign. In the developing zebrafish otic vesicle, the apical surface of the epithelium faces the fluid-filled lumen of the vesicle [2,8,40]. We used this prior knowledge to inform the orientation of the vectors by setting the value of a binary orientation-determining parameter to ‘in’ so that they point to a convergent point which falls on the side of the curved surface mesh that corresponds to the apical (lumenal) side of the epithelium at each cell. When a structure folds in opposing orientation, such as in the synthetic data generated for this study, ‘in’ sets the polarity direction vectors to point towards a global convergent point, in our case determined by the curvature of the whole synthetic epithelium.

Under-segmentation can cause missing regions or unwanted holes in the triangular mesh, introducing errors when ordering the triangular faces. Our pipeline attempts to repair these holes by detecting and then remeshing them where possible. Holes, when detected, are flagged as a warning to users about potential errors in the output. Normal vectors to the reconstructed surface represent the apico-basal axis of the epithelium and are generated for each segmented cell at their centroid position (Fig 1b and c).

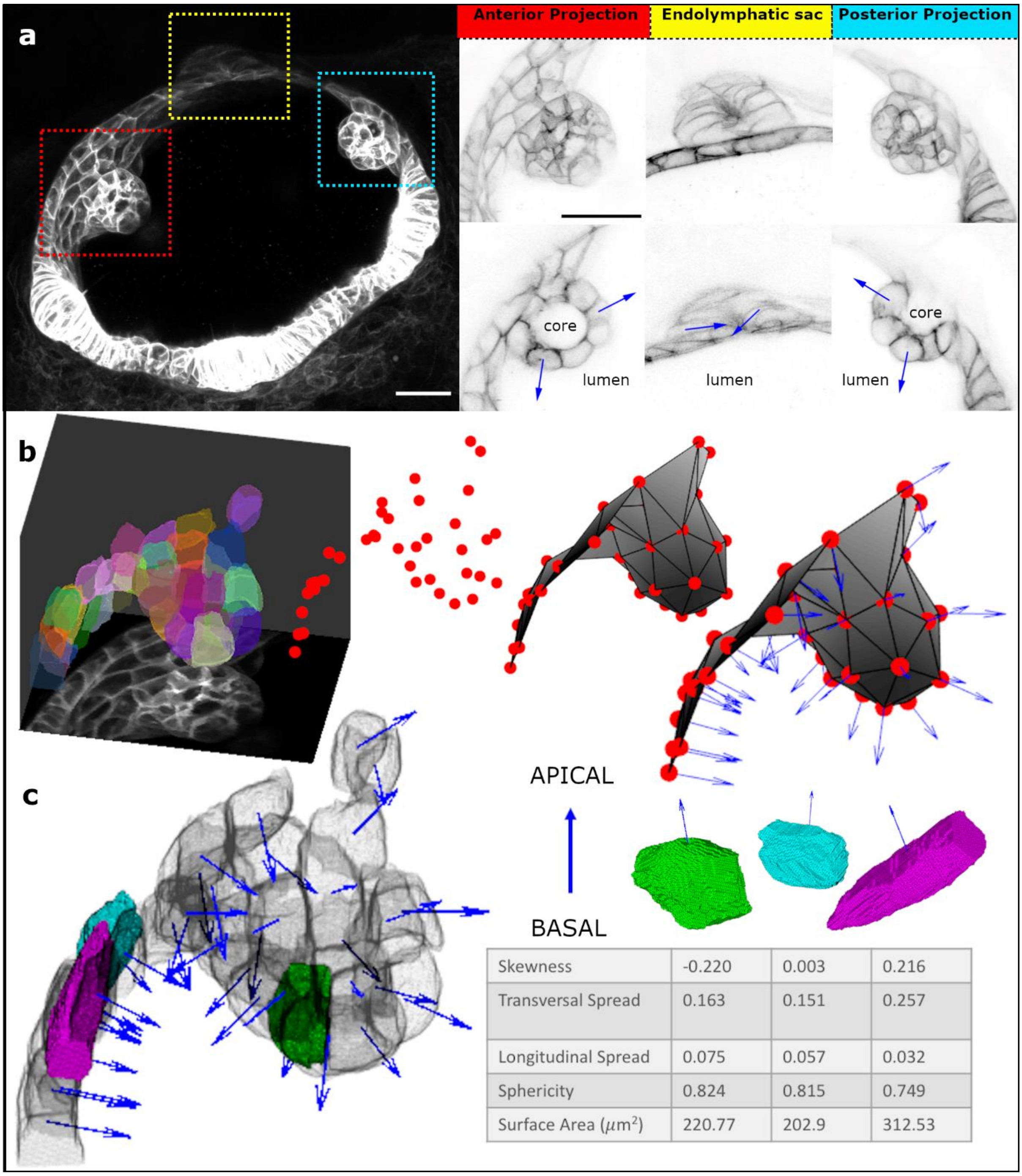

Skewness	-0.220	0.003	0.216
Transversal Spread	0.163	0.151	0.257
Longitudinal Spread	0.075	0.057	0.032
Sphericity	0.824	0.815	0.749
Surface Area (μm^2)	220.77	202.9	312.53

Fig 1: **Origami Image Analysis Pipeline**. a. Airyscan confocal fluorescence micrograph (maximum intensity projection (MIP) of 35 z-slices) of the developing zebrafish otic vesicle at 51.5 hours post fertilisation. Red box – anterior projection; yellow box – endolymphatic sac; cyan box – posterior projection. The ROIs are expanded alongside – top row MIPs, and bottom row single slices. Scale bars: 20 µm. Blue arrows mark the direction of apicobasal polarity (pointing towards the apical side). b. Polarity assignment on segmented data; ROI surrounding the anterior projection was segmented (here overlaid on the MIP) using ACME, centroids were generated for each segmented cell and a triangular surface mesh was produced from these centroids. Normal vectors (blue arrows) to this surface mesh represent the apico-basal axis. c. Cell shape features were computed concerning the assigned apico-basal

axis; here, three example cells are highlighted, alongside a 3D rendering showing their position in the anterior projection and the corresponding shape metrics in a table.

Computing shape features using 3D geometric moments

The shape of an object can be characterised using central geometric moments [41]. Geometric moments are widely used in object recognition and classification problems [42,43] since they (i) are simple to compute, (ii) organise features in orders of increasing detail, and (iii) can be extended to *n* dimensions. Each moment, $G_{ijk}^{(V)}$, is defined by the integral over the object (in our case, each segmented cell), of the Cartesian coordinates monomial $x^i y^j z^k$, where $i, j, k \geq 0$, with the origin of coordinates at the centroid.

In our analysis pipeline, 3D geometric moments were computed using the algorithm introduced in [35]. The defining continuous integrals are exactly computed within the triangular surface mesh generated for each individual segmented cell, split into a sum:

$$G_{ijk}^{(V)} = \sum_{c \epsilon\, Facets} sign(Vol_c) \int_{Tc} x^i\, y^j z^k\, dx\, dy\, dz, \qquad (1)$$

where each tetrahedron T_c is defined by a triangle in the surface mesh and the origin (cell centroid). The determinant gives the oriented volume of this tetrahedron,

$$Vol = \frac{1}{6} \begin{vmatrix} x_1 & x_2 & x_3 \\ y_1 & y_2 & y_3 \\ z_1 & z_2 & z_3 \end{vmatrix}. \qquad (2)$$

Considering its sign, the determinant allows the algorithm to be applied to shapes of any complexity and topology. The integral in each T_c is given by a closed formula involving only the Cartesian coordinates of the triangular vertices.

The geometric moments of low orders have simple, intuitive interpretations. The zeroth order moment $G_{000}^{(V)}$ provides the volume of the object, here an individual cell. For central moments, the first order moments are trivially null: $G_{100}^{(V)} = G_{010}^{(V)} = G_{001}^{(V)} = 0$. The second-order moments correspond to the spread (covariance tensor) of the distribution. So, the projection of the mass of each cell along the corresponding polarity vector represents the ‘spread’ as variance in mass ‘longitudinally’ (along the apico-basal axis) and ‘transversally' (along the epithelial plane). This allowed us to identify if cells were more or less columnar (tall cells) or squamous (flat cells) in shape. The third-order moments represent ‘skewness’, which is the deviation from symmetry. In our pipeline, skewness was measured along the polarity direction vector in the apico-basal direction, with positive skewness values indicating apical cell constriction and/or basal relaxation and negative values indicating basal cell constriction and/or apical expansion. A value of zero indicated no skew. Additionally, the sphericity of each cell was computed as the ratio of the cell surface area to the surface area of a sphere with the same volume as the cell [44], from 0 for a highly irregularly-shaped cell to 1 for a perfect sphere.

Results

Evaluation of Computed Cell Polarity Direction Vector

To evaluate the computed direction vectors denoting cell polarity, we generated 3D synthetic data representing curved, folding epithelia with varying degrees of curvature and height of folded peak in two opposing orientations (S2 Text and Fig 2a). To reflect real-world *in vivo* fluorescence imaging conditions, these synthetic data were corrupted with three incremental levels of Gaussian and Poisson noise (S2 Text and Fig 2a). Using the synthetic data, two types of error in computed polarity direction vectors were assessed: (1) an orientation flipping error, measured as the percentage of polarity vectors with an opposing orientation (opposite sign) to the polarity ground truth (S2 Text), and (2) direction accuracy, measured as the mean deviation angle between the polarity vectors produced by Origami, correctly oriented, and the polarity ground truth.

Of the two aspects of surface geometry analysed, height of folded peak (in two opposing directions), did not contribute significantly to orientation flipping errors (Linear Regression; $p = 0.86$, $R^2 = -0.04$). However, a larger radius of curvature of epithelium (a flatter epithelial sheet), did correlate with orientation flipping errors – albeit with a small effect of 0.08% increase for every 1 µm (5 pixels) increase in radius of curvature (Linear Regression; $p = 0.042$, $R^2 = 0.12$, effect), and a lower quality of segmentation output from ACME (Linear Regression $p < 0.001$, $R^2 = 0.46$; Fig 2b) computed as a Dice score. This meant a 0.2% reduction in Dice score for every 1 µm (5 pixels) increase in the radius of curvature. This correlation may be attributed to the reduced ability of ACME to segment flat, squamous cells in an epithelium oriented mostly along the lateral (XY) plane in data with anisotropic voxel resolution (here modelled using an anisotropic point spread function (PSF)). We found a correlation between noise applied to the synthetic images and errors in both polarity orientation flipping (ANOVA: $p \approx 0.001$; Tukey's contrasts showed 11.3% increase in errors at highest noise level compared with the lowest noise level applied – $p = 0.0039$) and segmentation output (ANOVA: $p < 0.01$; Tukey's contrasts showed 16.3% reduction in Dice score at highest noise level from the lowest noise level applied – $p = 0.0045$). Segmentation quality, in turn, influenced polarity orientation flipping, with errors below 1.5% at Dice scores above 0.8, but increasing with further decrease in Dice scores (Polynomial Regression; first-order: $p < 0.001$, Effect size = -28.78; second-order: $p < 0.01$, Effect size = 16.26; Fig 2c). Comparisons of many available segmentation algorithms when validating with fluorescent images from non-folded structures such as early-stage nematode embryos [16] or plant roots [18] have been shown to give Dice scores above 80%, suggesting a good performance under real experimental conditions.

Quantitative direction accuracy was evaluated in the synthetic data, for which, in contrast to data from real fluorescence images, a reliable ground truth could be generated from the known underlying surface functions. Compared to the polarity ground truth data, an overall offset of 10.6° ± 15.5° (mean ± std) was measured from our entire synthetic dataset. Just as for the polarity orientation flipping error, height of folded peak did not influence polarity direction accuracy (Linear Regression; $p = 0.39$, $R^2 = -0.01$), but there was a small effect of curvature of the epithelium with an additional 0.06° offset for every 1 µm (5 pixels) increase in radius of curvature of the epithelium (Linear Regression; $p = 0.005$, $R^2 = 0.24$). At the highest level of noise applied, errors in polarity orientation had a 6.6° greater offset than at the lowest noise level applied (Tukey's contrasts; $p = 0.003$). There was also a negative linear effect of segmentation quality with a 2.9° offset predicted for every 10% reduction in Dice score (Linear Regression; $p < 0.0001$, $R^2 = 0.53$; Fig 2c).

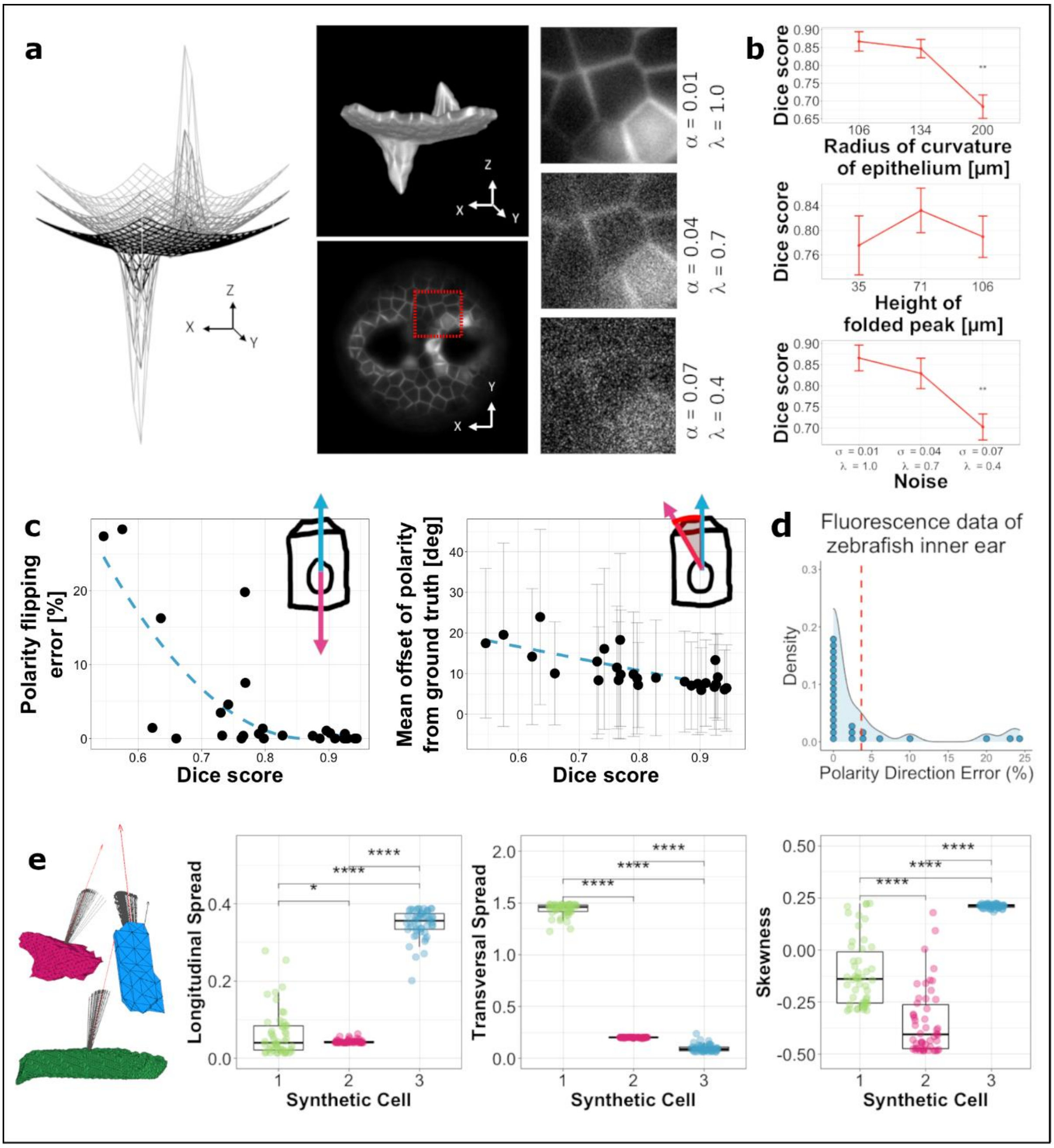

Fig 2: **Assessment of polarity assignment**. a. Surface meshes of synthetic epithelia for validating the Origami analysis pipeline. Alongside, 3D rendering of one of the synthetic epithelia (top) and a single 2D slice through it (bottom). Each image volume was corrupted with three levels of noise. b. The relationship between surface geometry/ noise and segmentation quality. Error bars represent the standard deviation. Tukey's pairwise comparisons with significant values depicted with asterisks; Dice score at radius of curvature of 200 μm (1000 pixels) compared to that at 106 μm (530 pixels) – p = 0.0004, Dice score at largest noise level compared to the lowest – p = 0.0045. c. Effect of segmentation quality on errors in orientation flipping (left) and direction offset in the computed polarity vectors (error bars in grey represent standard deviation). Dashed lines represent quadratic and linear fit to data respectively. d. Probability density of errors in polarity direction in real fluorescence data from zebrafish embryos.

Each dot represents the percentage error from a 3D segmented volume (n = 27; total of 949 segmented cells across all the images). The dashed line shows the mean error in the dataset (<4%). e. Sensitivity of cell shape metrics to errors in polarity orientation. Data points in the graphs are depicted with the same colour as the corresponding synthetic cell alongside. Tukey's pairwise comparisons with significant values depicted with asterisks; Longitudinal spread: 1-2 $p = 0.039$, 1-3 $p < 0.0001$, 2-3 $p < 0.0001$; Transversal Spread: 1-2 $p < 0.0001$, 1-3 $p < 0.0001$, 2-3 $p < 0.0001$; Skewness: 1-2 $p < 0.0001$, 1-3 $p < 0.0001$, 2-3 $p < 0.0001$.

We further tested the effect of such errors in direction accuracy on the direction-variant shape metrics computed by applying directional noise —with a mean equal to the measured mean error above —to polarity vectors of three example cells showing extreme shape features from the synthetic dataset and computed direction-variant shape metrics for each new displaced polarity vector ($n = 50$; Fig 2e). The resulting computed shape metrics could still successfully differentiate between the three cells, showing that direction accuracy errors (excluding orientation flipping errors) should not adversely affect the shape metrics computed. On the other hand, orientation flipping errors will affect shape metrics, but as shown above, these errors are predicted to be small for a well-segmented image volume and can be easily identified by visual inspection and corrected if needed using the Origami pipeline.

Additionally, orientation flipping errors were quantified from real light-sheet fluorescence microscopy data from structures in the developing zebrafish otic vesicle (Figs 1 and 3). For this, cells assigned the wrong orientation along the apico-basal axis – that is, facing the basal surface instead of the apical surface, and were identified by visual assessment in the Origami pipeline, showing errors in 3.65% of $n = 949$ cells analysed (Fig 2d).

Proof of Principle: Insights Into Cell Shape Dynamics During Epithelial Morphogenesis Within The Zebrafish Inner Ear

To further validate our method, we used Origami to characterise cell shape dynamics involved in the formation of different structures in the otic vesicle of the zebrafish embryo (Figs 1 and 3). We analysed light-sheet fluorescence image data from the anterior epithelial projection (AP) for the developing semicircular canal system, together with the endolymphatic sac (ES), at three developmental time points: 42.5 hours post fertilisation (hpf) (time point 1), 44.5 hpf (time point 2) and 50.5 hpf (time point 3), using three different fish for each time point. We also analysed the posterior epithelial projection (PP), a similar structure to the AP, but which develops later [40], at developmentally equivalent time points to that of the AP (46.5 hpf, 50.5 hpf and 60.5 hpf). The AP and PP are finger-like projections of the epithelium that move into the lumen of the vesicle, with the apical side of the cell on the outside of the curved projection surface [40]. By contrast, the ES forms as an invagination from dorsal otic epithelium, with the constricted apical surfaces of the cells lining the narrow lumen of the resultant short duct [8,45,46]. As the ES is formed through deformation of the epithelial sheet with opposite polarity to that of the epithelial projections, we expect cells in the ES and the projections to show significant differences in cell shape. Conversely, we do not expect significant differences in cell shape between the AP and PP cells, which form equivalent structures in the developing ear.

For each structure, the following shape attributes were computed at the single-cell level: surface area, sphericity, longitudinal spread, transversal spread and skewness. Since volume and surface area show high collinearity within our data (Pearson correlation coefficient = 0.98, 95% confidence intervals = [0.977, 0.984]), cell volume was excluded from further analysis. Although images included cells in the non-folding epithelium around the developing structures of interest, only cells from the folding epithelium were analysed. A multivariate analysis ({MANOVA.RM} package [47] in R [v 4.0.0]) of the dependence of cell shape attributes on the epithelial structure from which they are derived at different time points showed a significant difference between the three structures at the first two developmental times (Wald-type statistic; $p = 0.035$ (resampled $p = 0.001$) at time point 1 and $p < 0.001$ (resampled $p < 0.001$) at time point 2) but not at the final time point analysed ($p = 0.706$ (resampled $p = 0.038$)) for all shape attributes. Post-hoc Tukey's contrasts indicated that cells in the endolymphatic sac showed significantly different shape dynamics from those of cells in both projections (ES - AP $p = 0.006$, PP - ES $p = 0.012$ at time point 1; ES - AP $p = 0.0002$, PP - ES $p = 0.0002$ at time point 2 but ES - AP $p = 0.192$, PP - ES $p = 0.116$ at time point 3). There was no significant difference in the cell shape signature between cells in the anterior and posterior projections (Tukey's contrasts; PP - AP $p = 0.997$ at time point 1; PP - AP $p = 0.999$ at time point 2 and PP - AP $p = 0.896$ at time point 3). These results indicate that the cell shape features included were more similar than different for cells from the structures at the third time point analysed.

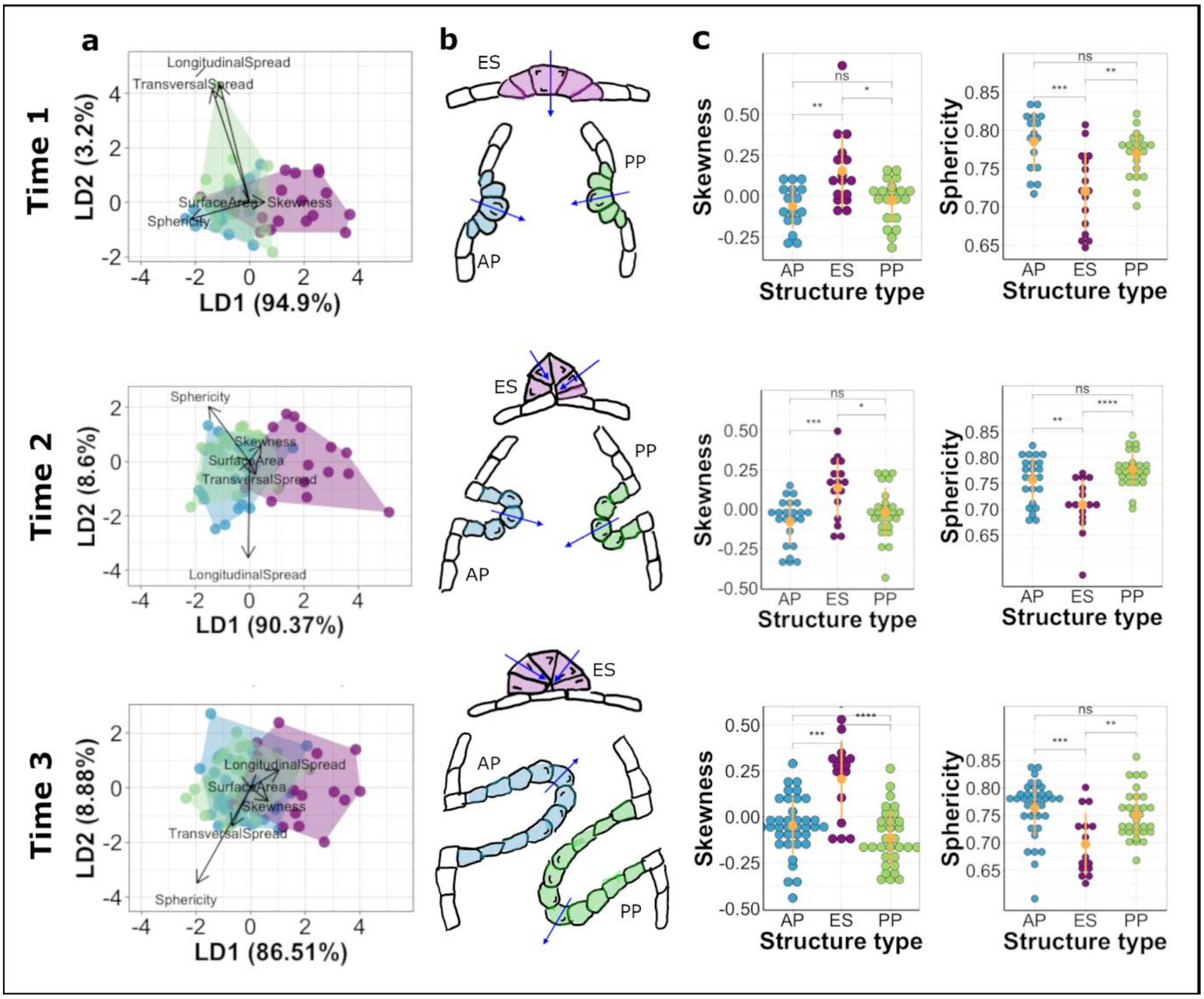

Fig 3: **Comparison of shape dynamics in developing structures of the zebrafish inner ear**. Rows represent each time point analysed. Data in blue represent cells from AP, green represent cells from PP and magenta represent ES. a. Linear discriminate analysis (LDA) biplots illustrate multivariate clustering of data – data from AP and PP show considerable overlap indicating similar shape signatures while data from ES show less overlap with the former. b. Schematic illustrations of cell shape signatures at the time points analysed showing cells in the ES having skew in the opposite direction to those in the projections and having less rounded shapes. Arrows indicate apico-basal polarity. c. Plots showing differences in skewness and sphericity between the structures at the time points analysed. Yellow dots with error lines represent mean and standard deviation for the data. p values for paired comparisons depicted are from Table 1.

Of the attributes analysed, skewness (Kruskal-Wallis test; $p = 0.008$ at time 1, $p = 0.004$ at time 2 and $p < 0.0001$ at time 3), sphericity (Kruskal-Wallis test; $p < 0.001$ at time 1, $p = 0.00012$ at time 2 and $p < 0.001$ at time 3) and surface area (Kruskal-Wallis test; $p < 0.001$ at time 1, $p < 0.0001$ at time 2 and $p = 0.018$ at time 3) described significant differences in cell shape across all the three time points analysed; cells in the endolymphatic sac were characterised by positive skewness values, smaller sphericity values and larger surface areas as compared with cells in both projections, which show negative values of skewness (Table 1 and Fig 3).

The differences in surface area are likely to be attributed to differences in sphericity between the cells in the three structures, but not in dimensions, as the transversal and longitudinal spread showed no significant differences.

Table 1: Paired comparisons using Wilcoxon rank sum exact test (p values – adjusted using 'Holm' correction)

	AP - ES			**PP - ES**			**AP - PP**		
Time point	1	2	3	1	2	3	1	2	3
Skewness	0.009	0.002	<0.001	0.036	0.036	<0.0001	0.42	0.286	0.047*
Sphericity	0.002	0.012	<0.001	0.005	<0.0001	0.007	0.149	0.228	0.07
Surface Area	0.001	<0.0001	0.032	0.001	<0.0001	0.013	0.887	0.85	0.912
Transversal Spread	0.057	0.062	1	0.357	0.062	1	0.357	0.897	1
Longitudinal Spread	1	0.88	0.054	1	0.81	0.102	1	0.46	0.582

*The differences in skewness between cells in the AP and PP at the 3rd time point tended towards significance. This might be attributed to differences in the lengths of projections, with cells at the leading end of the projection showing more extreme skewness values while cells along the lateral sides showing less skewed shape.

Availability and future directions

Origami is free to download from: https://github.com/cistib/origami. It is implemented within MATLAB (compatibility with version 2018b onwards) and includes additional tools for visualising cell shape metrics from complex folding epithelia at the single-cell level. Instructions for installation and use are included with the software.

Our software can accept pre-segmented data, making it compatible with segmentation algorithms of the user's choice, potentially allowing for data acquired using other 3D imaging techniques such as tomography to be analysed. Segmented data must represent cell shape accurately, and so the choice of imaging technique that can faithfully detect 3D cell shape alongside membrane or cytoplasm-based segmentation is critical.

We used *a priori* knowledge of the otic epithelium organisation to inform the orientation of the apico-basal axis of the epithelial sheet to face the lumen of the otic vesicle [2,8,40]. It is essential to know the organisation of the apico-basal axis of cells within any new structure studied to apply Origami - wherein, the orientation-determining parameter can then be set to always be 'in' or 'out' depending on if the polarity direction vector is required to point towards the inside or outside face of a curved structure. We also assumed that individual cells do not violate this organisation, as this cannot be detected without additional polarity-specific labels. In such a case, polarity vectors from our analysis can be complemented with information from polarity-specific labelling to track such behaviour. Moreover, to compute shape features along an alternative axis of polarity, the pipeline can accept pre-assigned polarity as a cell-specific vector-list to compute direction-variant shape features.

We expect Origami to be applied to studying a wide range of morphogenetic processes and contributing to our understanding of the biomechanical processes underpinning them.

Acknowledgements:

We thank N. van Hateren for assistance with imaging, S. Burbridge and M. Marzo for technical support, and the Sheffield Aquarium Team for zebrafish husbandry.

Supporting Information

S1 Software Code

Zip file containing MATLAB scripts and instructions for installing and running Origami software. Requires MATLAB (v 2018b onwards).

Supplementary Materials and Methods

Zebrafish husbandry

All zebrafish work was reviewed and approved by the Project Applications and Amendments Committee of the University of Sheffield Animal Welfare and Ethical Review Body (AWERB). Work was performed under licence from the UK Home Office and according to recommended standard husbandry conditions [1,2]. The transgenic line used to image the cell membranes in the otic vesicle was *Tg(smad6b:mGFP),* a gift from Robert Knight [3]. To facilitate imaging, the transgenic line was raised on a *casper* ($mitfa^{w2/w2}$; $mpv17^{a9/a9}$) (ZDB-GENO-080326-11) background that lacks all body pigmentation. Embryos were raised in E3 medium (5 mM NaCl, 0.17 mM KCl, 0.33 mM $CaCl_2$, 0.33 mM $MgSO_4$, 0.0001 % Methylene Blue). Embryonic stages are given as hours post fertilisation (hpf) at 28.5°C. For live imaging, zebrafish were anaesthetised with 0.5 mM Tricaine methylsulfonate and dechorionated.

Microscopy

Dechorionated embryos were mounted in 0.8% Low Melting Point Agarose in E3 for microscopy. All imaging was performed at 28°C and using the 488 nm excitation laser line corresponding to the GFP membrane label. Image volume files were cropped to include the structure of interest and a small flanking region of the epithelium surrounding it.

For Airyscan confocal microscopy (Fig 1a), dechorionated embryos were mounted laterally in 0.8% Low Melting Point Agarose in E3 in the centre of a 35mm Wilco glass-bottomed Petri dish. E3 with tricaine was added to the Petri dish after the agarose had set. The image stack of 35 *z*-slices was acquired in a ZEISS LSM 880 Airyscan Confocal Microscope with a 40X objective and a *z*-step size of 1 µm.

Light-sheet microscopy (data for pipeline validation): Dechorionated embryos were mounted in agarose in a glass capillary for imaging on the Zeiss Z1 Light-sheet microscope. The microscope chamber was filled with E3 with tricaine. Image stacks varying from 60 to 110 *z*-slices depending on the age of the embryo were acquired with a 20X objective, 2.3x zoom, and a *z*-step size of 0.5 µm.

Synthetic data generation

Synthetic images were generated in MATLAB (2018b, MathWorks) to resemble 3D volumes of folding, cell-membrane-labelled epithelia such as those in the zebrafish otic vesicle depicted in Fig 1a. Each synthetic epithelium was 160 µm x 160 µm along the epithelial plane (XY plane), consisted of about 320 individual cells, and showed two projecting peaks with opposing orientation of folding. The height of the peaks and the curvature of the epithelium were varied to three levels each, such that 9 individual synthetic epithelia were generated (Fig 2a).

The following function defined the surface geometry of each synthetic epithelium generated

$$Z = \sqrt{|a + X^2 + Y^2|} - b\left({X}/{5} - X^3 - Y^5\right)e^{(-X^2-5Y^2)} \qquad (S1)$$

where X and Y are positions on a regular square grid (21 x 21 points) ranging from ‘-4’ to ‘4’ units with an increment of ‘0.4’ units – where each unit = 20 µm. The parameter ‘a’ influences the radius of curvature of the epithelium (a = 5, 20, 80 with a resulting radius of curvature of 106 µm, 134 µm and 200 µm respectively) and ‘*b*’ controls the height of the folded peaks (*b* = 5, 10, 15 with resulting peaks of height 35 µm, 71 µm and 106 µm respectively). Centres of cells (*n* = 320) in the synthetic epithelium were initiated by randomly placing points on this surface, with a minimum distance of 8 µm between them and a padding of 8 µm from the edge of the grid. The resulting set of points were nearly equally spaced.

To convert these surfaces into image volumes, the cell centre positions were then resampled to a volume of isotropic resolution with pixel size of 0.2 µm, resulting in 800 pixels x 800 pixels x >800 pixels (since the *z* dimension was adjusted to accommodate cell positions spanning more than 800 pixels). A Voronoi diagram was generated from the resampled cell centres. The edges of the Voronoi cells were extended 5 µm (26 pixels) orthogonal to the epithelial surface to set cell height and 0.4 µm (2 pixels) in the epithelial plane to set cell membrane thickness. These extended Voronoi edges were used to define a 3D network of polygons as cell membranes. Pixels on the grid that lay within the cell membrane polygons were assigned an intensity value of '1'.

The synthetic images generated were then convolved with a Gaussian PSF using a Fast Fourier Transform (FFT)-based convolution (FFT-based convolution; Bruno Luong, MathWorks File Exchange, accessed Oct 2020) to resemble real-world imaging conditions. The PSF was simulated using the PSF Generator plugin in Fiji [4,5], assuming the following experimental parameters: Numerical Aperture of collection objective lens = 0.5, wavelength of illumination = 532 nm, voxel size = 0.2 µm x 0.2 µm x 0.2 µm. The resulting full width at half maximum (FWHM) of the PSF was 0.6 µm x 0.6 µm x 0.8 µm (3 pixels x 3 pixels x 4 pixels). Finally, after combining each of the images ($n = 9$) with the three levels of Gaussian and Poisson noise using the 'imnoise' function in MATLAB, 27 synthetic image volumes were generated for performing the validation tests. Ground truth to assess segmentation quality was produced from the 9 uncorrupted image volumes.

Polarity ground truth for the synthetic dataset was generated by producing surface normals to the surface functions described by equation (S1), using the SurfNorm function in MATLAB (version 2018b; MathWorks, Natick MA, US).

Membrane-based segmentation

The parameters used to segment our datasets in ACME were different for the synthetic dataset and the real light-sheet data in part, due to differences in voxel resolution (0.2 µm x 0.2 µm x

0.2 µm for the synthetic dataset and 0.1 µm x 0.1 µm x 0.5 µm for the light-sheet data). These parameters were as follows;

For synthetic epithelia:

1. Radius of median filter for denoising – 3.0 pixels (image volumes with noise level 2 and 3), 2.0 pixels (noise level 1)
2. Resampling ratio – 2.5, 2.5, 2.5 (all image volumes)
3. neighbourhood size for membrane signal enhancement filter – 2.0 (noise level 1 and 2), 3.0 (noise level 3)
4. neighbourhood size for Tensor voting – 1.0 (all image volumes)
5. watershed segmentation threshold – 2.0 (noise level 1 and 2), 3.0 (noise level 3)

For fluorescence *in-vivo* data:

1. Radius of median filter for denoising – 0.3 pixels
2. Resampling ratio – 2, 2, 0.39 (resampling to isotropic voxel resolution)
3. neighbourhood size for membrane signal enhancement filter – 0.7
4. neighbourhood size for Tensor voting – 1.0
5. watershed segmentation threshold – 2.0

Classifying cells

Cells were classified as lying within the folding structure or the neighbouring epithelium by clustering the centroids of the segmented cells by the mean curvature; that is, the average of the principal curvatures at each vertex [6,7] of the surface mesh generated in the first part of the Origami pipeline (Fig S1). The mean curvature values showed a bimodal distribution, which could be resolved into a population of points on the folding structure and another consisting of points on the neighbouring non-folding epithelium. Cells at the edges of the image volume were discarded to avoid broken cells.

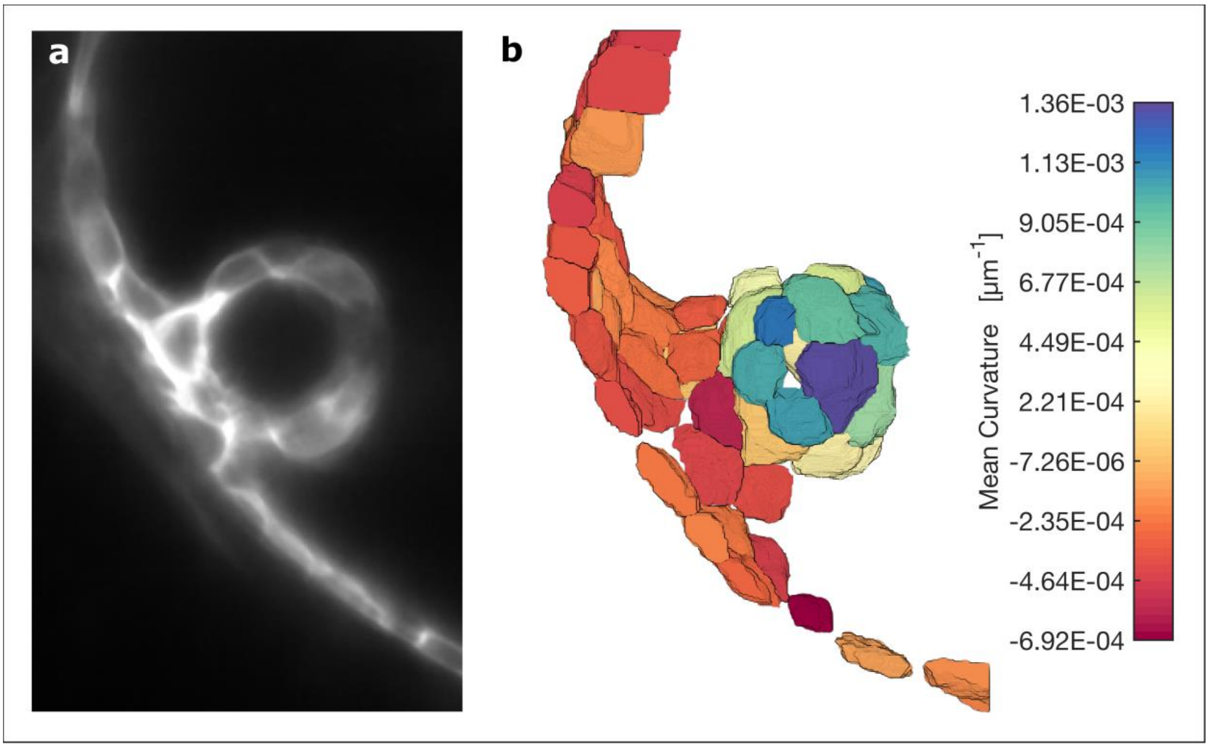

Fig S1: Cell-specific mean curvature of epithelium. a. Single slice through a light-sheet image volume of a region around an anterior projection in the otic vesicle of a 50.5 hpf zebrafish embryo. b. 3D rendering of segmented cells from the same region with individual cells assigned colour values corresponding to the mean curvature at the apical surface of the cell.

References:

1. Kam Z, Minden JS, Agard DA, Sedat JW, Leptin M. Drosophila gastrulation: analysis of cell shape changes in living embryos by three-dimensional fluorescence microscopy. Development (Cambridge, England). 1991;112: 365–70.

2. Alsina B, Whitfield TT. Sculpting the labyrinth: Morphogenesis of the developing inner ear. Seminars in Cell and Developmental Biology. Academic Press; 2017. pp. 47–59. doi:10.1016/j.semcdb.2016.09.015

3. Sui L, Alt S, Weigert M, Dye N, Eaton S, Jug F, et al. Differential lateral and basal tension drive folding of Drosophila wing discs through two distinct mechanisms. Nature Communications. 2018;9: 1–13. doi:10.1038/s41467-018-06497-3

4. Davidson LA. Epithelial machines that shape the embryo. Trends in Cell Biology. Elsevier Current Trends; 2012. pp. 82–87. doi:10.1016/j.tcb.2011.10.005

5. Pearl EJ, Li J, Green JBA. Cellular systems for epithelial invagination. Philosophical Transactions of the Royal Society B: Biological Sciences. 2017;372: 20150526. doi:10.1098/rstb.2015.0526

6. Huisken J, Swoger J, Del Bene F, Wittbrodt J, Stelzer EHK. Optical Sectioning Deep Inside Live Embryos by Selective Plane Illumination Microscopy. Science. 2004;305: 1007–1009. doi:10.1126/science.1100035

7. Ichikawa T, Nakazato K, Keller PJ, Kajiura-Kobayashi H, Stelzer EHK, Mochizuki A, et al. Live Imaging of Whole Mouse Embryos during Gastrulation: Migration Analyses of Epiblast and Mesodermal Cells. Heisenberg C-P, editor. PLoS ONE. 2013;8: e64506. doi:10.1371/journal.pone.0064506

8. Swinburne IA, Mosaliganti KR, Upadhyayula S, Liu T-L, Hildebrand DGC, Tsai TY-C, et al. Lamellar projections in the endolymphatic sac act as a relief valve to regulate inner ear pressure. eLife. 2018;7: 143826. doi:10.7554/eLife.37131

9. Blanchard GB, Murugesu S, Adams RJ, Martinez-Arias A, Gorfinkiel N. Cytoskeletal dynamics and supracellular organisation of cell shape fluctuations during dorsal closure. Development (Cambridge, England). 2010;137: 2743–52. doi:10.1242/dev.045872

10. Heller D, Hoppe A, Restrepo S, Gatti L, Tournier AL, Tapon N, et al. EpiTools: An Open-Source Image Analysis Toolkit for Quantifying Epithelial Growth Dynamics. Developmental Cell. 2016;36: 103–116. doi:10.1016/j.devcel.2015.12.012

11. Farrell DL, Weitz O, Magnasco MO, Zallen JA. SEGGA: a toolset for rapid automated analysis of epithelial cell polarity and dynamics. Development. 2017;144: 1725–1734. doi:10.1242/dev.146837

12. Merkel M, Etournay R, Popović M, Salbreux G, Eaton S, Jülicher F. Triangles bridge the scales: Quantifying cellular contributions to tissue deformation. Physical Review E. 2017;95: 032401. doi:10.1103/PhysRevE.95.032401

13. Sanchez-Corrales YE, Blanchard GB, Röper K. Radially-patterned cell behaviours during tube budding from an epithelium. eLife. 2018;7: e35717. doi:10.7554/eLife.35717

14. Mosaliganti KR, Noche RR, Xiong F, Swinburne IA, Megason SG. ACME: Automated Cell Morphology Extractor for Comprehensive Reconstruction of Cell Membranes. Murphy RF, editor. PLoS Computational Biology. 2012;8: e1002780. doi:10.1371/journal.pcbi.1002780

15. Stegmaier J, Amat F, Lemon WC, McDole K, Wan Y, Teodoro G, et al. Real-Time Three-Dimensional Cell Segmentation in Large-Scale Microscopy Data of Developing Embryos. Developmental cell. 2016;36: 225–40. doi:10.1016/j.devcel.2015.12.028

16. Cao J, Wong MK, Zhao Z, Yan H. 3DMMS: Robust 3D Membrane Morphological Segmentation of C. elegans embryo. BMC Bioinformatics. 2019;20: 176. doi:10.1186/s12859-019-2720-x

17. McQuin C, Goodman A, Chernyshev V, Kamentsky L, Cimini BA, Karhohs KW, et al. CellProfiler 3.0: Next-generation image processing for biology. Misteli T, editor. PLOS Biology. 2018;16: e2005970. doi:10.1371/journal.pbio.2005970

18. Eschweiler D, Spina T V., Choudhury RC, Meyerowitz E, Cunha A, Stegmaier J. CNN-based preprocessing to optimize watershed-based cell segmentation in 3d confocal microscopy images. Proceedings - International Symposium on Biomedical Imaging. IEEE Computer Society; 2019. pp. 223–227. doi:10.1109/ISBI.2019.8759242

19. Aigouy B, Prud'Homme B. EPySeg: a coding-free solution for automated segmentation of epithelia using deep learning. bioRxiv. 2020; 2020.06.30.179507. doi:10.1101/2020.06.30.179507

20. Stringer C, Wang T, Michaelos M, Pachitariu M. Cellpose: a generalist algorithm for cellular segmentation. Nature Methods. 2021;18: 100–106. doi:10.1038/s41592-020-01018-x

21. Cao J, Guan G, Ho VWS, Wong MK, Chan LY, Tang C, et al. Establishment of a morphological atlas of the Caenorhabditis elegans embryo using deep-learning-based 4D segmentation. Nature Communications. 2020;11: 1–14. doi:10.1038/s41467-020-19863-x

22. Barbier de Reuille P, Routier-Kierzkowska A-L, Kierzkowski D, Bassel GW, Schüpbach T, Tauriello G, et al. MorphoGraphX: A platform for quantifying morphogenesis in 4D. eLife. 2015;4: 1–20. doi:10.7554/eLife.05864

23. Takko H, Pajanoja C, Kurtzeborn K, Hsin J, Kuure S, Kerosuo L. ShapeMetrics: A userfriendly pipeline for 3D cell segmentation and spatial tissue analysis. Developmental Biology. 2020;462: 7–19. doi:10.1016/j.ydbio.2020.02.003

24. Leptin M, Grunewald B. Cell shape changes during gastrulation in Drosophila. Development (Cambridge, England). 1990;110: 73–84.

25. Plageman TF, Chauhan BK, Yang C, Jaudon F, Shang X, Zheng Y, et al. A trio-rhoA-shroom3 pathway is required for apical constriction and epithelial invagination. Development. 2011;138: 5177–5188. doi:10.1242/dev.067868

26. Nicolás-Pérez M, Kuchling F, Letelier J, Polvillo R, Wittbrodt J, Martínez-Morales JR. Analysis of cellular behavior and cytoskeletal dynamics reveal a constriction mechanism driving optic cup morphogenesis. eLife. 2016;5. doi:10.7554/eLife.15797.001

27. Perez-Vale KZ, Peifer M. Orchestrating morphogenesis: building the body plan by cell shape changes and movements. Development (Cambridge, England). NLM (Medline); 2020. doi:10.1242/dev.191049

28. Gillard G, Röper K. Control of cell shape during epithelial morphogenesis: recent advances. Current Opinion in Genetics and Development. Elsevier Ltd; 2020. pp. 1–8. doi:10.1016/j.gde.2020.01.003

29. Le Garrec JF, Ragni C V, Pop S, Dufour A, Olivo-Marin JC, Buckingham ME, et al. Quantitative analysis of polarity in 3D reveals local cell coordination in the embryonic mouse heart. Development (Cambridge). 2013;140: 395–404. doi:10.1242/dev.087940

30. Monier B, Gettings M, Gay G, Mangeat T, Schott S, Guarner A, et al. Apico-basal forces exerted by apoptotic cells drive epithelium folding. Nature. 2015;518: 245–248. doi:10.1038/nature14152

31. Hartmann J, Wong M, Gallo E, Gilmour D. An image-based data-driven analysis of cellular architecture in a developing tissue. eLife. 2020;9: 1–33. doi:10.7554/eLife.55913

32. Xiong F, Ma W, Hiscock TW, Mosaliganti KR, Tentner AR, Brakke KA, et al. Interplay of cell shape and division orientation promotes robust morphogenesis of developing epithelia. Cell. 2014;159: 415–427. doi:10.1016/j.cell.2014.09.007

33. Khan Z, Wang YC, Wieschaus EF, Kaschube M. Quantitative 4D analyses of epithelial folding during Drosophila gastrulation. Development (Cambridge). 2014;141: 2895–2900. doi:10.1242/dev.107730

34. Carney KR, Bryan CD, Gordon HB, Kwan KM. LongAxis: A MATLAB-based program for 3D quantitative analysis of epithelial cell shape and orientation. Developmental Biology. 2020;458: 1–11. doi:10.1016/j.ydbio.2019.09.016

35. Pozo JM, Villa-Uriol M-C, Frangi AF. Efficient 3D Geometric and Zernike Moments Computation from Unstructured Surface Meshes. IEEE Transactions on Pattern Analysis and Machine Intelligence. 2011;33: 471–484. doi:10.1109/TPAMI.2010.139

36. Amenta N, Bern M, Kamvysselis M. A new Voronoi-based surface reconstruction algorithm. Proceedings of the 25th annual conference on Computer graphics and interactive techniques - SIGGRAPH ’98. New York, New York, USA: ACM Press; 1998. pp. 415–421. doi:10.1145/280814.280947

37. Amenta N, Bern M. Surface reconstruction by Voronoi filtering. Discrete and Computational Geometry. 1999;22: 481–504. doi:10.1007/PL00009475

38. Bernardini F, Mittleman J, Rushmeier H, Silva C, Taubin G. The ball-pivoting algorithm for surface reconstruction. IEEE Transactions on Visualization and Computer Graphics. 1999;5: 349–359. doi:10.1109/2945.817351

39. Di Angelo L, Di Stefano P, Giaccari L. A new mesh-growing algorithm for fast surface reconstruction. CAD Computer Aided Design. 2011;43: 639–650. doi:10.1016/j.cad.2011.02.012

40. Waterman RE, Bell DH. Epithelial fusion during early semicircular canal formation in the embryonic zebrafish,Brachydanio rerio. The Anatomical Record. 1984;210: 101–114. doi:10.1002/ar.1092100113

41. Mukundan R, Ramakrishnan KR. Moment Functions in Image Analysis — Theory and Applications. Moment Functions in Image Analysis — Theory and Applications. WORLD SCIENTIFIC; 1998. doi:10.1142/3838

42. Millán RD, Dempere-Marco L, Pozo JM, Cebral JR, Frangi AF. Morphological characterization of intracranial aneurysms using 3-D moment invariants. IEEE Transactions on Medical Imaging. 2007;26: 1270–1282. doi:10.1109/TMI.2007.901008

43. Broggio D, Moignier A, Ben Brahim K, Gardumi A, Grandgirard N, Pierrat N, et al. Comparison of organs' shapes with geometric and Zernike 3D moments. Computer Methods and Programs in Biomedicine. 2013;111: 740–754. doi:10.1016/j.cmpb.2013.06.005

44. Wadell H. Volume, Shape, and Roundness of Rock Particles. The Journal of Geology. 1932;40: 443–451. doi:10.1086/623964

45. Abbas L, Whitfield TT. Nkcc1 (Slc12a2) is required for the regulation of endolymph volume in the otic vesicle and swim bladder volume in the zebrafish larva. Development. 2009;136: 2837–2848. doi:10.1242/dev.034215

46. Geng FS, Abbas L, Baxendale S, Holdsworth CJ, George Swanson A, Slanchev K, et al. Semicircular canal morphogenesis in the zebrafish inner ear requires the function of gpr126 (lauscher), an adhesion class G protein-coupled receptor gene. Development (Cambridge). 2013;140: 4362–4374. doi:10.1242/dev.098061

47. Friedrich S, Konietschke F, Pauly M. Analysis of Multivariate Data and Repeated Measures Designs with the R Package MANOVA.RM. Family Medicine. 2018;37(5): 53–65.

Supplementary References

1. Westerfield M. The Zebrafish Book. A Guide for the Laboratory Use of Zebrafish (Danio rerio), 5th Edition. University of Oregon Press, Eugene (Book). 2007.

2. Aleström P, D'Angelo L, Midtlyng PJ, Schorderet DF, Schulte-Merker S, Sohm F, et al. Zebrafish: Housing and husbandry recommendations. Laboratory Animals. 2020;54: 213–224. doi:10.1177/0023677219869037

3. Baxendale S, Whitfield TT. Methods to study the development, anatomy, and function of the zebrafish inner ear across the life course. Methods in Cell Biology. 2016;134: 165–209. doi:10.1016/bs.mcb.2016.02.007

4. Schindelin J, Arganda-Carreras I, Frise E, Kaynig V, Longair M, Pietzsch T, et al. Fiji: an open-source platform for biological-image analysis. Nature methods. 2012;9: 676–82. doi:10.1038/nmeth.2019

5. Kirshner H, Sage D, Unser M. 3D PSF models for fluorescence microscopy in ImageJ. Proceedings of the Twelfth International Conference on Methods and Applications of Fluorescence Spectroscopy, Imaging and Probes (MAF’11). 2011;1: 154.

6. Rusinkiewicz S. Estimating curvatures and their derivatives on triangle meshes. Proceedings 2nd International Symposium on 3D Data Processing, Visualization and Transmission, 2004 3DPVT 2004. IEEE; 2004. pp. 486–493. doi:10.1109/TDPVT.2004.1335277

7. Shabat Y Ben, Fischer A. Design of porous micro-structures using curvature analysis for additive-manufacturing. Procedia CIRP. Elsevier B.V.; 2015. pp. 279–284. doi:10.1016/j.procir.2015.01.057

3.3 Discussion

In this chapter, we present a new pipeline – *Origami* – to analyse cell morphology along the apico-basal axis in curved tissues. We used fluorescence microscopy images of the SSCs and the ES of the zebrafish inner ear, as they fold in opposite directions, and therefore present a good model for both evagination and invagination events.

We demonstrated that, at three individual time-points during formation of these curved structures, cells in the ES had significantly different shape signatures from those in the anterior and posterior projections of the SSCs. Generally, cells in the ES were characterised by positive skewness which suggested a smaller apical domain than the basal one; whereas cells in the epithelial projections were characterised by negative skewness, suggesting a smaller basal domain than the apical. This was no surprise as we knew that these structures form by folding the otic epithelium in opposite directions – the ES through invagination and the epithelial projections through evagination. In addition, cells of the epithelial projections displayed higher values of sphericity and smaller surface areas than those of the ES. This means that the cell shape signature in the ES and in the epithelial projections is not simply a mirror of each other along the apico-basal axis, as there are other shape attributes that differ apart from their skewness. Moreover, this suggests that the folding mechanisms driving the emergence of these structures are also unlikely to be simply mirrored but instead, different ones. At the three time-points analysed, there was no statistically significant difference in cell shape between the anterior and posterior projections. Again, this result was expected as our current understanding of these projections is that these are equivalent structures.

The *Origami* pipeline, as mentioned before, is capable of computing direction vectors denoting the epithelial apico-basal axis for individual cells. This addition to the the field makes the cell shape measurements much more relevant and meaningful when studying folding events. However, direction of cell polarity has to be given to the pipeline, either known from the literature or visualised through biochemical markers. For most people studying folding events this shouldn’t be a problem, but it can be a disadvantage if the direction of cell polarity is unknown. A weakness of this pipeline is the fact that it is unable to follow cells through time. Its strength lies on analysing cell shape at individual time-points without the need to match cells between them. It is possible to look at individual cell shape changes through time if using a second software to track the cells and then match the cell shape attributes for each cell from the different time-points (work developed in chapter four).

The work presented in this chapter was essential to develop and establish a cell shape analysis tool capable of addressing the complex tissue shape changes of the developing otic vesicle. So far, no such tool had been developed to specifically deal with the challenges of tissues undergoing folding or tissues with high levels of curvature. As a result, studies of tissue folding events can now benefit from this tool. In addition, this also meant that cell shape changes during early stages of semicircular canal and endolymphatic sac development could now be described in more detail. In this study, the cell shape analysis performed in the ES and the projections of the SSCs was done as a proof of principle for the *Origami* pipeline. To efficiently address this, only three cell shape attributes were analysed in more detail in these structures (skewness, sphericity and surface area). Other cell shape attributes need to be looked at in more detail in these structures. On the other hand, only three time-points were analysed and these did not cover the stages before the folding events. Moreover, as mentioned before, this pipeline does not include a tool to track cells which means that on its own, it does not allow one to follow shape changes of individual cells through time. In order to gain a more comprehensive understanding of the morphogenetic changes happening during otic tissue folding, we need to analyse individual cell shape changes through time at more frequent time-points, starting from before the tissue undergoing folding. These points are addressed in chapter four for the projections of the SSCs.

CHAPTER 4

Cell Shape Changes And Protein Redistribution During Epithelial Projection Formation

4.1 Introduction

In chapter three, two highly curved structures of the zebrafish inner ear were presented – the endolymphatic sac and the epithelial projections of the SSCs. Tissue folding events have been associated to the formation of both these structures, but not described in detail. In this chapter, my work will be focused on the mechanisms involved in the early stages of epithelial projection formation. Abnormalities during development of the SSCs, in particular of their shape and position, have been associated to numerous diseases (Abdelhak et al., 1997; Johnson and Lalwani, 2000; Li et al., 2010; Piotrowski et al., 2003; Rosa et al., 2011; Wineland et al., 2017), and therefore studying the changes in shape as these structures develop and the mechanisms underlying those is very important.

The zebrafish otic vesicle initially forms as a monolayer of cells (with some pseudostratified sections in the ventral region) with the apical cell surface on the luminal side of the vesicle (Waterman and Bell, 1984) (Figure 4.1A). SSC formation is initiated by the growth of lateral, anterior, posterior and ventral projections of monolayered epithelium into the lumen of the vesicle (Haddon and Lewis, 1996; Waterman and Bell, 1984). In the 80's, epithelial projection formation was presented as a protrusion of the otic wall into the vesicle (Waterman and Bell, 1984), and this term of 'protrusions' was used until recently. Only in early 2000's, the term of folding (and buckling) was associated to these protrusions (Babb-Clendenon et al., 2006). Recently, the epithelial projections that give rise to the zebrafish SSCs were described as invaginations (Munjal et al., 2021). Despite Munjal's work labelling projection formation as an invagination process, in the work presented in this thesis, including the published work in it, epithelial projection formation is described as an evagination event. The reason for this is the fact that the basal cell surfaces, and not the apical, are lining the inside of the curved epithelium, facing the acellular matrix-filled core of the projections. Though less common, evagination is not a newly described mechanism. However, in most systems in which tissue folds through evagination, the epithelium before folding exhibits either no particular curvature or a slight curvature in the direction of folding (same direction as projection/tube/bud formation). The formation of epithelial projections, seen during embryonic development of the zebrafish inner ear, are particularly interesting folding events as the otic epithelium folds in the opposite direction of the initial curvature exhibited by the tissue, therefore involving an inversion of curvature, and making each projection flanked by a ‘reverse curve’ (Wang et al., 2022).

A few cellular behaviours have been observed during elongation of the inner ear epithelial projections. Cells were described to become thinner, more squamous (2D measurements) and to maintain their volume (3D measurement) (Munjal et al., 2021). At a similar developmental stage, we have reported that these cells have a negative skewness (Mendonca et al., 2021) which indicates a smaller basal domain compared to the apical. F-actin, myosin-II and E-cadherin (E-cad) were shown to locate on the lateral and basal cell surfaces during projection elongation. In addition, blocking F-actin polymerisation with CytoD leads to abnormal shortened projections (Munjal et al., 2021). Several ECM genes have also been identified to be driving outgrowth and elongation of these epithelial projections (Busch-Nentwich et al., 2004; Jones et al., 2022; Munjal et al., 2021; Neuhauss et al., 1996). Despite these studies being insightful, there is yet to describe and explain the very initial changes happening in the otic tissue before and during the folding event that leads to the inversion of curvature of this tissue in the first place. In order to do this, I performed, with the help of the *Origami* pipeline, a 4D quantitative analysis of tissue and cell shape changes during early stages of projection formation; investigated the distribution of different cytoskeletal and adhesion proteins before and after the folding event; and disrupted the activity of myosin-II.

4.2 Results

4.2.1 Relative cell position within the epithelial projection can predict its relative position in relation to the initiating cells before the folding event

As previously described (Munjal et al., 2021; Waterman and Bell, 1984), the posterior projection of the zebrafish inner ear initiates its formation a few hours later than the anterior projection. To further investigate the timings of projection formation, I performed time-lapse Airyscan confocal imaging of the zebrafish otic vesicle between 36 and 55 hpf (only anterior and posterior projections were analysed). My observations confirm and extend those reported previously. For each wild-type embryo analysed, the onset of outgrowth for the anterior and posterior projections (AP and PP) happened at different time points (Figure 4.1E) - between 40 and 47.5 hpf for the AP; and between 41 and 49.5 hpf for the PP (N = 3 embryos, n = 3 APs, n = 3 PPs). The interval between the genesis of these two projections varied as well (ranging between one to four hours) (Figure 4.1E). As a result, at a given time-point, for example 46 hpf, the developmental stage of each projection can vary, within the same embryo and between different embryos (Figure 4.1B-D). Despite these variable starting times, all projections increased their growth rate with time, elongating faster at later time-points (Figure 4.1F). The overall growth rate for the six projections analysed varied between 1.6 to 2.2 μm per hour (Figure 4.1G).

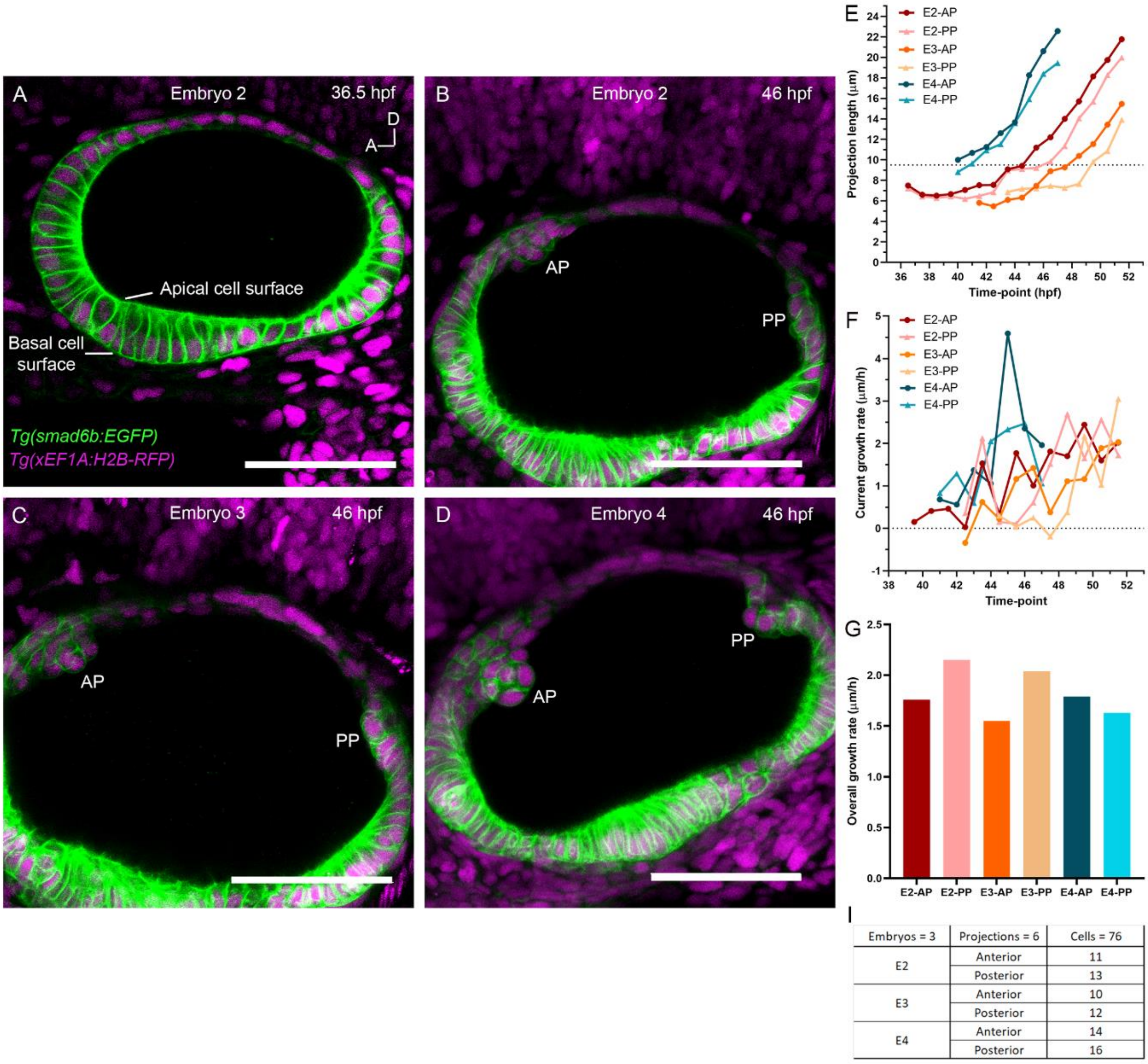

Embryos = 3	Projections = 6	Cells = 76
E2	Anterior	11
	Posterior	13
E3	Anterior	10
	Posterior	12
E4	Anterior	14
	Posterior	16

Figure 4.1 – Onset of epithelial projection outgrowth is variable.

(**A-D**) Inner ear of *Tg(smad6b:EGFP); Tg(xEF1A:H2B-RFP)* double transgenic embryos. Time-lapses were acquired in the Zeiss LSM 880 Airyscan confocal microscope between 36 and 55 hours post fertilisation (hpf). Picture **A** shows the otic vesicle at 36 hpf with the apical cell surface facing the lumen of the vesicle. Pictures **B-D** show the formation of anterior and posterior projections (AP and PP) at 46 hpf in three different embryos. Lateral views of the ear are shown with roughly the anterior to the left and dorsal to the top (A – anterior; D – dorsal). Scale bars measure 50 μm. A single *z*-slice is shown in picture **A** and a maximum intensity projection from a *z*-stack is shown in **B-D**. **(E)** Graph showing the length of anterior and posterior projections between 36hpf and 52hpf for embryos 2, 3 and 4 (E2, E3 and E4). Below 9.5 µm (dotted line in graph), projections are yet to form therefore, the length measured is the height of a cell which reflects the thickness of the epithelium. Projection length was measured on a *z*-slice from a *z*-stack acquired in an Airyscan confocal microscope as shown in Figure 4.3A by the white lines. **(F)** Graph showing the growth rate for each projection at each time-point. This increased with time. **(G)** Graph showing the overall growth rate for each projection. This was calculated by subtracting the value for projection length at the start of projection outgrowth (value closest to the dotted line in graph **E**) from the value of projection length at the last time-point; this number was then divided by the number of hours between those two time-points. **(I)** Table showing the number of cells tracked in each projection and each embryo that were included in the tracking analysis.

Other aspects of early projection formation I wanted to investigate were whether cell positions and neighbours before and after the folding event change or remain the same; and whether cell trajectories during that process are very different depending on the cell starting position. In order to start answering those questions, I performed manual cell tracking in time-lapses of the inner ear using Arivis (see Supp. Video 4 for example time-lapse). By tracking some of the cells that become part of the anterior and posterior projections, I was able to observe that cells located on the dorsal side of the projection, were also dorsally located in relation to the axes' origin before the folding event (Figure 4.2Ai-Aiii - cells 7, 10 and 11; and 4.2B); and cells on the ventral side of the projection were located more ventrally before the folding event (Figure 4.2Ai-Aiii, cells 3, 4 and 12; and 4.2B). Cells at the tip of the projection exhibited lower displacement in the *x* axis and higher displacement in the *y* axis (Figure 4.2Ai-Aiii, cells 1, 2 and 4; 4.2C and 4.2D). This means that these cells correspond to those nearest to the axes' origin – named here initiating cells. By contrast, cells closer to the base of the projection exhibited higher displacement in *x*, and lower in *y*, which means that they were located further away from the initiating cells before projection outgrowth (Figure 4.2Ai-Aiii, cells 5, 9, and 11; 4.2C and 4.2D). Despite track speed, length or straightness not showing a correlation with the initial cell position in the epithelium (Figure 4.2H-J), cells that moved faster had longer tracks (Figure 4.2G). No cell divisions were observed in the main body of the projections, only at the base and in the surrounding tissue (asterisks in Figure 4.2Aiii show two examples). Most cell divisions observed near or at the base of the projection, generated daughter cells that went into the projection (data not shown). However, I observed one cell division in which one of the daughter cells went into the projection, whilst the other didn't. This cell tracking analysis suggests that after projection outgrowth is initiated by a few cells, the cells that surround them, generally maintain their neighbours as they are incorporated into the epithelial projections. Finally, cells in the anterior and posterior epithelial projections seemed to come from a coherent region in the dorsolateral regions of the otic wall, instead of scattered regions (Supp. Video 5).

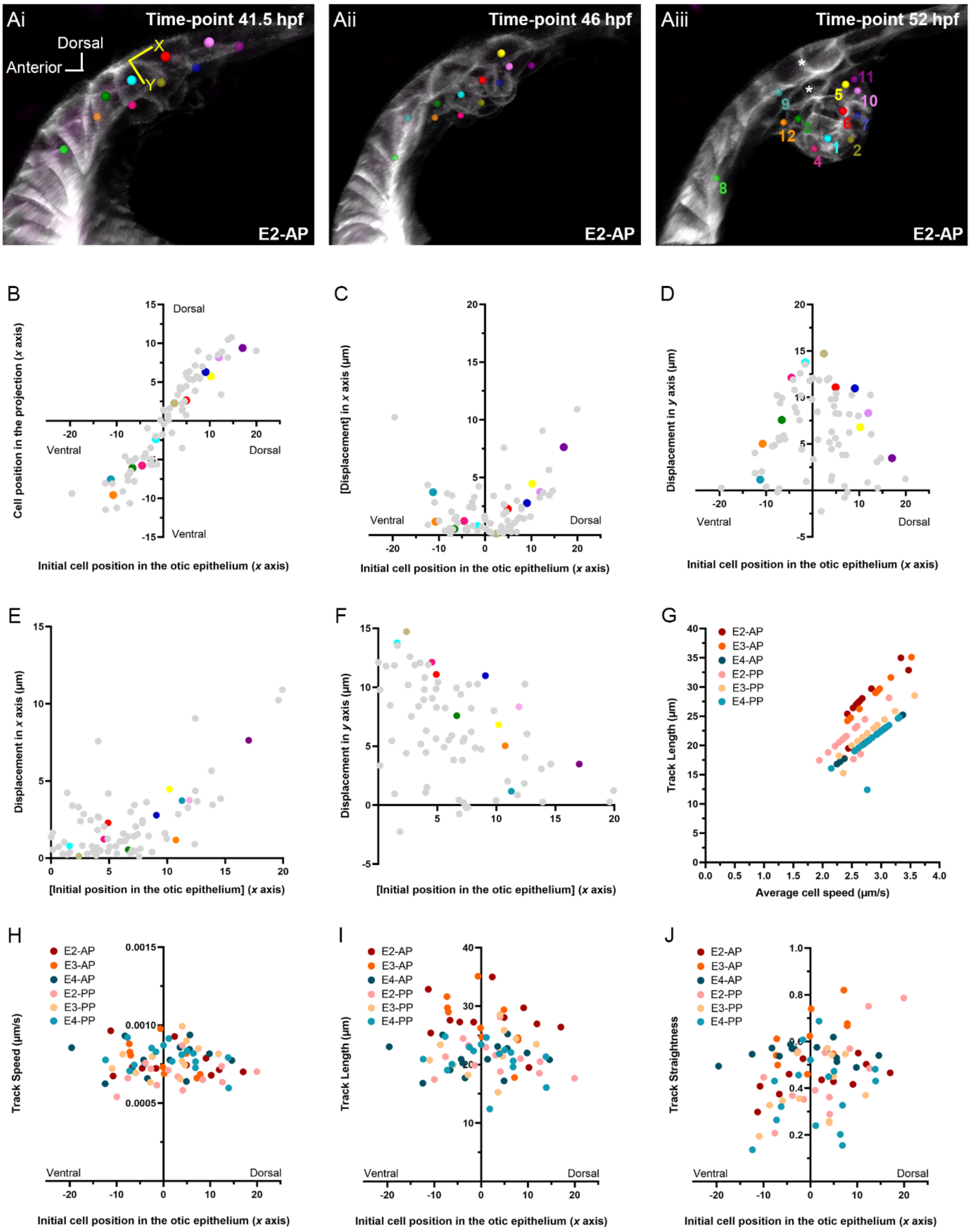

Figure 4.2 – Otic cells keep their neighbours as the epithelium undergoes folding to form the epithelial projections.

(Ai-Aiii) Maximum intensity projections of the anterior region of the otic vesicle from Embryo 2 (E2) showing the early stages of projection formation. Yellow axes (schematic) represent the new axes, determined based on the projection base-tip vector (see Methods 2.5.3.1 for details). Cell membranes are labelled with GFP and tracked cells are marked with coloured spheres. In **(Aiii)**, daughter cells of two recent cell divisions are marked with an asterisk. **(B)** Cell position in the otic epithelium before projection outgrowth positively correlated with its position in the projection at the final time-point recorded (Spearman correlation coefficient = 0.952, p = 8.8e-040). Initiating cells (closer to the origin of the axes) showed a smaller displacement in the x axis **(C)** and higher displacement in the y axis **(D)**; whilst cells further away from the initiating cells showed a higher displacement in the x axis **(C)** and a smaller displacement in the y axis **(D)**. **(E)** Graph showing a positive correlation between the absolute values of the initial cell position in the x axis and cell displacement during projection outgrowth in the same axis (Spearman correlation coefficient = 0.47, $p < 0.0001$). This means that cells further away from the initiating cells had higher displacement along the epithelium before joining the projection. **(F)** Graph showing a negative correlation between the absolute values of the initial cell position in the x axis and cell displacement during projection outgrowth in the y axis (direction of projection growth) (Spearman correlation coefficient = -0.45, $p < 0.0001$). This means that initiating cells, which are the closest to the axes origin, moved the furthest away from the otic wall and became the cells at the tip of the projection. **(G)** Graph showing a positive correlation between track length and average cell speed (Spearman correlation coefficient = 0.615, p = 3.5e-009). Each data point is a cell. **(H-J)** These graphs show different track features in relation to the initial cell position in the x axis. Neither track speed, length nor straightness showed a correlation with initial cell's position.

4.2.2 Otic epithelium cells undergo a skewness inversion that is reflected at the tissue level through an inversion of tissue curvature

To start unpacking the tissue-level and cellular events underlying projection outgrowth, I measured the length of the apical and basal surfaces of the folding tissue from a two-dimensional optical section over time (Figure 4.3Ai-Aiii). Before the projection formed, both basal and apical surfaces of the otic epithelium started with a similar length (Figure 4.3Ai, B and C). For all projections there was a time point at which the length of the apical surface started increasing whilst that of the basal surface decreased (Figure 4.3Aii, B and C). To standardise the staging of each projection, I determined time-point zero for each projection to be the time point at which these reached their lowest basal surface length (also coincident with the onset of outgrowth of the projection) (Figure 4.3Aii and C). After this initial folding event, the projection started to elongate, and the lengths of both apical and basal surfaces increased (Figure 4.3Aiii and C).

In order to investigate the cellular shape changes involved here, I performed 3D cell segmentation of Airyscan data sets at hourly intervals and extracted cell shape metrics using the *Origami* pipeline (see Methods 2.5.2) (Mendonca et al., 2021). The term 'projection cells' refers to cells that become part of the projection which were identified through tracking, whereas the term 'surrounding cells' includes cells in the proximity of projection cells, mostly on the ventral side (and a few on located dorsally). Note that 'surrounding cells' can be a transient state until the projection reaches its full length, as until then, surrounding cells can still be incorporated in the projection.

One of the cell shape features measured in this pipeline is the mean curvature. Measuring this feature in projection cells, allowed me to confirm that the otic epithelium undergoes a clear inversion of curvature. At the start of the time-lapse, the mean curvature for both projection and surrounding cells was negative, indicating that the otic epithelium was curved with the apical domain making up the inner surface (Figure 4.3Ai and D; Supp. Figure 1B). This is also confirmed by the findings on cell skewness measurements. Before projection formation, the skewness of most cells in the projection-forming regions was positive (Figure 4.3J; Supp. Figure 1C), indicating that their cell mass was skewed toward the basal domain and therefore the apical domain was smaller (Figure 4.3M). Although cell skewness of surrounding cells remained positive and did not change significantly throughout projection formation, cells that became part of the projections showed a significant reduction in their skewness between time-points -3 and 1, exhibiting on average negative values during that time (Figure 4.3J). This means that leading up to and during the folding event, some projection cells inverted their skewness, now exhibiting a smaller basal domain (Figure 4.3J, K and M). During a similar time (between time-points -3 and -1), there is a significant increase in mean curvature in projection cells, indicating the start of the tissue curvature inversion (Figure 4.3D). Once the folding had happened (time-point 1), the average values for mean curvature became positive (Figure 4.3Aii and D), indicating that this group of cells was now curved basally.

Next, I examined which projection cells were inverting their curvature and skewness (all projections analysed - posterior projection from embryo two (E2) used as an example). At time-point 0, there was a negative correlation between cell skewness and mean curvature ($r = -0.515$, $p = 0.001$) (Figure 4.3G). At that time-point, I observed that initiating cells, which are those that ended up closer to the tip of the projection, seemed to be the ones inverting their skewness and eventually their curvature (Figure 4.3 E, K, H and I - cells 3,6 and 7; Supp. Figure 4.1B and C). In contrast, cells that end up near the base of the projection, hadn't undergone this inversion of skewness or curvature (Figure 4.3 E, K, H and I - cells 5.1 and 9). After the folding event, when the projection starts elongating, no strong correlation was found between the position of cells within the projections and their skewness or curvature (data not shown), which means that the shape profile of the cells at the tip and of those at the base of the projection was more uniform.

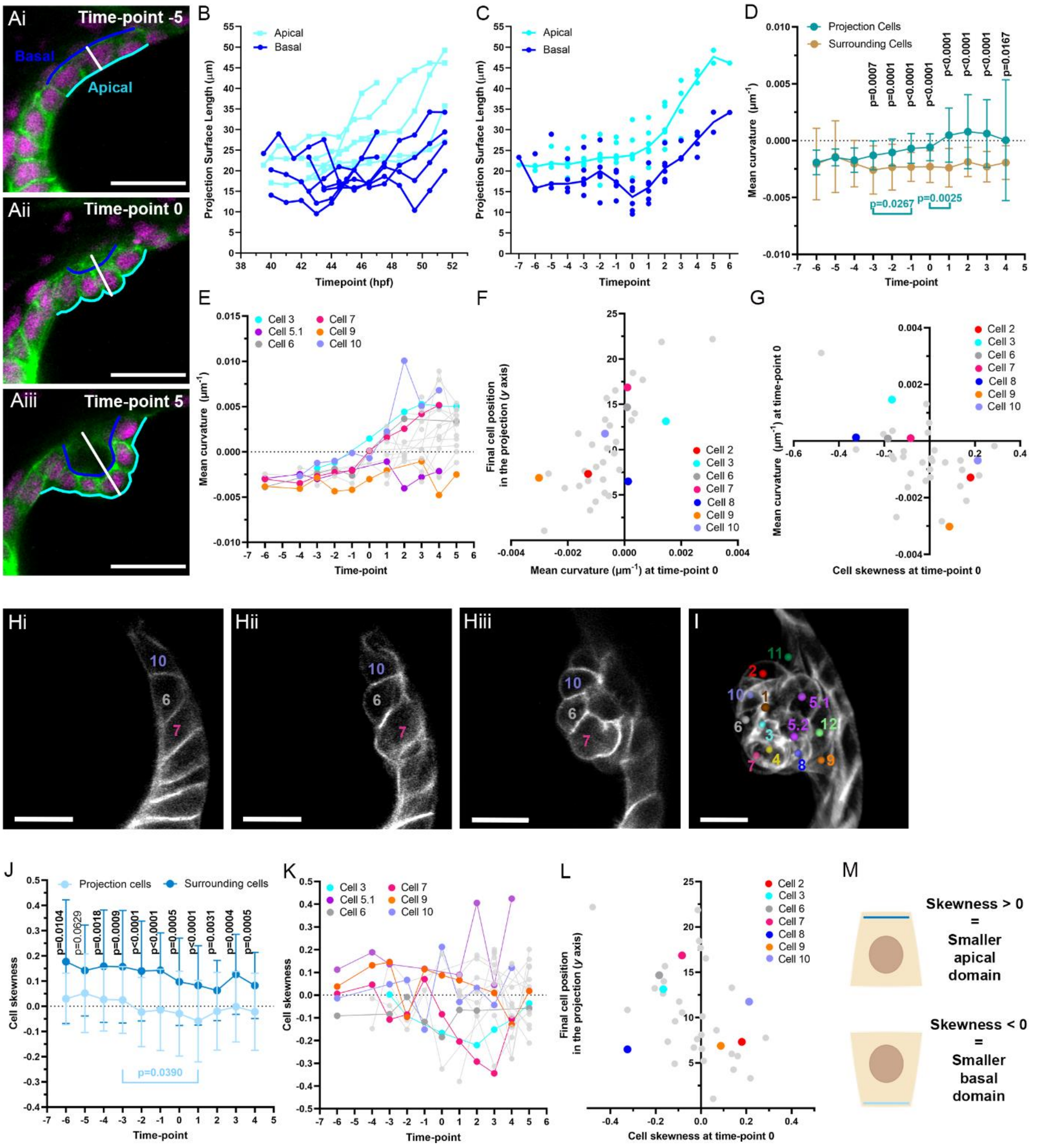

Figure 4.3 – Cells in the otic epithelium that become part of the projections undergo an inversion of skewness and tissue curvature.

(Ai-Aiii) *z*-slices of an anterior projection imaged on an Airyscan confocal microscope illustrating the stage before **(Ai)** and once the folding had happened **(Aii),** and during projection outgrowth **(Aiii)**. Dark and light blue lines demonstrate how the basal and apical surface length of the projections, respectively, were traced and measured. Scale bar measures 20 µm. Graph **(B)** shows the measurements for the apical and basal surface length of the 6 projections analysed. To standardise the staging of each projection, in graph **(C)**, I designated time-point zero for each projection to be the time-point at which these reach their lowest basal surface length. Graph (**D**) shows the measurements for mean curvature in projection cells changing to positive values after the folding event, and remaining negative in the surrounding cells. Graph **(E)** highlights the changes in mean curvature for some cells from the posterior projection of embryo two. Graph **(F)** shows a strong positive correlation between the mean curvature of a projection cell at time-point 0, and its final position in the projection along the *y* axis (Spearman correlation coefficient = 0.701, $p < 0.0001$). Graph **(G)** shows a negative correlation between cell skewness and mean curvature at time-point 0 (Spearman correlation coefficient = -0.515, $p = 0.001$)**. (H)** *z*-slices from the posterior projection of embryo two highlighting a few cells at time-points -3 **(Hi)**, 0 **(Hii)**, and 3 **(Hiii)**. Scale bar measures 10 µm. **(I)** Maximum intensity projection of a *z*-stack from the posterior projection of embryo two showing all cells that were tracked. Graph **(J)** shows the three-dimensional cell skewness being inverted (negative values) in cells that became part of the projections, and remaining positive for surrounding cells. (**D** and **J**) Mean and standard deviation are shown in these graphs. To compare the two populations of cells at each time-point, I performed multiple unpaired *t*-tests with Welch's correction (*p* values shown in black), and to compare each population of cells over time I used a mixed-effect model with Tukey's post-test correction for multiple comparisons (*p* values shown in light blue/green). Graph **(K)** highlights the changes in skewness for some cells from the posterior projection of embryo two. Graph **(L)** presents the final cell position in the projection along the *y* axis over cell skewness at time-point 0 (Spearman correlation coefficient = -0.428, $p = 0.009$). Diagram in **(M)** demonstrates what a cell could look like when it has either a positive or negative value for skewness.

4.2.3 Projection cells undergo basal constriction and apical rounding during the folding event

This cell shape change measured through inversion of skewness in projection cells could either be caused by a reduction of the basal domain, for instance through basal constriction, an expansion of the apical domain, or both. To test whether basal constriction was behind skewness inversion in projection cells, I took measurements of the width of the apical and basal domains of individual cells in embryos fixed every five hours (Figure 4.4F). These were stained with Phalloidin to visualise the tissues. Except from the first stage, 40 hpf, I staged the embryos by the thickness of the epithelium or length of projection. The table in Figure 4.4H shows how these stages match to the time-point system used so far. Between 40 hpf and the 5-12 µm stage, period when the folding event happens, the otic epithelium cells showed a dramatic cell shape change involving a significant reduction of the basal domain width while the apical domain remained unchanged between these stages (Figure 4.4A, A', B, B' and G). By doing the ratio of the apical over the basal width, I obtained a measure of 2D skewness in projection cells. I was able to observe a similar inversion of skewness during the folding event (Figure 4.4E) to the one showed in the 3D cell shape analysis (Figure 4.3J). The measurements of the apical and basal cell width showed that basal constriction, and not apical expansion, was the cell shape change that led to the skewness inversion. Basal constriction was restricted to the region of projection outgrowth and not seen in the surrounding tissue (Figure 4.4B and C marked with an asterisk). Basal constriction was not the only cell shape change occurring in the projection cells during the folding event. Between 40 hpf and the 5-12 µm stage, I observed a rounding of the apical surface in these cells (Figure 4.4B and B'). This was shown through a significant increase in curvature of the apical cell surface (Figure 4.4F and G). This cell shape change was observed in both fixed samples (Figure 4.44B and B') and live embryos (Figure 4.3Hii and Hiii), and was restricted to cells in the epithelial projections.

Between the stages 5-12 µm and > 25 µm, when projections elongate, there was an increase in apical and basal cell width. In addition, between the stages 12-25 µm and > 25 µm, the curvature of the apical cell surface reduced significantly. As a result of these changes, cells in the projection looked more flat and squamous than during the folding event.

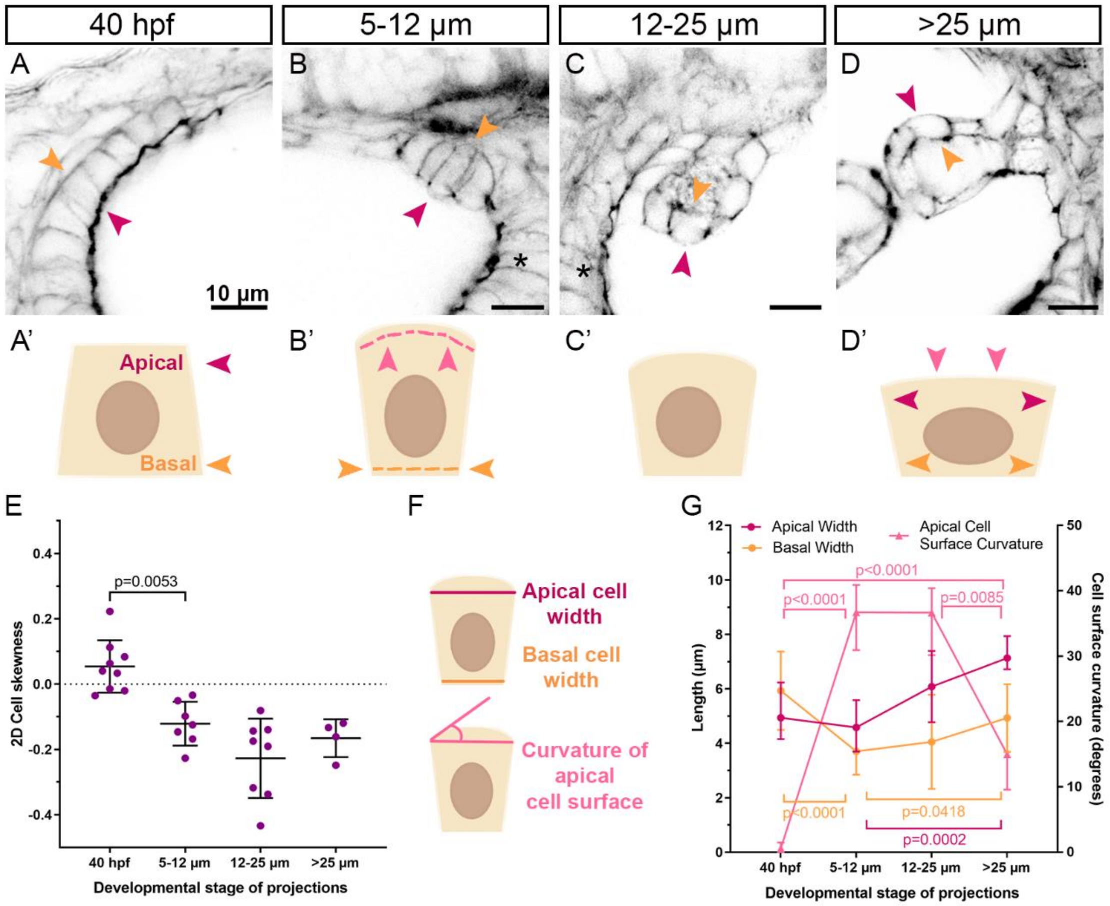

H

Stage in fixed samples	Time-point from time-lapses
40 hpf	up to -3
5-12 µm	between -3 and 0
12-25 µm	after 0
> 25 µm	after 5

I

Measurement	Stage	Embryos	Projections	Cells
Apical and Basal width	40 hpf	6	12	36
	5-12 µm	4	7	21
	12-25 µm	7	8	24
	> 25 µm	3	4	12
Apical curvature	40 hpf	3	6	18
	5-12 µm	3	3	9
	12-25 µm	3	3	9
	> 25 µm	6	12	36
2D Skewness	40 hpf	3	9	
	5-12 µm	4	7	
	12-25 µm	7	8	
	> 25 µm	4	4	

Figure 4.4 – Cells in the projection undergo basal constriction and apical rounding during the tissue folding event.

(**A-D**) Phalloidin-stained fixed samples imaged on a Nikon inverted confocal microscope with a 40X oil immersion objective. A single slice of a *z*-stack is shown here. Magenta and orange arrowheads point to where the apical and basal surface are in the epithelium respectively, and asterisks mark an example region of surrounding tissue (outside the region of projection outgrowth). **(B-D)** These stages are labelled by the thickness of the epithelium and projection length. **(A'-D')** Diagrams of cells representing dominant cell shape present in the projection cells. Magenta and orange arrowheads point to the apical or basal cell width and pink arrowheads point to the apical surface. **(E)** Graph showing the changes in

2D skewness of projection cells as the tissue folds. Values over zero indicate cells are constricted apically, whilst values below zero indicate cells are constricted basally. Each data point is the average skewness of three cells in one projection. A Brown-Forsythe and Welch ANOVA with Dunnett's T3 post-test for multiple comparisons was performed. **(F)** Simplified diagram of cells to show how apical width, basal width and the curvature of the apical cell surface were measured from an optical slice of a *z*-stack. This was done in Fiji, using the 'Straight line' tool for the width and the 'Angle' tool for the apical curvature. **(G)** Graph showing the apical and basal width on the left *y* axis and the curvature of apical cell surface on the right *y* axis during projection formation. Since only the basal width data passed the normality test, the median and the interquartile range are shown by the horizontal lines, except for basal width which shows mean and standard deviation. For basal width, a Brown-Forsythe and Welch ANOVA with Dunnett's T3 post-test for multiple comparisons was performed. For the apical width and apical cell surface curvature, a Kruskal-Wallis with Dunn's post-test for multiple comparisons was performed. Table (**H**) shows the equivalent time-points used in the cell tracking and 3D cell shape data from the time-lapses, to the stages used here for the 2D data from fixed samples. Table (**I**) shows the number of embryos, projections and cells analysed at each stage for the different data sets presented in graphs (**E**) and (**G**).

4.2.4 Cells in the epithelial projections are also undergoing elongation of the apico-basal axis during tissue folding

At early stages of inner ear development, when this organ is an otic vesicle, cells in the anterior and posterior poles (dorsolateral region) of the inner ear are columnar, but cells change their shape as the lumen of the otic vesicle expands, becoming thinner (Hoijman et al., 2015). In addition, as described in the introduction chapter (section 1.2.1), a dorso-ventral pattern starts forming in the otic vesicle in which dorsal cells become more squamous, and ventral cells more columnar. I was interested to see whether projection cells followed that same trend/pattern or whether they behave differently. In order to do that, I used the *Origami* pipeline to measure longitudinal spread (known as palisading in neurulation), which is a measure of the spread of cell mass along the apico-basal axis (higher values represent a more columnar cell, whereas lower values indicate a more squamous cell). Most surrounding cells analysed were located ventrally of the projection cells, and for this reason, surrounding cells exhibited a higher longitudinal spread than projection cells before time-point 0 (Figure 4.5A; Figure 4.3Hi; Supp. Figure 1D). Surrounding cells started thinning from the earliest time-point, as expected, demonstrated by a reduction of longitudinal spread between time-points -6 and 0 (Figure 4.5A). Projection cells followed that same trend between time-points -6 and -4, but between time-points -3 and 0 – during the folding event - they significantly increased their longitudinal spread, differentiating them from the behaviour of the surrounding cells (Figure 4.5A). In addition, at time-points -3 and 0, cells that would later contribute to a projection, followed the dorso-ventral pattern of the ear: dorsal cells were less columnar than the ventral ones (Figure 4.3Hi and Hii; Figure 4.5C and D). After the folding event (after time-point 0), projection and surrounding cells had similar values of longitudinal spread, which remained unchanged for 4 hours (Figure 4.5A). In addition, at this stage, longitudinal spread in projection cells showed no correlation with their position along the dorso-ventral axis (Figure 4.5E), which meant that they no longer followed the dorso-ventral pattern seen in the rest of the inner ear. These results showed that projection cells elongated their apico-basal axis at the time of tissue folding (and curvature inversion) which is coincident with the other two cell shape changes reported - basal constriction and apical rounding.

Two other cell shape features were measured: volume and sphericity. Overall, both of these features were similar between projection and surrounding cells (Figure 4.5F and G). There was a slight decrease of volume in surrounding cells between time-points -6 and -3 (Figure 4.5F), a similar time to when these cells reduced their longitudinal spread (Figure 4.5A). In contrast, projection cells decreased their volume later on, between the end of the folding event and a couple of hours after that (time-points -1 and 2) (Figure 4.5F). When it comes to sphericity, surrounding cells kept the same level of sphericity throughout, whereas projection cells had a slight reduction in sphericity between time-points -4 and -2, and a slight increase between time-points -2 and -1 (Figure 4.5G).

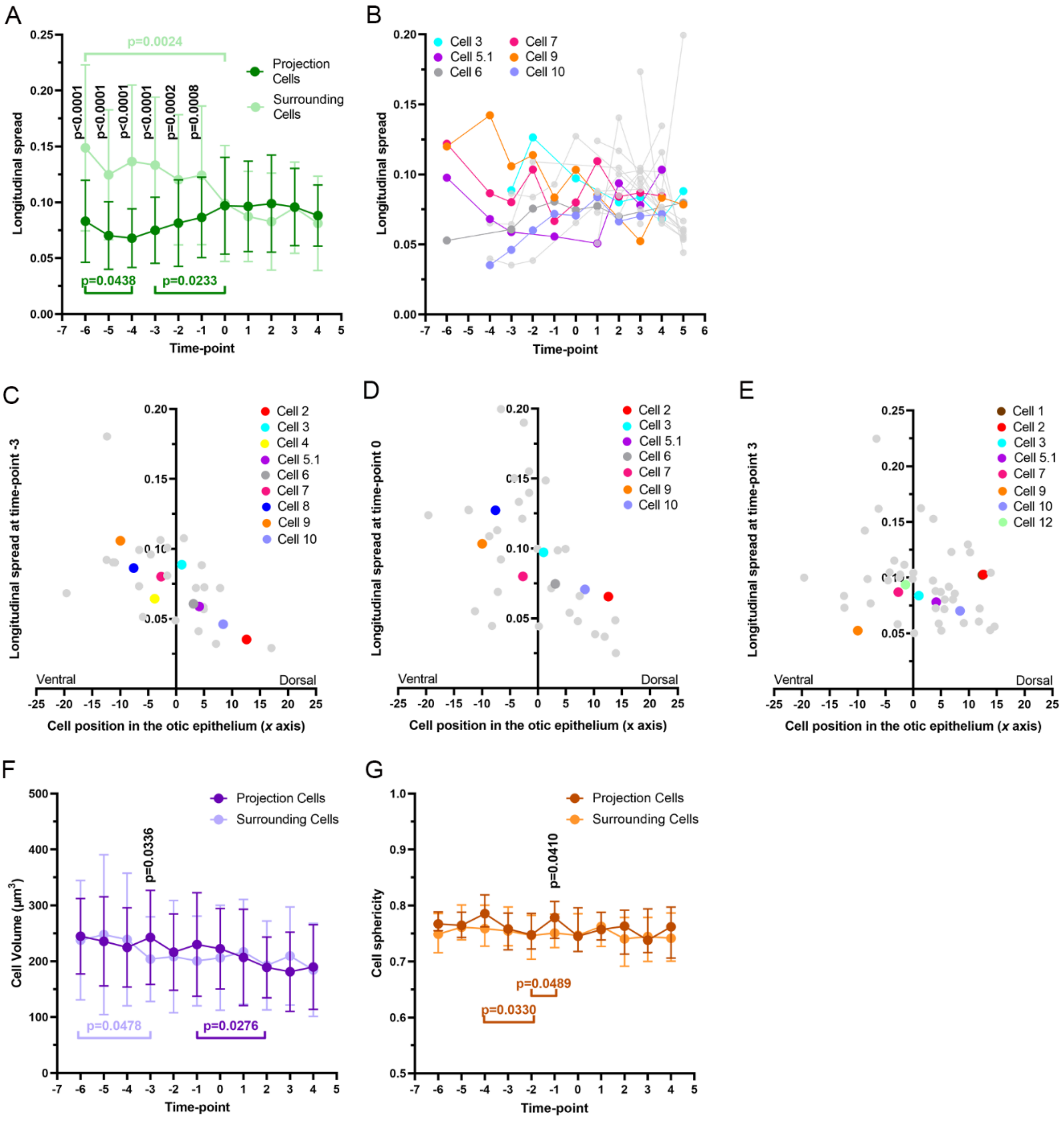

Figure 4.5 – Projection cells undergo elongation of the apico-basal axis and volume reduction during the tissue folding event.

(A) Graph showing the changes in longitudinal spread in surrounding and projection cells before and during the folding event. **(B)** Graph highlighting changes in longitudinal spread for some cells from the posterior projection of embryo 2. **(C-E)** Graphs showing the longitudinal spread of projection cells at time-points -3 (Spearman correlation coefficient = -0.633, p < 0.001), 0 (Spearman correlation coefficient = -0.538, p = 0.001) and 3 (Spearman correlation coefficient = -0.201, p = 0.170) over their initial position in the otic epithelium. **(F)** Graph showing a small reduction in volume in surrounding and projection cells. **(G)** Graph showing an unchanged sphericity in surrounding cells and slight changes in projection cells. To compare the two populations of cells at each time-point in graphs (**A**) and (**F**), I performed multiple unpaired t-tests with Welch's correction (p values shown in black). Mean and standard deviation are shown in these graphs. In graph (**G**), I performed a Mann-Whitney test as this data set didn’t pass the normality test (*p* values shown in black). Median and interquartile range are shown in this graph. To compare each population of cells over time in graphs (**A**), (**F**) and (**G**), I used a mixed-effect model with Tukey's post-test correction for multiple comparisons (*p* values shown in light and dark green, purple and orange respectively).

4.2.5 Cell shape changes in the epithelial projection cells are accompanied by drastic redistribution of adhesion and cytoskeletal proteins

Quantitative analysis of cell shape in the epithelial projections revealed how dynamic these cells are. Cell shape changes are often associated with modifications in the cytoskeletal network (Krueger et al., 2018; Kupaeva et al., 2018; Spencer et al., 2015) and positioning of cell-cell junctions (Araya et al., 2019). To examine the cell-cell adhesion complexes present in the projections, I performed an antibody stain for E-cadherin (E-cad) as a read out for adherens junctions. The signal intensity was measured in both the apical and basal halves of cells before and after the folding event. Before the folding event, there was slightly more E-cad signal detected in the apical half of the cells (Figure 4.6A, A' and D – 40 hpf). At this stage, E-cad was mainly distributed along the lateral and sub-apical regions of the cell. As cells in the projection started undergoing basal constriction and the tissue folded, E-cad showed a drastic change in its distribution to the basal half of the cells (Figure 4.6D- 5-12µm). Images of the staining show E-cad present in the basolateral domain of these cells and was no longer as close to the apical cell surface as before (Figure 4.6A and A’- 5-12µm). E-cad remained basolaterally located at later stages (Figure 4.6A and D – 12-25 µm). Just like the cell chape changes reported here, this redistribution of E-cad from the sub-apical to the basolateral domain appeared to be restricted to the projection cells and was not a generic phenomenon happening throughout the otic vesicle (note that signal was only quantified in projection cells). For instance, in the crista (asterisk in Supp. Figure 2A’), E-cad retained a similar distribution pattern to earlier stages (Supp. Figure 2A).

To visualise filamentous actin, I performed a phalloidin staining. Before projection formation, the signal was stronger in the apical half of cells, mainly present at the apical cell surface and apical cell-cell junctions (puncta) throughout the otic vesicle (Figure 4.6B and E – 40 hpf; Supp. Figure 2B). Once projection cells started changing their shape, the distribution of phalloidin signal changed significantly. Generally, the phalloidin signal became evenly distributed along the apico-basal axis but still present at the apical cell-cell junctions (puncta) (Figure 4.6B and

E - 5-12 µm). In some cells, however, F-actin showed a basolateral distribution, as well as being present at the apical junctions, which was more consistent at later stages (Figure 4.6B and E – 5-12 µm and 12-25 µm). Imaging of fixed *Tg(actβ2:myl12.1-EGFP)* embryos revealed that myosin-II signal was evenly distributed along the apico-basal axis in projection cells before the folding event (Figure 4.6C and F – 40 hpf), unlike E-cad or F-actin. However, when the shape of projection cells started changing, myosin-II signal showed a significant change in its distribution and, similarly to E-cad, became stronger in the basal half of the projection cells (Figure 4.6C and F - 5-12 µm and 12-25 µm). Images show myosin-II located to the basolateral domain and depleted from the apical cell surface but present at the apical cell-cell junctions (puncta) (Figure 4C - 5-12 µm and 12-25 µm). Again, this apical to basolateral shift of F-actin and myosin II was restricted to the tissue of the projections and not seen in the rest of the ear, where it remains apically located (signal quantified in projection cells only) (Supp. Figure 2B, B', C and C').

Given that I observed projection cells undergoing an inversion of skewness and E-cad, F-actin and myosin-II re-locating from the apical to the basolateral domain of cells, I wanted to investigate whether projection cells could be inverting their apicobasal polarity when the otic epithelium folds. First, I performed an antibody staining for ZO-1, a protein present in zonula occludens (tight) junctions and commonly used as an apical marker (Hoijman et al., 2015). I found that ZO-1 protein remained exclusively in apical cell-cell junctions (puncta) throughout the formation of the projections, before and during folding of the tissue, as in the rest of the otic epithelium (Figure 4.6G and G'; Supp. Figure 2D and D'; *N*=6 embryos, *n*=12 projections at each time point). I also performed an antibody staining for Pard3, a polarity protein required for apical domain establishment (Horikoshi et al., 2009). There was more Pard3 present in the apical half of cells, including the apical cell surface, before the folding event (Figure 4.6H, H' and I – 40 hpf). Despite measurements of Pard3 signal not differing in a significant way before and after folding, Pard3 appeared to localise to apical cell-cell junctions (puncta), similarly to ZO-1, and along the lateral cell region during and after the folding event (Figure 4.6H, H' and I - 5-12 µm, 12-25 µm and >25 µm; Supp. Figure 2E and E'). These results indicate that despite the inversion of skewness and drastic shift of adhesion and cytoskeletal proteins from the apical to the basolateral domain, projection cells retain their apicobasal polarity throughout the folding event.

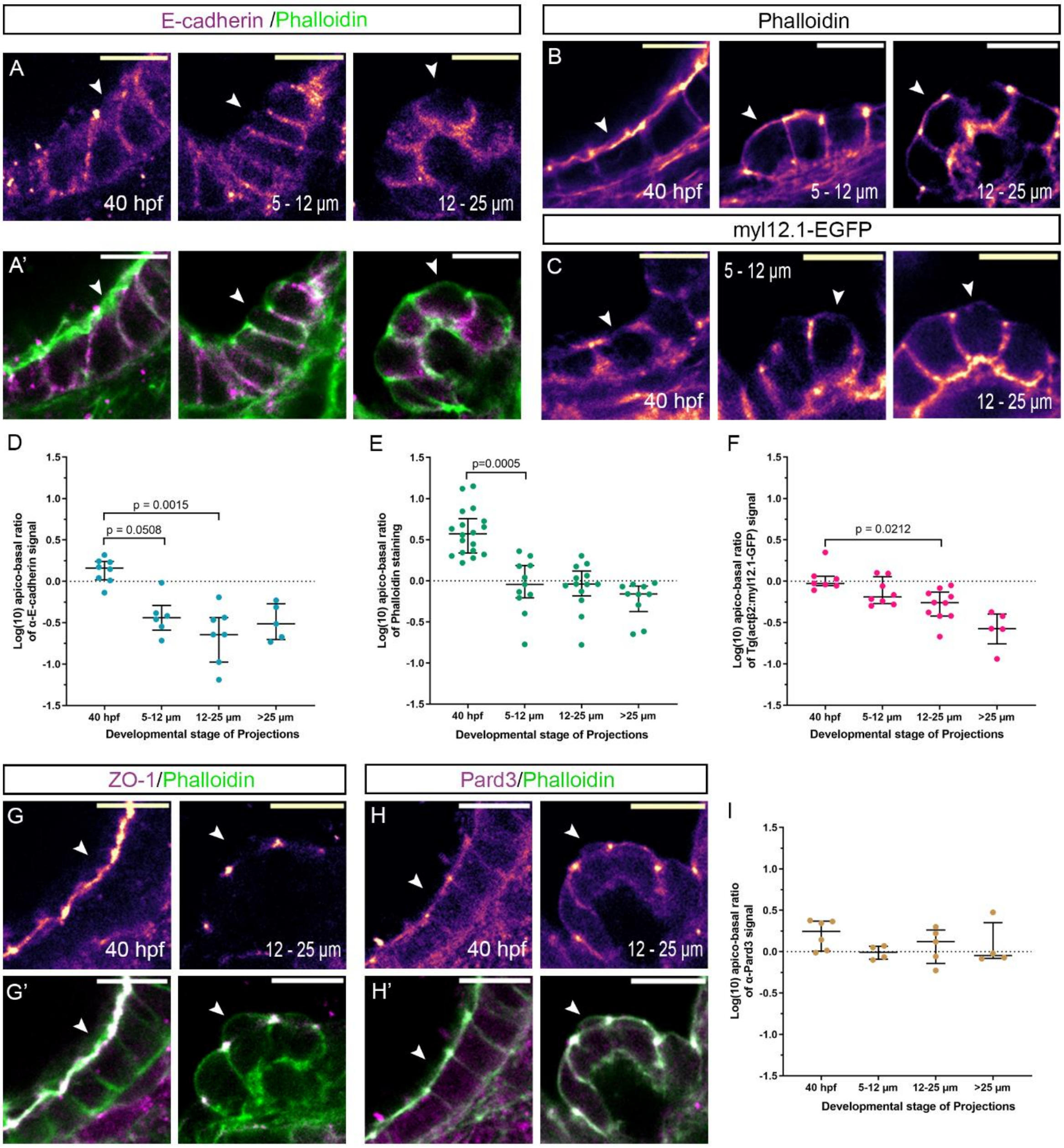

Figure 4.6 – Adhesion and cytoskeletal proteins of projection cells shift from the apical to the basolateral domain but the tissue retains its apico-basal polarity.

E-cadherin (**A** and **A'**), ZO-1 (**G** and **G'**) and Pard3 (**H** and **H'**) antibody staining, phalloidin staining (**A'**, **B**, **G'** and **H'**) and GFP boost of *Tg(actβ2:myl12.1-EGFP)* fixed embryos (**C**) were performed. Pictures were taken on a Nikon inverted confocal microscope with a 40X oil immersion objective. A single slice of a *z*-stack is shown in each picture. Arrowheads point to the apical surface of the epithelium. Scale bars measure 10 µm. Graphs (**D-F** and **I**) show the Log(10) of the ratio of staining signal in the apical half of the cells over the staining signal in the basal half of the cells (see methods 2.5.4 for details). Each data point represents a measurement over three cells in a developing projection.

The median and interquartile range are shown by the horizontal lines. A Kruskal-Wallis with Dunn's post-test correction for multiple comparisons was performed.

4.2.6 Myosin-II is required for normal projection formation

Having observed projection cells undergoing basal constriction and apical rounding and a redistribution of F-actin and myosin-II at the time of curvature inversion, I considered the role of the actomyosin cytoskeleton in these processes. It was described that the folding of the zebrafish optic cup involves basal constriction of the retinal cells partly due to the accumulation of myosin at the basal surface in scattered neuroblasts (Nicolás-Pérez et al., 2016). I hypothesised that inverting epithelium curvature could rely on contraction of actin filaments due to myosin-II activity. In order to test this, I blocked myosin activity in an actin-detached state using the myosin-II specific inhibitor blebbistatin (Kovács et al., 2004). Treatment of zebrafish embryos with 25 µM and 50 µM blebbistatin at 42 hpf (just before the start of anterior and posterior projection formation) for six hours, disrupted the formation and elongation of epithelial projections (Figure 4.7). All control (DMSO-treated) embryos formed at least one projection and nearly 70% (n = 12) formed both the anterior and posterior projections compared to 90% (n = 16) in the E3 control group (Figure 4.7A,B and E). In contrast, nearly 30% (n = 10) of blebbistatin-treated embryos failed to form either anterior or posterior projections, and only 10% (n = 2) of 50 µM blebbistatin-treated embryos formed both projections (Figure 4.7C-E). Most importantly, projections that were able to form in the blebbistatin-treated embryos were significantly shorter than those in the controls but no significant difference in projection width was found (only measured for anterior projections) (Figure 4.7A-D’, G and H). Ears of blebbistatin-treated embryos looked slightly smaller compared to those of control groups. The inhibition of myosin-II activity is likely to affect other morphogenetic processes in the embryo; however, I measured the body length of all embryos and blebbistatin-treated embryos continued to grow during treatment and reached the same length as those in the control groups (Figure 4.7J). At the time of treatment, the lateral projection was already starting to form (two embryos already had a visible lateral projection at 42 hpf – Figure 4.7F). The development of this structure was not affected as, across all groups, all embryos at 48 hpf (n = 18 per group) but one formed the lateral projection (Figure 4.7F).

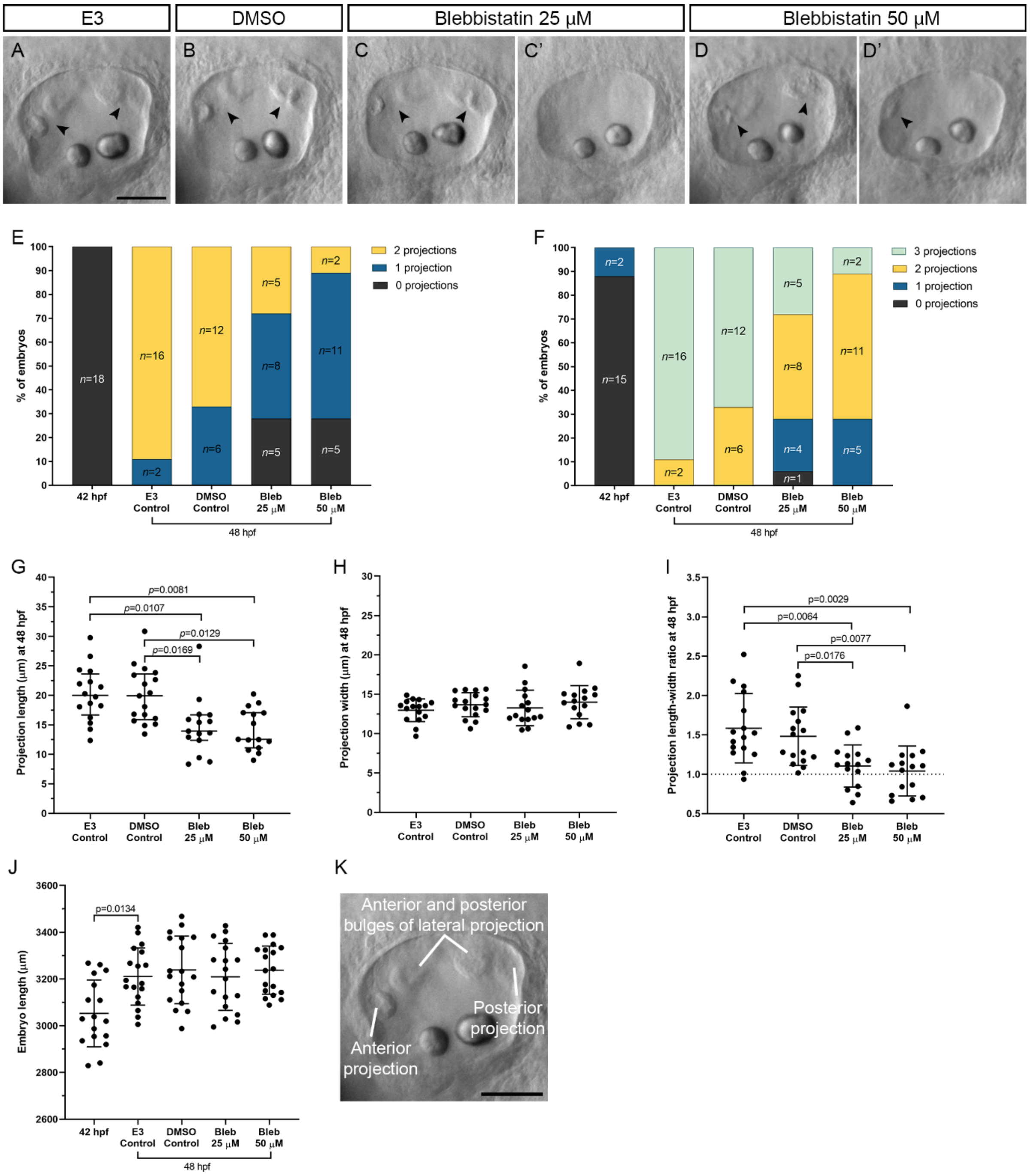

Figure 4.7 – Myosin-II activity is required for normal projection formation.

A blebbistatin treatment for six hours (42-48hpf) was performed on zebrafish embryos to block myosin-II activity. Representative images of their inner ear are shown in **A-D’** for the respective groups. Scale bars measure 50 µm. Blebbistatin treatment disrupted projection formation (**E-F**). It resulted in a significant reduction of projection length (**G**), but not width (**H**) resulting in a change of projection aspect ratio (**I**). Embryo body length (**H**) was not affected. In graph (**G**), median and interquartile range are shown by the horizontal lines, and a Kruskal-Wallis with Dunn's post-test correction for multiple comparisons was performed. In graphs (**H-J**), mean and standard deviation are shown by the horizontal lines, and a Brown-Forsythe ANOVA with a Dunnett's T3 post-test correction for multiple comparisons was performed. n in (**E**) and (**F**) is the number of ears analysed (one per embryo). (**K**) Example picture of the inner ear from a lateral view and relevant structures labelled.

When embryos were treated at a later stage (48 hpf for four hours), after formation of the lateral, anterior and posterior projections, blocking myosin-II activity did not seem to interfere with projection elongation (formation of ventral projection was not considered here since it starts developing later) (Figure 4.8). The number of epithelial projections in blebbistatin-treated embryos did not differ from the number in the controls (Figure 4.8A-D) and projections across the three groups did not differ significantly in length or width either (Figure 4.8E-G). These results suggest that myosin-II activity is important for inversion of otic epithelium curvature and projection formation in a time-dependent manner. It is likely to be required just before folding and during the first cell shape changes, but possibly not once the tissue has folded, as blocking its activity at that time did not seem to affect maintenance of projection structure nor its growth.

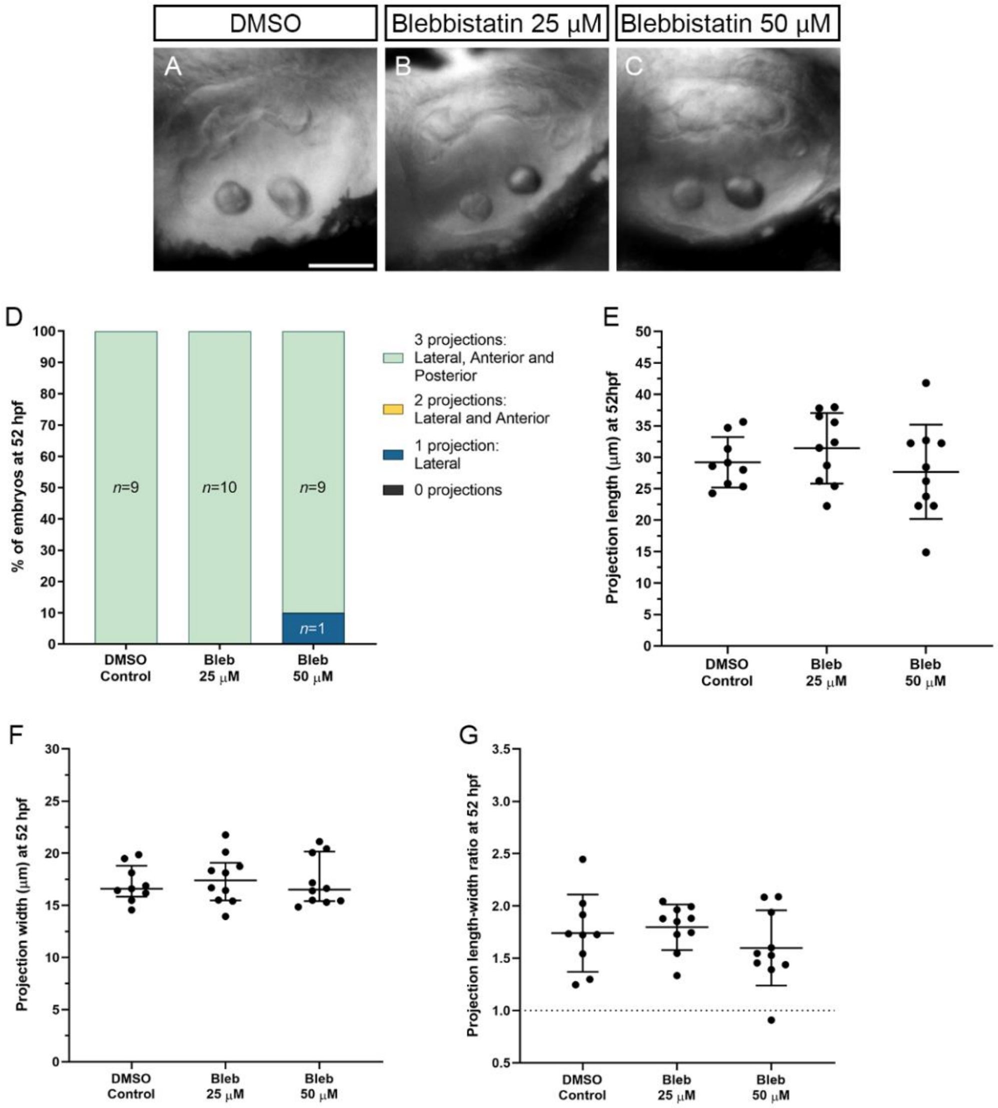

Figure 4.8 – Myosin-II activity might not be required for projection elongation or structure maintenance.

A blebbistatin treatment for four hours (48-52hpf) was performed on zebrafish embryos to block myosin II activity. Representative images of their inner ear are shown in **A-C** for the respective groups. Scale bars measure 50 µm. Blebbistatin treatment at this later stage did not disrupt projection growth. The number of projections (**D**), projection length (**E**), width (**F**) and projection aspect ratio (**G**) were the same in blebbistatin-treated as in the control embryos. In graphs (**E**) and (**G**), mean and standard deviation are shown by the horizontal lines, and a Brown-Forsythe ANOVA with a Dunnett's T3 post-test correction for multiple comparisons was performed. In graph (**F**), median and interquartile range are shown by the horizontal lines, and a Kruskal-Wallis with Dunn's post-test correction for multiple comparisons was performed. n in (**D**) is the number of ears analysed (one per embryo).

4.3 Discussion

4.3.1 Overview

Observations in this chapter showed that the outgrowth of the anterior and posterior epithelial projections of the SSCs is preceded by another stage of projection development that is characterised by drastic cell shape changes – basal constriction, apical rounding and elongation of the apico-basal axis – that result in inversion of tissue curvature. In addition, I demonstrated that these changes in cell shape are coincident with a clear redistribution of the actomyosin cytoskeleton and E-cad adhesion protein from the apical and sub-apical regions to the basolateral domain. Finally, experiments where myosin-II activity was disrupted, suggested a possible role for myosin-II in the early stages of projection formation.

The results presented in this chapter, not only add to the current understanding of cellular behaviours involved in folding events by evagination, but they also expand our knowledge of SSC development in the zebrafish inner ear. By providing a detailed description of the early stages of epithelial projection formation in the wild-type embryo, I hope to establish a helpful basis for future phenotypic studies.

4.3.2 Projection outgrowth and cell tracking

My first observation was that the onset of outgrowth of the anterior and posterior projections was variable, but their growth rate was similar. There could be a couple of different reasons for this variability. One could simply be that there is a natural variation in live embryos that is more detectable at this particular stage or with higher resolution microscopy. Another reason could be the side effects of the anaesthetic. Despite tricaine being commonly used, it was shown that using tricaine for long periods of time (28 hours) can slow down the development of the embryos in a variable way (2-6 hours) (Kimmel et al., 1995). The time-lapse I performed lasted fifteen to twenty hours, which means that there was a chance of some variable delay. One way these time-lapses could be done differently in the future is by taking advantage of the α-bungarotoxin mRNA, which can be injected at 1-cell stage, and it immobilises the embryos with apparently no effect on the embryo’s health (Swinburne et al., 2015).

The cell tracking analysis revealed that cells that end up near the tip of the projections, travel the furthest away from the otic wall and that these are the initiating cells. Cells around these initiating cells (located ventrally or dorsally), generally keep their relative positions and their neighbours as they become part of the projections themselves. One big challenge I had while manually tracking the cells, was the low signal intensity of cells located medially to the initiating cells which made it impossible for me to track them. This weaker signal could be due to the limitations of the Airyscan confocal microscope and its reduced ability to detect structures that are located deeper in the tissues. In addition, I couldn't find a way to drift correct the drift in the *z*-axis (medio-lateral axis of the embryo). For these reasons, I didn't think it was appropriate to interpret the measurements of position or displacement in the *z* axis.

4.3.3 Cell shape changes

Using the epithelial projections of the SSCs in the development of the zebrafish inner ear as a model, I also presented, in this chapter, some of the mechanisms involved in folding an already curved epithelium through evagination. This includes cell shape changes and redistribution of cytoskeletal and adhesion proteins.

Before otic epithelium folding, cell skewness was positive for most projection and surrounding cells. This was expected since the curvature of the otic tissue at this time is negative (Figure 4.3D) – apical cell surface makes up the inner surface of the curved epithelium. Measurements of cell skewness also revealed a striking difference between projection cells and surrounding ones. Whereas surrounding cells kept a positive skewness throughout (smaller apical domain than basal domain), projection cells, inverted their skewness, which means the basal domain became smaller than the apical (Figure 4.3J). Unexpectedly, from the earliest time-point analysed, the average skewness for cells that would become part of the projection was already lower than the average skewness of surrounding cells (Figure 4.3J). I was expecting that until some point before the folding event there would be no distinction between these two groups of cells. Maybe the tracking and cell shape analysis needs to be performed from an earlier time-point to check if this is true.

The 2D cell shape analysis performed here, was a helpful tool to complement the 3D cell shape analysis. It revealed that the inversion of skewness happening during the inversion of tissue curvature was most likely generated by a constriction of the basal cell surface and not by an expansion (widening) of the apical cell surface. However, I did observe a rounding of the apical cell surface. Basal constriction has been reported to be accompanied by apical expansion (Gutzman et al., 2018), but not by apical rounding. Rounding of the apical surface in epithelial projection cells could be happening due to different reasons. A passive rounding of the apical surface could be a secondary effect of basal constriction and reduction of the basal half of the cell. This could lead the cell contents to be pushed apically, putting pressure on the apical membrane, and therefore cause it to round. Laser ablation experiments and measurement of membrane recoiling speed could help understand whether the apical membrane is under some sort of tension. It could, alternatively, be an active process involving depolymerisation of actin in the apical domain accompanied by its assembly in the basolateral domain. This is supported by my observations of depletion of the actomyosin cytoskeleton from the apical cell surface and its accumulation on the basolateral region of the cells in the folding tissue. A reverse process happens during phase I of otic placode invagination in the chick embryo, where activation of myosin-II causes depolymerisation of actin in the basal domain and its apical enrichment, leading to basal expansion followed by apical constriction (Sai and Ladher, 2008). Blocking basal constriction and measuring apical domain shape changes could also help determine whether apical expansion and rounding is dependent on basal constriction.

Finally, 3D cell shape analysis also revealed that projection cells also undergo an elongation of the apico-basal axis at the time of basal constriction and apical rounding. Interestingly, basal cell constriction has been shown to allow cell elongation during notochord tubulogenesis in the ascidian *Ciona intestinalis* (Dong et al., 2011).

4.3.4 Redistribution of proteins

Through staining techniques, I was able to investigate the location of different proteins - F-actin, myosin-II (transgenic line was used), E-cad, ZO-1 and Pard3 – before, during and after the folding event. I showed that the actomyosin cytoskeleton and E-cad changed from being mainly located in the apical half of the cells to becoming located mostly in the basal half of the cells. More specifically, these proteins adopted a basolateral distribution during and after the folding event, and became absent from the apical cell surface (F-actin and myosin-II) and sub-apical regions (E-cad) of the cell.

This E-cad basal shift in the folding tissue could mean that adherens junctions are repositioning to facilitated this process. Basal shift of junctions during epithelium folding has been previously reported to be associated with initiation of epithelium folding in *Drosophila* gastrulation (Wang et al., 2012). In this case, this shift was regulated by polarity proteins Bazooka/Par-3 and Par-1 (Wang et al., 2012). Future work could be done to investigate the role of Pard3 in folding the otic epithelium. Using Pard-3 zebrafish mutant embryos, one could check whether epithelial projections form and whether E-cad undergoes this basal shift.

An independent study has also described a shift of actomyosin from the apical to the basal domain of projection cells, and myosin-II was showed to be present in basal tethers which are required for tissue stiffness and give the epithelial projections an anisotropic shape during their elongation (Munjal et al., 2021). However, the role of myosin-II activity at earlier stages, in particular during the folding event, was discarded, and instead, all credit was given to the hyaluronan pressure (ECM component) made over the basal cell surface of the projection cells (Munjal et al., 2021). Disrupting myosin-II activity with a blebbistatin treatment (in this chapter) revealed that myosin-II activity is likely to be required for initiation of projection formation and for the early stages of its elongation, since the number of projections formed under the drug treatment was reduced and projections were shorter. Imaging *Tg(actβ2:myl12.1-EGFP)* embryos (active myosin-II reporter line) following a blebbistatin treatment could be informative regarding the penetrance and efficiency of this drug.

Localised accumulation and redistribution of cytoskeletal, adhesion and polarity proteins, are often found to be driving cell shape changes during epithelium folding (Gutzman et al., 2008; Gutzman et al., 2015; Nicolás-Pérez et al., 2016; Wang et al., 2012). As reviewed in chapter one, studies have shown the role of myosin-II activity in accumulating F-actin and promoting contraction of cellular domains when enriched, contributing to basal or apical constriction. Further experiments are required to understand the link between the redistribution of proteins and the changes in cell shape reported in this chapter. One example could be to perform confocal microscopy imaging of the zebrafish inner ear following a blebbistatin treatment, perform cell segmentation and run that data through the *Origami* pipeline to measure cell shape changes. This would allow further investigation of the role of myosin-II activity in changing the shape of projection cells (especially in constricting the basal cell surface) and inverting the tissue curvature. A similar experiment with the drug Cytochalasin D could be performed to investigate the role of F-actin in different cell shape changes seen during otic tissue folding.

CHAPTER 5

Presence Of Chondroitin Sulphate And Requirement For Heparan Sulphate Biosynthesis In The Developing Zebrafish Inner Ear

5.1 Introduction

Chapter four explored tissue and cell behaviours involved in the early stages of SCC development – the formation of the epithelial projections through inversion of otic tissue curvature and its evagination into the lumen of the otic vesicle. In this chapter, a different aspect of the same event is studied: the dynamic activity of the ECM. The ECM, as explained in chapter one, is a non-cellular but vital component of tissues and it can be quite dynamic, changing its composition through time and in different tissues and organisms. Several ECM components have been identified during morphogenesis of the zebrafish inner including glycosaminoglycans like hyaluronan (Busch-Nentwich et al., 2004; Haddon and Lewis, 1991); proteoglycans like versican and dermacan (Geng et al., 2013; Suk et al., 2004); link proteins like hapln (Thisse and Thisse, 2008); glycoproteins like laminin that function as bridges between the ECM macromolecules (Sztal et al., 2011); and fibrillar proteins like collagen (Busch-Nentwich et al., 2004). Here I introduce the three ECM components, which will feature in the manuscript presented in this chapter: hyaluronan, and chondroitin sulphate and heparan sulphate proteoglycans (CSPGs, HSPGs).

5.1.1 Hyaluronan

Hyaluronan is a single chain polysaccharide, present across vertebrates and in some bacteria, with alternating sugar building blocks of N-acetyl-glucosamine and glucuronic acid. It is particularly abundant in loose connective tissue, functioning as a central, structural macromolecule around which other matrix molecules and cell surface molecules bind (reviewed in (Fraser et al., 1997; Garantziotis and Savani, 2019; Mouw et al., 2014). This ability of hyaluronan to interact with so many other molecules, makes hyaluronan a crucial player in a variety of scenarios, including morphogenesis, tissue damage and inflammation, cell migration, and cancer establishment and resistance.

Due to its intrinsic properties, multiple hyaluronan chains can form a network with themselves or with other matrix macromolecules like collagen fibres, providing different levels of stiffness to the ECM and determining its permeability to other substances (reviewed in (Comper and Laurent, 1978)). As the main glycosaminoglycan present in the ECM, hyaluronan is the primary contributor to the viscoelastic properties of the ECM. This is conferred by the numerous negatively charged carboxylate groups balanced by sodium ions, which allow hydrophilic hyaluronan to swell and therefore, apply osmotic forces to its surrounding environment (Cowman et al., 2015). This particular property of the hyaluronan molecule supports the idea that the finger-like projections of otic epithelium, seen at early stages of SCC development, are pushed into the lumen of the vesicle by the swelling of hyaluronan in the basal extracellular space (Busch-Nentwich et al., 2004; Haddon and Lewis, 1991; Toole, 2001).

Hyaluronan is synthesised by hyaluronan synthases 1, 2 and 3 (HAS1, HAS2, HAS3) depending on the biological context. For example, HAS2 has been known to be required for the development of the endocardial cushions of the heart (another case of epithelial folding) (Lagendijk et al., 2011). In contrast, in the inner ear, HAS3 is expressed (Geng et al., 2013; Munjal et al., 2021; Thisse and Thisse, 2005), and is thought to be responsible for synthesising hyaluronan; when its gene is downregulated, epithelial projections of the SSCs fail to form properly (Munjal et al., 2021). Hyaluronan is naturally degraded by oxidative and nitrative stresses, and by different hyaluronidases (reviewed in (Garantziotis and Savani, 2019). Hyaluronidase injections in the inner ear have been performed to demonstrate the requirement for hyaluronan in maintaining the growth of the projections (Geng et al., 2013; Haddon and Lewis, 1991; Munjal et al., 2021).

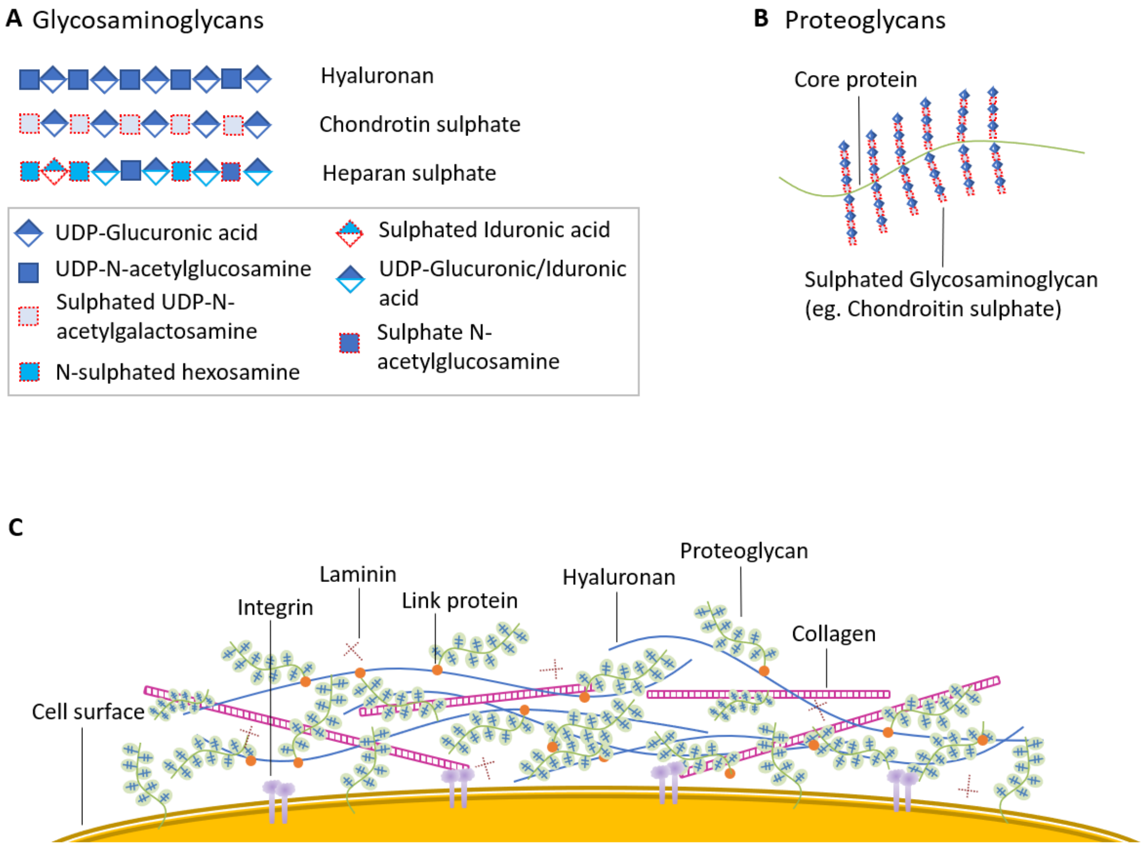

Figure 5.1 - Glycosaminoglycans and proteoglycans in the extracellular matrix.

Glycosaminoglycans like hyaluronan and proteoglycans make up a considerable proportion of the extracellular matrix (ECM). (**A**) Diagram of glycosaminoglycan (GAG) chains for hyaluronan, chondroitin sulphate and heparan sulphate. Alternating sugars make up the building blocks of these chains with some alterations of sulphated groups for the heparan and chondroitin sulphate GAGs. (**B**) Generic diagram of proteoglycan structure is shown here, including a core protein and glycosaminoglycan chains covalently bound to it. (**B**) Example diagram of the ECM structure. Main structural components include hyaluronan chains and collagen fibres. Proteoglycans can be found linked to hyaluronan through link proteins, collagen, cell membrane or free in the ECM. Adhesive glycoprotein laminin and transmembrane linker integrin are also shown. Abbreviation: UDP - Uridine diphosphate.

5.1.2 Proteoglycans

Proteoglycans are composed of a core protein which anchors sulphated glycosaminoglycans, such as chondroitin and heparan sulphate (reviewed in (Iozzo and Schaefer, 2015; Mouw et al., 2014)). For this reason, these matrix molecules share some properties and roles with hyaluronan, including its ability to interact with water, swell and apply osmotic pressure.

Proteoglycans are also able to bind several ligands, including morphogens and chemokines, anchor to the cell surface, bind to hyaluronan by link proteins, or to other major structural matrix proteins like collagen (Kreuger et al., 2006).

5.1.2.1 Chondroitin sulphate proteoglycans

CSPGs can span from the cell surface, like phosphacan; through the pericellular space, like collagen XV; and to the extracellular space (the furthest away from the cells), like aggrecan and versican (reviewed in (Iozzo and Schaefer, 2015)). The pericellular space is where the basal lamina is located – a form of ECM that is near the basal cell surface of epithelia and works as a supporting structure, protective barrier and communication mediator between tissues and their external environment (reviewed in (Yurchenco, 2011)). Similarly to hyaluronan, chondroitin sulphate chains also consist of repeated dissacharides of glucuronic acid and N-acetylgalactosamine, except that in this case *O*-sulphate groups are added to the chain (Mouw et al., 2014). Together with dermacan sulphate proteoglycans, CSPGs play a structural role within the ECM in a variety of contexts such as the neural tissues, cartilages, tendons and corneas. They also contribute to the viscoelastic nature of the ECM and to the organisation of collagen fibres.

Biosynthesis of chondroitin sulphate chains involve the enzyme chondroitin sulphate synthase 1 (CHSY1), and mutations in the *chsy1* gene are causative for the Temtamy preaxial brachydactyly syndrome, which is mainly characterised by malformations in the limbs, deafness and growth retardation (Li et al., 2010). Genes for this and other enzymes involved in the polymerisation and modification of chondroitin sulphate chains have been shown to be expressed in the zebrafish inner ear. In addition, genes for one of the core proteins of chondroitin sulphate proteoglycans - versican - are strongly expressed during morphogenesis of the SSCs of the zebrafish inner ear (Geng et al., 2013). Both of these are presented in more detail in the manuscript included in this chapter. Moreover, disruption of *chsy1* function in zebrafish embryos through morpholino injection leads to abnormal development of the epithelial projections of the SSCs and of the atrioventricular canal of the heart (Li et al., 2010; Peal et al., 2009).

5.1.2.2 Heparan sulphate proteoglycans

HSPGs are found mostly at the cell surface, like syndecan; and in the pericellular space, like perlecan, agrin and collagen XVIII (reviewed in (Bishop et al., 2007)). In this context, heparan sulphate proteoglycans play two key roles. The first is modifying and presenting growth factors near the cell surface; and the second is generating and maintaining morphogen gradients during morphogenesis and regenerative processes.

Enzymes called exostosin glycosyltransferases 1, 2 and 3 (EXT1, 2, and 3) are responsible for polymerising heparan sulphate chains. Mutations in the genes *ext1*, and *ext2* lead to hereditary multiple exostoses/osteochondromas, a disease characterised by cartilage-capped bony tumours (Koziel et al., 2004; Stickens et al., 2005). Details of the phenotype of the zebrafish *ext2* mutant, including in the inner ear, are given later in the manuscript presented in this chapter. In the chick inner ear however, HSPGs were demonstrated to be important for the folding event that happens during otic cup invagination (Moro-Balbás et al., 2000). Degradation of heparan sulphate by injecting heparinase III prior to the folding event disrupted this morphogenetic process, preventing inner ear development (Moro-Balbás et al., 2000). In addition, the mRNA of the extracellular 6-O-endosulfatases - Sulf1 and Sulf2 – which remove sulphate groups from heparan sulphate chains and therefore regulate their signalling activity, have been shown to be present during chick and mouse inner ear development (Freeman et al., 2015).

5.2 Manuscript

Declaration of content and author contribution:

This chapter is a published manuscript that contains collaborative work of myself, Dr. Elvira Diamantopoulou, Dr. Sarah Baxendale and Prof. Tanya T. Whitfield, supervised also by Prof. Tanya T. Whitfield. I have included this manuscript in this thesis firstly, because it follows on from the previous chapter by addressing another mechanism involved in the development of epithelial projections; and secondly, because I have contributed with significant work as a shared first author. This includes acquiring, curating and analysing all the data displayed in Figures 1, 2K-L and 4, Supplementary Figure 1, and Supplementary Movies 1 – 4; writing a draft version of the methods for this experimental work; reviewing and editing. Contributions from all authors are as follows:

Data collection, curation, and analysis: AAJ, SB, ED, TTW.

Project administration and supervision: SB, TTW.

Funding acquisition: SB, TTW.

Writing: TTW, with input from all other authors.

This is a Frontiers in Cell and Developmental Biology paper.

Citation: Jones AA, Diamantopoulou E, Baxendale S and Whitfield TT (2022) Presence of chondroitin sulphate and requirement for heparan sulphate biosynthesis in the developing zebrafish inner ear. Front. Cell Dev. Biol. 10:959624.

https://doi.org/10.3389/fcell.2022.959624

Editor: Berta Alsina, Pompeu Fabra University, Spain

Reviewers: Bryan Douglas Crawford, University of New Brunswick Fredericton, Canada. Stefan Heller, Stanford University, United States

Received: 01 June 2022; **Accepted:** 12 July 2022; **Published:** 26 August 2022.

Data Availability: The original contributions presented in the study are included in the article/Supplementary Material; further inquiries can be directed to the corresponding author.

Funding: This work was funded by the Biotechnology and Biological Sciences Research Council (BBSRC: BB/J003050 to TTW, BB/M01021X/1 and BB/S007008/1 to TTW and SB). AAJ was funded by a Doctoral Training Award from the Biotechnology and Biological Sciences Research Council BBSRC White Rose Doctoral Training Partnership in Mechanistic Biology (BB/M011151/1). ED was funded by a PhD studentship from the University of Sheffield (314420). Imaging was carried out in the Wolfson Light Microscopy Facility, supported by a BBSRC ALERT14 award to TTW and SB for light-sheet microscopy (BB/M012522/1). The Sheffield zebrafish aquarium facilities were supported by the Medical Research Council (MRC: G0700091). The funders had no role in study design, data collection and analysis, decision to publish, or preparation of the manuscript.

Conflict of interest: The authors declare that the research was conducted in the absence of any commercial or financial relationships that could be construed as a potential conflict of interest.

Presence of chondroitin sulphate and requirement for heparan sulphate biosynthesis in the developing zebrafish inner ear

Ana A. Jones[†], Elvira Diamantopoulou[†], Sarah Baxendale and Tanya T. Whitfield*

Development, Regeneration and Neurophysiology, School of Biosciences, and Bateson Centre, University of Sheffield, Sheffield, S10 2TN, UK

[†]These authors contributed equally to this work and share first authorship

*Correspondence:

Tanya T. Whitfield t.whitfield@sheffield.ac.uk

OrcIDs:

Sarah Baxendale 0000-0002-6760-9457

Elvira Diamantopoulou 0000-0002-9336-7965

Ana A. Jones 0000-0002-9602-4917

Tanya T. Whitfield 0000-0003-1575-1504

Key words: extracellular matrix; HSPG; CSPG; *ext2*; epithelial morphogenesis; heparan sulphate proteoglycan; chondroitin sulphate proteoglycan; versican; keratan sulphate; semicircular canals; otoliths; zebrafish

Abstract

Epithelial morphogenesis to form the semicircular canal ducts of the zebrafish inner ear depends on the production of the large glycosaminoglycan hyaluronan, which is thought to contribute to the driving force that pushes projections of epithelium into the lumen of the otic vesicle. Proteoglycans are also implicated in otic morphogenesis: several of the genes coding for proteoglycan core proteins, together with enzymes that synthesise and modify their polysaccharide chains, are expressed in the developing zebrafish inner ear. In this study, we demonstrate the highly specific localisation of chondroitin sulphate to the sites of epithelial projection outgrowth in the ear, present before any morphological deformation of the epithelium. Staining for chondroitin sulphate is also present in the otolithic membrane, whereas the otoliths are strongly positive for keratan sulphate. We show that heparan sulphate biosynthesis is critical for normal epithelial projection outgrowth, otolith growth and tethering. In the *ext2* mutant ear, which has reduced heparan sulphate levels, but continues to produce hyaluronan, epithelial projections are rudimentary, and do not grow sufficiently to meet and fuse to form the pillars of tissue that normally span the otic lumen. Staining for chondroitin sulphate and expression of *versican b,* a chondroitin sulphate proteoglycan core protein gene, persist abnormally at high levels in the unfused projections of the *ext2* mutant ear. We propose a model for wild-type epithelial projection outgrowth in which hyaluronan and proteoglycans are linked to form a hydrated gel that fills the projection core, with both classes of molecule playing essential roles in zebrafish semicircular canal morphogenesis.

Contribution to the field

The zebrafish inner ear, which develops from the otic vesicle, is an excellent exemplar of epithelial morphogenesis. Generation of the complex three-dimensional structure of the semicircular canal ducts begins with events that deform the epithelium to generate protrusions or projections of tissue that move into the otic vesicle lumen. It has long been appreciated that the large, space-filling glycosaminoglycan hyaluronan (HA), a component of the extracellular matrix, plays an important role in this morphogenetic process. More recent work has highlighted the importance of differential tissue stiffness in shaping the projections. A further set of players are also likely to have essential roles: the sulphated proteoglycans. We identify patches of chondroitin sulphate deposition that prefigure the initial sites of deformation in the otic epithelium. We also show that the ear defects in a zebrafish mutant that fails to synthesise heparan sulphate are very similar to those generated through disruption of HA production. In addition to defects in epithelial morphogenesis, mutants have otolith tethering defects, indicating that heparan sulphate is also required for adhesion of the otoliths to sensory epithelium in the zebrafish inner ear.

Introduction

Morphogenesis of the vertebrate inner ear is an excellent exemplar of epithelial morphogenesis. Development of this organ system involves a series of events that shape and fold the otic epithelium, converting it from a fluid-filled vesicle into a series of interlinked sensory chambers and tubes (Alsina and Whitfield, 2017). In the zebrafish, morphogenesis of the semicircular canal ducts is initiated when finger-like protrusions or projections of epithelium move into the lumen of the vesicle. Between days 2 and 3 of embryonic development, anterior, posterior and ventral projections fuse in a stereotyped sequence with corresponding bulges from a lateral projection. These fusion events create three new columns or pillars of tissue that span the otic lumen, defining the three semicircular canals (Haddon and Lewis, 1996; Waterman and Bell, 1984).

It has long been recognised that the extracellular matrix (ECM) plays a critical role in formation and outgrowth of the epithelial projections in the zebrafish and *Xenopus* ear. Electron microscopy studies revealed that the acellular cores of the projections are filled with ‘fibrillar and granular material’, and that cells of the projection epithelium are rich in endoplasmic reticulum and lack a basal lamina, consistent with high levels of ECM production and secretion (Haddon and Lewis, 1991a; Waterman and Bell, 1984b). A major ECM component of the projection cores is the glycosaminoglycan (GAG) hyaluronan (also known as hyaluronic acid or HA) (Busch-Nentwich et al., 2004b; Haddon and Lewis, 1991a; Toole, 2001a). Haddon and Lewis first proposed that localised synthesis and retention of this large, space-filling polymer could act as a driving force for the outgrowth of epithelial projections into the lumen of the *Xenopus* otic vesicle (Haddon and Lewis, 1991a). In support of this hypothesis, localised enzymatic digestion of HA blocks projection outgrowth in both *Xenopus* (Haddon and Lewis, 1991a) and zebrafish (Geng et al., 2013b; Munjal et al., 2021a). Moreover, reducing HA production in zebrafish, via morpholino-mediated knockdown of *dfna5* (orthologue of the human deafness autosomal dominant *DFNA5* gene) or *hyaluronan synthase* (*has3*), or genetic mutation of *UDP-glucose dehydrogenase* (*ugdh*), compromises projection outgrowth (Busch-Nentwich et al., 2004b; Munjal et al., 2021a; Neuhauss et al., 1996b; Walsh and Stainier, 2001).

The zebrafish *ugdh* (*jekyll*) mutant otic phenotype is severe, with very small and rudimentary projections, even by 6 days post fertilisation (dpf) (Neuhauss et al., 1996b). The *ugdh* gene, which is expressed in the epithelial projections of the zebrafish ear (Busch-Nentwich et al., 2004b; Walsh and Stainier, 2001), is an orthologue of *sugarless* (*sgl*) in *Drosophila* (Häcker et al., 1997), and codes for the enzyme UDP-glucose 6-dehydrogenase (Ugdh). Ugdh catalyses the production of glucuronic acid, an essential building block not only of HA, but also of various proteoglycans, including heparan sulphate, chondroitin sulphate and keratan sulphate proteoglycans (HSPGs, CSPGs, KSPGs) (Zimmer et al., 2021), suggesting that deficiencies of these molecules might also contribute to the *ugdh* mutant phenotype.

Proteoglycans are negatively charged ECM molecules consisting of sulphated GAG chains attached to a protein core, with widespread roles in animal development (Bülow and Hobert, 2006). Chondroitin sulphate proteoglycans (CSPGs) are already implicated in zebrafish otic morphogenesis. The CSPG core protein gene *versican a* (*vcana*) is highly expressed in the epithelial projections during their growth phase, but is rapidly down-regulated on fusion to form pillars (Geng et al., 2013b). The zebrafish ear expresses chondroitin synthase and glycosyltransferase genes coding for enzymes involved in the polymerisation of CS chains (Filipek-Górniok et al., 2013a; Li et al., 2010b), together with sulfotransferase genes involved in CS modification (Habicher et al., 2015). Morpholino-mediated knockdown of *chondroitin synthase 1* (*chsy1*) leads to epithelial projection defects in the zebrafish ear (Li et al., 2010b). Here, we use immunohistochemistry to show that localised deposition of CS prefigures the sites of projection outgrowth in wild-type zebrafish ears.

To test the role of heparan sulphate (HS) in zebrafish semicircular canal morphogenesis, we have examined the otic phenotype of the *exostosin 2* (*ext2/dackel*) mutant, which lacks the function of a glycosyltransferase involved in HS biosynthesis (Lee et al., 2004). Mutants have a global reduction in HS levels by 5 days post fertilisation (dpf), and form a model for the human autosomal dominant condition multiple osteochondromas (Clément et al., 2008; Holmborn et al., 2012; Lee et al., 2004). Homozygous zebrafish *ext2* mutations disrupt development of cartilage, bone and teeth (Clément et al., 2008; Schilling et al., 1996; Wiweger et al., 2012; Wiweger et al., 2014), pectoral fins (van Eeden et al., 1996), the retinotectal projection (Karlstrom et al., 1996; Lee et al., 2004; Trowe et al., 1996), and the lateral line (Venero Galanternik et al., 2015). These pleiotropic effects reflect the widespread requirement of HSPGs for the activity of various developmental signalling pathways (Fischer et al., 2011; Norton et al., 2005; Venero Galanternik et al., 2015). Otic defects were noted in *ext2* mutants (Whitfield et al., 1996), but were not characterised in detail. We now show that *ext2* mutants have otic defects similar to those seen after disruption of HA or CS, demonstrating an essential role for HS biosynthesis in epithelial projection outgrowth and formation of the semicircular canal system. Our results indicate that the otic ECM is composed of both HA and proteoglycans, and that the loss of either class of molecule compromises the early steps of semicircular canal morphogenesis.

MATERIALS AND METHODS

Animals

Standard zebrafish husbandry methods were employed (Aleström et al., 2020; Westerfield, 2007). The wild-type strain used was AB (ZDB-GENO-960809-7), and the *ext2* mutant allele used was *dak*^{tw25e} (ZDB-ALT-980203-1459) (Haffter et al., 1996). This allele has a T>A mutation in exon 5, introducing a STOP codon and predicting a truncation of the protein sequence at amino acid 227 (Lee et al., 2004). In all examples shown, mutant embryos were homozygous for the zygotic *dak*^{tw25e} allele. For some experiments, fish were crossed onto a *nacre* (*mitfa*$^{-/-}$; ZDB-GENO-990423–18) background, which has reduced body pigmentation, facilitating visualisation of staining patterns (Lister et al., 1999). The phenotypically wild-type sibling embryos shown in Fig. 1 and Fig. 4E,E' were from a cross between parents heterozygous for mutations in *tbx1*^{tm208} (ZDB-ALT-980203-1362). Embryos were raised in E3 embryo medium (5 mM NaCl, 0.17 mM KCl, 0.33mM $CaCl_2$, 0.33 mM $MgSO_4$) (Westerfield, 2007) at 28.5°C. In some cases, to obtain the desired stage, embryos were raised at temperatures ranging from 23°C to 33°C, and staged according to the equivalent hours post fertilisation (hpf) at 28.5°C using a conversion formula (Kimmel et al., 1995c). Methylene blue (0.0001%) was added to reduce fungal growth, and where necessary, 0.003% 1-phenyl 2-thiourea (PTU; 0.003%) was added to block the development of pigmentation. We use the term embryo throughout to refer to zebrafish embryos and larvae from 0–5 days post fertilisation (dpf).

Genotyping

The *dak*^{tw25e} mutation introduces an *Mse*I restriction site into the genomic DNA sequence, allowing the identification of mutant embryos at early stages (up to 48 hours post fertilisation (hpf), before the onset of any obvious phenotype) by genotyping. Forward (5'-GGCTTCTCCACATGGACCTA-3') and reverse (5'-CCGAGGACTGGAAGAAAAAC-3') primers were used to amplify genomic DNA from individual embryos by PCR. The amplified product (188 base pairs, bp) was digested with *Mse*I (New England Biolabs, R0525S), which cuts the mutant sequence to generate two fragments of 158 bp and 30 bp.

Immunofluorescence and phalloidin staining

Embryos were dechorionated and fixed at the desired stages in 4% paraformaldehyde for 2–4 hours at room temperature (except 40 hpf embryos, which were fixed overnight at 4°C). Fixed embryos were permeabilised in PBS-Tr (phosphate-buffered saline (PBS),1% Triton X-100) for 3 × 5 minutes, blocked in Blocking Solution (PBS-Tr with the addition of 10% sheep or donkey serum, depending on the secondary antibody used) for 60 minutes, and incubated overnight at 4°C in Blocking Solution and 1% DMSO, with the addition of the relevant primary antibody at the following concentrations: anti-Chondroitin Sulphate (CS) (C8035 mouse monoclonal, Sigma-Aldrich), 1:100; anti-Keratan Sulphate (KS) (3H1 mouse anti-rat monoclonal, R. U. Margolis and R. J. Margolis, Developmental Studies Hybridoma Bank), 1:100. Embryos were washed in PBS-Tr for 3 × 5 minutes and 4 × 30 minutes, and then incubated overnight at 4ºC in Blocking Solution and 1% DMSO with the addition of an Alexa-647-conjugated goat anti-mouse secondary antibody (A21235, Invitrogen; 1:200). Embryos were counterstained for F-actin by the addition of Alexa Fluor 488 Phalloidin (8878, Cell Signalling Technology, 1:100 from a 6.6 µM stock), to the secondary antibody staining step. Embryos were washed in PBS-Tr for 4 × 5 minutes, and stored in PBS-Tr at 4°C before mounting. Staining with the secondary antibody only gave no signal in the ear (not shown). As an additional control, embryos from the same batch were stained with primary antibodies to CS or KS in the same experiment, using the same secondary antibody. Each primary antibody gave a different and reproducible staining pattern (Supplementary Fig. S1). Staining experiments were performed in duplicate, and at least two embryos were imaged for each genotype and stage.

Hyaluronic acid binding protein staining

The protocol for HABP staining was adapted from (Munjal et al., 2021a). Embryos were dechorionated at 57 hpf and fixed in 4% paraformaldehyde at room temperature for 2 hours. Embryos were washed in PBS for 3 × 5 minutes, before permeabilisation with ice-cold acetone at -20°C for 7 minutes. Embryos were washed in PBS-Tr for 3 × 5 minutes and blocked in PBS-Tr containing 5% BSA for 60 minutes at room temperature. Embryos were incubated in blocking solution containing biotinylated Hyaluronan Binding Protein (HABP from EMD Millipore, 1:100 dilution of 0.5 µg/µl stock) at 4°C, overnight. Embryos were washed 3 × 15 minutes with PBS (detergent was avoided due to low binding affinity of HABP to HA). Embryos were incubated with Streptavidin Alexa Fluor 546 (Invitrogen S11225, 1:500) and counterstained for F-actin with Alexa Fluor 488 Phalloidin (8878, Cell Signalling Technology, 1:100 from a 6.6 µM stock). Embryos were washed for 3 × 15 minutes with PBS before mounting for imaging.

Whole-mount *in situ* hybridisation

Embryos were dechorionated and fixed in 4% paraformaldehyde overnight at 4°C. Fixed embryos were rinsed in PBS, dehydrated through a methanol series, and stored in methanol at -20°C. Whole-mount in situ hybridisation to the genes listed in Supplementary Table 1 was performed based on the standard protocol (Thisse and Thisse, 2008a) with minor modifications. Data shown in Figures 2 and 7 are representative of two individual experiments for each gene (*n*=50 embryos analysed per embryonic stage).

Microscopy and photography

For live imaging, zebrafish embryos were anaesthetised in 4% (w/v) tricaine (MS222) in E3 medium and mounted in 3% (w/v) methylcellulose in a cavity created by cutting a small window in three layers of electrical insulation tape stuck on a glass slide, and coverslipped. For immunofluorescence, fixed embryos were dissected to remove the yolk and eyes, and then mounted laterally in 1–1.5% Low Melting Point Agarose in PBS in the centre of a 35-mm Wilco glass-bottomed Petri dish. Image stacks (*z*-step, 1 µm) were acquired on a Nikon A1 confocal microscope with a 40× objective using the 488 and 647nm excitation laser lines. HABP-stained embryos were mounted in low-melting point agarose in glass capillaries and imaged using the Zeiss Z1 light-sheet microscope. Image stacks were acquired with a 20× objective using the 488 and 561 excitation laser lines. Images were taken dorsally with the embryo rotated by 25° to obtain the best view of the acellular core of the lateral projection in the ear.

Images of live embryos and those stained using in situ hybridisation were acquired on an Olympus BX-51 compound microscope equipped with a C3030ZOOM camera and CELL B software, or a Micropublisher 6 camera and Ocular software. Images for the measurements shown in Fig. 2 and Supplementary Fig. S2 were acquired on a Zeiss Axio Zoom.V16 microscope. Unless otherwise stated, embryos were oriented laterally, with anterior to the left. Single channel images are displayed in inverted grayscale. Images were processed in Fiji (Schindelin et al., 2012), and figures were assembled with Adobe Photoshop v22.5.1.

Otolith displacement (‘tapping’) assay

Anaesthetised *ext2* mutants (*N*=8) and phenotypically wild-type siblings (*N*=8) at 5 dpf were individually mounted in 4% methylcellulose in a cavity made by cutting a window in four layers of electrical insulation tape on a microscope slide, and covered with a coverslip. The slide was then gently tapped on the benchtop for 10 seconds. Images were taken before and after tapping.

This protocol was adapted from an earlier study, where it was used to measure otolith tethering in zebrafish mutants for *otogelin* and *tecta* (Stooke-Vaughan et al., 2015).

Measurements and statistical analysis

Ear and otolith morphometric measurements were made from 2D micrographs in Fiji (Schindelin et al., 2012). Data were analysed and presented using GraphPad Prism v9.1.2. Statistical tests used are stated in the relevant figure legend.

Results

Foci of chondroitin sulphate staining prefigure emergence of the semicircular canal projections in wild-type ears

Versican genes, which code for the core proteins of chondroitin sulphate proteoglycans (CSPGs), are expressed in a dynamic pattern in the zebrafish ear, with maximum mRNA expression levels during projection outgrowth (Geng et al., 2013). To examine the distribution of chondroitin sulphate (CS) in the ear, we stained fixed samples with an antibody to CS. In phenotypically wild-type embryos (see Materials and Methods), anti-CS antibody staining revealed reproducible, small (10–20 µm diameter) foci that prefigure the emergence (evagination) of the lateral, anterior, posterior and ventral semicircular canal projections (Fig. 1 and Supplementary Movie 1; additional examples at different stages in Fig. 4 and Supplementary Fig. S1A). For the anterior projection, staining was present at 40 hpf on the apical (lumenal) side of the epithelium (Fig. 1A–C; see also Fig. 4A,A'), with foci of staining present at the base of the lateral, anterior and posterior projections at 45–50 hpf (Fig. 1E). For the ventral projection at 48–50 hpf, staining was present in a discrete patch or streak on the basal side of the epithelium, beneath a small group of cells that were about to evaginate to form the projection (Fig. 1E; Supplementary Movie 1). By contrast, CS staining was absent from cells invaginating to form the endolymphatic duct, a short tube that extends from dorsal otic epithelium (Fig. 1D,F). At later stages, after fusion of epithelial projections and bulges to form pillars, there was very little CS staining evident in the cores of the pillars or lateral projection in wild-type ears (Supplementary Movie 3; see also Fig. 4E,G). Positive staining for CS also marked the otolithic membrane overlying sensory hair cells of the utricular macula (asterisks, Fig. 1E, Supplementary Fig. S1A–A", Supplementary Movie 3).

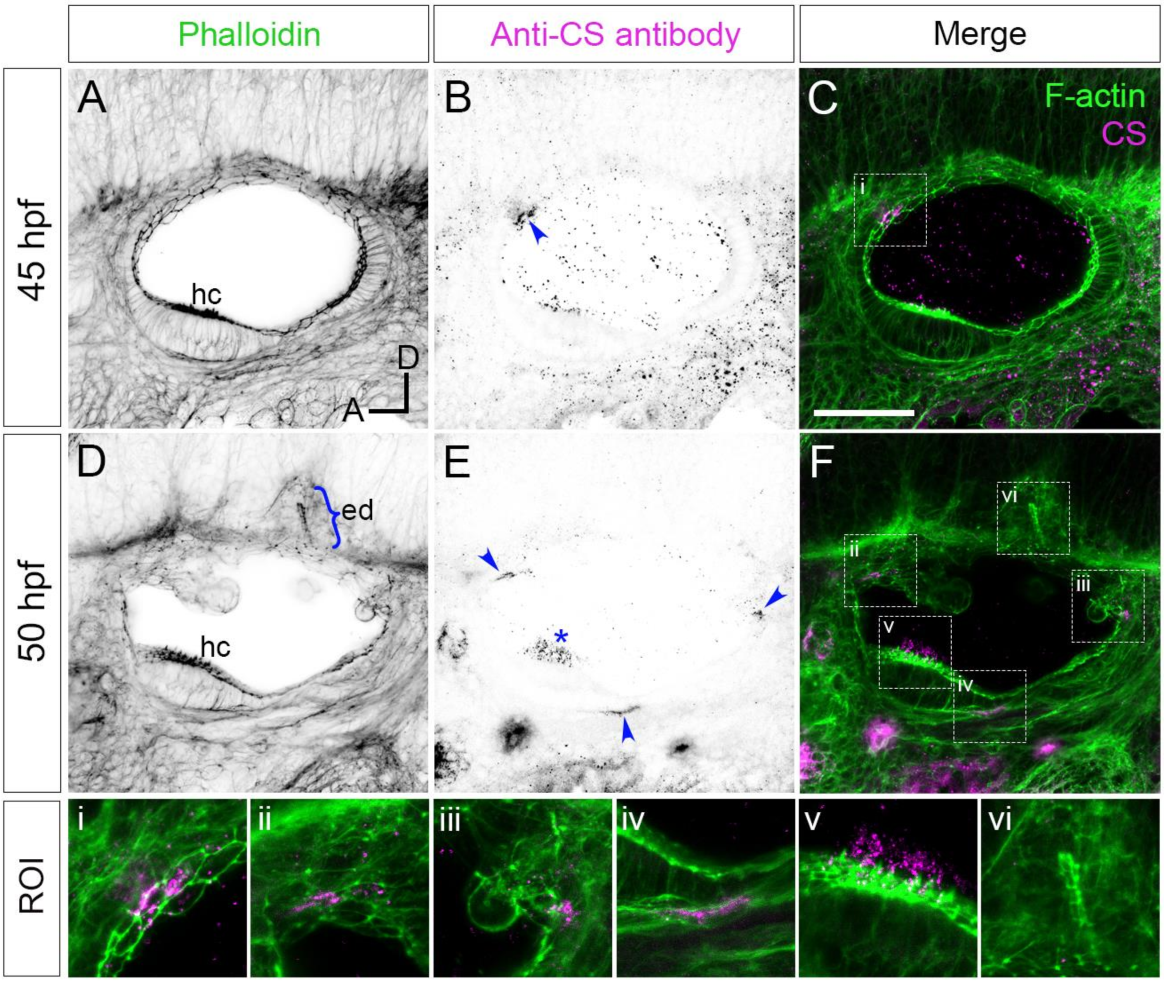

Figure 1. Staining for chondroitin sulphate in phenotypically wild-type zebrafish ears marks sites of epithelial projection outgrowth

(A–F) Confocal images of Alexa-phalloidin (green) and anti-CS antibody (magenta) whole-mount stains of phenotypically wild-type ears (see Materials and Methods). Blue arrowheads mark foci of chondroitin sulphate (CS) staining associated with the emergence (evagination) of epithelial projections from the otic epithelium; blue bracket marks the invaginating endolymphatic duct (ed); blue asterisk marks staining in the otolithic membrane overlying hair cells of the anterior (utricular) macula. Boxed areas highlight regions of interest (ROI), enlarged in the bottom row of panels: (i), apical focus of CS staining at 45 hpf prefiguring site of emergence of the anterior projection; (ii, iii), foci of CS staining associated with the anterior and posterior projections, respectively, at 50 hpf; (iv), basal focus of CS staining prefiguring site of emergence of the ventral projection; (v), CS staining in the utricular otolithic membrane; (vi), absence of CS stain in the endolymphatic duct. All panels are lateral views with anterior to left, and dorsal to top (orientation shown in A: A, anterior; D, dorsal). Scale bar in C, 50 µm (applies to A–F). Abbreviations: CS, chondroitin sulphate; ed, endolymphatic duct; hc, stereociliary bundles on the apices of hair cells in the anterior (utricular) macula. Additional examples and developmental stages are shown in Fig. 4, Supplementary Fig. S1 and Supplementary Movie 1.

The ears of *ext2* mutants, which have reduced heparan sulphate biosynthesis, have epithelial projection and otolith defects

To test the role of heparan sulphate (HS) biosynthesis in otic morphogenesis, we imaged the developing ear in live zebrafish *ext2* (*dak*^{tw25e}) homozygous mutant embryos, at developmental stages when the otic epithelium is undergoing morphogenetic deformation to form the semicircular canal system (2–5 days post fertilisation, dpf). Otic development normally progresses by the formation of epithelial projections and bulges that fuse to form pillars of tissue spanning the otic lumen (Haddon and Lewis, 1996b; Waterman and Bell, 1984b). At 48 hours post fertilisation (hpf), the *ext2* mutant otic vesicle was rounder in shape than that of phenotypically wild-type sibling embryos (Figs 2,4). The lateral projection formed an anterior bulge, but formation of the posterior and ventral bulges was delayed or absent (Fig. 2A,F'). By 72 hpf, epithelial projections in the wild-type ear had fused to form three pillars in all cases (*N*=16 embryos; *n*=32 ears; Fig. 2C'). By contrast, in *ext2* mutants at 72 hpf, the anterior projection had fused in some ears (*N*=4 embryos; *n*=5/8 ears), but the posterior projection had only fused in 1/8 mutant ears examined, and the ventral projection remained very small in all ears examined (*n*=8/8). Unfused projections were also present in the ear at 4 and 5 days post fertilisation (dpf) (Fig. 2D',F',H'), and the ears, although smaller than normal, became swollen, visible in a dorsal view (Fig. 2F,F'; further examples in Fig. 6). Some mutant ears also had abnormal out-pocketings of the epithelium, not present in the wild type (black arrowheads, Fig. 2D',H').

Measurements of ear size at 72 hpf indicated that the *ext2* mutant ears were narrower in the anteroposterior dimension in a lateral view ('ear width') than in the wild type, with more variation in size and shape (Fig. 2I, Supplementary Fig. S2). Ear height in *ext2* mutants was also more variable, but the mean value was not significantly different from the wild type (Fig. 2I, Supplementary Fig. S2). Two otoliths were present in the *ext2* mutant ear, but were smaller than normal at 72 hpf (Fig. 2J). However, the otoliths stain strongly with an antibody to keratan sulphate, as in the wild type (Fig. 2K,L, Supplementary Fig. S1B–B"). Phalloidin staining confirmed that all five sensory patches (two maculae and three cristae) were present in the *ext2* mutant ear at 3–5 dpf, and contained differentiated hair cells (Fig. 2K,L; additional examples in Fig. 4).

The *ext2* gene is expressed maternally and ubiquitously up to 36 hpf (Lee et al., 2004); transcript levels were found to be reduced in *ext2* mutants as measured by qPCR at 5 dpf (Wiweger et al., 2014). We used in situ hybridisation to examine the spatial expression pattern of *ext2* beyond 36 hpf (Supplementary Fig. S3). Expression of *ext2* was regionalised at 50 and 72 hpf, with highest levels in the brain and retina, spinal cord, pectoral fin and pharyngeal region, whereas expression in the somites, lens and heart was weaker or undetectable. Expression was present in both the ear and lateral line neuromasts. mRNA for *ext2* was still expressed in *ext2* mutants, but levels appeared slightly reduced throughout, including in the ear at 72 hpf (Supplementary Fig. S3).

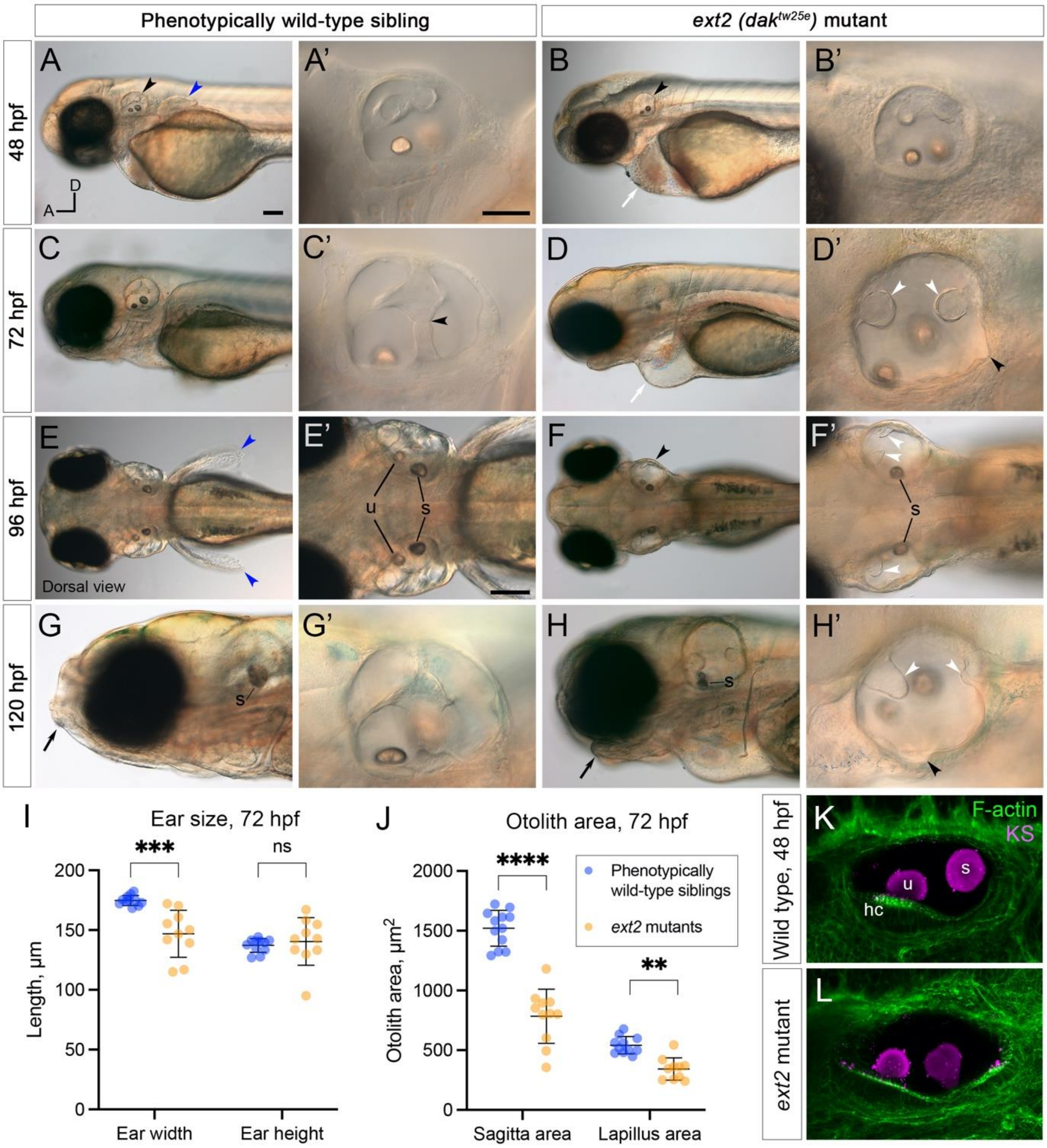

Figure 2. Morphological defects in the inner ear of *ext2* mutant embryos

(A–H') Live DIC images of phenotypically wild-type sibling and *ext2* homozygous mutant embryos at 48–120 hpf. The otic vesicle (enlarged in the second and fourth columns) is marked with a black arrowhead in A,B,F. Note the absence of the pectoral fin bud (A,E, blue arrowheads in wild type), cardiac oedema (B,D, white arrows), and abnormal jaw (G,H, black arrows) in the mutant. At 72 hpf, epithelial projections have fused and formed pillars in the wild-type ear (black arrowhead in C' marks the fusion plate of the ventral pillar), whereas in the *ext2* mutant ear, the projections stayed small and often did not fuse (white arrowheads, D',F',H'). Black arrowheads in D' and H' mark abnormal out-pocketings of the epithelium. Scale bars: A, 100 µm (also applies to B,C,D,E,F,G,H); A', 50 µm (also applies to B’,C’,D’,G’,H’); E’, 100 µm (also applies to F’). All panels are lateral views with anterior to the left (orientation shown in A: A, anterior; D, dorsal), apart from E–F’ (dorsal views, anterior to the left). **(I, J)** Morphometric measurements of ear width and height (I), and otolith area (J), traced from micrographs at 72 hpf (N=6 embryos, n=12 ears of each genotype (some data points missing)). See Supplementary Figure S2 for details. Horizontal bars show mean +/- standard deviation. Two-way ANOVA (mixed-effects model) with Šídák’s correction for multiple comparisons: ns, not significant; $^{**}p$=0.0082; $^{***}p$=0.0008; $^{****}p<0.0001$. **(K, L)** Ears at 48 hpf, stained with Alexa phalloidin (green) and an antibody to keratan sulphate (magenta). Abbreviations: hc, hair cells in the utricular macula; s, saccular otolith (sagitta); u, utricular otolith (lapillus).

Expression of *vcanb* and *chsy1* mRNA persists abnormally in the unfused epithelial projections of the *ext2* mutant ear

We next tested the expression of *versican b* (*vcanb*) and *chondroitin synthase 1* (*chsy1*) mRNA in the wild-type and *ext2* mutant ear. Expression of *vcanb* in the wild-type ear is very similar to that of *vcana* (Geng et al., 2013), with high levels of expression in the epithelial projections as they evaginate and grow out into the lumen of the ear, becoming rapidly down-regulated after fusion to form a pillar (Fig. 3A,C,E). Expression remains in the dorsolateral septum of the wild-type ear at 72 hpf (Fig. 3C,C’), more weakly at 5 dpf (Fig. 3E). Expression in the *ext2* mutants showed some striking differences to the wild-type pattern. At 48 hpf, otic *vcanb* mRNA expression levels were lower in all *ext2* mutants tested (26/26) (Fig. 3B). However, by 72 hpf, *vcanb* expression in the unfused epithelial projections was abnormally high, and persisted until at least 5 dpf (Fig. 3D,D’,F). Mutants can easily be distinguished by their lack of pectoral fins, normally a strong site of *vcanb* expression at 50 hpf (Fig. 3A,B). Expression of *vcanb* in the periderm of the second arch (epidermis of the developing operculum) was also considerably reduced in *ext2* mutants (Fig. 3C,D). The *chsy1* transcript, known to be expressed in the outgrowing projections of the wild-type ear (Li et al., 2010), was also mildly up-regulated in the unfused projections of the *ext2* mutant ear at 72 hpf, although overall levels in the brain of *ext2* mutants were slightly lower than in the wild type (Fig. 3G,H).

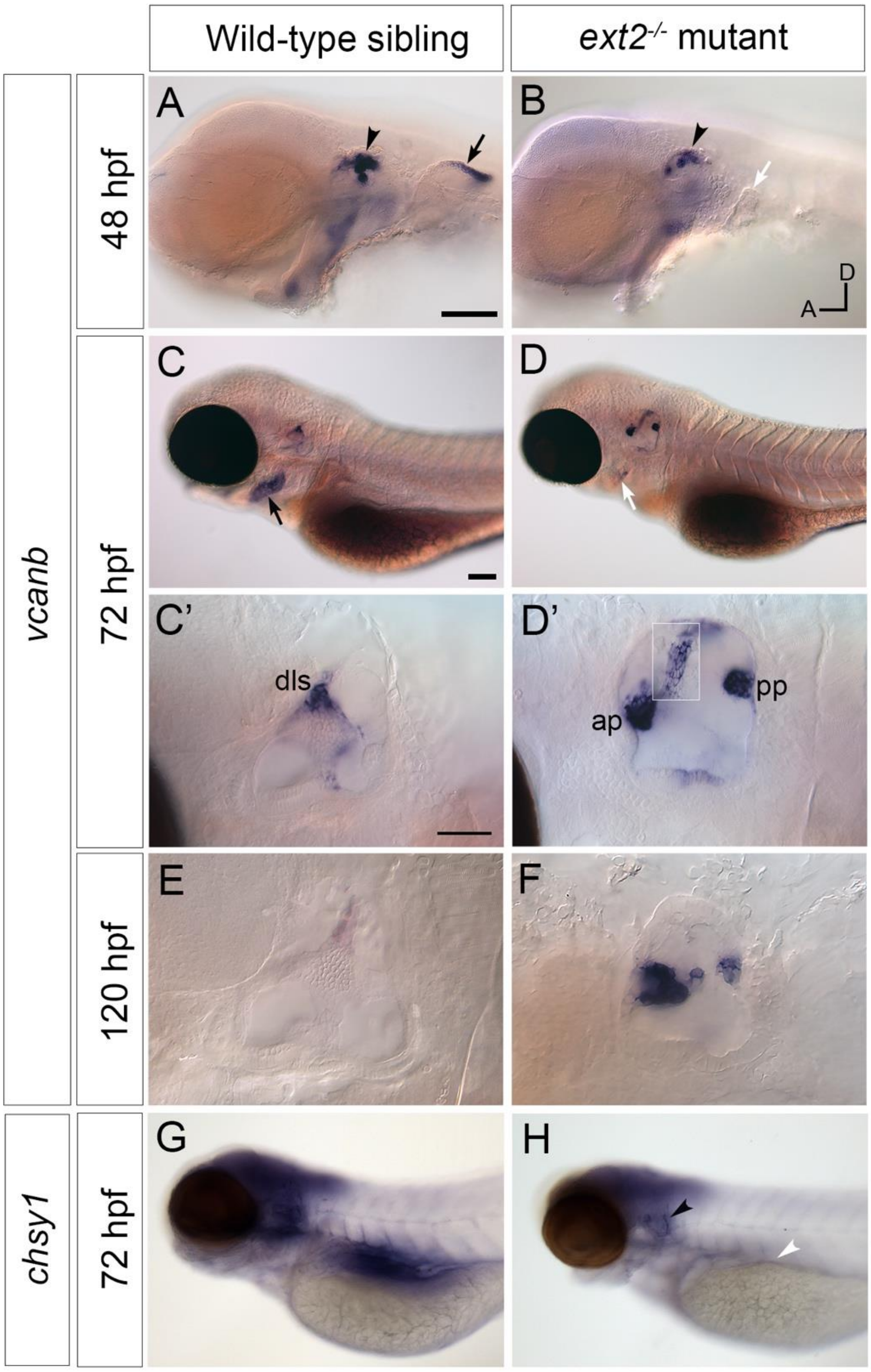

Figure 3. Expression of *vcanb* and *chsy1* in the *ext2* mutant ear

(A–H) In situ hybridisation to *vcanb* (A–F) and *chsy1* (G,H) mRNA in phenotypically wild-type sibling and *ext2* mutant embryos. **(A)** Expression of *vcanb* is present in the ear (black arrowhead) and pectoral fin (black arrow) in sibling embryos. **(B)** Only a rudimentary pectoral fin bud is present in the *ext2* mutant, and the associated *vcanb* staining is missing (white arrow). **(C,D)** At 72 hpf, *vcanb* expression is strongly reduced in the periderm of the second arch (future operculum) in *ext2* mutants (black arrow in C, white arrow in D). **(C',D')** Enlargements of the ears shown in C and D, respectively. Expression of *vcanb* is now down-regulated in the pillars of the wild-type ear, remaining only in the dorsolateral septum (dls). In the *ext2* mutant, expression persists abnormally in the unfused anterior and posterior projections (ap, pp, D') and in an abnormal pillar-like structure (boxed insert of same ear taken at a different focal plane). **(E,F)** *vcanb* expression persists abnormally in the unfused projections in mutant ears until at least 120 hpf. **(G,H)** Overall levels of *chsy1* expression are slightly reduced in *ext2* mutants (H); expression is missing in the viscera (white arrowhead), but persists in unfused epithelial projections in the ear (black arrowhead). All panels are lateral views with anterior to the left, dorsal to the top (orientation shown in B: A, anterior; D, dorsal). Scale bars: in A, 100 μm (also applied to B); in C, 100 μm (also applies to D,G,H); in C', 50 μm (also applies to D').

The pattern of chondroitin sulphate staining is altered, but hyaluronan is still present, in the *ext2* mutant ear

Overall levels of chondroitin sulphate (CS) were previously found to be normal in zebrafish *ext2* mutants at 6 dpf by reverse-phase ion-pair high-performance liquid chromatography (Holmborn et al., 2012). We used antibody staining to examine the spatial pattern of chondroitin sulphate (CS) in *ext2* mutant ears (Fig. 4; Supplementary Movies 2,4). The apical staining seen in phenotypically wild-type sibling ears at 40–45 hpf was not present in the mutant, even at later stages (Fig. 4A–B'). Basal staining prefiguring projection outgrowth was delayed relative to that in the wild type, but otherwise appeared normal (Fig. 4C–F'). At 48 hpf, a discrete patch of CS staining was found directly posterior to the anterior (utricular) macula in both wild-type and mutant embryos, marking the site of emergence of the ventral projection. In the example shown in Fig. 4F', staining was specifically localised to the basal side of the cells that have just started to evaginate and move into the otic lumen. By 65 hpf, little CS signal remained in the acellular cores of the semicircular canal pillars in the wild-type ear (Fig. 4G,G'; Supplementary Movie 3). By contrast, CS staining in the *ext2* mutant ear, like expression of *vcanb,* persisted abnormally and strongly in the unfused epithelial projections (Fig. 4H, H', Supplementary Movie 4). Staining for CS indicated that an otolithic membrane was present in the *ext2* mutant, although staining at 65 hpf was reduced compared with that in the wild type, possibly indicating a thinner membrane (Fig. 4G–H', blue asterisks; Supplementary Movies 3,4).

To test whether hyaluronan (HA) is produced in the *ext2* mutant ear, we stained embryos for the expression of *ugdh*, a gene required for the production of HA, and with a biotinylated hyaluronic acid binding protein (HABP). Expression of *ugdh* was present, but reduced in levels, throughout the head of *ext2* mutant embryos, including in the ear (Supplementary Fig. S4). Staining with HABP indicated that HA was still present in the cores of the unfused epithelial projections of the *ext2* mutant ear (Supplementary Fig. S5).

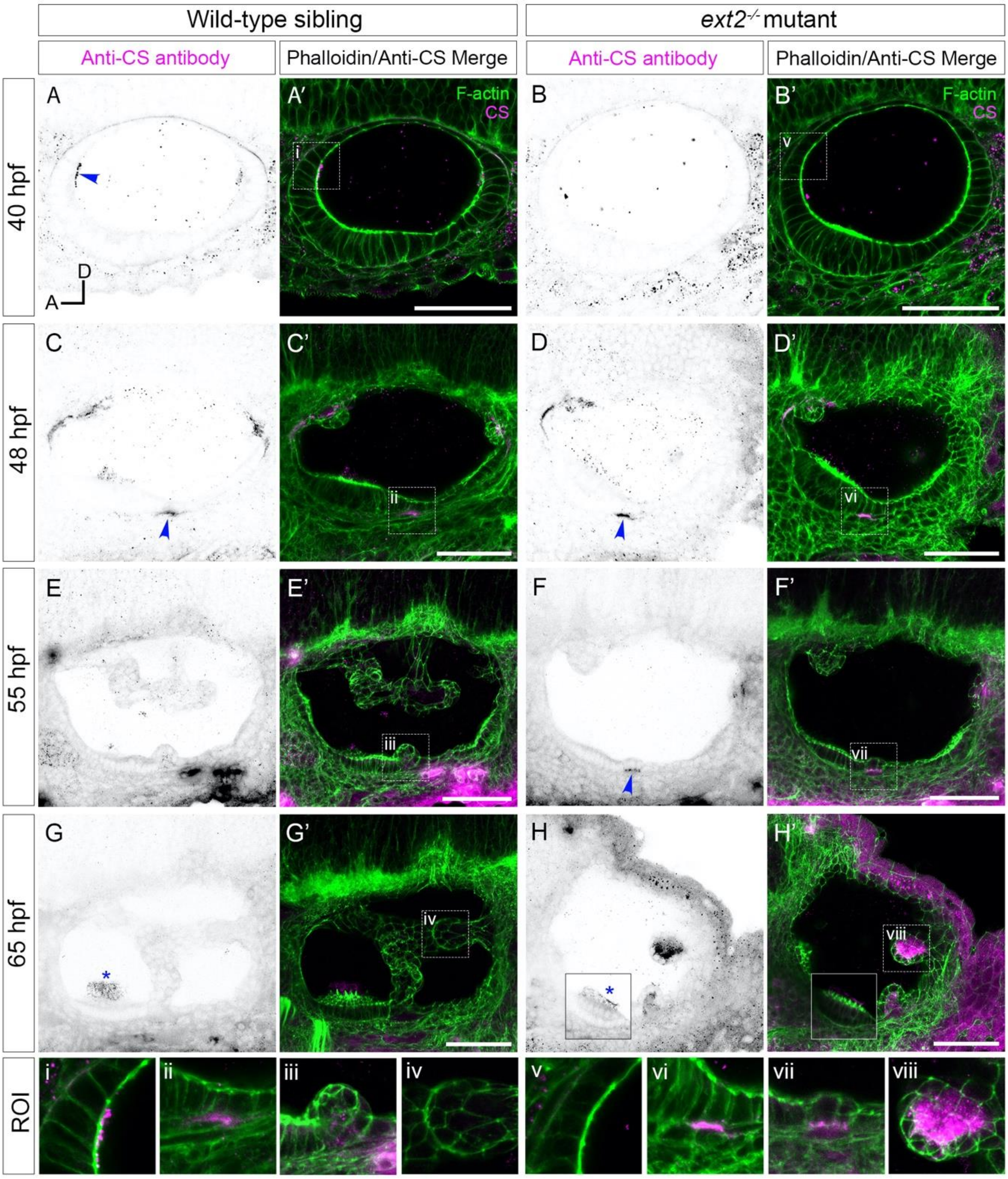

Figure 4. Staining for chondroitin sulphate in the *ext2* mutant ear is delayed at early stages, but accumulates abnormally in unfused epithelial projections by 65 hpf

(A–H') Confocal images of Alexa-phalloidin (green) and anti-CS antibody (magenta) whole-mount stains of phenotypically wild-type sibling and *ext2* mutant ears (see Materials and Methods). Blue arrowheads mark foci of chondroitin sulphate (CS) staining associated with the emergence (evagination) of epithelial projections from the otic epithelium; blue asterisks mark staining in the otolithic membrane overlying hair cells of the anterior (utricular) macula. Boxed areas highlight regions of interest (ROI), enlarged in the bottom row of panels: (i, v), apical focus of CS staining at 40 hpf, absent in the *ext2* mutant, prefiguring site of emergence of the anterior projection in the wild-type ear; (ii, vi), foci of CS staining associated with the ventral projection at 48 hpf; (iii, vii), CS staining in the emerging ventral projection, delayed in the *ext2* mutant; (iv, viii) no detectable staining in the wild-type posterior projection (iv) contrasts with strong staining in the unfused posterior projection in the *ext2* mutant. The boxed area in the lower left of H, H’ is taken from a different focal plane in the stack to show the anterior (utricular) macula and otolithic membrane. All images are maximum intensity projections (MIPs) of between 3 and 10 selected *z*-slices, with the exception of the images at 40 hpf, which are single *z*-slices. All images are lateral views with anterior to left and dorsal to top (orientation shown in A: A, anterior; D, dorsal). Scale bars, 50 µm. Abbreviation: CS, chondroitin sulphate.

Otoliths in the *ext2* mutant ear are not tethered correctly to the saccular macula

The posterior otolith (sagitta) frequently appeared misplaced in *ext2* mutants between 72 hpf and 5 dpf (Figure 2G,H), indicating defective tethering to its cognate sensory patch (the saccular macula). To investigate further, we performed a simple experiment to test whether the otolith could become dislodged after tapping the slide on which the fish was mounted (see Methods). Images of the ears were taken before and after tapping (Fig. 5). In wild-type ears, all saccular otoliths (sagittae) remained in place after tapping (*N*=8 embryos, *n*=16 otoliths), whereas in 7 out of 8 *ext2* mutant embryos, one or both sagittae were displaced (Fig. 5). Unlike the sagitta, the anterior otolith (lapillus) did not appear misplaced in any of the mutant embryos after tapping (*N*=8 mutant embryos).

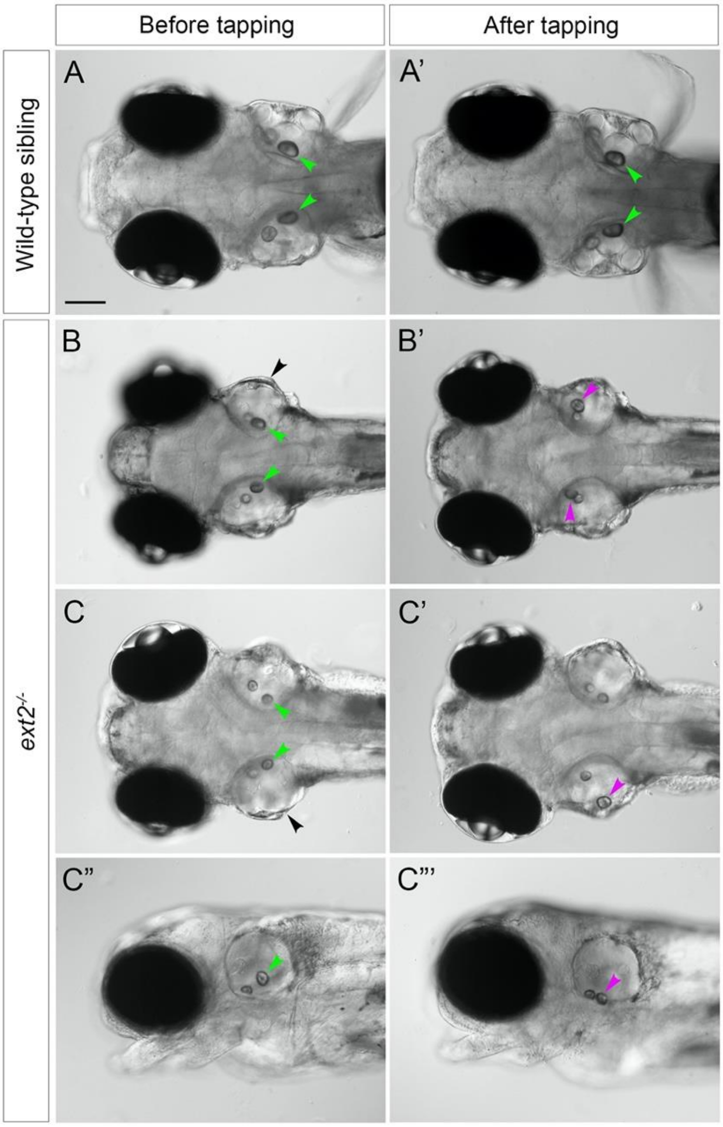

Figure 5. Saccular otoliths are not tethered correctly in the homozygous *ext2* mutant ear at 5 dpf

(A–C"') Live DIC images of embryos at 5 dpf, before (left-hand column) and after (right-hand column) tapping. In phenotypically wild-type sibling embryos (A,A'), saccular otoliths (green arrowheads) remain in place after tapping (in this example, one of the utricular otoliths in A' has become slightly displaced). In *ext2* mutant embryos (B–C'''), the saccular otolith in one or both ears becomes displaced (magenta arrowheads show new position after tapping). A–C' are dorsal views with anterior to the left; C",C"' are lateral views of the embryo shown in C,C'. Note also the swollen ear morphology in the *ext2* mutants (B,C, black arrowheads). In all panels, anterior is to the left. Scale bar in A, 100 µm (applies to all panels).

Genes involved in otolith formation and tethering show reduced expression in the *ext2* mutant ear

To test whether the otolith size and tethering defects reflect changes in the expression of genes coding for otolith matrix or otolithic membrane components, we examined the expression of selected markers using in situ hybridisation (Fig. 6). Expression of *otolith matrix protein* (*otomp*) mRNA was significantly reduced in both the anterior and the posterior maculae in *ext2*$^{-/-}$ mutants (Figure 6A–B’). Expression of *starmaker* (*stm*) was present in both maculae in *ext2* mutants, with levels slightly reduced in the posterior (saccular) macula (Fig. 6H,H’). We also analysed the expression of mRNA for *otogelin* (*otog*) and *alpha-tectorin* (*tecta*). Expression of *otog* was significantly reduced in the anterior (utricular) macula of *ext2* mutants at 24 hpf, and was absent from the posterior (saccular) macula from 72–120 hpf (Fig. 6C–F’). Expression of *otog* in the three sensory cristae was also reduced in *ext2* mutants (Fig. 6E,E’). However, expression of *tecta* mRNA appeared normal in the *ext2* mutant ear (Fig. 6G–G’).

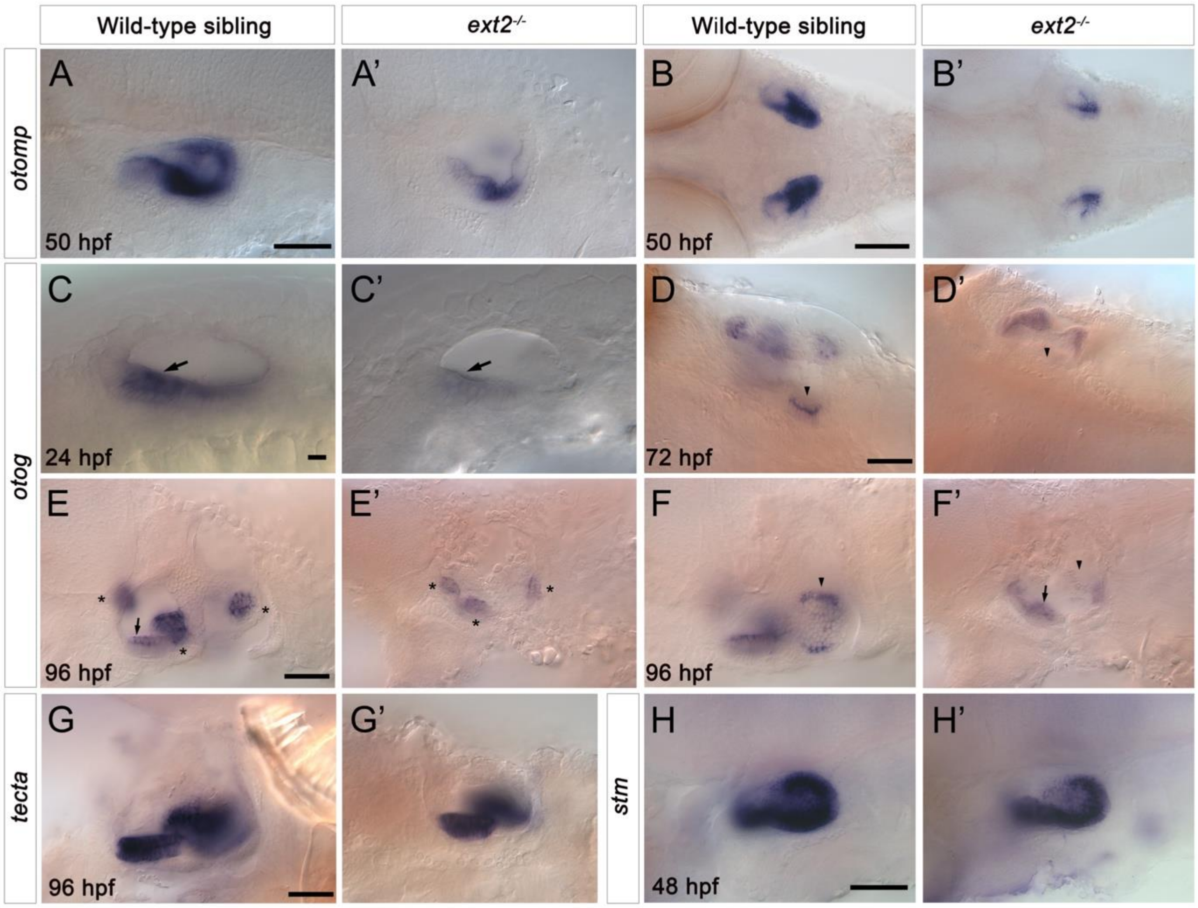

Figure 6. Expression of *otomp*, *otog* and *stm* is reduced in the saccular macula of the *ext2*$^{-/-}$ mutant ear

(A–H') In situ hybridisation to otolith marker genes in the ears of phenotypically wild-type sibling and *ext2* mutant embryos. **(A–B')** Levels of *otomp* expression in the *ext2* mutant ear (A',B') at 50 hpf were reduced compared with the wild type (A,B). **(C–F')** Expression of *otog* at 24 hpf (C,C'), 72 hpf (D,D') and 96 hpf (E-F') was significantly reduced in the *ext2* mutant ear. The images in F and F' show a more medial focal plane of the same ears depicted in E and E', respectively. **(G,G')** Expression of *tecta* in the *ext2* mutant ear was unaltered at 96 hpf. **(H,H')** Expression of *stm* expression at 48 hpf was reduced in the posterior macula of the *ext2* mutant ear. Arrowheads mark the posterior (saccular) macula; arrows mark the anterior (utricular) macula; asterisks mark the cristae. All images are lateral views with anterior to the left, apart from B,B',D,D' (dorsal views with anterior to the left). In all panels, anterior is to the left. Scale bars: in A, 50 μm for A'; in B, 100 μm for B'; in C, 10 μm for C'; in D, 50 μm for D'; in E, 50 μm for E'-F'; in G, 50 μm for G'; in H, 50 μm for H'.

Discussion

Presence of chondroitin sulphate marks initial sites of evagination of the otic epithelium

An unsolved question in zebrafish semicircular canal duct morphogenesis is what establishes the site of evagination of each of the epithelial projections, where a small number of cells start to move towards the lumen of the ear, involving a localised inversion of curvature of the epithelial sheet. To begin to answer this, our results identify the earliest signs of projection outgrowth: exquisitely localised patches of CS staining marking the sites where the epithelium will deform, present before any obvious morphological changes. These observations corroborate the finding that *chsy1*, which codes for the enzyme Chondroitin synthase 1, is expressed in the epithelial projections of the ear, and is required for their normal morphogenesis (Li et al., 2010). A similar transient and spatially restricted pattern of CS staining has been observed in the developing zebrafish heart, where it is required for normal atrioventricular canal formation (Peal et al., 2009). In the ear, CS staining was absent from cells forming the endolymphatic duct (ED), a tube that invaginates from dorsal otic epithelium. Unlike the evaginating epithelial projections, formation of the ED does not require any inversion of epithelial curvature. ED cells show apical constriction (Swinburne et al., 2018), and differ significantly in shape from those of the epithelial projections (Mendonca et al., 2021). Thus, the presence or absence of CS distinguishes between deformations of the epithelium with opposite orientations in the zebrafish ear; it will be interesting to see whether this is a general principle.

Growth of the epithelial projections in the zebrafish ear requires both hyaluronan and proteoglycans: proposal for a hyaluronan-proteoglycan-driven mechanism

Numerous lines of evidence support a model in which the synthesis of the non-sulphated GAG hyaluronan (HA), a giant linear polysaccharide of several million Daltons (Toole, 2001), acts to propel the epithelial projections into the lumen of the anamniote inner ear. Local enzymatic digestion of HA, or a systemic block to HA biosynthesis, results in rudimentary epithelial projections that fail to meet and fuse (Busch-Nentwich et al., 2004; Geng et al., 2013; Haddon and Lewis, 1991; Munjal et al., 2021). However, the similar otic phenotypes in zebrafish morphants for *chsy1* (Li et al., 2010) and mutants for *ext2* (this work) demonstrate that synthesis of chondroitin sulphate (CS) and heparan sulphate (HS), respectively, are also critical for normal epithelial projection outgrowth. As HA is still present in *ext2* mutant ears, this argues that HA alone is not sufficient for normal epithelial projection outgrowth, and that CSPGs and

HSPGs are likely to play a role. In addition, ECM proteins expressed in the projections, such as the Type II collagens (Geng et al., 2013), might also contribute to projection outgrowth.

One of the remarkable aspects of semicircular canal morphogenesis in the zebrafish or *Xenopus* ear is the finger-like nature of the evaginating epithelial protrusions or projections, differing markedly from the walls of the flattened out-pocketings or pouches of the otic epithelium that form in the amniote ear (Alsina and Whitfield, 2017). In the mouse, reciprocal signalling between otic epithelium and periotic mesenchyme, resulting in mesenchymal cell proliferation, is thought to be required to drive the epithelial walls of the pouches together to meet at a fusion plate (Pirvola et al., 2004; Salminen et al., 2000). By contrast, the epithelial projections in zebrafish are not underlain by mesenchyme as they grow into the otic lumen; instead, each projection has an acellular (matrix-filled) core. With only three or four cells at their tip (Waterman and Bell, 1984), these projections represent a highly anisotropic mode of growth. Haddon and Lewis recognised that HA must not only be synthesised locally but also be held in place in order to generate localised outgrowth (Haddon and Lewis, 1991). Munjal and colleagues have extended this model, proposing that differential tissue stiffness, mediated by tensioned cell tethers, in combination with isotropic pressure from HA, acts to shape the projections (Munjal et al., 2021).

It is also possible that aggregation of proteoglycans and HA could generate a local expansion of the ECM beneath cells of the projection. HSPGs and CSPGs bind to HA via hyaluronan-proteoglycan link proteins (Haplns), generating large charged aggregates (Toole, 2001). The Hapln genes *hapln1a* and *hapln3* are expressed in the epithelial projections of the zebrafish ear (Geng et al., 2013). Addition of proteoglycans is sufficient to cause the ‘drastic swelling’ of HA films in vitro, where linear HA chains, normally present in a random coil configuration, become stretched on incorporation of relatively small quantities of proteoglycan (Attili and Richter, 2013; Chang et al., 2016; Richter et al., 2018). There are interesting parallels with the Hapln1a-dependent left-sided expansion of the cardiac ECM that occurs in the developing zebrafish heart prior to looping (Derrick et al., 2021). In the ear, anisotropy of the matrix in the projection cores, mediated by the stretching of HA chains driven by localised incorporation of proteoglycan, or alignment of other fibrillar components such as collagen, could help to direct projection outgrowth: this idea remains to be tested. The sulphation of HSPGs and CSPGs also confers a strong negative charge, important for hydration of the matrix. Diversity in the proteoglycan sulphation pattern, mediated by the enzymes coded for by *sulf* genes, some of which are expressed in the zebrafish ear (Gorsi et al., 2010; Habicher et al., 2015; Meyers et al., 2013), might provide further local heterogeneity in the mechanical properties of the otic ECM.

Implications for cell signalling in the developing ear

As in other species, zebrafish proteoglycans play an important role in the correct function of various signalling pathways, including Fgf, BMP and Wnt (Fischer et al., 2011; Li et al., 2010; Meyers et al., 2013; Norton et al., 2005; Venero Galanternik et al., 2015). Although this was not the focus of our study, it is likely that disrupted signalling also contributes to the morphogenetic and patterning defects in the *ext2* mutant ear. Expression of *fgf8a* in the utricular macula appears relatively normal in the ears of *ext2*^{tw25e} mutants at 48 hpf, but the Fgf target gene *etv5b* is down-regulated in various tissues, including the otic vesicle (Fischer et al., 2011). By contrast, expression of the Fgf target gene *pea3* appeared unchanged in the ear in *ext2* mutants or by treatment with SU5402 alone, but was strongly down-regulated in SU5402-treated *ext2* mutants (Fischer et al., 2011). A detailed comparison of otic phenotypes will be important to reveal any similarities between the ears of *ext2* mutants and those with disrupted Fgf, BMP or Wnt signalling.

Development and tethering of otoliths in the *ext2* mutant ear

In addition to semicircular canal defects, the *ext2* mutant ear has otolith size and tethering abnormalities. Morpholino-mediated knockdown of *otomp* has been linked to slowed otolith growth (Murayama et al., 2005), and *otomp* expression is reduced in *ext2* mutant ears. Although otoliths were small in the *ext2* mutant, they stained for keratan sulphate (KS) as in the wild type. Keratan sulphate proteoglycans (KSPGs) are well-known constituents of amniote otoconia (Lundberg et al., 2015). In the chicken, alpha-Tectorin, a major glycoprotein constituent of the tectorial membrane, has characteristics of a ‘light’ KSPG (Killick and Richardson, 1997), and KS on alpha-Tectorin might account for the otolithic membrane KS staining seen in the zebrafish. In zebrafish, Otogelin and alpha-Tectorin, respectively, establish and maintain otolith adhesion to the macula during otolith growth and biomineralisation (Stooke-Vaughan et al., 2015). A loss of adhesion of the sagitta (saccular otolith) in *ext2* mutants might be attributed to the lack of *otogelin* expression in the saccular macula. However, the early *ext2* mutant phenotype does not resemble that of the *otogelin* mutant, where only one otolith forms in each mutant ear (Stooke-Vaughan et al., 2015). Instead, the loss of saccular otolith tethering in the *ext2* mutant is more reminiscent of the mutant phenotype for *tecta*, where the sagittae can become dislodged between 3 dpf and 5 dpf, but the lapilli (utricular otoliths) are unaffected (Stooke-Vaughan et al., 2015). *tecta* mRNA is expressed normally in the *ext2* mutant ear, and so it is not possible to attribute the otolith tethering defect to a loss of alpha-Tectorin. However, the *ext2* mutant phenotype suggests that one or more HSPGs are required for formation of a normal otolithic membrane and for normal otolith tethering. Given the capacity of HS to interact with a large number of proteins (Vallet et al., 2022), HS-protein binding is likely to contribute to otolith tethering in the zebrafish ear.

Conclusion

In summary, our data show that the temporally- and spatially-restricted presence of CS marks the sites of epithelial projection outgrowth in the zebrafish ear. In addition, otic defects in the *ext2* mutant demonstrate that HS biosynthesis is essential for the evagination and growth of the epithelial projections, and for otolith tethering. These findings suggest that CSPGs and HSPGs, as well as HA, play important roles in semicircular canal duct morphogenesis, and are likely to impact both the mechanical and signalling properties of the otic epithelium.

Ethics statement

Zebrafish were maintained according to recommended guidelines (Aleström et al., 2020). All animal work was reviewed by the University of Sheffield Animal Welfare and Ethical Review Body (AWERB), and performed under licence from the UK Home Office (P66320E4E).

Acknowledgements

We thank Henry Roehl for providing the dak^{tw25e} zebrafish mutant line and the *ext2* cDNA, for sharing reagents, and for advice on expression patterns. We thank the Sheffield Aquarium Team for expert care of the fish, Nick van Hateren for help with imaging, and Sarah Burbridge and Mar Marzo for technical assistance.

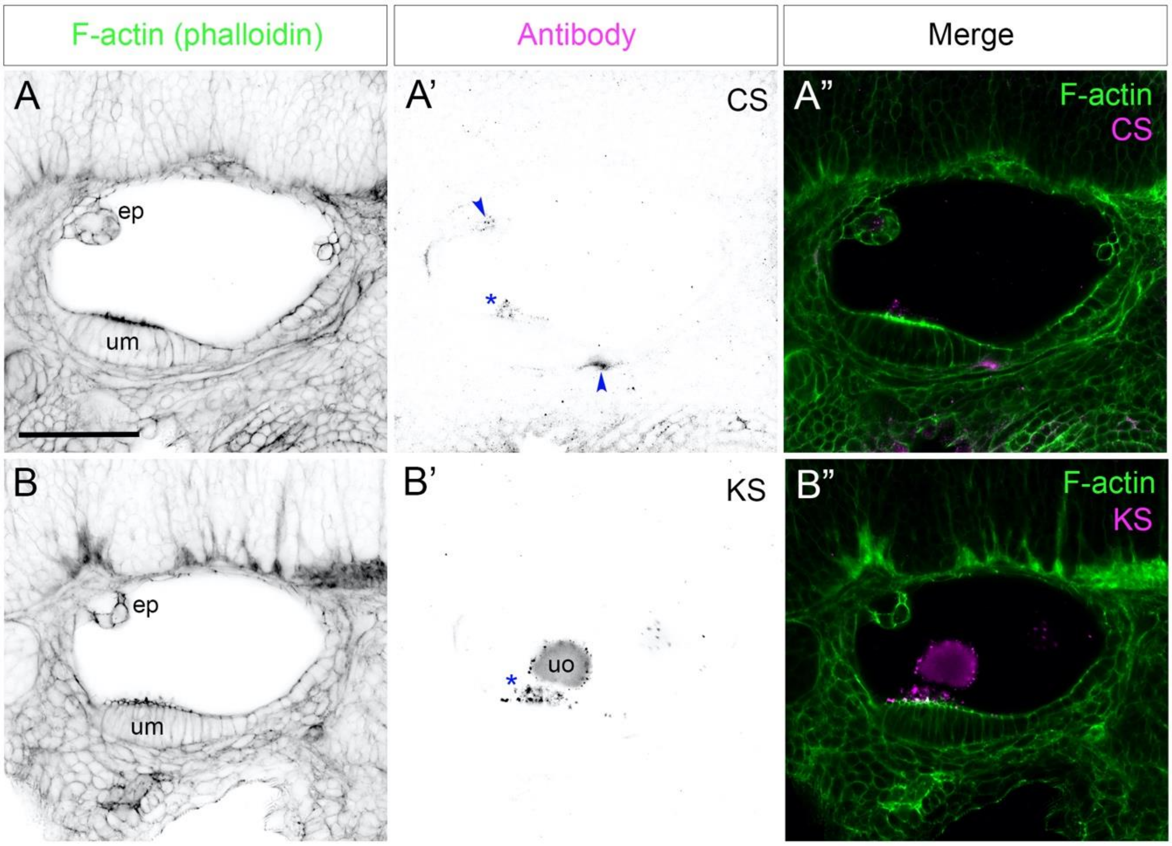

Supplementary Figure S1. Antibodies to chondroitin sulphate and keratan sulphate give distinct and reproducible staining patterns in the wild-type zebrafish ear

Antibody staining experiment from the same batch of embryos (phenotypically wild-type siblings from a cross between *ext2*$^{+/-}$ heterozygous parents), performed under the same conditions, with the same secondary antibody. **(A–A")** Phalloidin stain for F-actin (A) and antibody stain for chondroitin sulphate (A') at 48 hpf. Arrowheads mark small patches of stain associated with the outgrowing anterior epithelial projection (ep) and on the basal side of the epithelium where the ventral projection will emerge. **(B–B")** Phalloidin stain for F-actin (B) and antibody stain for keratan sulphate (B') at 48 hpf. Both antibodies mark the otolithic membrane (asterisk). Lateral views; anterior to the left, dorsal to the top. Abbreviations: CS, chondroitin sulphate; ep, anterior epithelial projection; KS, keratan sulphate; um, utricular macula; uo, utricular otolith. Scale bar in A, 50 µm (applies to all panels).

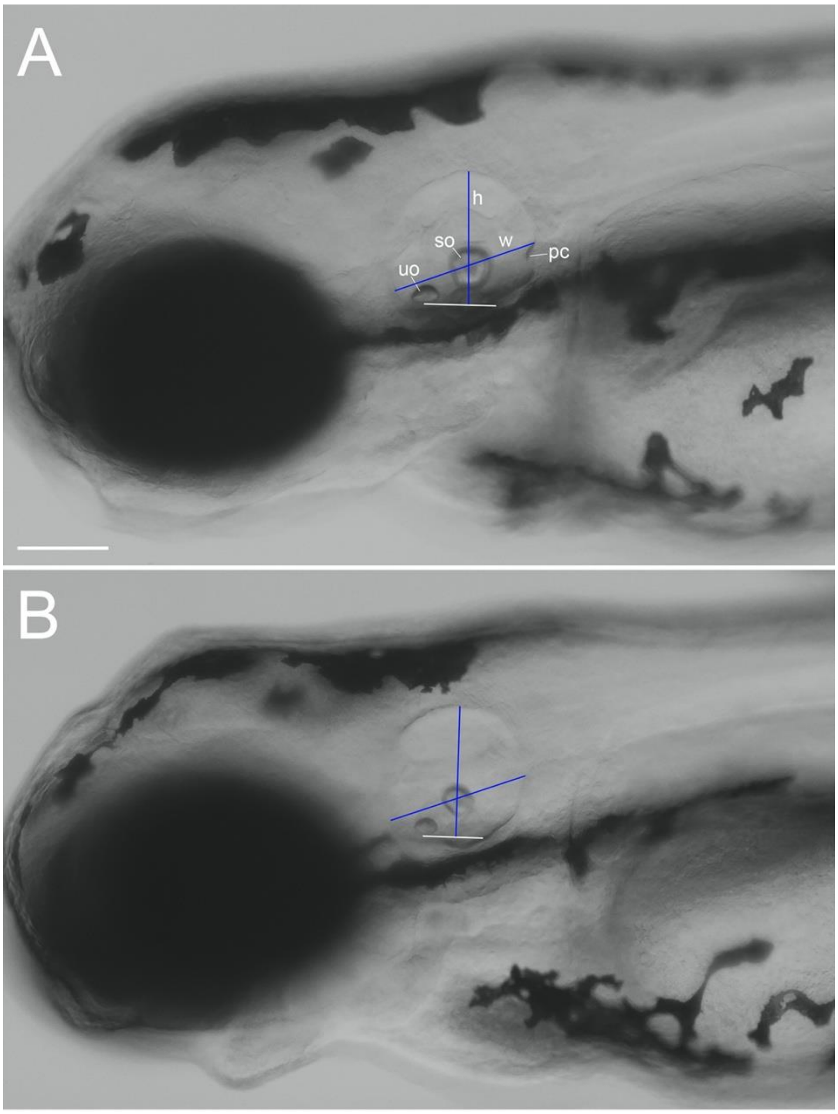

Supplementary Figure S2. Morphometric measurements of ear and otolith size in *ext2* mutants

Head of a phenotypically wild-type sibling embryo **(A)** and *ext2* homozygous mutant **(B)** at 72 hpf. Blue lines show measurements taken in Fiji of ear width (w) from the dorsal side of the posterior crista (pc), through the saccular otolith (so, sagitta) to the anterior of the ear. Ear height (h) was measured from a position level with the ventral side of the utricular otolith (uo; lapillus), shown by the horizontal white line, to the dorsal-most point of the ear. Otolith areas were traced from the same images in Fiji. Lateral views; anterior to the left. Scale bar in A, 100 µm.

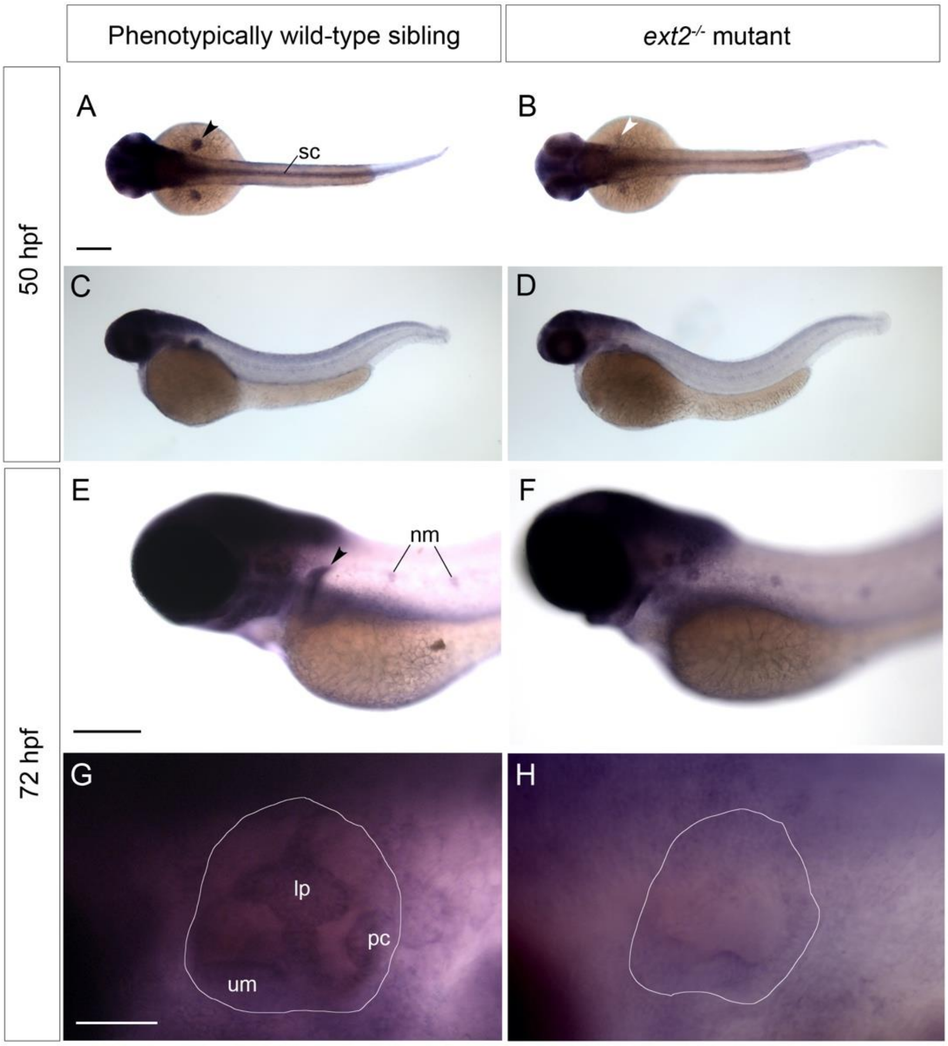

Supplementary Figure S3. Expression of *ext2* in wild-type and *ext2* mutant embryos at 50 and 72 hpf

(A–H) In situ hybridisation to *ext2* in phenotypically wild-type sibling and *ext2* mutant embryos at 50 and 72 hpf. Expression in the wild type (A,C,E,G) was regionalised by 50 hpf, with highest levels in the head and brain, pectoral fin buds (black arrowheads), spinal cord (sc) and posterior lateral line neuromasts (nm), and lower expression in the heart and somites. In *ext2* mutants (B,D,F,H), expression was present in a normal spatial pattern, but at reduced levels. Note reduced expression in the rudimentary fin buds at 50 hpf (B, white arrowhead). (G,H) Detailed view of the otic vesicle (outlined) at 72 hpf shows reduced expression of *ext2* in the *ext2* mutant ear. A,B, dorsal views; C–H, lateral views; all images are anterior to the left. Abbreviations: lp, lateral projection; nm, posterior lateral line neuromast; pc, posterior crista; um, utricular (anterior) macula. Scale bar in A, 200 µm (applies to A–D); in E, 200 µm (applies to E,F); in G, 50 µm (applies to G,H).

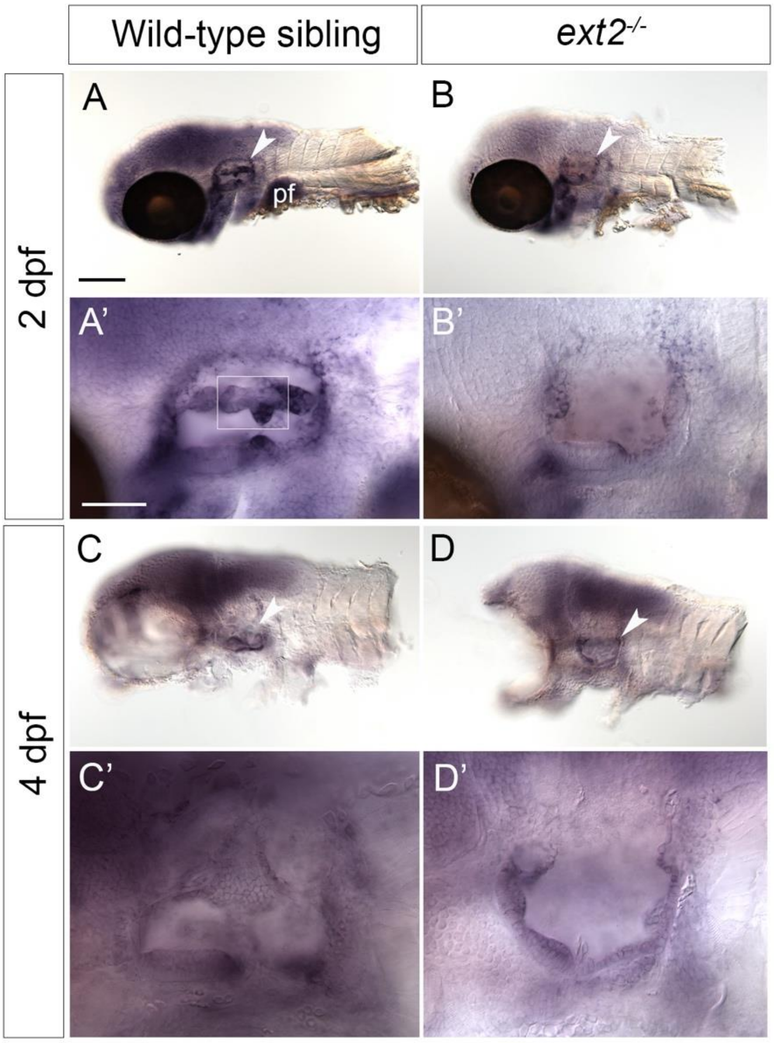

Supplementary Figure S4. Expression of *ugdh* is present, but reduced, in *ext2* mutant embryos, including in the ear

(A–D') In situ hybridisation to *ugdh* in phenotypically wild-type sibling and *ext2* mutant embryos. In wild-type embryos (A,C), expression is present throughout the brain, pectoral fin (pf) and in the ear (arrowhead; enlarged in A',C'). The box in A' is an overlay from a different focal plane to the main image, to show strong expression in the epithelial projections, including the ventral bulge from the lateral projection. In the *ext2* mutant (B,D), expression is present in a similar spatial pattern but levels appear reduced throughout, including in the ear (arrowhead; enlarged in B',D'). The eyes have been removed in C and D for ease of mounting. All images are lateral views with anterior to the left. Scale bar in A, 200 µm (applies to A–D); scale bar in A', 50 µm (applies to A'–D').

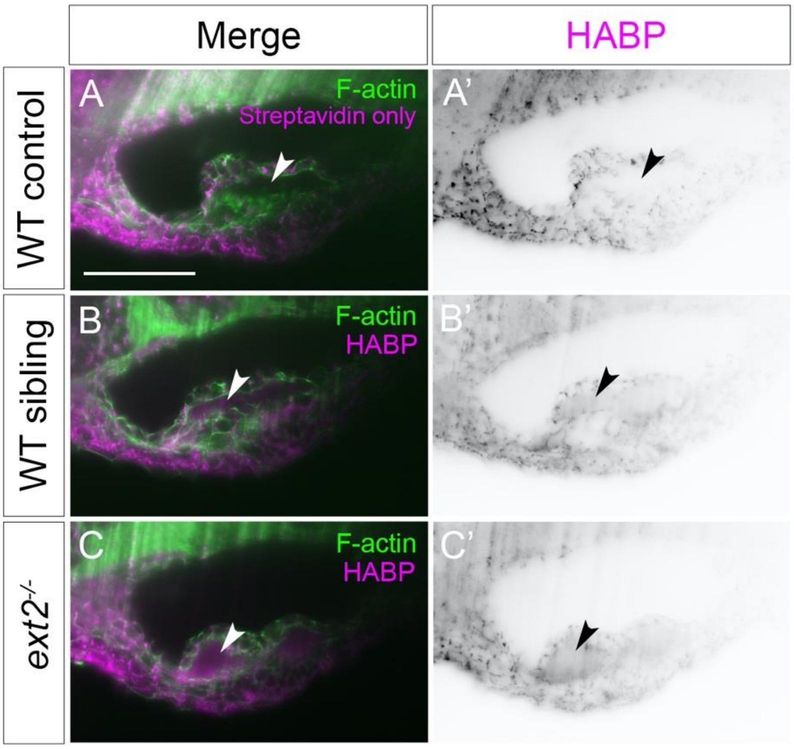

Supplementary Figure S5. HA is still present in the lateral projection of the *ext2* mutant ear

(A–C') Light-sheet fluorescence images of the lateral projection at 48 hpf. **(A, A')** Control sample (wild type, streptavidin only; no HABP). Non-specific background staining was present on the skin of control samples, but levels of fluorescence in the core of the lateral projection (arrowhead) were low. **(B–C')** In phenotypically wild-type sibling embryos (B,B') and in *ext2* mutants (C,C'), staining was present in the core of the lateral projection (arrowheads), highlighted in the single channel images (HABP, inverted grayscale). Dorsal views; anterior to the left. Scale bar in A, 50 µm (applies to all panels).

Supplementary Movie 1. Chondroitin sulphate staining in the wild-type ear at 48 hpf

A series of *z*-slices through a phenotypically wild-type sibling ear at 48 hpf stained with anti-chondroitin sulphate (magenta) and Alexa phalloidin for F-actin (green). Lateral view with anterior to the left; the movie plays from lateral to medial. The epidermis over the ear is strongly positive for CS. CS staining is present in the posterior bulge of the lateral projection and in a patch or streak beneath ventral otic epithelium. Weak staining in the cores of the anterior and lateral projections is visible towards the end of the movie. Note the lack of CS staining in the endolymphatic duct. Scale bar, 50 µm.

Supplementary Movie 2. Chondroitin sulphate staining in the *ext2* mutant ear at 48 hpf

A series of *z*-slices through an *ext2* mutant ear at 48 hpf stained with anti-chondroitin sulphate (magenta) and Alexa phalloidin for F-actin (green). The epidermis over the ear is strongly positive for CS. Strong CS staining is evident in the posterior bulge of the lateral projection, together with a discrete patch beneath ventral otic epithelium. Lateral view with anterior to the left; the movie plays from lateral to medial. Scale bar, 50 µm.

Supplementary Movie 3. Chondroitin sulphate staining in the wild-type ear at 65 hpf

A series of *z*-slices through a phenotypically wild-type sibling ear at 65 hpf stained with anti-chondroitin sulphate (magenta) and Alexa phalloidin for F-actin (green). The epidermis over the ear is strongly positive for CS. The projections in the ear have now fused to form three pillars, and there is very little CS staining visible in the cores of the pillars or lateral projection at this stage. CS staining is present in the otolithic membrane overlying hair cells of the utricular (anterior) macula. Lateral view with anterior to the left; the movie plays from lateral to medial. Scale bar, 50 µm.

Supplementary Movie 4. Chondroitin sulphate staining in the *ext2* mutant ear at 65 hpf

A series of *z*-slices through an *ext2* mutant ear at 65 hpf stained with anti-chondroitin sulphate (magenta) and Alexa phalloidin for F-actin (green). The epidermis over the ear is strongly positive for CS. The cores of the posterior bulge, posterior projection and unfused ventral projection are all strongly positive for CS. CS staining in the otolithic membrane is present, but weaker than in the wild type. Lateral view with anterior to the left; the movie plays from lateral to medial. Scale bar, 50 µm.

Supplementary Table 1. List of genes used to generate in situ hybridisation probes, with references of original characterisation

Gene	**ZFIN ID**	**Reference**
chsy1	ZDB-GENE-030131-3127	(Li et al., 2010)
ext2	ZDB-GENE-041124-3	(Söllner et al., 2003)
otog	ZDB-GENE-120228-1	(Stooke-Vaughan et al., 2015)
otomp	ZDB-GENE-040709-1	(Murayama et al., 2005)
stm	ZDB-GENE-031112-4	(Söllner et al., 2003)
tecta	ZDB-GENE-110411-120	(Stooke-Vaughan et al., 2015)
ugdh	ZDB-GENE-011022-1	(Busch-Nentwich et al., 2004)
vcanb (formerly *dermacan, cspg2b*)	ZDB-GENE-030131-2185	(Kang et al., 2004)

References

Aleström, P., D'Angelo, L., Midtlyng, P. J., Schorderet, D. F., Schulte-Merker, S., Sohm, F. and Warner, S. (2020). Zebrafish: Housing and husbandry recommendations. Lab Anim 54, 213–224.

Alsina, B. and Whitfield, T. T. (2017). Sculpting the labyrinth: Morphogenesis of the developing inner ear. Semin Cell Dev Biol 65, 47–59.

Attili, S. and Richter, R. P. (2013). Self-assembly and elasticity of hierarchical proteoglycan-hyaluronan brushes. Soft Matter 9, 10473–10483.

Bülow, H. E. and Hobert, O. (2006). The molecular diversity of glycosaminoglycans shapes animal development. Annu Rev Cell Dev Biol 22, 375–407.

Busch-Nentwich, E., Söllner, C., Roehl, H. and Nicolson, T. (2004). The deafness gene dfna5 is crucial for ugdh expression and HA production in the developing ear in zebrafish. Development 131, 943–951.

Chang, P. S., McLane, L. T., Fogg, R., Scrimgeour, J., Temenoff, J. S., Granqvist, A. and Curtis, J. E. (2016). Cell Surface Access Is Modulated by Tethered Bottlebrush Proteoglycans. Biophys J 110, 2739–2750.

Clément, A., Wiweger, M., von der Hardt, S., Rusch, M. A., Selleck, S. B., Chien, C.-B. and Roehl, H. H. (2008). Regulation of Zebrafish Skeletogenesis by ext2 / dackel and papst1 / pinscher. 4, e1000136.

Derrick, C. J., Sánchez-Posada, J., Hussein, F., Tessadori, F., Pollitt, E. J. G., Savage, A. M., Wilkinson, R. N., Chico, T. J., van Eeden, F. J., Bakkers, J., et al. (2021). Asymmetric Hapln1a drives regionalized cardiac ECM expansion and promotes heart morphogenesis in zebrafish development. Cardiovasc Res 1–15.

Filipek-Górniok, B., Holmborn, K., Haitina, T., Habicher, J., Oliveira, M. B., Hellgren, C., Eriksson, I., Kjellén, L., Kreuger, J. and Ledin, J. (2013). Expression of chondroitin/dermatan sulfate glycosyltransferases during early zebrafish development. Developmental Dynamics 242, 964–975.

Fischer, S., Filipek-Gorniok, B. and Ledin, J. (2011). Zebrafish Ext2 is necessary for Fgf and Wnt signaling, but not for Hh signaling.

Geng, F.-S., Abbas, L., Baxendale, S., Holdsworth, C. J., Swanson, A. G., Slanchev, K., Hammerschmidt, M., Topczewski, J. and Whitfield, T. T. (2013). Semicircular canal morphogenesis in the zebrafish inner ear requires the function of gpr126 (lauscher), an adhesion class G protein-coupled receptor gene. Development 140, 4362–4374.

Gorsi, B., Whelan, S. and Stringer, S. E. (2010). Dynamic Expression Patterns of 6-O Endosulfatases During Zebrafish Development Suggest a Subfunctionalisation Event for sulf2. 3312–3323.

Habicher, J., Haitina, T., Eriksson, I., Holmborn, K., Dierker, T., Ahlberg, P. E. and Ledin, J. (2015). Chondroitin/dermatan sulfate modification enzymes in zebrafish development. PLoS One 10, 1–18.

Häcker, U., Lin, X. and Perrimon, N. (1997). The Drosophila sugarless gene modulates Wingless signaling and encodes an enzyme involved in polysaccharide biosynthesis. Development 124, 3565–3573.

Haddon, C. M. and Lewis, J. H. (1991). Hyaluronan as a propellant for epithelial movement: The development of semicircular canals in the inner ear of Xenopus. Development 112, 541–550.

Haddon, C. and Lewis, J. (1996). Early ear development in the embryo of the zebrafish, Danio rerio. J Comp Neurol 365, 113–28.

Haffter, P., Granato, M., Brand, M., Mullins, M. C., Hammerschmidt, M., Kane, D. A., Odenthal, J., van Eeden, F., Jiang, Y.-J., Heisenberg, C. P., et al. (1996). The identification of genes with unique and essential functions in the development of the zebrafish, Danio rerio. Development 123, 1–36.

Holmborn, K., Habicher, J., Kasza, Z., Eriksson, A. S., Filipek-Gorniok, B., Gopal, S., Couchman, J. R., Ahlberg, P. E., Wiweger, M., Spillmann, D., et al. (2012). On the roles and regulation of chondroitin sulfate and heparan sulfate in zebrafish pharyngeal cartilage morphogenesis. Journal of Biological Chemistry 287, 33905–33916.

Kang, J. S., Oohashi, T., Kawakami, Y., Bekku, Y., Izpisúa Belmonte, J. C. and Ninomiya, Y. (2004). Characterization of dermacan, a novel zebrafish lectican gene, expressed in dermal bones. Mech Dev 121, 301–312.

Karlstrom, R. O., Trowe, T., Klostermann, S., Baier, H., Brand, M., Crawford, A. D., Grunewald, B., Haffter, P., Hoffmann, H., Meyer, S. U., et al. (1996). Zebrafish mutations affecting retinotectal axon pathfinding. Development 123, 427–438.

Killick, R. and Richardson, G. P. (1997). Antibodies to the sulphated, high molecular mass mouse tectorin stain hair bundles and the olfactory mucus layer. Hear Res 103, 131–141.

Kimmel, C. B., Ballard, W. W., Kimmel, S. R., Ullmann, B. and Schilling, T. F. (1995). Stages of embryonic development of the zebrafish. Developmental Dynamics 203, 253–310.

Lee, J. S., von der Hardt, S., Rusch, M. A., Stringer, S. E., Stickney, H. L., Talbot, W. S., Geisler, R., Nüsslein-Volhard, C., Selleck, S. B., Chien, C.-B., et al. (2004). Axon sorting in the optic tract requires HSPG synthesis by ext2 (dackel) and extl3 (boxer). Neuron 44, 947–960.

Li, Y., Laue, K., Temtamy, S., Aglan, M., Kotan, L. D., Yigit, G., Canan, H., Pawlik, B., Nürnberg, G., Wakeling, E. L., et al. (2010). Temtamy preaxial brachydactyly syndrome is caused by loss-of-function mutations in chondroitin synthase 1, a potential target of BMP signaling. Am J Hum Genet 87, 757–767.

Lister, J. A., Robertson, C. P., Lepage, T., Johnson, S. L. and Raible, D. W. (1999). nacre encodes a zebrafish microphthalmia-related protein that regulates neural-crest-derived pigment cell fate. Development 126, 3757–3767.

Lundberg, Y. W., Xu, Y., Thiessen, K. D. and Kramer, K. L. (2015). Mechanisms of Otoconia and Otolith Development. 239–253.

Mendonca, T., Jones, A. A., Pozo, J. M., Baxendale, S., Whitfield, T. T. and Frangi, A. F. (2021). Origami: Single-cell 3D shape dynamics oriented along the apico-basal axis of folding epithelia from fluorescence microscopy data. PLoS Comput Biol 17, e1009063.

Meyers, J. R., Planamento, J., Ebrom, P., Krulewitz, N., Wade, E. and Pownall, E. (2013). Sulf1 modulates BMP signaling and is required for somite morphogenesis and development of the horizontal myoseptum. Dev Biol 378, 107–121.

Munjal, A., Hannezo, E., Tsai, T. Y., Mitchison, T. J. and Megason, S. G. (2021). Extracellular hyaluronate pressure shaped by cellular tethers drives tissue morphogenesis. Cell 184, 6313-6325.e18.

Murayama, E., Herbomel, P., Kawakami, A., Takeda, H. and Nagasawa, H. (2005). Otolith matrix proteins OMP-1 and Otolin-1 are necessary for normal otolith growth and their correct anchoring onto the sensory maculae. Mech. Dev. 122, 791–803.

Neuhauss, S. C. F., Solnica-Krezel, L., Schier, A. F., Zwartkruis, F., Stemple, D. L., Malicki, J., Abdelilah, S., Stainier, D. Y. R. and Driever, W. (1996). Mutations affecting craniofacial development in zebrafish. Development 123, 357–367.

Norton, W. H. J., Ledin, J., Grandel, H. and Neumann, C. J. (2005). HSPG synthesis by zebrafish Ext2 and Extl3 is required for Fgf10 signalling during limb development. 8, 4963–4973.

Peal, D. S., Burns, C. G., Macrae, C. A. and Milan, D. (2009). Chondroitin sulfate expression is required for cardiac atrioventricular canal formation. Dev. Dyn. 238, 3103–3110.

Pirvola, U., Zhang, X., Mantela, J., Ornitz, D. M. and Ylikoski, J. (2004). Fgf9 signaling regulates inner ear morphogenesis through epithelial-mesenchymal interactions. Dev. Biol. 273, 350–360.

Richter, R. P., Baranova, N. S., Day, A. J. and Kwok, J. C. (2018). Glycosaminoglycans in extracellular matrix organisation: are concepts from soft matter physics key to understanding the formation of perineuronal nets? Curr Opin Struct Biol 50, 65–74.

Salminen, M., Meyer, B. I., Bober, E. and Gruss, P. (2000). Netrin 1 is required for semicircular canal formation in the mouse inner ear. Development 127, 13–22.

Schilling, T. F., Piotrowski, T., Grandel, H., Brand, M., Heisenberg, C.-P., Jiang, Y.-J., Beuchle, D., Hammerschmidt, M., Kane, D. A., Mullins, M. C., et al. (1996). Jaw and branchial arch mutants in zebrafish I: branchial arches. Development 123, 329–344.

Schindelin, J., Arganda-Carreras, I., Frise, E., Kaynig, V., Longair, M., Pietzsch, T., Preibisch, S., Rueden, C., Saalfeld, S., Schmid, B., et al. (2012). Fiji: An open-source platform for biological-image analysis. Nat Methods 9, 676–682.

Söllner, C., Burghammer, M., Busch-Nentwich, E., Berger, J., Schwarz, H., Riekel, C. and Nicolson, T. (2003). Control of crystal size and lattice formation by Starmaker in otolith biomineralization. Science 302, 282–6.

Stooke-Vaughan, G. A., Obholzer, N. D., Baxendale, S., Megason, S. G. and Whitfield, T. T. (2015). Otolith tethering in the zebrafish otic vesicle requires Otogelin and alpha-Tectorin. Development 142, 1137–1145.

Swinburne, I. A., Mosaliganti, K. R., Upadhyayula, S., Liu, T. L., Hildebrand, D. G. C., Tsai, T. Y. C., Chen, A., Al-Obeidi, E., Fass, A. K., Malhotra, S., et al. (2018). Lamellar projections in the endolymphatic sac act as a relief valve to regulate inner ear pressure. Elife 7, 1–34.

Thisse, C. and Thisse, B. (2008). High-resolution in situ hybridization to whole-mount zebrafish embryos. Nat Protoc 3, 59–69.

Toole, B. P. (2001). Hyaluronan in morphogenesis. Semin Cell Dev Biol 12, 79–87.

Trowe, T., Klostermann, S., Baier, H., Granato, M., Crawford, A. D., Grunewald, B., Hoffmann, H., Karlstrom, R. O., Meyer, S. U., Müller, B., et al. (1996). Mutations disrupting the ordering and topographic mapping of axons in the retinotectal projection of the zebrafish, Danio rerio. Development 123, 439–450.

Vallet, S. D., Berthollier, C., Ricard, S., Current, F. and Alpes, G. (2022). The glycosaminoglycan interactome 2.0. Am J Physiol Cell Physiol.

van Eeden, F. J. M., Granato, M., Schach, U., Brand, M., Furutani-Seiki, M., Haffter, P., Hammerschmidt, M., Heisenberg, C.-P., Jiang, Y.-J., Kane, D. A., et al. (1996). Genetic analysis of fin formation in the zebrafish , Danio rerio. Development 255–262.

Venero Galanternik, M., Kramer, K. L. and Piotrowski, T. (2015). Heparan Sulfate Proteoglycans Regulate Fgf Signaling and Cell Polarity during Collective Cell Migration. Cell Rep 10, 414–428.

Walsh, E. C. and Stainier, D. Y. R. (2001). UDP-glucose dehydrogenase required for cardiac valve formation in zebrafish. Science (1979) 293, 1670–1673.

Waterman, R. E. and Bell, D. H. (1984). Epithelial fusion during early semicircular canal formation in the embryonic zebrafish, Brachydanio rerio. Anat Rec 210, 101–114.

Westerfield, M. (2007). The Zebrafish Book: A Guide for the Laboratory Use of Zebrafish (Danio rerio). Eugene: University of Oregon Press.

Whitfield, T. T., Granato, M., van Eeden, F. J. M., Schach, U., Brand, M., Furutani-Seiki, M., Haffter, P., Hammerschmidt, M., Heisenberg, C., Jiang, Y.-J., et al. (1996). Mutations affecting development of the zebrafish inner ear and lateral line. Development 123, 241–254.

Wiweger, M. I., Zhao, Z., van Merkesteyn, R. J., Roehl, H. H. and Hogendoorn, P. C. (2012). HSPG-deficient zebrafish uncovers dental aspect of multiple osteochondromas. PLoS One 7, e29734.

Wiweger, M. I., De Andrea, C. E., Scheepstra, K. W. F., Zhao, Z. and Hogendoorn, P. C. W. (2014). Possible effects of EXT2 on mesenchymal differentiation - Lessons from the zebrafish. Orphanet J Rare Dis 9, 1–11.

Zimmer, B. M., Barycki, J. J. and Simpson, M. A. (2021). Integration of Sugar Metabolism and Proteoglycan Synthesis by UDP-glucose Dehydrogenase. Journal of Histochemistry and Cytochemistry 69, 13–23.

5.3 Discussion

In this chapter we added to the existing knowledge of ECM components involved in SSC development, which so far, has been mainly focused on the role of hyaluronan. We demonstrated the presence of chondroitin sulphate in the extracellular space of the epithelial projections of the SSCs, and the requirement for heparan sulphate for normal SCC development. This is the beginning of creating a better and more complete picture of the role of the inner ear ECM.

Since we knew that versican genes (which code for the core protein of CSPGs) are expressed in the zebrafish inner ear during formation of the epithelial projections, it was not a surprise to observe chondroitin sulphate present at the extracellular space of the otic epithelium at this stage (Geng et al., 2013). The interesting observations were that first, this deposition of chondroitin sulphate preceded the event of tissue inversion and evagination; and second, the patches of chondroitin sulphate precisely delineated the sites that would undergo tissue folding. These observations raise questions of the possible requirement for the ECM to be established prior to the tissue folding event in order to facilitate it. An example of this happens during zebrafish midbrain-hindbrain boundary formation. Here, the ECM adhesive glycoprotein laminin is required not only for tissue folding, but also for cellular basal constriction (Gutzman et al., 2008). An important next step would be to investigate whether the absence of chondroitin sulphate would prevent folding of the otic epithelium and any of the cell shape changes reported in chapter four. This could be done using the *csgalnact1a;chsy1* or *csgalnact1a;csgalnact2* zebrafish double mutants, in which the genes for some chondroitin sulphate biosynthetic enzymes have been knocked out (Habicher et al., 2022).

It was clear from the anti-chondroitin sulphate antibody staining performed in this chapter, that chondroitin sulphate is only present in the extracellular space of the otic epithelium during a time window that starts a few hours before the folding of the otic tissue. During formation of the endocardial cushions of the zebrafish heart, chondroitin sulphate is also visible in a precise time window just like in the inner ear. It is deposited before pushing a layer of endocardial cells away from a layer of myocardial cells and into the heart. These endocardial cells then undergo EMT back into the ECM to form the cushions of the heart which give rise to the cardiac valves. Chemical and genetic downregulation of chondroitin sulphate prevented endocardial cushion formation by disrupting the migratory activity of the endocardial cells (Peal et al., 2009).

It would be relevant to investigate whether the otic cells forming the epithelial projections express any genes associated with migratory behaviour. Two starting candidates could be the *secreted phosphoprotein 1* (*spp1*) and the *T-box transcription factor 1* (*tbx1*) genes. Upregulation of *spp1* is seen in migrating cells, and loss of *ssp1* expression in the zebrafish heart, due to chondroitin sulphate downregulation, has been suggested to contribute to endocardial cells losing their ability to migrate and form the endocardial cushions of the heart (Alonso et al., 2007; Peal et al., 2009; Saika et al., 2007). In addition, *ssp1* has been found to be expressed in the mouse inner ear (Kim et al., 2014). *tbx1* zebrafish mutants are unable to form the SSCs and in most cases the epithelial projections are also absent (Dutton et al., 2009). Interestingly, it was reported that *tbx1* regulates tissue reshaping through ECM-cell interactions that support cell migration (Alfano et al., 2019; Zhong et al., 2019).

Both *ext2* zebrafish mutants (data in this chapter) and *chsy1* zebrafish morphants exhibit truncated or absent epithelial projections, a similar phenotype to the one observed in embryos where hyaluronan production is reduced (Busch-Nentwich et al., 2004; Geng et al., 2013; Haddon and Lewis, 1991; Jones et al., 2022; Li et al., 2010b; Munjal et al., 2021). This, together with our observation of hyaluronan being present in *ext2* mutants, indicates that hyaluronan is not sufficient to drive epithelial projection outgrowth. It also suggests that chondroitin and heparan sulphate glycosaminoglycans are likely to play a role in this step of inner ear morphogenesis. For these two sulphated glycosaminoglycans and for hyaluronan is left to investigate their role in the event that precedes projection outgrowth, which involves inversion of the otic tissue curvature to initiate evagination, and cell shape changes (reported in chapter four). In chapter six, I explore the role of hyaluronan production in tissue curvature inversion, initiation of projection outgrowth and projection elongation. Future work to investigate the role of hyaluronan, heparan and chondroitin sulphate on cell shape changes during epithelial projection formation could be done using, *has3*, *ext2* and *chsy1* mutants respectively. After acquiring time-lapses of the developing inner ear in these three contexts, our cell shape analysis pipeline – Origami – could be performed and results then compared to the findings from the wild-type embryos presented in chapter four.

CHAPTER 6

The Role Of Hyaluronan In The Formation Of Epithelial Projections

6.1 Introduction

In chapter five, sulphated glycosaminoglycans were shown to have an essential role in the development and shaping of the epithelial projections. In this chapter, I investigated the role of another glycosaminoglycan - the hyaluronan.

As explained in chapter five, has3 is the enzyme responsible for the biosynthesis of hyaluronan in the zebrafish inner ear. Through *in situ* hybridisation *has3* mRNA was shown to be present in the otic tissue, at least, from around 45 hpf to 57 hpf, covering all stages of anterior and posterior projections' formation and growth (Munjal et al., 2021). Zebrafish morphants (*dfna5* and *has3*) and mutants (*ugdh* and *ext2*) which fail to produce hyaluronan and sulphated glycosaminoglycans (GAGs), have a delay in projection outgrowth and projections look short as they fail to elongate (Busch-Nentwich et al., 2004; Jones et al., 2022; Munjal et al., 2021; Neuhauss et al., 1996). In addition, injection of hyaluronidase into the core of epithelial projections in both Xenopus (Haddon and Lewis, 1991) and zebrafish (Geng et al., 2013; Munjal et al., 2021) ears was shown to lead to projection collapse. These experiments demonstrated the requirement for hyaluronan for normal projection outgrowth and maintenance of elongated projections. However, they do not inform us as to whether the presence of hyaluronan in the basal extracellular space of epithelial projections is required, not only for projection elongation and maintenance, but also for the tissue folding event that precedes it. Moreover, the time-window during which production of new hyaluronan, is required is still unknown. These questions will be explored in this chapter.

4-Methylumbelliferone (4-MU) has been commonly used to inhibit synthesis of hyaluronan (Kakizaki et al., 2004; Long et al., 2018; Missinato et al., 2015; Nagy et al., 2015; Ouyang et al., 2017; Vigetti et al., 2009). According to the literature, 4-MU can inhibit production of hyaluronan in four different ways. One way is by reducing the expression of hyaluronan synthase (HAS) and UDP-glucose 6-dehydrogenase (UGDH) mRNAs (Kultti et al., 2009; Vigetti et al., 2009), both of which are involved in the production of hyaluronan (Figure 6.1). A second mode of action of 4-MU is by covalently binding to one of the building blocks of hyaluronan – UDP-glucuronic acid (UDP-GlcA) – via the UDP-glucuronosyltransferase (UGT) (Kakizaki et al., 2004), leading to the synthesis of 4-MU-glucuronide (Kultti et al., 2009) (Figure 6.1). Thirdly, 4-MU was also found to induce a slight reduction of the levels of the other hyaluronan building block - UDP-N-acetylglucosamine (UDP-GlcNAc) (Jokela et al., 2008). As a result, the cellular pools of UDP-GlcA and UDP-GlcNAc decrease in the cytosol and so does the production of hyaluronan. Finally, the 4-MU-glucuronide was also shown to mildly inhibit hyaluronan synthesis (Nagy et al., 2019). Chondroitin and heparan sulphate, present and involved in the development of epithelial projections of the zebrafish inner ear (see chapter five), are sulphated GAGs that also use UDP-GlcA as one of their building blocks (Lindahl et al., 2017). However, it has been shown that reducing the availability of UDP-GlcA caused a decrease in hyaluronan synthesis without having an effect on the production of other GAGs (Vigetti et al., 2006). This is due to the fact that UDP-sugar levels are not affected inside the Golgi, where sulphated GAGs are synthesised (Vigetti et al., 2014).

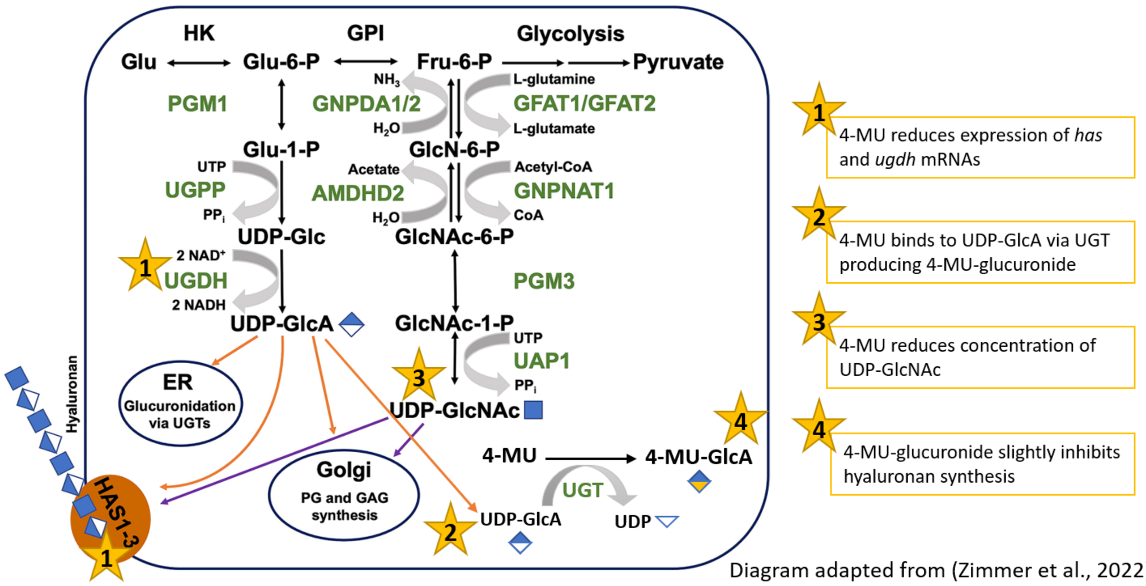

4-MU reduces expression of *has* and *ugdh* mRNAs

4-MU binds to UDP-GlcA via UGT producing 4-MU-glucuronide

4-MU reduces concentration of UDP-GlcNAc

4-MU-glucuronide slightly inhibits hyaluronan synthesis

Diagram adapted from (Zimmer et al., 2022).

Figure 6.1 – Synthesis of hyaluronan and its precursors, and modes of action of 4-MU.

Hyaluronan building blocks, UDP-GlcA and UDP-GlcNAc, are synthesised through a chain of reactions that use glucose as the initial substrate. Within the options for their downstream fates, they can both be taken up by the hyaluronic acid synthase (HAS) to produce hyaluronan, and into the Golgi to participate in the synthesis of proteoglycans (PG) and glycosaminoglycans (GAGs). Upon 4-MU treatment hyaluronan synthesis should drastically reduce as this drug exhibits four modes of action that disrupt this process (stars 1-4). Relevant abbreviations: Glucose (Glu), Uridine diphosphate (UDP), UDP-glucose 6-dehydrogenase (UGDH), UDP-glucuronic acid (UDP-GlcA), UDP-N-acetylglucosamine (UDP-GlcNAc), UDP-glucuronosyltransferase (UGT), 4-Methylumbelliferone (4-MU), 4-MU-glucuronide (4-MU-GlcA).

6.2 Results

6.2.1 Optimising the protocol for 4-MU treatment

Based on a few examples from the literature (Missinato et al., 2015; Ouyang et al., 2017), I decided to start with three different concentrations of 4-MU – 250 µM, 500 µM and 1000 µM. I used wild-type embryos and *adgrg6*^{tk256a} mutant embryos. The reason to use these *adgrg6*^{tk256a} embryos initially, was that they continuously produce ECM components which leads to swollen epithelial projections (Geng et al., 2013), offering a nice chance to see the impact of stopping production of hyaluronan in the ear. The drug was diluted in DMSO, and administered to the whole embryo via the water in which they were being raised at three different time points (40, 45 and 50 hpf) with the idea of targeting the times at which the different projections develop. Treatment duration was five hours, the drug was washed and pictures were then taken around 24 hours after the drug administration time (see methods 2.2.2 for details).

At 65 hpf, the ears of DMSO control embryos had a fused anterior projection and the posterior and ventral projections were touching or fusing with the respective bulge of the lateral projection. At 73 and 79 hpf, the ears of DMSO control embryos had all projections fused and the three pillars formed. I was not able to see any difference between the DMSO treated and the 250 µM or the 500 µM 4-MU treated embryos at any time point (data not shown). However, embryos treated with 1000 µM 4-MU showed a range of responses, and the strongest effect was seen in embryos treated at the earliest time-point (40 hpf). At 40 hpf, the ears of wild-type 4-MU-treated embryos showed normal anterior and posterior projections, already fusing to the lateral projection, but the ventral bulge and ventral projection were slightly smaller and had not yet fused compared to the DMSO-treated embryos (Figure 6.2A and A’). On the other hand, the *adgrg6*^{tk256a} mutant embryos, treated at the same time, showed a drastic reduction of the lateral, anterior and posterior projections (Figure 6.2B and B’), while the ventral bulge and ventral projection did not appear to form at all (white star in Figure 6.2B’). Wild-type embryos treated at 45 hpf did not show any difference from the controls (Figure 6.2C and C’); however, the *adgrg6*^{tk256a} mutant treated embryos were unable to form a ventral projection (Figure 6.2D and D’). Embryos treated at the latest stage (50hpf) only showed difference from the controls in the *adgrg6*^{tk256a} mutant group, where all projections formed but looked less swollen (and unfused) (Figure 6.2F and F’).

Through these results I have showed that the 4-MU reached the zebrafish ear by administering via water and that production of hyaluronan might be happening at different times in different regions of the ear depending on the epithelial projection. The fact that the overall effect of this treatment was fairly mild, suggested the need to make some improvements to the protocol. First, was to image the embryos straight after the treatment is finished in order to avoid the projections to develop once the drug is washed out. Second, was to increase the length of treatment, and thirdly was to start the treatment earlier, as the strongest effect was seen at the earliest time-point.

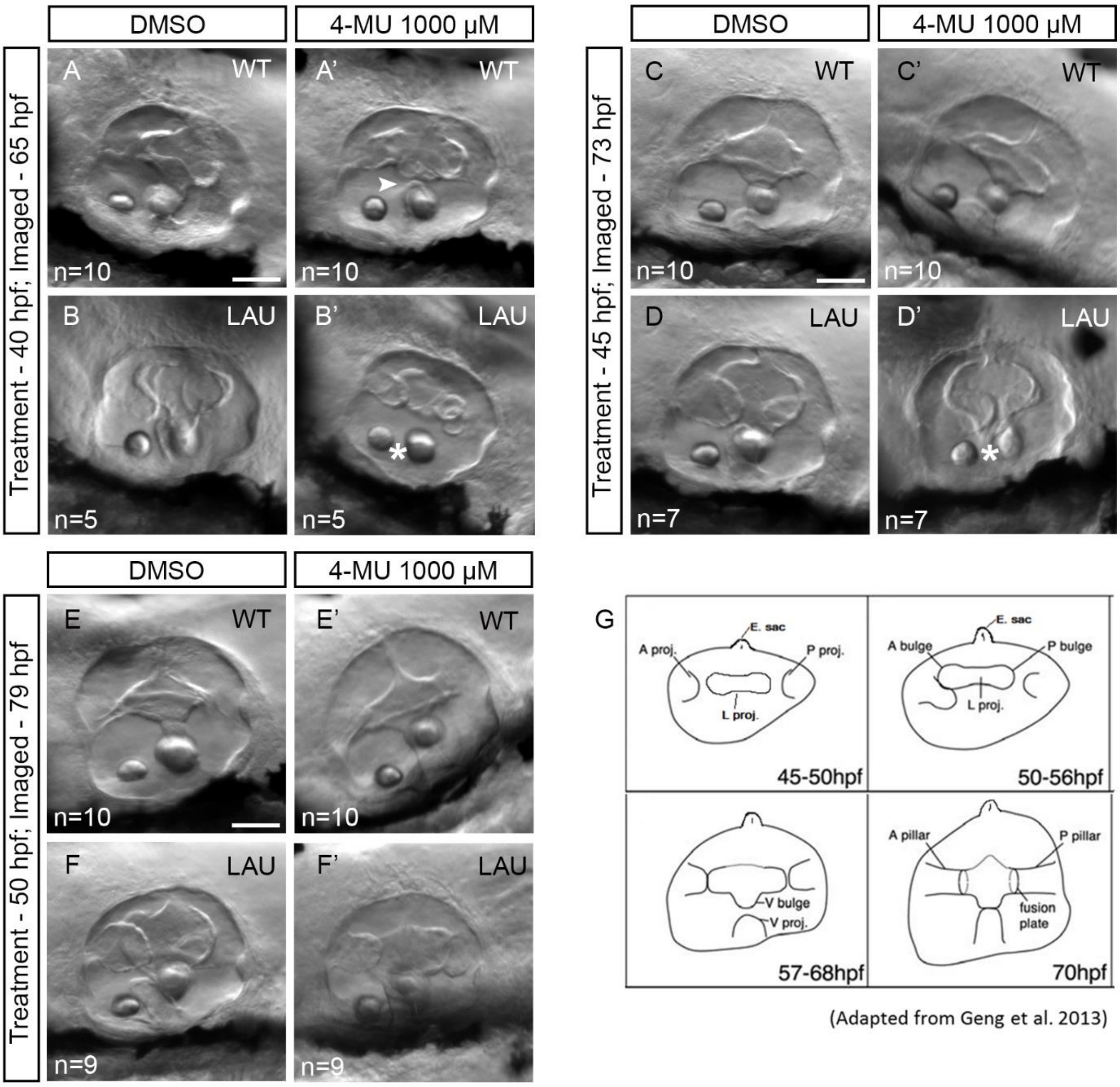

(Adapted from Geng et al. 2013)

Figure 6.2 – Blocking production of hyaluronan leads to smaller and/or absent projections in mutant embryos where these structures are normally swollen.

Pictures were taken in the ZEISS Axio Zoom.V16 microscope. Anterior is to the left, while dorsal is to the top. Scale bars measure 50 µm. Inner ear of wild-type (WT) and *adgrg6*^{tk256a} mutant (LAU) embryos treated for 5 hours with 1000 µM of 4-MU (using DMSO for control) and washed after treatment. (**A-**

B’) Embryos treated at 40 hpf and imaged at 65 hpf. White arrowhead points to smaller and yet to fuse ventral bulge and projection. White asterisk indicates the lack of ventral projection. (**C-D’**) Embryos treated at 45 hpf and imaged at 73 hpf. White asterisk indicates the lack of ventral projection. (**E-F’**) Embryos treated at 50 hpf and imaged at 79 hpf. (**G**) Diagram of the inner ear showing the outgrowth of the projections: lateral (L proj.), anterior (A proj.), posterior (P proj.) and ventral (V proj).

6.2.2 Synthesis of hyaluronan appears to be required for initiation of projection formation and projection elongation

The findings reported in chapter five were insightful in order to choose how much earlier to start the 4-MU treatment. As reported (Jones et al., 2022), the deposition of chondroitin sulphate starts as early as 40 hpf for the anterior and posterior projections, before the otic epithelium exhibits any other signs of folding or outgrowth. It is possible that other GAGs like hyaluronan might also initiate production and extracellular deposition at a similar time. For this reason, 4-MU was administered at 36 hpf with the aim of preventing the initiation of synthesis of hyaluronan. The treatment was performed at four concentrations – 150, 250, 500 and 1000 µM – for twelve hours.

Around 49 hpf, control embryos had three projections – lateral, anterior and posterior (Figure 6.3A, E, H and I). By contrast, 4-MU-treated embryos exhibited a range of phenotypes in a dose-dependent manner (one ear analysed per embryo). Embryos treated with 150 µM of 4-MU showed normal projection development (Figure 6.3B and H). Those treated with 250 µM of 4-MU showed some delay in projection development (Figure 6.3C, C’ and H). Embryos treated with higher doses of 4-MU were unable to form normal projections and projections were lacking altogether in 50% of embryos (Figure 6.3F-G and I). Whilst 60% of 500 µM 4-MU-treated embryos still presented one truncated projection (Figure 6.3F’ and I), embryos treated with the highest dose of 4-MU (1000 µM) were more severely affected and 75% were unable to form projections (Figure 6.3G and I).

Embryo length measurements revealed that 4-MU-treated embryos were significantly shorter than control embryos (Figure 6.3J). The elongation of their body axis seemed to be more severely affected than the development of the projections of the inner ear, as embryos treated with the lowest dose (150 µM) exhibit normal ears but were significantly shorter than control embryos. Ear size was not measured, but the images show that this was also affected by the treatments (except the 4-MU 150 µM treatment), and requires further analysis.

Taken together, these results suggest that synthesis of hyaluronan is required for projection elongation and suggest that it might be also necessary for the initiation of projection outgrowth.

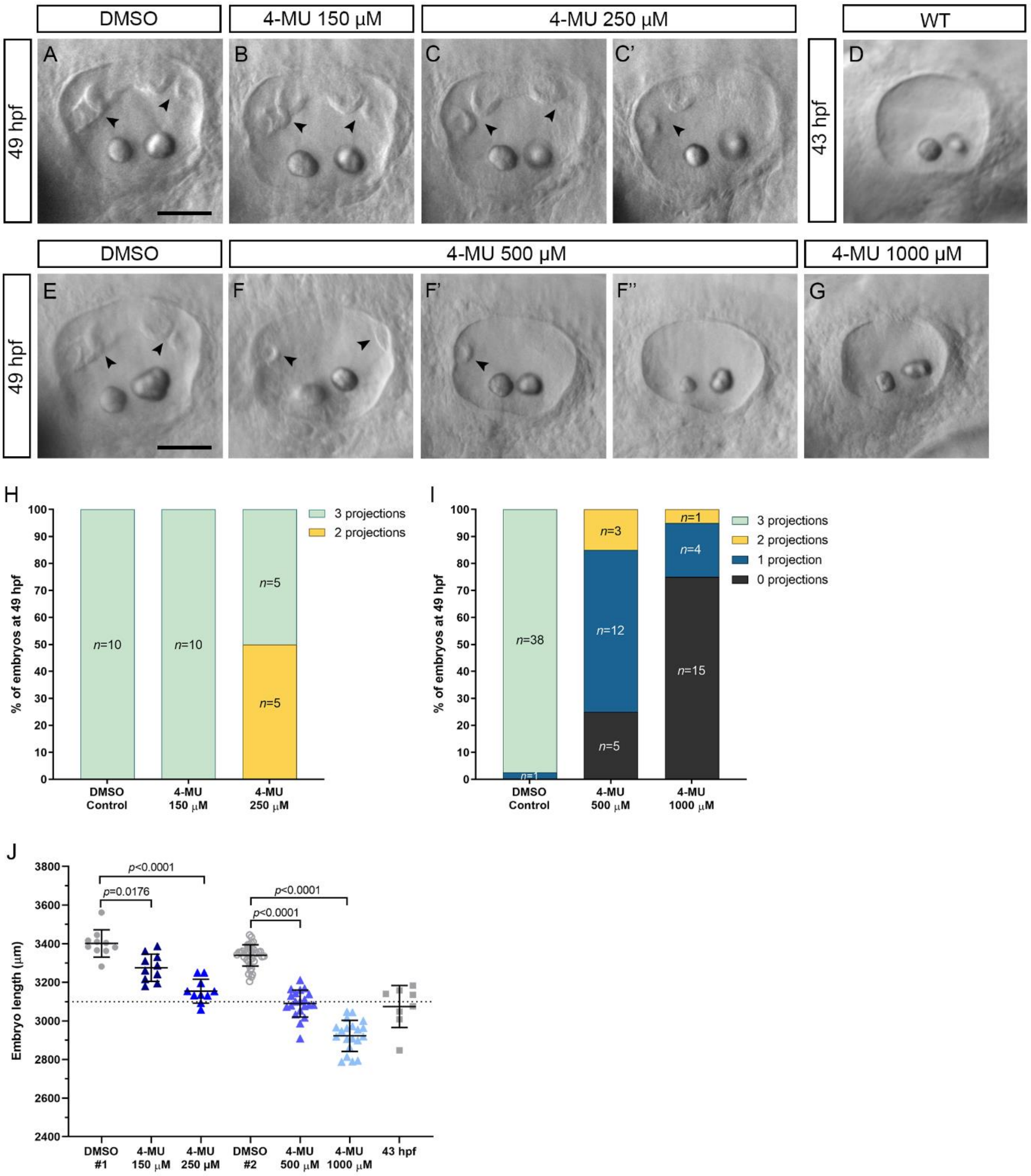

Figure 6.3 – Blocking synthesis of hyaluronan in the inner ear leads to absent or abnormal epithelial projections, but also a significant reduction in embryo length.

Embryos were treated with 4-MU for twelve hours (36-48 hpf) and representative pictures of their otic vesicles are shown in **A-G** for the respective groups. Pictures were taken in the ZEISS Axio Zoom.V16 microscope. Scale bars measure 50 µm. (**H** and **I**) Graphs showing number of projections formed in the ear for each treatment group reveal that blocking synthesis of hyaluronan prevents projection formation. (**J**) Treatment with 4-MU causes a significant reduction in embryo length. Mean and standard deviation are shown by the horizontal lines and a Brown-Forsythe ANOVA with a Dunnett’s T3 post-test correction for multiple comparisons was performed.

I then performed a twelve hour 4-MU treatment on wild-type embryos between 48 and 60 hpf. The aim was to disrupt the development of the ventral projection and, at the same time, test whether production of hyaluronan is required during later stages of projection elongation and fusion (by looking at the effect in the anterior and posterior projections). At 60 hpf, the anterior and the posterior projections are fused with the respective bulge of the lateral projection in the control embryos (black arrowheads in Figure 6.4A and Figure 6.4D). In half of the control embryos, the ventral projection touches the ventral bulge of the lateral projection (white arrowhead in Figure 6.4A and Figure 6.4D), whilst in the other half, both structures are present but not yet touching (white arrowhead in Figure 6.4A’ and D). In contrast, in 4-MU treated embryos, the ventral projection did not form (Figure 6.4B-D) and the ventral bulge from the lateral projection was only present in 20% of the embryos (white arrowhead in Figure 6.4B’ and Figure 6.4D). Fusion of anterior and posterior projections in the 500 µM 4-MU group was unaffected (Figure 6.4D) but the resulting pillars looked misshapen (black arrowheads in Figure 6.4 B and B’). At the highest dose of 4-MU, the posterior projection did not manage to fuse with the posterior bulge of the lateral projection in 80% of the embryos (black star in Figure 6.4C and Figure 6.4D). Embryo length was significantly reduced in both 4-MU-treated groups compared to the control embryos (Figure 6.4E), and ear size was also affected in the 1000 µM 4-MU group (not quantified).

Together, these experiments suggest that synthesis of hyaluronan is likely to be mostly required before and during initiation of projection outgrowth. In addition, production of hyaluronan at later stages of projection elongation or when they are at the stage of fusing to form the pillars did not seem to be as necessary.

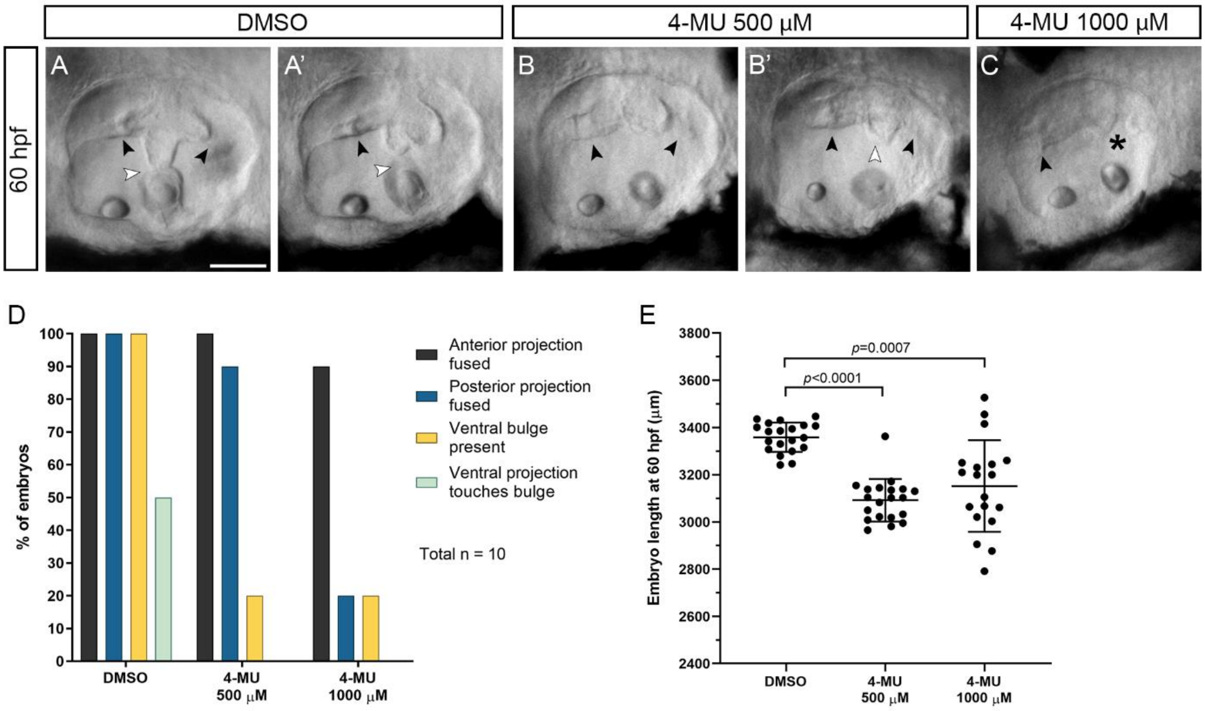

Figure 6.4 – Blocking synthesis of hyaluronan before ventral projection formation prevents its outgrowth but not later stages of elongation and fusion of the anterior and posterior projections.

Wild-type embryos were treated with 4-MU for twelve hours (48-60 hpf) and representative pictures of their otic vesicles are shown in **A-C** for the respective groups. Pictures were taken in the ZEISS Axio Zoom.V16 microscope. Scale bars measure 50 μm. Black Arrowheads point to anterior and posterior fused projections (pillars). White arrowheads point to ventral projections or ventral bulges of lateral projection. Black star marks an unfused posterior projection. (**D**) Graph showing stage of development of epithelial projections formed in the ear for each treatment group reveals that blocking synthesis of hyaluronan at early (but not later) stages prevents projection formation. (**E**) Treatment with 4-MU causes a significant reduction in embryo length. Mean and standard deviation are shown by the horizontal lines and a Kruskal-Wallis with a Dunn's post-test correction for multiple comparisons was performed.

6.2.3 Hyaluronan might be dispensable for inversion of tissue curvature that precedes projection outgrowth

Following the previous results, I wanted to investigate further at which key stage during early epithelial projection formation the presence of hyaluronan is required: whether it is only necessary after inversion of tissue curvature, to invert tissue curvature or even to induce the first set of cell shape changes (reported in chapter four). I performed a 12 hour 4-MU treatment (500 μM) from 36 to 48 hpf, fixed the embryos and stained these with Phalloidin. In order to be able to see more detail at the tissue and cell level I then imaged the embryos in a confocal microscope. Only anterior and posterior projections were considered here.

At 48 hpf, control embryos showed mature anterior projections that were in contact with the anterior bulge of the lateral projection (Figure 6.5A), and posterior projections that were partially elongated but were not yet in contact with the lateral projection (Figure 6.5D). In contrast, all embryos treated with 500 μM 4-MU exhibited abnormal projection development with a range of phenotypes, just as reported in (Figure 6.3F-F’’). Only in about 20% of cases a projection was formed, but these were shorter compared to those in control embryos (Figure 6.5B and G). This corroborates with findings presented in Figures 6.3 and 6.4, suggesting that hyaluronan is required for normal outgrowth and early stages of projection elongation. Interestingly, in roughly 65% of cases, the otic tissue inverted its curvature and cells underwent shape changes (Figure 6.5C, E and G). In contrast, in just under 30% of cases, there were no signs of cell shape change or tissue inverting its curvature (Figure 6.5F and G). These results indicate that there is a possibility for cell shape changes and inversion of tissue curvature to occur independently of hyaluronan production.

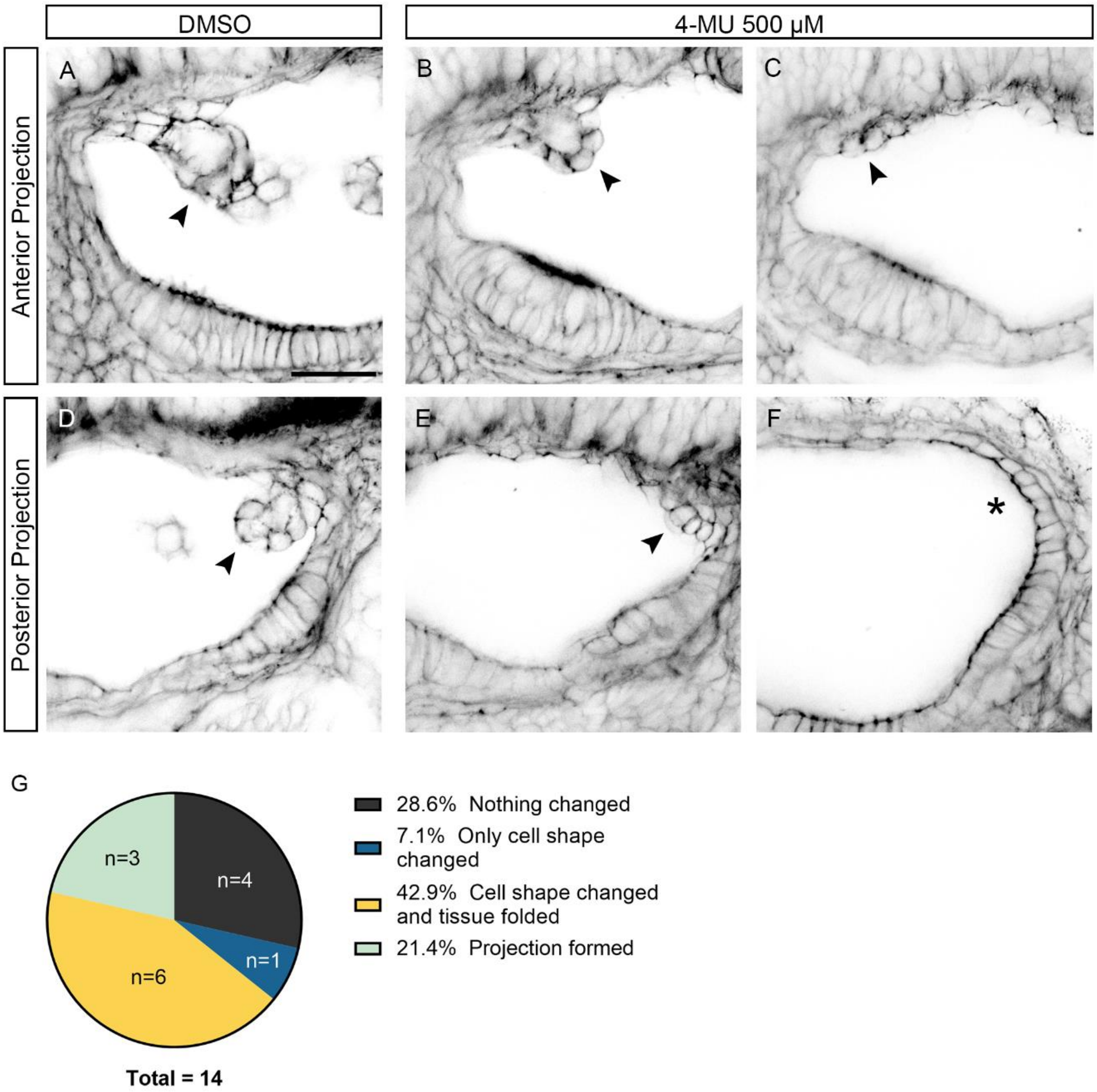

Figure 6.5 – Blocking synthesis of hyaluronan in the inner ear only causes a mild disruption of the folding event preceding projection elongation.

Embryos were treated with 500 μM 4-MU for twelve hours (36-48hpf). Phalloidin-stained fixed samples imaged on a Nikon inverted confocal microscope with a 40X oil immersion objective. Representative images of the variety of phenotypes in projection formation and development are shown (**B**, **C**, **E**, **F**) alongside with controls (**A** and **D**). Scale bar measures 25 μm. Black arrowheads point to developing projections or the region of projection outgrowth and black asterisk marks the absence of projection formation. (**G**) Graph showing number of cases (n is the number of projections/projection forming regions) in which projection formation was disrupted at a certain stage following drug treatment.

6.3 Discussion

In this chapter I successfully developed a protocol to block hyaluronan synthesis through 4-MU treatment in the zebrafish inner ear. I also showed the likely requirement of hyaluronan production for initiation of projection outgrowth and elongation, although further studies might be needed to rule out any effect of a systemic delay of embryonic and otic growth and development. The lack of a strong effect on 4-MU-treated wild-type embryos in Figure 6.2, could have meant that either a) the treatment did not work, b) that hyaluronan was not required for projection development, or c) that once the drug was washed out, synthesis of hyaluronan was able to re-start, and epithelial projections were able to catch up to match the developmental stage of control embryos. Despite the *adgrg6*^{tk256a} mutant embryos continuously producing ECM components (Geng et al., 2013), stopping production of hyaluronan at any time showed more effect compared to wild-type 4-MU-treated embryos.

500 μM of 4-MU seemed to be a good working concentration to administer via water in order to study the development of the epithelial projections in the zebrafish inner ear as it led to a range of interesting phenotypes (Figure 6.3). In particular, the rounder ears with short projections shown in Figure 6.3F and F’ resembled the phenotypes reported in *jekyll*^{m151} (Neuhauss et al., 1996) and *dak*^{tw25e} (Jones et al., 2022) mutant embryos and in *dfna5* morphant embryos (Busch-Nentwich et al., 2004). Lower concentrations had little effect and the highest dose (1000 μM) made the embryos look slightly unhealthy and occasionally caused death (data not shown).

In response to results of shorter embryo length following 4-MU treatment presented in Figures 6.3 and 6.4, one could argue for an overall developmental delay or even arrest. However, *has2* morphants (embryos that lack hyaluronan synthase and therefore have reduced hyaluronan) have been shown to have reduced body length due to blocking of convergence of lateral cells to form the dorsal shield, which consequently disrupts extension (Bakkers et al., 2004). Similarly, *chsy1* morphants, which lack chondroitin sulphate synthase and show reduced levels of chondroitin sulphate, also have reduced body length (Li et al., 2010). This could explain the shorter embryo length in 4-MU-treated embryos. In addition, I was able to see that the effect of this drug on body axis length is more severe than in the inner ear (partial decoupling of the two phenotypes). 500 μM 4-MU-treated embryos presented a body length comparable to WT 43 hpf embryos but the inner ears of the 4-MU-treated embryos were more developed (60% looked like 45hpf and 15% looked like 48hpf), already exhibiting a less round shape and early forming projections compared to its length-matched WT embryos (Figure 6.3D, and F-F’’).

It was not possible to uncouple the rounder shape of the ear (younger looking shape) and the lack of projections seen in treated embryos, but there is a chance that these two processes are linked. One argument to support this is that, mutants without anterior and posterior epithelial projections also have a rounder/younger looking ear (pointing again to an interdependence between these two morphogenetic events). Examples of this include the *tbx1* mutants, *n-cad* mutants (Babb-Clendenon et al., 2006), and *eya1* mutants (Kozlowski et al., 2005). This is speculative, but perhaps the force and tension generated from the otic tissue being ‘pushed’ and bending into the ear and forming the epithelial projections might contribute to a change in the overall shape and size of the ear.

Following the work done in this chapter, it would be important to perform staining protocols to test whether there is remaining hyaluronan in 4-MU-treated embryos and compare these to control embryos. This could help understanding the variability of phenotypes within the 500 μM 4-MU treated group. Biotinylated hyaluronic acid binding protein (HABP), for instance, has been used to show the presence of hyaluronan in the basal extracellular space of the epithelial projections (Busch-Nentwich et al., 2004; Jones et al., 2022; Munjal et al., 2021). A staining for HABP would confirm the reduction or even absence of hyaluronan in the inner ear in response to 4-MU. Another option is to use a hyaluronan transgenic reporter line. 4-MU and hyaluronidase treatments of trabecular meshwork cells showed that blocking hyaluronan synthesis can lead to reduction of versican mRNA and protein concentration as well as changes in its distribution (Keller et al., 2012). As versican genes are known to be specifically expressed in the epithelial projections until fusion stage (Geng et al., 2013), performing an *in situ* hybridisation for *versicana* or *versicanb* mRNA after a 4-MU treatment would clarify if and how transcription of the genes coding for the core protein of this proteoglycan is affected when hyaluronan production is blocked. In addition, performing an antibody stain for chondroitin sulphate would also confirm whether synthesis of sulphated GAGs in the inner ear is in fact unaffected by 4-MU treatment. Finally, as the inversion of tissue curvature seems to be disrupted, but not prevented, when hyaluronan synthesis is blocked by 4-MU treatment (Figure 6.5) and its absence is confirmed by staining techniques, it would be interesting to investigate whether the re-distribution of adhesion and cytoskeletal proteins from the apical to the basolateral domain reported in chapter four is disrupted. Although administering 4-MU via water affects the whole organism, it is a quick method which has been used successfully in zebrafish embryos (Missinato et al., 2015; Ouyang et al., 2017). However, if one wanted to target the ear alone, injections of the compound could potentially be performed in the inner ear.

Previously, hyaluronan had been shown to be important for the elongation and maintenance of epithelial projections (Busch-Nentwich et al., 2004; Munjal et al., 2021; Neuhauss et al., 1996). As these studies used mutants and morphants, there was no chance to manipulate hyaluronan synthesis specifically, and as a result it was not yet fully known from which stage of projection development hyaluronan was required. As projection outgrowth cannot happen without the tissue folding event that precedes it, it was important to know if hyaluronan has a role at this early stage of projection formation. I have shown that although synthesis of hyaluronan in the inner ear might be contributing for a successful start of projection outgrowth and elongation to the point of contact with the bulge of the lateral projection; the production of hyaluronan might be dispensable for the inversion of tissue curvature and the cell shape changes that precede projection outgrowth.

CHAPTER 7

Synopsis

7.1 Overview

Tissue shape and function are intrinsically linked, and so when organs fail to acquire the right shape, their function is compromised (Campbell and Casanova, 2015; Kashgari et al., 2020; Molè et al., 2020; Sidhaye and Norden, 2017; Yamada et al., 2019). For this reason, studying the morphogenetic processes responsible for generating shape during embryonic development is crucial. Epithelial folding is, amongst others, a common and essential tissue shape generating process. Although there seems to be a slight change in recent years, the vast majority of literature on epithelial folding events is still focused on *Drosophila* morphogenesis, on folding through invagination (Kolsch et al., 2007; Spencer et al., 2015; Wang et al., 2012; Weng and Wieschaus, 2017), and relying on image analysis tools that are often limited to two and sometimes three dimensions (Krueger et al., 2018; Merks et al., 2018; Sanchez-Corrales et al., 2018; Sui et al., 2018). Therefore, there is a clear gap in the literature when it comes to understanding the cellular mechanisms and the three and four-dimensional changes in folding events in vertebrate organisms and in particular, folding events through evagination.

A strength of this project is the addition of a third and fourth dimension to cell shape analysis which is, not only popular, but highly advantageous and useful in the field of tissue morphogenesis. In chapter three, I recorded two types of folding events during inner ear development – formation of the endolymphatic sac and the epithelial projections of the semicircular canals – using light-sheet fluorescence microscopy. This data, after being segmented with ACME software (Mosaliganti et al., 2012), was used to develop a pipeline – *Origami* – able to extract 3D direction-variant cell shape metrics along the apico-basal axis in highly curved epithelia (Mendonca et al., 2021). Results from this work showed a significant difference between cell shape in structures in the inner ear that are formed by folding the otic epithelium in opposite directions. Cells in the epithelial projections showed negative values of skewness, meaning that their basal domain is smaller than the apical. In contrast, cells in the endolymphatic sac, showed a positive skewness (smaller apical domain than the basal). This is the first time a cell shape analysis tool is specifically designed to address the challenges of tissues with high levels of curvature. This pipeline has the potential to serve the communities of developmental biologists and biomedical scientists studying cell shape changes in different contexts.

As explained in chapter four, the term ‘folding’ had not been associated with the formation of the epithelial projections of the semicircular canals until recently (Babb-Clendenon et al., 2006; Munjal et al., 2021). In addition, apart from the pressure exerted on the otic epithelium by hyaluronan (Munjal et al., 2021), morphogenetic processes involved in the folding event that initiates formation of the epithelial projections were still unknown. The work in chapters four to six shed some light on those mechanisms. In chapter four, I recorded the development of the epithelial projections using high-resolution fluorescence confocal microscopy and performed a detailed 4D quantitative analysis of tissue and cell shape changes during early epithelial projection formation. I showed that the relative position of projection cells within the anterior and posterior poles of the otic vesicle (in relation to the initiating cells) before the folding event, can be predicted by the relative final cell position within the projection in relation to its tip. In addition, with the help of the *Origami* pipeline, I discovered that the very first cell shape changes were coincident with the folding event: cells increased their longitudinal spread (elongation along the apico-basal axis), underwent basal constriction and apical rounding. Cell shape changes at this stage had not been reported before. In addition, this rounding of the apical cell surface, seems to be a newly described cellular behaviour in folding epithelia through evagination.

In the same chapter, I also demonstrate that relocation of cytoskeletal (F-actin and myosin-II) and adhesion (E-cad) proteins from the apical to the basolateral domain happens alongside with the folding event and changes in cell shape. Despite this, projection cells did not invert their polarity as ZO-1 and Pard3 remained apically located throughout the folding event. To further understand the mechanisms underlying otic epithelium folding, I disrupted the activity of myosin-II using blebbistatin. Preliminary results showed that there is potential for a role of myosin-II in the early stages of projection formation, including the folding event characterised by basal constriction and basal accumulation of myosin-II, unlike what was suggested in the literature, which suggests myosin-II to be involved only in providing an anisotropic shape to the projection (Munjal et al., 2021). This initial characterisation of the distribution of cytoskeletal, adhesion and polarity proteins in the cells undergoing shape changes, provides the basic knowledge to start investigating the mechanisms underlying inversion of epithelium curvature through evagination.

During projection outgrowth, it was known that hyaluronan (Haddon and Lewis, 1996; Waterman and Bell, 1984), versican (Geng et al., 2013) and ECM enzymes (Filipek-Górniok et al., 2013; Geng et al., 2013; Li et al., 2010; Munjal et al., 2021; Neuhauss et al., 1996) were produced by projection cells. In addition, hyaluronan has been presented as the propellant for projection elongation. In chapter five, the role of the ECM in epithelial projection formation was further investigated and sulphated glycosaminoglycans were shown to also be key players in this morphogenetic process (Jones et al., 2022). One surprise of this work was the observation of chondroitin sulphate patches deposited on the basal extracellular space marking the sites of epithelial projection outgrowth and preceding any other signs of folding. This was an unreported cellular behaviour. The same study reveals a role for heparan sulphate, not only in epithelial projection formation, but also in adhesion of the otoliths to the sensory otic epithelium. Finally, in chapter six, I studied in more detail the stages of projection formation during which hyaluronan is required. Blocking hyaluronan production with 4-MU, before the folding event, severely disrupted the start of projection outgrowth and early stages of elongation however, in most cases, cell shape changes and otic tissue folding still occurred. This result suggests that production of hyaluronan might not be crucial for the folding event that precedes projection outgrowth. In addition, blocking hyaluronan production at later stages, after projection formation had started, did not seem to have much effect on late stages of projection elongation or fusion. These experiments suggest that there is a point in projection outgrowth when projections might no longer need production of new hyaluronan, but simply the presence of hyaluronan filling their cores (Geng et al., 2013; Haddon and Lewis, 1991; Munjal et al., 2021; Waterman and Bell, 1984). Taken together, findings from chapter six narrowed down the time-window during which hyaluronan production is required in projection development.

7.2 Future directions

Folding an epithelial layer during embryogenesis is a complex morphogenetic process. Despite this study deepening our understanding of the cell shape changes and cellular mechanisms involved in folding the otic tissue during early semicircular canal formation, there are still unknown aspects of this tissue folding process to be investigated in the future.

The *Origami* pipeline was a key tool in helping describing the cell shape changes happening during early epithelial projection formation. This pipeline can now be used, for example, to analyse cell shape in embryos where projection outgrowth is disrupted, either due to a mutation or following a drug treatment (such as 4-MU or blebbistatin). Using the Airyscan confocal microscope, I have recorded the development of the inner ear in live zebrafish *tbx1*^{tm208} homozygous mutant embryos (data not shown) but due to time limitations, I was unable to analyse this data. This data could be used as an example of a scenario where epithelial projections do not form, showing what happens to the shape of the cells in the otic wall when they are no longer able to engage in epithelial projection formation. The *adgrg6*^{tk256a} mutant embryos could also provide insightful information and help understanding the effect (if any) of overproduction of ECM components in tissue and cell shape of epithelial projections.

One aspect I did not investigate in the epithelial projections, and would give more insight about formation and maintenance of this structure, was how the cells are packed in this curving/curved epithelium. Are the neighbours of each cell the same in the apical surface and the basal surface? This difference in cell contacts along the apico-basal axis has been reported to help stabilising the three-dimensional packing in tubular or curved epithelia by compensating the difference in area between the two surfaces of the tissue (Gómez-Gálvez et al., 2018b).

It is clear from the work presented in chapter four that cell shape changes are happening alongside the re-distribution of cytoskeletal and adhesion proteins. However, there are still a number of questions left to answer. In what way are these proteins contributing to the different changes in cell and tissue morphology? Is there a key player that is both required and sufficient to induce the cell shape changes described? Preventing actin and myosin-II polymerisation and activity respectively could be done to see whether it is possible to prevent their basal shift and cell shape changes like apical rounding and basal constriction. Despite myosin-II being observed in basal tethers during projection elongation and suggested to be required for maintaining its stiffness and an anisotropic structure, I think myosin-II is playing a different role at earlier stages. Blebbistatin treatments to disrupt myosin-II activity, presented in chapter four, dramatically reduced the number of projections formed, suggesting myosin-II to be a strong candidate for driving of cell shape changes in this system. I suspect that analysing cell shape changes following a blebbistatin treatment would show a reduced basal constriction, and maybe lack of apical rounding as well. This is speculation but something that can definitely be done in the future to confirm the role of myosin-II in driving cell shape changes during early formation of epithelial projections. Something I have not addressed as well is the apico-basal elongation observed in projection cells at the time of folding and protein redistribution. Microtubule activity has been reported to be involved in this type of cell shape change during *Xenopus* neural tube closure (Lee et al., 2007). Microtubules are also involved in the assembly of adherens junctions and in the delivery of regulators of junction dynamics (Vasileva and Citi, 2018), and so there is a chance that microtubules could be involved, in one way or the other, in the formation of epithelial projections. The transgenic line recently generated in our lab to highlight growing microtubules - *Tg(sox10:EB3-GFP)* (S. Baxendale, unpublished) - can definitely be used to help investigating microtubule dynamics during otic epithelium folding.

Despite results from chapter six suggesting that hyaluronan might not be required for tissue curvature inversion and cell shape changes, the *Origami* pipeline should be used next to carefully analyse cell shape changes in the otic tissue following a 4-MU treatment. I expect that initial cell shape changes during curvature inversion remain undisturbed. Having said that, and knowing how the ECM has such an essential role in re-shaping the otic epithelium during epithelial projection formation, there is a need to investigate whether the ECM is acting as more than just a passive substrate and perhaps as an active inducer of certain cellular behaviours. For example, as discussed in chapter five, there is a possibility that the ECM in the inner ear promotes certain semi-migratory behaviours in projection cells. There are several examples of communication between the ECM and the intracellular space being mediated by the transmembrane receptor integrin in the context of tissue re-shaping during morphogenesis (Bhat and Riley, 2011a; Gunawan et al., 2019; Hayes et al., 2012; Mateos et al., 2020). No integrin has been described to be specifically expressed in the epithelial projections of the inner ear, but there are a couple whose mRNA has been shown to be transcribed in the ear at relevant developmental stages. One of them is integrin-alpha-5 (Itga5) (Thisse et al., 2001), so by performing an *in situ* hybridisation staining for *itga5*, I observed that the mRNA for this integrin is expressed not only in the epithelial projections but also in the endolymphatic sac, both of which are structures that result from tissue folding events (data not shown). This is something that could be further investigated for example through examination of the inner ear phenotype in *itga5* zebrafish mutants.

7.3 Conclusion

It is clear from the literature that in each organism/structure, tissue folding is being driven by a combination of different mechanisms (Pearl et al., 2017; Sawyer et al., 2010; Varner and Nelson, 2014). In the zebrafish otic vesicle, I propose that ECM production by specific groups of cells in the otic vesicle could be the triggering event preceding tissue folding (Figure 7.1). This is followed by a shift of E-cad and of the actomyosin cytoskeleton from the apical/sub-apical domain to the basolateral and basal domain of these cells which is accompanied by drastic cell shape changes (Figure 7.1). These include cell elongation, basal constriction and apical rounding, and are coincident with the folding of the otic epithelium. After this inversion of curvature of the otic epithelium, projection elongation takes place (Figure 7.1).

With my research, I have provided some insight into the cellular behaviours involved in folding and re-shaping the otic epithelium during early stages of semicircular canal development in the zebrafish inner ear. Moreover, I established the epithelial projections as a new model for studying tissue curvature inversion through evagination.

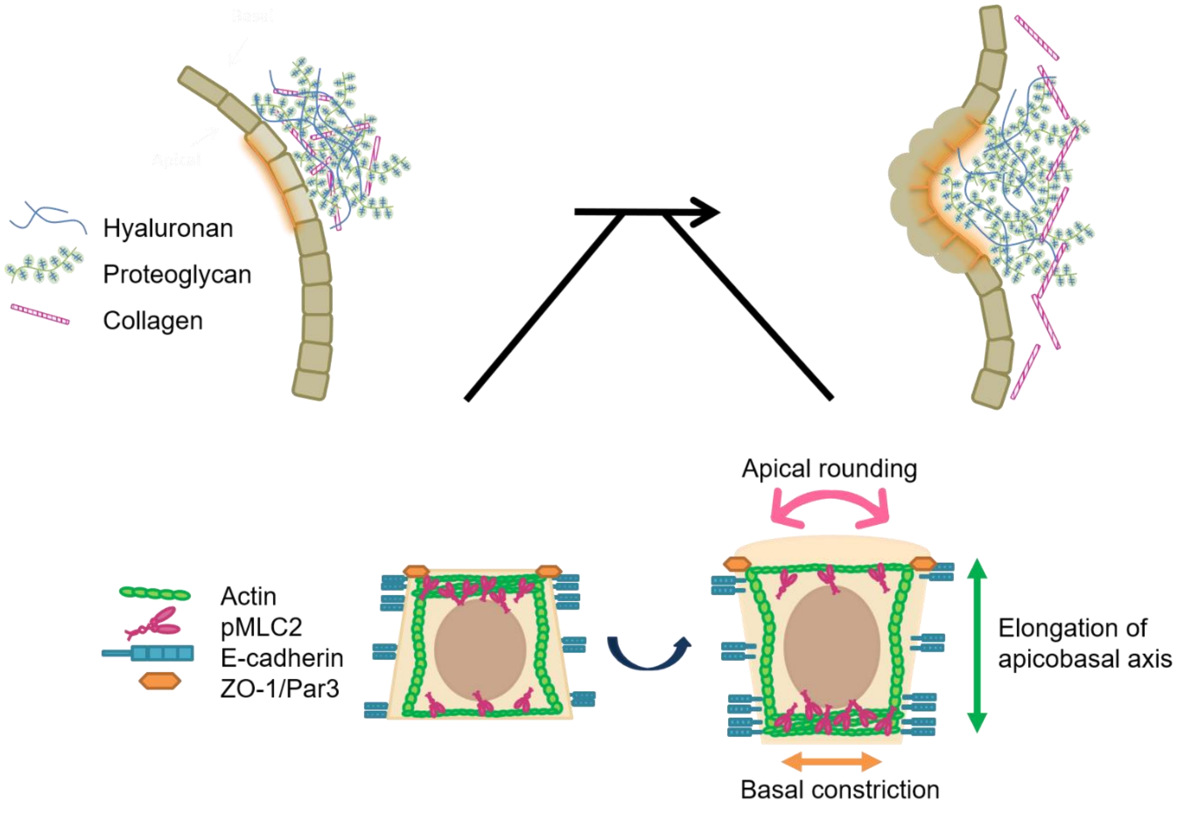

Figure 7.1 - Diagram summarising cellular and tissue behaviours during early stages of epithelial projection formation.

ECM deposition delineating the place of otic tissue evagination is the first observed process associated to the formation of epithelial projections. Next, cells in this region change their shape by undergoing apical rounding, elongation of the apicobasal axis and basal constriction. This is coincident with redistribution of cytoskeletal and adhesion proteins from the apical and subapical domains to the basal domain (highlighted in orange within the otic cells). As a result, the curvature of the otic tissue is inverted and evagination is initiated to form the epithelial projections of the semicircular canals.

SUPPLEMENTARY DATA

Supplementary Video 1 – Manually segmented endolymphatic sac of the zebrafish inner ear at 50.5 hpf.

Manually segmented cells from the dorsal region of the zebrafish inner ear at 50.5 hours post fertilisation (hpf) with the endolymphatic sac located in the middle. This structure forms through invagination as the apical cell surface makes up the inner surface of the curved epithelium. A single cell in the endolymphatic sac is highlighted in blue. Manual segmentation was performed in Fiji (see methods 2.5.1 for details).

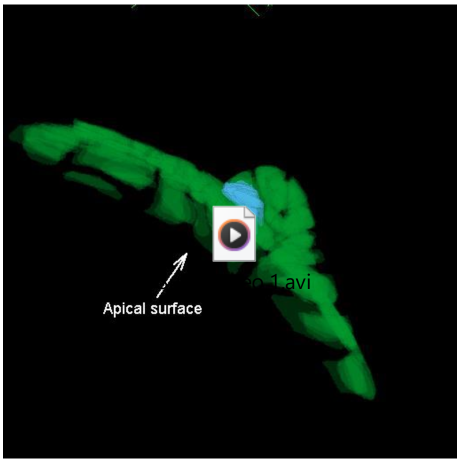

Supplementary Video 2 – Manually segmented posterior epithelial projection of the zebrafish inner ear at 48.5 hpf.

Manually segmented cells from the anterior dorsolateral region of the zebrafish inner ear at 48.5 hours post fertilisation (hpf) with the anterior projection located in the middle. This structure forms through evagination as the apical cell surface makes up the outer surface of the curved epithelium. A single cell in the posterior projection is highlighted in blue. Manual segmentation was performed in Fiji (see methods 2.5.1 for details).

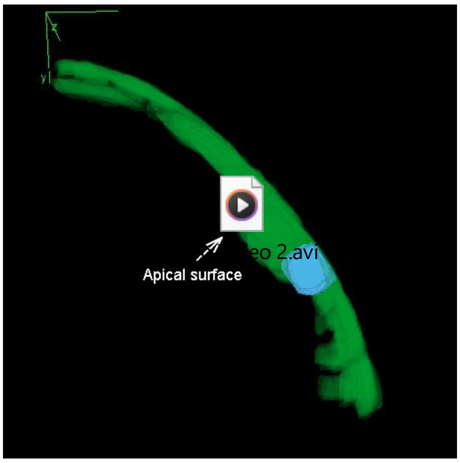

Supplementary Video 3 – Manually segmented anterior pillar of the zebrafish inner ear at 62.5 hpf.

Manually segmented cells from the anterior pillar (tubular structure) of the zebrafish inner ear at 62.5 hours post fertilisation (hpf). The anterior pillar is formed by the fusion of the anterior projection with the anterior bulge of the lateral projection. Manual segmentation was performed in Fiji (see methods 2.5.1 for details).

Supplementary Video 4 – Time-lapse the zebrafish inner ear from 39.5 to 52 hpf.

Time-lapse of the inner ear of a *Tg(smad6b:EGFP); Tg(xEF1A:H2B-RFP)* double transgenic embryo. Maximum intensity projection is shown to visualise formation of the anterior (left side) and posterior (right side) projections. Time-lapse was acquired in the Zeiss LSM 880 Airyscan confocal microscope, with time-points shown here between 39.5 and 52 hours post fertilisation (hpf).

Supplementary Video 5 – Formation of the posterior epithelial projection in zebrafish inner ear. Time-lapse of the inner ear posterior projection of a *Tg(smad6b:EGFP); Tg(xEF1A:H2B-RFP)* double transgenic embryo. Maximum intensity projection is shown to visualise a cohesive group of cells in the otic epithelium engaging in the formation of the posterior projection. Time-lapse was acquired in the Zeiss LSM 880 Airyscan confocal microscope, with time-points shown here between 43.5 and 51.5 hours post fertilisation (hpf). Dorsal side is to the top and posterior to the right. Coloured spheres mark tracked cells that become part of the projection.

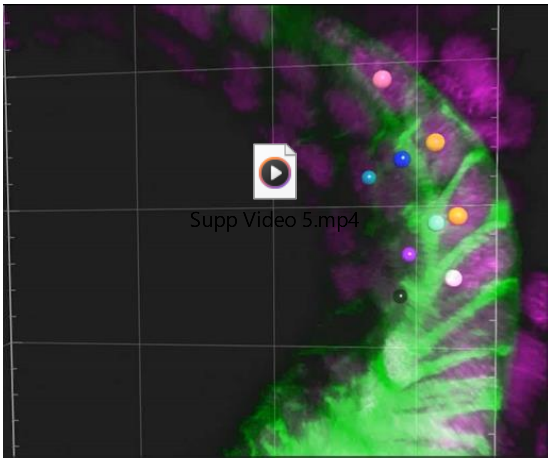

Supplementary Figure 1 – 3D cell shape changes in projection cells before and during folding of the otic epithelium.

(A) Maximum intensity projections of *z*-stacks of the posterior region of the otic vesicle of embryo 2. These were acquired in the Airyscan ZEISS LSM 880 confocal microscope. Cell membranes are transgenically labelled (*Tg(smad6b:EGFP)*), and cells marked by the coloured spheres were tracked. Scale bar measures 20 µm. **(B-D)** 3D pictures of segmented cells of the posterior region of the otic vesicle of embryo 2. In **(B)**, cells are colour coded with darker green for higher values of mean curvature and dark brown for lower values of mean curvature. In **(C)**, cells are colour coded with darker blue for higher values of cell skewness and lighter blue/white for lower values of cell skewness. In **(D)**, cells are colour coded with darker green for higher values of longitudinal spread and lighter green/white for lower values of longitudinal spread.

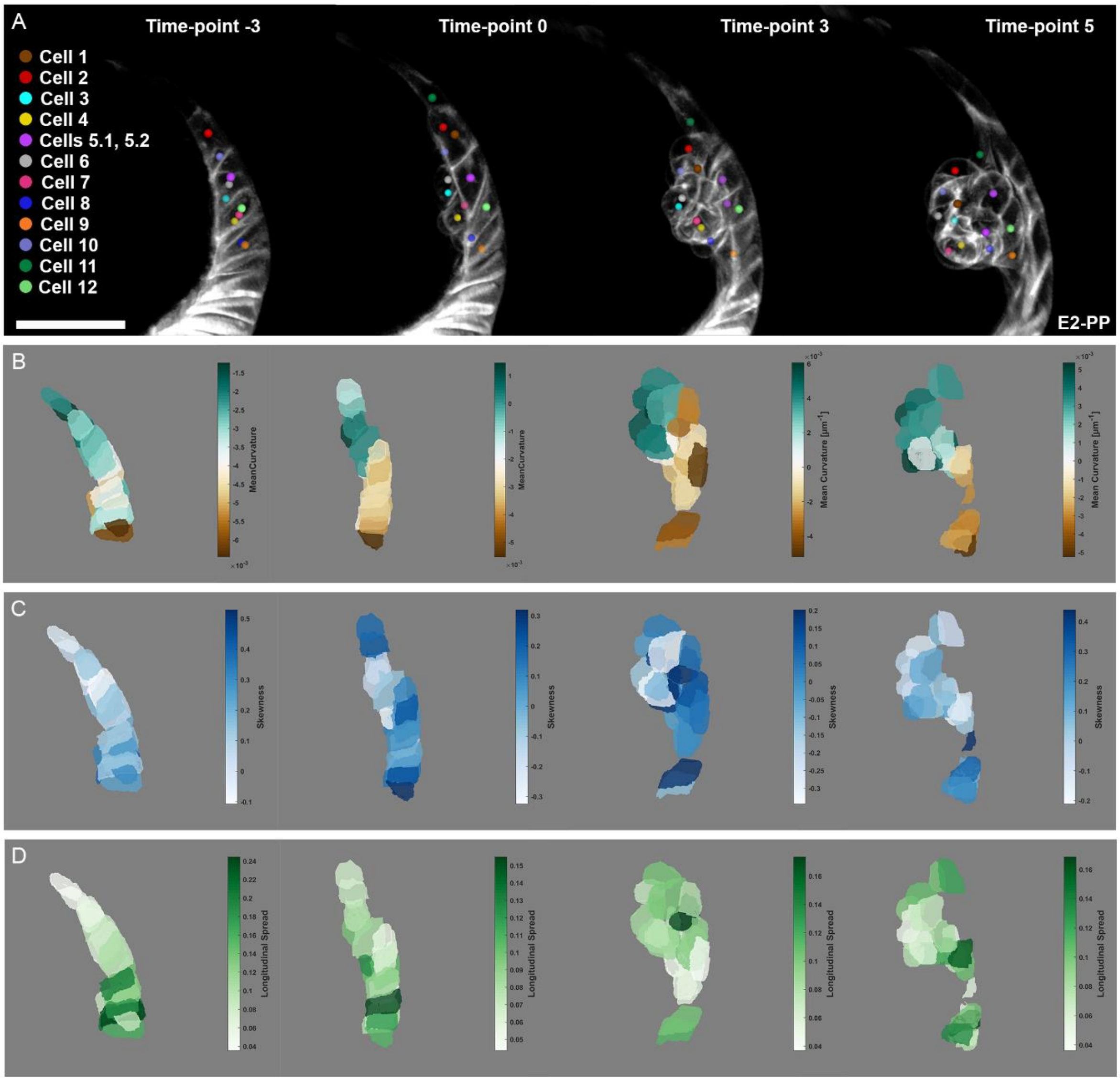

Supplementary Figure 2 – Adhesion, cytoskeletal and polarity proteins before and after the folding event.

Shift of Ecad (**A** and **A'**), phalloidin (**B** and **B'**) and myosin-II (**C** and **C'**) from apical to basolateral domain of projection cells is shown here. E-cadherin (**A** and **A'**), ZO-1 (**D** and **D'**) and Pard3 (**E** and **E'**) antibody staining, phalloidin staining (**B** and **B'**) and GFP boost of *Tg(actβ2:myl12.1-EGFP)* fixed embryos (**C and C'**) were performed. Pictures were taken on a Nikon inverted confocal microscope with a 40X oil immersion objective. A single slice of a *z*-stack is shown in each picture. Arrowheads point to the apical surface of the epithelium and asterisks mark an example of surrounding tissue. Scale bars measure 20 µm.

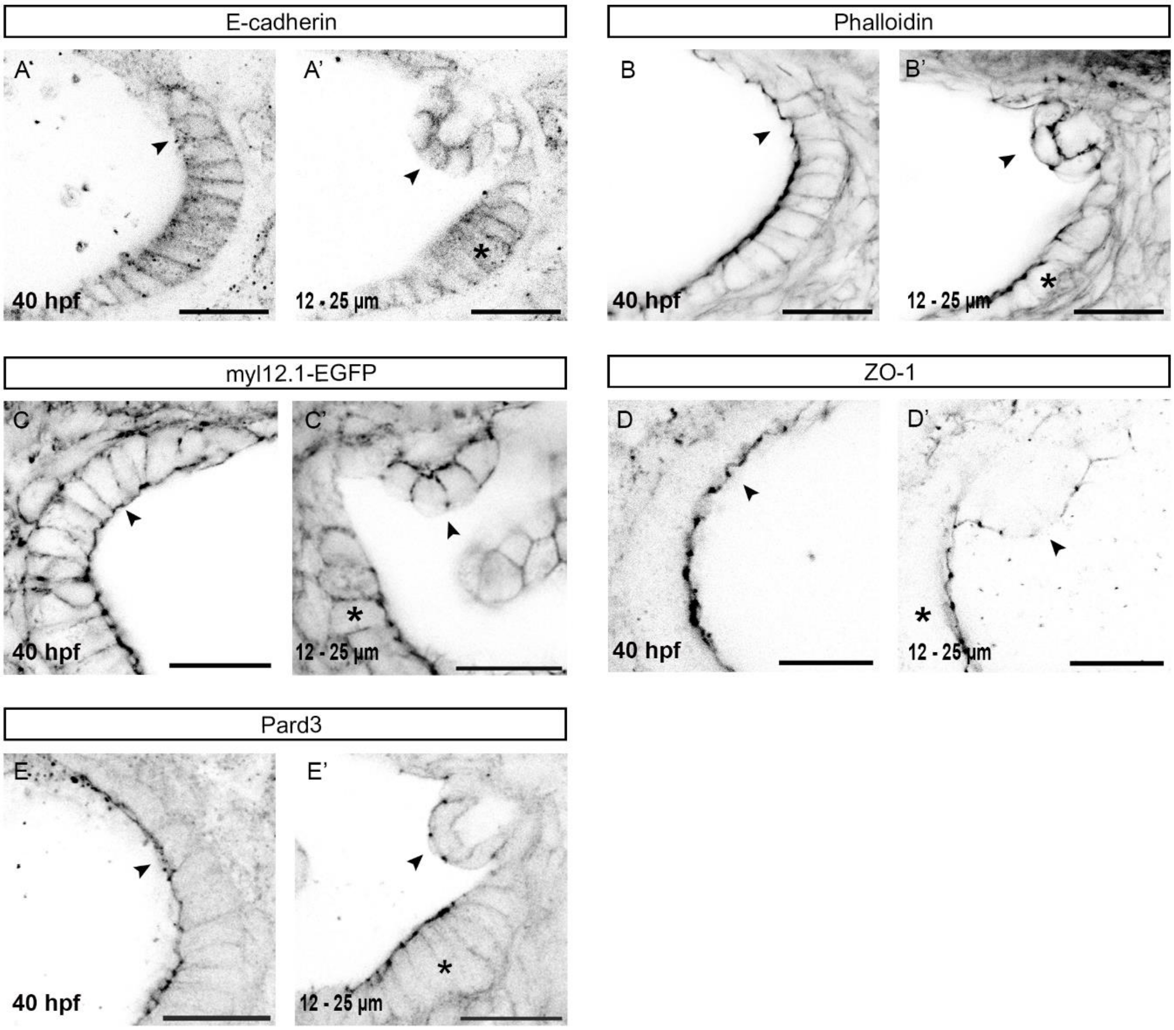

REFERENCES

Abdelhak, S., Kalatzis, V., Heilig, R., Com Pain, S., Samson, D., Vincent, C., Weil, D., Cruaud, C., Sahly, I., Leibovici, M., et al. (1997). A human homologue of the Drosophila eyes absent gene underlies Branchio-Oto-Renal (BOR) syndrome and identifies a novel gene family. *Nat Genet* **15**, 157–164.

Abelló, G., Khatri, S., Radosevic, M., Scotting, P. J., Giráldez, F. and Alsina, B. (2010). Independent regulation of Sox3 and Lmx1b by FGF and BMP signaling influences the neurogenic and non-neurogenic domains in the chick otic placode. *Dev Biol* **339**, 166–178.

Adam, J., Myat, A., Roux, I. Le, Eddison, M., Henrique, D., Ish-Horowicz, D. and Lewis, J. (1998). Cell fate choices and the expression of Notch, Delta and Serrate homologues in the chick inner ear: parallels with Drosophila sense-organ development. *Development* **125**, 4645–4654.

Adams, M. W., Loftus, A. F., Dunn, S. E., Joens, M. S. and Fitzpatrick, J. A. J. (2015). Light Sheet Fluorescence Microscopy (LSFM). In *Current Protocols in Cytometry* (ed. Robinson, J. P.), Darzynkiewicz, Z.), Hoffman, R.), Nolan, J. P.), Rabinovitch, P. S.), and Watkins, S.), pp. 12.37.1-12.37.15. Hoboken, NJ, USA: John Wiley & Sons, Inc.

Alestrom, P., Angelo, L. D., Midtlyng, P. J., Schorderet, D. F., Schulte-Merker, S., Sohm, F. and Warner, S. (2020). Zebrafish : Housing and husbandry recommendations. *Lab Anim* **54**, 213–224.

Alfano, D., Altomonte, A., Cortes, C., Bilio, M., Kelly, R. G. and Baldini, A. (2019). Tbx1 regulates extracellular matrix-cell interactions in the second heart field. *Hum Mol Genet* **28**, 2295–2308.

Alonso, S. R., Tracey, L., Ortiz, P., Pérez-Gómez, B., Palacios, J., Pollán, M., Linares, J., Serrano, S., Sáez-Castillo, A. I., Sánchez, L., et al. (2007). A high-throughput study in melanoma identifies epithelial-mesenchymal transition as a major determinant of metastasis. *Cancer Res* **67**, 3450–3460.

Alsina, B. and Whitfield, T. T. (2016). Sculpting the labyrinth: Morphogenesis of the developing inner ear. *Semin Cell Dev Biol* **65**, 47–59.

Alvarez, I. S. and Navascués, J. (1990). Shaping, invagination, and closure of the chick embryo otic vesicle: Scanning electron microscopic and quantitative study. *Anat Rec* **228**, 315–326.

Araya, C., Häkkinen, H.-M., Carcamo, L., Cerda, M., Savy, T., Rookyard, C., Peyriéras, N. and Clarke, J. D. (2018). Cdh2 coordinates Myosin-II dependent internalisation of the zebrafish neural plate. *bioRxiv*.

Araya, C., Häkkinen, H. M., Carcamo, L., Cerda, M., Savy, T., Rookyard, C., Peyriéras, N. and Clarke, J. D. W. (2019). Cdh2 coordinates Myosin-II dependent internalisation of the zebrafish neural plate. *Sci Rep* **9**, 1–13.

Arnold, T. R., Stephenson, R. E. and Miller, A. L. (2017). Rho GTPases and actomyosin: Partners in regulating epithelial cell-cell junction structure and function. *Exp Cell Res* **358**, 20–30.

Aumailley, M. and Gayraud, B. (1998). Structure and biological activity of the extracellular matrix. *J Mol Med* **76**, 253–265.

Babb-Clendenon, S., Shen, Y. C., Liu, Q., Turner, K. E., Mills, M. S., Cook, G. W., Miller, C. A., Gattone, V. H., Barald, K. F. and Marrs, J. A. (2006). Cadherin-2 participates in the morphogenesis of the zebrafish inner ear. *J Cell Sci* **119**, 5169–5177.

Bailey, A. P. and Streit, A. (2005). Sensory Organs: Making and Breaking the Pre-Placodal Region. In *Current Topics in Developmental Biology*, pp. 167–204. Elsevier.

Bakkers, J., Kramer, C., Pothof, J., Quaedvlieg, N. E. M., Spaink, H. P. and Hammerschmidt, M. (2004). Has2 is required upstream of Rac1 to govern dorsal migration of lateral cells during zebrafish gastrulation. *Development* **131**, 525–537.

Baldera, D., Baxendale, S., van Hateren, N. J., Marzo, M., Glendenning, E., Geng, F. S., Yokoya, K., Knight, R. D. and Whitfield, T. T. (2023). Enhancer trap lines with GFP driven by smad6b and frizzled1 regulatory sequences for the study of epithelial morphogenesis in the developing zebrafish inner ear. *J Anat*.

Barembaum, M. and Bronner-Fraser, M. (2007). Spalt4 mediates invagination and otic placode gene expression in cranial ectoderm. *Development* **134**, 3805–3814.

Barrallo-Gimeno, A. and Nieto, M. A. (2005). The Snail genes as inducers of cell movement and survival: Implications in development and cancer. *Development* **132**, 3151–3161.

Barrett, K., Leptin, M. and Settleman, J. (1997). The Rho GTPase and a Putative RhoGEF Mediate a Signaling Pathway for the Cell Shape Changes in Drosophila Gastrulation. *Cell* **91**, 905–915.

Bedzhov, I. and Zernicka-Goetz, M. (2014). Self-organizing properties of mouse pluripotent cells initiate morphogenesis upon implantation. *Cell* **156**, 1032–1044.

Beis, D., Bartman, T., Jin, S.-W., Scott, I. C., D'Amico, L. A., Ober, E. A., Verkade, H., Frantsve, J., Field, H. A., Wehman, A., et al. (2005). Genetic and cellular analyses of zebrafish atrioventricular cushion and valve development. *Development* **132**, 4193–4204.

Belal, A. J. and Antunez, J. (1980). Pathology of endolymphatic hydrops. *J Laryngol Otol* **94**, 1231–1240.

Bhat, N. and Riley, B. B. (2011a). Integrin-α5 coordinates assembly of posterior cranial placodes in zebrafish and enhances Fgf-dependent regulation of otic/epibranchial cells. *PLoS One* **6**,.

Bhat, N. and Riley, B. B. (2011b). Integrin-α5 coordinates assembly of posterior cranial placodes in zebrafish and enhances Fgf-dependent regulation of otic/epibranchial cells. *PLoS One* **6**,.

Bhat, N., Kwon, H. J. and Riley, B. B. (2013). A gene network that coordinates preplacodal competence and neural crest specification in zebrafish. *Dev Biol* **373**, 107–117.

Bishop, J. R., Schuksz, M. and Esko, J. D. (2007). Heparan sulphate proteoglycans fine-tune mammalian physiology. *Nature* **446**, 1030–1037.

Bray, D. and White, J. (1988). Cortical flow in animal cells. *Science (1979)* **239**, 883–888.

Brown, S. T., Wang, J. and Groves, A. K. (2005). Dlx gene expression during chick inner ear development. *Journal of Comparative Neurology* **483**, 48–65.

Bryan, C. D., Chien, C. bin and Kwan, K. M. (2016). Loss of laminin alpha 1 results in multiple structural defects and divergent effects on adhesion during vertebrate optic cup morphogenesis. *Dev Biol* **416**, 324–337.

Bryan, C. D., Casey, M. A., Pfeiffer, R. L., Jones, B. W. and Kwan, K. M. (2020). Optic cup morphogenesis requires neural crest-mediated basement membrane assembly. *Development (Cambridge)* **147**,.

Busch-Nentwich, E., Sollner, C., Roehl, H. and Nicolson, T. (2004). The deafness gene dfna5 is crucial for ugdh expression and HA production in the developing ear in zebrafish. *Development* **131**, 943–951.

Buxboim, A. and Discher, D. E. (2012). Mechanical Interactions between Cells and Tissues. In *Polymer Science: A Comprehensive Reference*, pp. 201–209. Elsevier.

Camarata, T., Krcmery, J., Snyder, D., Park, S., Topczewski, J. and Simon, H. G. (2010). Pdlim7 (LMP4) regulation of Tbx5 specifies zebrafish heart atrio-ventricular boundary and valve formation. *Dev Biol* **337**, 233–245.

Campbell, K. and Casanova, J. (2015). A role for E-cadherin in ensuring cohesive migration of a heterogeneous population of non-epithelial cells. *Nat Commun* **6**, 1–11.

Campbell, K. and Casanova, J. (2016). A common framework for EMT and collective cell migration. *Development* **143**, 4291–4300.

Campbell, K., Casanova, J. and Skaer, H. (2010). Mesenchymal-to-epithelial transition of intercalating cells in Drosophila renal tubules depends on polarity cues from epithelial neighbours. *Mech Dev* **127**, 345–357.

Cao, J., Guan, G., Ho, V. W. S., Wong, M. K., Chan, L. Y., Tang, C., Zhao, Z. and Yan, H. (2020). Establishment of a morphological atlas of the Caenorhabditis elegans embryo using deep-learning-based 4D segmentation. *Nat Commun* **11**,.

Chi, N. C., Shaw, R. M., Val, S. De, Kang, G., Jan, L. Y., Black, B. L. and Stainier, D. Y. R. (2008). Foxn4 directly regulates tbx2b expression and atrioventricular canal formation. *Genes Dev* 734–739.

Christophorou, N. A. D., Mende, M., Lleras-Forero, L., Grocott, T. and Streit, A. (2010). Pax2 coordinates epithelial morphogenesis and cell fate in the inner ear. *Dev Biol* **345**, 180–190.

Comper, W. D. and Laurent, T. C. (1978). Physiological function of connective tissue polysaccharides. *Physiol Rev* **58**, 255–315.

Coravos, J. S. and Martin, A. C. (2016). Apical Sarcomere-like Actomyosin Contracts Nonmuscle Drosophila Epithelial Cells. *Dev Cell* **39**, 346–358.

Costa, M., Sweeton, D. and Wieschaus, E. (1993). Gastrulation in Drosophila: Cellular mechanisms of morphogenetic movements. In *The development of Drosophila melanogaster.*, pp. 425–465.

Costa, M., Wilson, E. T. and Wieschaus, E. (1994). A putative cell signal encoded by the folded gastrulation gene coordinates cell shape changes during Drosophila gastrulation. *Cell* **76**, 1075–1089.

Cowman, M. K., Schmidt, T. A., Raghavan, P. and Stecco, A. (2015). Viscoelastic Properties of Hyaluronan in Physiological Conditions. *F1000Res* **4**, 622.

Cunliffe, V. T. (2004). Histone deacetylase 1 is required to repress Notch target gene expression during zebrafish neurogenesis and to maintain the production of motoneurones in response to hedgehog signalling. *Development* **131**, 2983–2995.

Czyz, J. and Wobus, A. M. (2001). Embryonic stem cell differentiation: The role of extracellular factors. *Differentiation* **68**, 167–174.

Dai, J. S. (2015). Euler-Rodrigues formula variations, quaternion conjugation and intrinsic connections. *Mech Mach Theory* **92**, 144–152.

Davidson, L. A. (2012). Epithelial machines that shape the embryo. *Trends Cell Biol* **22**, 82–87.

Dawes-Hoang, R. E., Parmar, K. M., Christiansen, A. E., Phelps, C. B., Brand, A. H. and Wieschaus, E. F. (2005). folded gastrulation, cell shape change and the control of myosin localization. *Development* **132**, 4165–4178.

Dierick, H. A. and Bejsovec, A. (1998). Functional analysis of Wingless reveals a link between intercellular ligand transport and dorsal-cell-specific signaling. *Development* **125**, 4729–4738.

Dong, B., Deng, W. and Jiang, D. (2011). Distinct cytoskeleton populations and extensive crosstalk control Ciona notochord tubulogenesis. *Development* **138**, 1631–1641.

Driever, W. and Nüsslein-Volhard, C. (1988). The bicoid protein determines position in the Drosophila embryo in a concentration-dependent manner. *Cell* **54**, 95–104.

Dutton, K., Abbas, L., Spencer, J., Brannon, C., Mowbray, C., Nikaido, M., Kelsh, R. N. and Whitfield, T. T. (2009). A zebrafish model for Waardenburg syndrome type IV reveals diverse roles for Sox10 in the otic vesicle. *Dis Model Mech* **2**, 68–83.

Dyballa, S., Savy, T., Germann, P., Mikula, K., Remesikova, M., Špir, R., Zecca, A., Peyriéras, N. and Pujades, C. (2017). Distribution of neurosensory progenitor pools during inner ear morphogenesis unveiled by cell lineage reconstruction. *Elife* **6**, 1–22.

Dzamba, B. J., Jakab, K. R., Marsden, M., Schwartz, M. A. and DeSimone, D. W. (2009). Cadherin Adhesion, Tissue Tension, and Noncanonical Wnt Signaling Regulate Fibronectin Matrix Organization. *Dev Cell* **16**, 421–432.

Edelblum, K. L. and Turner, J. R. (2015). Epithelial Cells. In *Mucosal Immunology*, pp. 187–210. Elsevier.

Elliott, A. D. (2020). Confocal Microscopy: Principles and Modern Practices. *Curr Protoc Cytom* **92**,.

Ernst, S., Liu, K., Agarwala, S., Moratscheck, N., Avci, M. E., Nogare, D. D., Chitnis, A. B., Ronneberger, O. and Lecaudey, V. (2012). Shroom3 is required downstream of FGF signalling to mediate proneuromast assembly in zebrafish. *Development* **139**, 4571–4581.

Espina, J. A., Cordeiro, M. H. and Barriga, E. H. (2023). Tissue interplay during morphogenesis. *Semin Cell Dev Biol*.

Filipek-Górniok, B., Holmborn, K., Haitina, T., Habicher, J., Oliveira, M. B., Hellgren, C., Eriksson, I., Kjellén, L., Kreuger, J. and Ledin, J. (2013). Expression of chondroitin/dermatan sulfate glycosyltransferases during early zebrafish development. *Developmental Dynamics* **242**, 964–975.

Fraser, J. R. E., Laurent, T. C. and Laurent, U. B. G. (1997). Hyaluronan: Its nature, distribution, functions and turnover. In *Journal of Internal Medicine*, pp. 27–33. Blackwell Publishing Ltd.

Freeman, S. D., Keino-Masu, K., Masu, M. and Ladher, R. K. (2015). Expression of the Heparan Sulfate 6-O-endosulfatases, Sulf1 and Sulf2, in the Avian and Mammalian Inner Ear Suggests a Role for Sulfation during Inner Ear Development. *Developmental Dynamics* **244**, 168–180.

Freter, S., Muta, Y., Mak, S. S., Rinkwitz, S. and Ladher, R. K. (2008). Progressive restriction of otic fate: The role of FGF and Wnt in resolving inner ear potential. *Development* **135**, 3415–3424.

Fuse, N., Yu, F. and Hirose, S. (2013). Gprk2 adjusts Fog signaling to organize cell movements in Drosophila gastrulation. *Development (Cambridge)* **140**, 4246–4255.

Garantziotis, S. and Savani, R. C. (2019). Hyaluronan biology: A complex balancing act of structure, function, location and context. *Matrix Biology* **78–79**, 1–10.

Geng, F.-S., Abbas, L., Baxendale, S., Holdsworth, C. J., Swanson, A. G., Slanchev, K., Hammerschmidt, M., Topczewski, J. and Whitfield, T. T. (2013). Semicircular canal morphogenesis in the zebrafish inner ear requires the function of gpr126 (lauscher), an adhesion class G protein-coupled receptor gene. *Development* **140**, 4362–4374.

Gheisari, E., Aakhte, M. and Müller, H.-A. J. (2020). Gastrulation in Drosophila melanogaster: Genetic control, cellular basis and biomechanics. *Mech Dev* **163**, 103629.

Gilmour, D., Rembold, M. and Leptin, M. (2017). From morphogen to morphogenesis and back. *Nature* **541**, 311–320.

Gómez-Gálvez, P., Vicente-Munuera, P., Tagua, A., Forja, C., Castro, A. M., Letrán, M., Valencia-Expósito, A., Grima, C., Bermúdez-Gallardo, M., Serrano-Pérez-Higueras, Ó., et al. (2018a). Scutoids are a geometrical solution to three-dimensional packing of epithelia. *Nat Commun* **9**, 1–14.

Gómez-Gálvez, P., Vicente-Munuera, P., Tagua, A., Forja, C., Castro, A. M., Letrán, M., Valencia-Expósito, A., Grima, C., Bermúdez-Gallardo, M., Serrano-Pérez-Higueras, Ó., et al. (2018b). Scutoids are a geometrical solution to three-dimensional packing of epithelia. *Nat Commun* **9**, 1–14.

Gracia, M., Theis, S., Proag, A., Gay, G., Benassayag, C. and Suzanne, M. (2019). Mechanical impact of epithelial−mesenchymal transition on epithelial morphogenesis in Drosophila. *Nat Commun* **10**,.

Graham, A. and Begbie, J. (2000). Neurogenic placodes: a common front. *Trends Neurosci* **23**, 313–316.

Grau, Y., Carteret, C. and Simpson, P. (1984). Mutations and chromosomal rearrangements affecting the expression of snail, a gene involved in embryonic patterning in drosophila melanogaster. *Genetics* **108**, 347–360.

Gray, J. J. and Kline, M. (1980). Olinde Rodrigues' Paper of 1840 on Transformation Groups. *Arch Hist Exact Sci* **21**, 375–385.

Gross, J. C., Chaudhary, V., Bartscherer, K. and Boutros, M. (2012). Active Wnt proteins are secreted on exosomes. *Nat Cell Biol* **14**, 1036–1045.

Gunawan, F., Gentile, A., Fukuda, R., Tsedeke, A. T., Jiménez-Amilburu, V., Ramadass, R., Iida, A., Sehara-Fujisawa, A. and Stainier, D. Y. R. (2019). Focal adhesions are essential to drive zebrafish heart valve morphogenesis. *Journal of Cell Biology* **218**, 1039–1054.

Guthrie, S., Turint, L. and Warner, A. (1988). *Patterns of junctional communication during development of the early amphibian embryo*.

Gutzman, J. H., Graeden, E. G., Lowery, L. A., Holley, H. S. and Sive, H. (2008). Formation of the zebrafish midbrain-hindbrain boundary constriction requires laminin-dependent basal constriction. *Mech Dev* **125**, 974–983.

Gutzman, J. H., Sahu, S. U. and Kwas, C. (2015). Non-muscle myosin IIA and IIB differentially regulate cell shape changes during zebrafish brain morphogenesis. *Dev Biol* **397**, 103–115.

Gutzman, J. H., Graeden, E., Brachmann, I., Yamazoe, S., Chen, J. K. and Sive, H. (2018). Basal constriction during midbrain-hindbrain boundary morphogenesis is mediated by Wnt5b and Focal Adhesion Kinase. **6**, 1–8.

Habicher, J., Varshney, G. K., Waldmann, L., Snitting, D., Allalou, A., Zhang, H., Ghanem, A., Öhman Mägi, C., Dierker, T., Kjellén, L., et al. (2022). Chondroitin/dermatan sulfate glycosyltransferase genes are essential for craniofacial development. *PLoS Genet* **18**,.

Häcker, U. and Perrimon, N. (1998). DRhoGEF2 encodes a member of the Dbl family of oncogenes and controls cell shape changes during gastrulation in Drosophila. *Genes Dev* **12**, 274–284.

Haddon, C. M. and Lewis, J. H. (1991). Hyaluronan as a propellant for epithelial movement: the development of semicircular canals in the inner ear of Xenopus. *Development* **112**, 541–550.

Haddon, C. and Lewis, J. (1996). Early ear development in the embryo of the zebrafish, Danio rerio. *Journal of Comparative Neurology* **365**, 113–128.

Haddon, C., Jiang, Y., Smithers, L. and Lewis, J. (1998). Delta-Notch signalling and the patterning of sensory cell differentiation in thezebrafish ear: evidence from the mind bomb mutant. *Development* 4637–4644.

Hammond, K. L. and Whitfield, T. T. (2006). The developing lamprey ear closely resembles the zebrafish otic vesicle: otx1 expression can account for all major patterning differences. *Development* **133**, 1347–1357.

Hammond, K. L., Loynes, H. E., Mowbray, C., Runke, G., Hammerschmidt, M., Mullins, M. C., Hildreth, V., Chaudhry, B. and Whitfield, T. T. (2009). A late role for bmp2b in the morphogenesis of semicircular canal ducts in the zebrafish inner ear. *PLoS One* **4**, e4368.

Hammond, K. L., van Eeden, F. J. M. and Whitfield, T. T. (2010). Repression of Hedgehog signalling is required for the acquisition of dorsolateral cell fates in the zebrafish otic vesicle. *Development* **137**, 1361–1371.

Harden, M. V., Pereiro, L., Ramialison, M., Wittbrodt, J., Prasad, M. K., Mccallion, A. S. and Whitlock, K. E. (2012). Close association of olfactory placode precursors and cranial neural crest cells does not predestine cell mixing. *Developmental Dynamics* **241**, 1143–1154.

Hartmann, J., Wong, M., Gallo, E. and Gilmour, D. (2020). An image-based data-driven analysis of cellular architecture in a developing tissue. *Elife* **9**, 1–33.

Hayes, J. M., Hartsock, A., Clark, B. S., Napier, H. R. L., Link, B. A. and Gross, J. M. (2012). Integrin α5/fibronectin1 and focal adhesion kinase are required for lens fiber morphogenesis in zebrafish. *Mol Biol Cell* **23**, 4725–4738.

Hayward, D. C., Miller, D. J. and Ball, E. E. (2004). Snail expression during embryonic development of the coral Acropora: Blurring the diploblast/triploblast divide? *Dev Genes Evol* **214**, 257–260.

Hilfer, S. R. and Randolph, G. J. (1993). Immunolocalization of basal lamina components during development of chick otic and optic primordia. *Anat Rec* **235**, 443–452.

Hoijman, E., Rubbini, D., Colombelli, J. and Alsina, B. (2015). Mitotic cell rounding and epithelial thinning regulate lumen growth and shape. *Nat Commun* **6**, 1–13.

Holmborn, K., Habicher, J., Kasza, Z., Eriksson, A. S., Filipek-Gorniok, B., Gopal, S., Couchman, J. R., Ahlberg, P. E., Wiweger, M., Spillmann, D., et al. (2012). On the roles and regulation of chondroitin sulfate and heparan sulfate in zebrafish pharyngeal cartilage morphogenesis. *Journal of Biological Chemistry* **287**, 33905–33916.

Horikoshi, Y., Suzuki, A., Yamanaka, T., Sasaki, K., Mizuno, K., Sawada, H., Yonemura, S. and Ohno, S. (2009). Interaction between PAR-3 and the aPKC-PAR-6 complex is indispensable for apical domain development of epithelial cells. *J Cell Sci* **122**, 1595–1606.

Huff, J. (2015). The Airyscan detector from ZEISS: confocal imaging with improved signal-to-noise ratio and super-resolution. *Nat Methods* **12**, ii.

Hurle, J. M. and Colvee, E. (1982). *Surface changes in the embryonic interdigital epithelium during the formation of the free digits: a comparative study in the chick and duck foot*.

Iozzo, R. V. and Schaefer, L. (2015). Proteoglycan form and function: A comprehensive nomenclature of proteoglycans. *Matrix Biology* **42**, 11–55.

Jakeman, L. B., Williams, K. E. and Brautigam, B. (2014). In the presence of danger: The extracellular matrix defensive response to central nervous system injury. *Neural Regen Res* **9**, 377–384.

John, A. and Rauzi, M. (2021). Composite morphogenesis during embryo development. *Semin Cell Dev Biol* **120**, 119–132.

Johnson, J. and Lalwani, A. (2000). Sensorineural and conductive hearing loss associated with lateral semicircular canal malformation. *Laryngoscope* **110**, 1673–1679.

Jokela, T. A., Jauhiainen, M., Auriola, S., Kauhanen, M., Tiihonen, R., Tammi, M. I. and Tammi, R. H. (2008). Mannose inhibits hyaluronan synthesis by down-regulation of the cellular pool of UDP-N-acetylhexosamines. *Journal of Biological Chemistry* **283**, 7666–7673.

Jones, A. A., Diamantopoulou, E., Baxendale, S. and Whitfield, T. T. (2022). Presence of chondroitin sulphate and requirement for heparan sulphate biosynthesis in the developing zebrafish inner ear. *Front Cell Dev Biol* **10**,.

Kakizaki, I., Kojima, K., Takagaki, K., Endo, M., Kannagi, R., Ito, M., Maruo, Y., Sato, H., Yasuda, T., Mita, S., et al. (2004). A novel mechanism for the inhibition of hyaluronan biosynthesis by 4-methylumbelliferone. *Journal of Biological Chemistry* **279**, 33281–33289.

Kam, Z., Minden, J. S., Agard, D. A., Sedat, J. W. and Leptin, M. (1991). *Drosophila gastrulation: analysis of cell shape changes in living embryos by three-dimensional fluorescence microscopy*.

Kashgari, G., Meinecke, L., Gordon, W., Ruiz, B., Yang, J., Ma, A. L., Xie, Y., Ho, H., Plikus, M. v., Nie, Q., et al. (2020). Epithelial Migration and Non-adhesive Periderm Are Required for Digit Separation during Mammalian Development. *Dev Cell* **52**, 764-778.e4.

Kaufmann, A., Mickoleit, M., Weber, M. and Huisken, J. (2012). Multilayer mounting enables long-term imaging of zebrafish development in a light sheet microscope. *Development* **139**, 3242–3247.

Keller, P. J., Schmidt, A. D., Wittbrodt, J. and Stelzer, E. H. K. (2008). Reconstruction of Zebrafish Early Embryonic Development by Scanned Light Sheet Microscopy. *Science (1979)* **322**, 1065–1069.

Keller, K. E., Sun, Y. Y., Vranka, J. A., Hayashi, L. and Acott, T. S. (2012). Inhibition of Hyaluronan Synthesis Reduces Versican and Fibronectin Levels in Trabecular Meshwork Cells. *PLoS One* **7**, 1–12.

Kerridge, S., Munjal, A., Philippe, J. M., Jha, A., De Las Bayonas, A. G., Saurin, A. J. and Lecuit, T. (2016). Modular activation of Rho1 by GPCR signalling imparts polarized myosin II activation during morphogenesis. *Nat Cell Biol* **18**, 261–270.

Khan, Z., Wang, Y.-C., Wieschaus, E. F. and Kaschube, M. (2014). Quantitative 4D analyses of epithelial folding during Drosophila gastrulation. *Development* **141**, 2895–2900.

Khatri, S. B., Edlund, R. K. and Groves, A. K. (2014). Foxi3 is necessary for the induction of the chick otic placode in response to FGF signaling. *Dev Biol* **391**, 158–169.

Kim, H. J., Ryu, J., Woo, H. M., Cho, S. S., Sung, M. K., Kim, S. C., Park, M. H., Park, T. and Koo, S. K. (2014). Patterns of gene expression associated with Pten deficiency in the developing inner ear. *PLoS One* **9**,.

Kimmel, C. B., Ballard, W. W., Kimmel, S. R., Ullmann, B. and Schilling, T. F. (1995a). Stages of embryonic development of the zebrafish. *Developmental Dynamics* **203**, 253–310.

Kimmel, C. B., Ballard, W. W., Kimmel, S. R., Ullmann, B. and Schilling, T. F. (1995b). Stages of embryonic development of the zebrafish. *Dev Dyn* **203**, 253–310.

Kinoshita, N., Sasai, N., Misaki, K. and Yonemura, S. (2008). Apical accumulation of Rho in the neural plate is important for neural plate cell shape change and neural tube formation. *Mol Biol Cell* **19**, 2289–2299.

Kolsch, V., Seher, T., Fernandez-Ballester, G. J., Serrano, L. and Leptin, M. (2007). Control of Drosophila Gastrulation by Apical Localization of Adherens Junctions and RhoGEF2. *Science (1979)* **315**, 384–386.

Kovács, M., Tóth, J., Hetényi, C., Málnási-Csizmadia, A. and Seller, J. R. (2004). Mechanism of blebbistatin inhibition of myosin II. *Journal of Biological Chemistry* **279**, 35557–35563.

Koziel, L., Kunath, M., Kelly, O. G. and Vortkamp, A. (2004). *Ext1-Dependent Heparan Sulfate Regulates the Range of Ihh Signaling during Endochondral Ossification*.

Kozlowski, D. J., Whitfield, T. T., Hukriede, N. A., Lam, W. K. and Weinberg, E. S. (2005). The zebrafish dog-eared mutation disrupts eya1, a gene required for cell survival and differentiation in the inner ear and lateral line. *Dev Biol* **277**, 27–41.

Kreuger, J., Spillmann, D., Li, J. and Lindahl, U. (2006). Interactions between heparan sulfate and proteins: the concept of specificity. *J Cell Biol* **174**, 323–327.

Krueger, D., Tardivo, P., Nguyen, C. and de Renzis, S. (2018). Downregulation of basal myosin- II is required for cell shape changes and tissue invagination . *EMBO J* **37**, 1–16.

Kultti, A., Pasonen-Seppänen, S., Jauhiainen, M., Rilla, K. J., Kärnä, R., Pyöriä, E., Tammi, R. H. and Tammi, M. I. (2009). 4-Methylumbelliferone inhibits hyaluronan synthesis by depletion of cellular UDP-glucuronic acid and downregulation of hyaluronan synthase 2 and 3. *Exp Cell Res* **315**, 1914–1923.

Kumai, M., Nishii, K., Nakamura, K., Takeda, N., Suzuki, M. and Shibata, Y. (2000). Loss of connexin45 causes a cushion defect in early cardiogenesis. *Development* **127**, 3501–3512.

Kupaeva, D. M., Vetrova, A. A., Kraus, Y. A. and Kremnyov, S. v. (2018). Epithelial folding in the morphogenesis of the colonial marine hydrozoan, Dynamena pumila. *BioSystems* **173**, 157–164.

Ladher, R. K. (2017). Changing shape and shaping change: Inducing the inner ear. *Semin Cell Dev Biol* **65**, 39–46.

Lagendijk, A. K., Goumans, M. J., Burkhard, S. B. and Bakkers, J. (2011). MicroRNA-23 Restricts Cardiac Valve Formation by Inhibiting Has2 and Extracellular Hyaluronic Acid Production. *Circ Res* **109**, 649–657.

Landry, M. J., Rollet, F. G., Kennedy, T. E. and Barrett, C. J. (2018). Layers and Multilayers of Self-Assembled Polymers: Tunable Engineered Extracellular Matrix Coatings for Neural Cell Growth. *Langmuir* **34**, 8709–8730.

Lang, H., Bever, M. M. and Fekete, D. M. (2000). Cell proliferation and cell death in the developing chick inner ear: Spatial and temporal patterns. *Journal of Comparative Neurology* **417**, 205–220.

Lee, C., Scherr, H. M. and Wallingford, J. B. (2007). Shroom family proteins regulate -tubulin distribution and microtubule architecture during epithelial cell shape change. *Development* **134**, 1431–1441.

Leptin, M. and Grunewald, B. (1990). *Cell shape changes during gastrulation in Drosophila*.

Lewis, W. H. (1947). Mechanics of invagination. *Anat Rec* **97**, 139–156.

Li, Y., Laue, K., Temtamy, S., Aglan, M., Kotan, L. D., Yigit, G., Canan, H., Pawlik, B., Nürnberg, G., Wakeling, E. L., et al. (2010a). Temtamy preaxial brachydactyly syndrome is caused by loss-of-function mutations in chondroitin synthase 1, a potential target of BMP signaling. *Am J Hum Genet* **87**, 757–767.

Li, Y., Laue, K., Temtamy, S., Aglan, M., Kotan, L. D., Yigit, G., Canan, H., Pawlik, B., Nürnberg, G., Wakeling, E. L., et al. (2010b). Temtamy Preaxial Brachydactyly Syndrome Is Caused by Loss-of-Function Mutations in Chondroitin Synthase 1, a Potential Target of BMP Signaling. *The American Journal of Human Genetics* **87**, 757–767.

Lindahl, U., Couchman, J., Kimata, K. and Esko, J. D. (2017). *Essentials of Glycobiology*. Third. (ed. Varki A), Cummings RD), Esko JD), Stanley P), Hart GW), Aebi M), Darvill AG), Kinoshita T), Packer NH), Prestegard JHSchnaar RL), et al.) Cold Spring Harbor Laboratory Press.

Lister, J. A., Robertson, C. P., Lepage, T., Johnson, S. L. and Raible, D. W. (1999). nacre encodes a zebrafish microphthalmia-related protein that regulates neural-crest-derived pigment cell fate. *Development* **126**, 3757–3767.

Long, K. R., Newland, B., Florio, M., Kalebic, N., Langen, B., Kolterer, A., Wimberger, P. and Huttner, W. B. (2018). Extracellular Matrix Components HAPLN1, Lumican, and Collagen I Cause Hyaluronic Acid-Dependent Folding of the Developing Human Neocortex. *Neuron* **99**, 702-719.e7.

Maier, E. C. and Whitfield, T. T. (2014). RA and FGF Signalling Are Required in the Zebrafish Otic Vesicle to Pattern and Maintain Ventral Otic Identities. *PLoS Genet* **10**,.

Maier, E. C., Saxena, A., Alsina, B., Bronner, M. E. and Whitfield, T. T. (2014). Sensational placodes: Neurogenesis in the otic and olfactory systems. *Dev Biol* **389**, 50–67.

Maître, J.-L., Berthoumieux, H., Frederik, S., Krens, G., Salbreux, G., Jülicher, F., Paluch, E. and Heisenberg, C.-P. (2012). Adhesion Functions in Cell Sorting by Mechanically Coupling the Cortices of Adhering Cells. *Science (1979)* **338**, 253–256.

Manning, A. J. and Rogers, S. L. (2014). The Fog signaling pathway: Insights into signaling in morphogenesis. *Dev Biol* **394**, 6–14.

Manning, A. J., Peters, K. A., Peifer, M. and Rogers, S. L. (2013). Regulation of epithelial morphogenesis by the gprotein-coupled receptor mist and its ligand fog. *Sci Signal* **6**,.

Martin, P. and Swanson, G. J. (1993). Descriptive and Experimental Analysis of the Epithelial Remodellings That Control Semicircular Canal Formation in the Developing Mouse Inner Ear. *Dev Biol* **159**, 549–558.

Martin, A. C., Kaschube, M. and Wieschaus, E. F. (2009). Pulsed contractions of an actin–myosin network drive apical constriction. *Nature* **457**, 495–499.

Martin, A. C., Gelbart, M., Fernandez-Gonzalez, R., Kaschube, M. and Wieschaus, E. F. (2010). Integration of contractile forces during tissue invagination. *Journal of Cell Biology* **188**, 735–749.

Mason, F. M., Tworoger, M. and Martin, A. C. (2013). Apical domain polarization localizes actin-myosin activity to drive ratchet-like apical constriction. *Nat Cell Biol* **15**, 926–936.

Mateos, C. S. C., Valencia-Expósito, A., Palacios, I. M. and Martín-Bermudo, M. D. (2020). Integrins regulate epithelial cell shape by controlling the architecture and mechanical properties of basal actomyosin networks. *PLoS Genet* **16**,.

McCarroll, M. N., Lewis, Z. R., Culbertson, M. D., Martin, B. L., Kimelman, D. and Nechiporuk, A. V. (2012). Graded levels of Pax2a and Pax8 regulate cell differentiation during sensory placode formation. *Development* **139**, 2740–2750.

Mendonca, T., Jones, A. A., Pozo, J. M., Baxendale, S., Whitfield, T. T. and Frangi, A. F. (2021). Origami: Single-cell 3D shape dynamics oriented along the apico-basal axis of folding epithelia from fluorescence microscopy data. *PLoS Comput Biol* **17**,.

Merks, A. M., Swinarski, M., Meyer, A. M., Müller, N. V., Özcan, I., Donat, S., Burger, A., Gilbert, S., Mosimann, C., Abdelilah-Seyfried, S., et al. (2018). Planar cell polarity signalling coordinates heart tube remodelling through tissue-scale polarisation of actomyosin activity. *Nat Commun* **9**,.

Mikut, R., Dickmeis, T., Driever, W., Geurts, P., Hamprecht, F. A., Kausler, B. X., Ledesma-Carbayo, M. J., Marée, R., Mikula, K., Pantazis, P., et al. (2013). Automated Processing of Zebrafish Imaging Data: A Survey. *Zebrafish* **10**, 401–421.

Missinato, M. A., Tobita, K., Romano, N., Carroll, J. A. and Tsang, M. (2015). Extracellular component hyaluronic acid and its receptor Hmmr are required for epicardial EMT during heart regeneration. *Cardiovasc Res* **107**, 487–498.

Molè, M. A., Galea, G. L., Rolo, A., Weberling, A., Nychyk, O., de Castro, S. C., Savery, D., Fassler, R., Ybot-González, P., Greene, N. D. E., et al. (2020). Integrin-Mediated Focal Anchorage Drives Epithelial Zippering during Mouse Neural Tube Closure. *Dev Cell* **52**, 321–334.

Morize, P., Christiansen, A. E., Costa, M., Parks, S. and Wieschaus, E. (1998). Hyperactivation of the folded gastrulation pathway induces specific cell shape changes. *Development* **125**, 589–597.

Moro-Balbás, J. A., Gato, A., Alonso, M. I., Martín, P. and de la Mano, A. (2000). Basal lamina heparan sulphate proteoglycan is involved in otic placode invagination in chick embryos. *Anat Embryol (Berl)* **202**, 333–343.

Morsli, H., Tuorto, F., Choo, D., Postiglione, M. P., Simeone, A. and Wu, D. K. (1999). Otx1 and Otx2 activities are required for the normal development of the mouse inner ear. *Development* **126**, 2335–2343.

Mosaliganti, K. R., Noche, R. R., Xiong, F., Swinburne, I. A. and Megason, S. G. (2012). ACME : Automated Cell Morphology Extractor for Comprehensive Reconstruction of Cell Membranes. **8**,.

Mosaliganti, K. R., Swinburne, I. A., Chan, C. U., Obholzer, N. D., Green, A. A., Tanksale, S., Mahadevan, L. and Megason, S. G. (2019). Size control of the inner ear via hydraulic feedback. *Elife* **8**, 1–30.

Mott, J. D. and Werb, Z. (2004). Regulation of matrix biology by matrix metalloproteinases. *Curr Opin Cell Biol* **16**, 558–564.

Mouw, J. K., Ou, G. and Weaver, V. M. (2014). Extracellular matrix assembly: a multiscale deconstruction. *Nat Rev Mol Cell Biol* **15**, 771–785.

Munjal, A., Hannezo, E., Tsai, T. Y. C., Mitchison, T. J. and Megason, S. G. (2021). Extracellular hyaluronate pressure shaped by cellular tethers drives tissue morphogenesis. *Cell* **184**, 6313-6325.e18.

Nagy, N., Kuipers, H. F., Frymoyer, A. R., Ishak, H. D., Bollyky, J. B., Wight, T. N. and Bollyky, P. L. (2015). 4-Methylumbelliferone treatment and hyaluronan inhibition as a therapeutic strategy in inflammation, autoimmunity, and cancer. *Front Immunol* **6**, 1–11.

Nagy, N., Gurevich, I., Kuipers, H. F., Ruppert, S. M., Marshall, P. L., Xie, B. J., Sun, W., Malkovskiy, A. v., Rajadas, J., Grandoch, M., et al. (2019). 4-Methylumbelliferyl glucuronide contributes to hyaluronan synthesis inhibition. *Journal of Biological Chemistry* **294**, 7864–7877.

Neuhauss, S. C., Solnica-Krezel, L., Schier, A. F., Zwartkruis, F., Stemple, D. L., Malicki, J., Abdelilah, S., Stainier, D. Y. and Driever, W. (1996). Mutations affecting craniofacial development in zebrafish. *Development* **123**, 357–67.

Nibu, Y., Zhang, H., Bajor, E., Barolo, S., Small, S. and Levine, M. (1998). *dCtBP mediates transcriptional repression by Knirps, Krü ppel and Snail in the Drosophila embryo*.

Nicolás-Pérez, M., Kuchling, F., Letelier, J., Polvillo, R., Wittbrodt, J. and Martínez-Morales, J. R. (2016). Analysis of cellular behavior and cytoskeletal dynamics reveal a constriction mechanism driving optic cup morphogenesis. *Elife* **5**, 1–24.

Oda, H., Tsukita, S. and Takeichi, M. (1998). Dynamic Behavior of the Cadherin-Based Cell–Cell Adhesion System duringDrosophilaGastrulation. *Dev Biol* **203**, 435–450.

Ohta, S., Mansour, S. L. and Schoenwolf, G. C. (2010). BMP / SMAD signaling regulates the cell behaviors that drive the initial dorsal-specific regional morphogenesis of the otocyst. *Dev Biol* **347**, 369–381.

Ohyama, T., Mohamed, O. A., Taketo, M. M., Dufort, D. and Groves, A. K. (2006). Wnt signals mediate a fate decision between otic placode and epidermis. *Development* **133**, 865–875.

Ouyang, X., Panetta, N. J., Talbott, M. D., Payumo, A. Y., Halluin, C., Longaker, M. T. and Chen, J. K. (2017). Hyaluronic acid synthesis is required for zebrafish tail fin regeneration. *PLoS One* **12**, 1–22.

Padanad, M. S., Bhat, N., Guo, B. W. and Riley, B. B. (2012). Conditions that influence the response to Fgf during otic placode induction. *Dev Biol* **364**, 1–10.

Peal, D. S., Burns, C. G., Macrae, C. A. and Milan, D. (2009). Chondroitin sulfate expression is required for cardiac atrioventricular canal formation. *Developmental Dynamics* **238**, 3103–3110.

Peal, D. S., Lynch, S. N. and Milan, D. J. (2011). Patterning and development of the atrioventricular canal in zebrafish. *J Cardiovasc Transl Res* **4**, 720–726.

Pearl, E. J., Li, J. and Green, J. B. A. (2017). Cellular systems for epithelial invagination. *Philosophical Transactions of the Royal Society B: Biological Sciences* **372**, 20150526.

Pei, D., Shu, X., Gassama-Diagne, A. and Thiery, J. P. (2019). Mesenchymal–epithelial transition in development and reprogramming. *Nat Cell Biol* **21**, 44–53.

Piotrowski, T., Ahn, D. G., Schilling, T. F., Nair, S., Ruvinsky, I., Geisler, R., Rauch, G. J., Haffter, P., Zon, L. I., Zhou, Y., et al. (2003). The zebrafish van gogh mutation disrupts tbx1, which is involved in the DiGeorge deletion syndrome in humans. *Development* **130**, 5043–5052.

Pirvola, U., Zhang, X., Mantela, J., Ornitz, D. M. and Ylikoski, J. (2004). Fgf9 signaling regulates inner ear morphogenesis through epithelial–mesenchymal interactions. *Dev Biol* **273**, 350–360.

Qi, D., Bergman, M., Aihara, H., Nibu, Y. and Mannervik, M. (2008). Drosophila Ebi mediates Snail-dependent transcriptional repression through HDAC3-induced histone deacetylation. *EMBO Journal* **27**, 898–909.

Rauzi, M., Krzic, U., Saunders, T. E., Krajnc, M., Ziherl, P., Hufnagel, L. and Leptin, M. (2015). Embryo-scale tissue mechanics during Drosophila gastrulation movements. *Nat Commun* **6**,.

Rembold, M., Ciglar, L., Omar Yáñez-Cuna, J., Zinzen, R. P., Girardot, C., Jain, A., Welte, M. A., Stark, A., Leptin, M. and Furlong, E. E. M. (2014). A conserved role for Snail as a potentiator of active transcription. *Genes Dev* **28**, 167–181.

Rodríguez-Aznar, E., Barrallo-Gimeno, A. and Nieto, M. A. (2013). Scratch2 prevents cell cycle re-entry by repressing miR-25 in postmitotic primary neurons. *Ann Intern Med* **158**, 5095–5105.

Romand, R., Krezel, W., Beraneck, M., Cammas, L., Fraulob, V., Messaddeq, N., Kessler, P., Hashino, E. and Dollé, P. (2013). Retinoic Acid Deficiency Impairs the Vestibular Function. *The Journal of Neuroscience* **33**, 5856–5866.

Rosa, R. F. M., Silva, A. P. da, Goetze, T. B., Bier, B. de A., Almeida, S. T. de, Paskulin, G. A. and Zen, P. R. G. (2011). Ear abnormalities in patients with oculo-auriculo-vertebral spectrum (Goldenhar syndrome). *Braz J Otorhinolaryngol* **77**, 455–460.

Roth, S., Stein, D. and Niisslein-Volhard, C. (1989). *A Gradient of Nuclear Localization of the dorsal Protein Determines Dorsoventral Pattern in the Drosophila Embryo*.

Rushlow, C. A., Han, K., Manley, J. L. and Levine, M. (1969). *The Graded Distribution of the dorsal Morphogen Is Initiated by Selective Nuclear Transport in Drosophila*.

Sai, X. R. and Ladher, R. K. (2008). FGF Signaling Regulates Cytoskeletal Remodeling during Epithelial Morphogenesis. *Current Biology* **18**, 976–981.

Sai, X., Yonemura, S. and Ladher, R. K. (2014). Junctionally restricted RhoA activity is necessary for apical constriction during phase 2 inner ear placode invagination. *Dev Biol* **394**, 206–216.

Saika, S., Shirai, K., Yamanaka, O., Miyazaki, K. I., Okada, Y., Kitano, A., Flanders, K. C., Kon, S., Uede, T., Kao, W. W. Y., et al. (2007). Loss of osteopontin perturbs the epithelial-mesenchymal transition in an injured mouse lens epithelium. *Laboratory Investigation* **87**, 130–138.

Salminen, M., Meyer, B. I., Bober, E. and Gruss, P. (2000). netrin 1 is required for semicircular canal formation in the mouse inner ear. *Development* **127**, 13–22.

Sanchez-Corrales, Y. E., Blanchard, G. B. and Röper, K. (2018). Radially-patterned cell behaviours during tube budding from an epithelium. *Elife* **7**, e35717.

Sanders, T. A., Llagostera, E. and Barna, M. (2013). Specialized filopodia direct long-range transport of SHH during vertebrate tissue patterning. *Nature* **497**, 628–632.

Sandmann, T., Girardot, C., Brehme, M., Tongprasit, W., Stolc, V. and Furlong, E. E. M. (2007). A core transcriptional network for early mesoderm development in Drosophila melanogaster. *Genes Dev* **21**, 436–449.

Sawyer, J. M., Harrell, J. R., Shemer, G., Sullivan-Brown, J., Roh-Johnson, M. and Goldstein, B. (2010). Apical constriction: A cell shape change that can drive morphogenesis. *Dev Biol* **341**, 5–19.

Schuknecht, H. and Gulya, A. (1983). Endolymphatic hydrops. An overview and classification. *The Annals of otology, rhinilogy and laryngology. Supplement* **Sep-Oct**, 1–20.

Sidhaye, J. and Norden, C. (2017). Concerted action of neuroepithelial basal shrinkage and active epithelial migration ensures efficient optic cup morphogenesis. *Elife* **6**, 1–29.

Simpson, P. (1983). Maternal-zygotic gene interactions during formation of the dorsoventral pattern in drosophila embryos. *Genetics* **105**, 615–632.

Sinn, R. and Wittbrodt, J. (2013). An eye on eye development. *Mech Dev* **130**, 347–358.

Spear, P. C. and Erickson, C. A. (2012). Interkinetic nuclear migration: A mysterious process in search of a function. *Dev Growth Differ* **54**, 306–316.

Spencer, A. K., Siddiqui, B. A. and Thomas, J. H. (2015). Cell shape change and invagination of the cephalic furrow involves reorganization of F-actin. *Dev Biol* **402**, 192–207.

St Johnston, D. and Sanson, B. (2011). Epithelial polarity and morphogenesis. *Curr Opin Cell Biol* **23**, 540–546.

Stickens, D., Zak, B. M., Rougler, N., Esko, J. D. and Werb, Z. (2005). Mice deficient in Ext2 lack heparan sulfate and develop exostoses. *Development* **132**, 5055–5068.

Streuli, C. (1999). Extracellular matrix remodelling and cellular differentiation. *Curr Opin Cell Biol* 634–640.

Stringer, C., Wang, T., Michaelos, M. and Pachitariu, M. (2021). Cellpose: a generalist algorithm for cellular segmentation. *Nat Methods* **18**, 100–106.

Suhail, Y., Cain, M. P., Vanaja, K., Kurywchak, P. A., Levchenko, A., Kalluri, R. and Kshitiz (2019). Systems Biology of Cancer Metastasis. *Cell Syst* **9**, 109–127.

Sui, L., Alt, S., Weigert, M., Dye, N., Eaton, S., Jug, F., Myers, E. W., Jülicher, F., Salbreux, G. and Dahmann, C. (2018). Differential lateral and basal tension drive folding of Drosophila wing discs through two distinct mechanisms. *Nat Commun* **9**,.

Suk, J., Oohashi, T., Kawakami, Y., Bekku, Y. and Izpisu, J. C. (2004). Characterization of dermacan , a novel zebrafish lectican gene, expressed in dermal bones. **121**, 301–312.

Sulistomo, H. W., Nemoto, T., Yanagita, T. and Takeya, R. (2019). Formin homology 2 domain– containing 3 (Fhod3) controls neural plate morphogenesis in mouse cranial neurulation by regulating multidirectional apical constriction. *Journal of Biological Chemistry* **294**, 2924–2934.

Sumigray, K. D., Terwilliger, M. and Lechler, T. (2018). Morphogenesis and Compartmentalization of the Intestinal Crypt. *Dev Cell* **45**, 183-197.e5.

Sweeton, D., Parks, S., Costa, M. and Wieschaus, E. (1991). Gastrulation in Drosophila: the formation of the ventral furrow and posterior midgut invaginations. *Development* **112**, 775–789.

Swinburne, I. A., Mosaliganti, K. R., Green, A. A. and Megason, S. G. (2015). Improved Long-Term Imaging of Embryos with Genetically Encoded α-Bungarotoxin. *PLoS One* **10**, e0134005.

Swinburne, I. A., Mosaliganti, K. R., Upadhyayula, S., Liu, T.-L., Hildebrand, D. G. C., Tsai, T. Y.-C., Chen, A., Al-Obeidi, E., Fass, A. K., Malhotra, S., et al. (2018). Lamellar projections in the endolymphatic sac act as a relief valve to regulate inner ear pressure. *Elife*.

Sztal, T., Berger, S., Currie, P. D. and Hall, T. E. (2011). Characterization of the laminin gene family and evolution in zebrafish. *Developmental Dynamics* **240**, 422–431.

Taylor, J. M., Nelson, C. J., Bruton, F. A., Baghbadrani, A. K., Buckley, C., Tucker, C. S., Rossi, A. G., Mullins, J. J. and Denvir, M. A. (2019). Adaptive prospective optical gating enables day-long 3D time-lapse imaging of the beating embryonic zebrafish heart. *Nat Commun* **10**, 1–15.

Theveneau, E., Steventon, B., Scarpa, E., Garcia, S., Trepat, X., Streit, A. and Mayor, R. (2013). Chase-and-run between adjacent cell populations promotes directional collective migration. *Nat Cell Biol* **15**, 763–772.

Thisse, C. and Thisse, B. (2005). High Throughput Expression Analysis of ZF-Models Consortium Clones. *ZFIN Direct Data Submission*.

Thisse, C. and Thisse, B. (2008). High-resolution in situ hybridization to whole-mount zebrafish embryos. *Nat Protoc* **3**, 59–69.

Thisse, B., Stoetzel, C., Gorostiza-Thisse, C. and Perrin-Schmitt, F. (1988). *Sequence of the twist gene and nuclear localization of its protein in endomesodermal cells of early Drosophila embryos*.

Thisse, B., Pflumio, S., Furthauer, M., Loppin, B., Heyer, V., Degrave, A., Woehl, R., Lux, A., Steffan, T., Charbonnier, X. Q., et al. (2001). Expression of the zebrafish genome during embryogenesis (NIH R01 RR15402-01). *ZFIN Direct Data Submission* **5**, 0–2.

Tomer, R., Khairy, K., Amat, F. and Keller, P. J. (2012). Quantitative high-speed imaging of entire developing embryos with simultaneous multiview light-sheet microscopy. *Nat Methods* **9**, 755–763.

Toole, B. P. (2001). Hyaluronan in morphogenesis. *Semin Cell Dev Biol* **12**, 79–87.

Torres-Paz, J. and Whitlock, K. E. (2014). Olfactory sensory system develops from coordinated movements within the neural plate. *Developmental Dynamics* **243**, 1619–1631.

Trinh, L. A. and Stainier, Y. R. (2004). Fibronectin Regulates Epithelial Organization during Myocardial Migration in Zebrafish. *Dev Cell* **6**, 371–382.

Turner, F. R. and Mahowald, A. P. (1977). *Scanning Electron Microscopy of Drosophila melanogaster Em bryogenesis II. Gastrulation and Segmentation*.

Varner, V. D. and Nelson, C. M. (2014). Cellular and physical mechanisms of branching morphogenesis. *Development* **141**, 2750–2759.

Vasileva, E. and Citi, S. (2018). The role of microtubules in the regulation of epithelial junctions. *Tissue Barriers* **00**, 1–20.

Vigetti, D., Ori, M., Viola, M., Genasetti, A., Karousou, E., Rizzi, M., Pallotti, F., Nardi, I., Hascall, V. C., de Luca, G., et al. (2006). Molecular cloning and characterization of UDP-glucose dehydrogenase from the amphibian Xenopus laevis and its involvement in hyaluronan synthesis. *Journal of Biological Chemistry* **281**, 8254–8263.

Vigetti, D., Rizzi, M., Viola, M., Karousou, E., Genasetti, A., Clerici, M., Bartolini, B., Hascall, V. C., de Luca, G. and Passi, A. (2009). The effects of 4-methylumbelliferone on hyaluronan synthesis, MMP2 activity, proliferation, and motility of human aortic smooth muscle cells. *Glycobiology* **19**, 537–546.

Vigetti, D., Viola, M., Karousou, E., de Luca, G. and Passi, A. (2014). Metabolic control of hyaluronan synthases. *Matrix Biology* **35**, 8–13.

Visetsouk, M. R., Falat, E. J., Garde, R. J., Wendlick, J. L. and Gutzman, J. H. (2018). Basal epithelial tissue folding is mediated by differential regulation of microtubules. *Development (Cambridge)* **145**,.

Wang, J., Sridurongrit, S., Dudas, M., Thomas, P., Nagy, A., Schneider, M. D., Epstein, J. A. and Kaartinen, V. (2005). *Atrioventricular cushion transformation is mediated by ALK2 in the developing mouse heart*.

Wang, Y.-C., Khan, Z., Kaschube, M. and Wieschaus, E. F. (2012). Differential positioning of adherens junctions is associated with initiation of epithelial folding. *Nature* **484**, 390–393.

Wang, Y., Stonehouse-Smith, D., Cobourne, M. T., Green, J. B. A. and Seppala, M. (2022). Cellular mechanisms of reverse epithelial curvature in tissue morphogenesis. *Front Cell Dev Biol* **10**,.

Waterman, R. E. and Bell, D. H. (1984). Epithelial Fusion During Early Semicircular Canal Development in the Zebrafish, Brachydanio-Rerio. *Anatomical Record* **205**, A210–A210.

Weng, M. and Wieschaus, E. (2017). Polarity protein Par3/Bazooka follows myosin-dependent junction repositioning. *Physiol Behav* **176**, 139–148.

Westerfield, M. (2007). *The Zebrafish Book: A Guide for the Laboratory Use of Zebrafish (Danio rerio)*. 5th ed. Eugene: University of Oregon Press.

Williams, C. M., Engler, A. J., Slone, R. D., Galante, L. L. and Schwarzbauer, J. E. (2008). Fibronectin expression modulates mammary epithelial cell proliferation during acinar differentiation. *Cancer Res* **68**, 3185–3192.

Wineland, A., Menezes, M. D., Shimony, J. S., Shinawi, M. S., Hullar, T. E. and Hirose, K. (2017). Prevalence of semicircular canal hypoplasia in patients with charge syndrome 3c syndrome. *JAMA Otolaryngol Head Neck Surg* **143**, 168–177.

Wood, W., Jacinto, A., Grose, R., Woolner, S., Gale, J., Wilson, C. and Martin, P. (2002). Wound healing recapitulates morphogenesis in Drosophila embryos. *Nat Cell Biol* **4**, 907–912.

Wu, X. and Hammer, J. A. (2021). ZEISS airyscan: optimizing usage for fast, gentle, super-resolution imaging. In *Methods in Molecular Biology*, pp. 111–130. Humana Press Inc.

Yamada, S., Lav, R., Li, J., Tucker, A. S. and Green, J. B. A. (2019). Molar Bud-to-Cap Transition Is Proliferation Independent. *J Dent Res* **98**, 1253–1261.

Yao, D., Zhao, F., Wu, Y., Wang, J., Dong, W., Zhao, J., Zhu, Z. and Liu, D. (2014). Dissecting the Differentiation Process of the Preplacodal Ectoderm in Zebrafish. *Developmental Dynamics* **243**, 1338–1351.

Yu, H., Mouw, J. K. and Weaver, V. M. (2011). Forcing form and function: Biomechanical regulation of tumor evolution. *Trends Cell Biol* **21**, 47–56.

Yurchenco, P. D. (2011). Basement membranes: Cell scaffoldings and signaling platforms. *Cold Spring Harb Perspect Biol* **3**, 1–27.

Zhong, Y., Li, Y. and Zhang, H. (2019). Silencing TBX1 Exerts Suppressive Effects on Epithelial–Mesenchymal Transition and Inflammation of Chronic Rhinosinusitis Through Inhibition of the TGFβ-Smad2/3 Signaling Pathway in Mice. *Am J Rhinol Allergy*.

Zoltan-Jones, A., Huang, L., Ghatak, S. and Toole, B. P. (2003). Elevated Hyaluronan Production Induces Mesenchymal and Transformed Properties in Epithelial Cells. *Journal of Biological Chemistry* **278**, 45801–45810.